Delft University of Technology

Dynamics of the Caribbean

Ocean Eddies and Thermohaline Staircases

van der Boog, C.G.

DOI

Publication date
2021

Document Version
Final published version

Citation (APA)

Important note
To cite this publication, please use the final published version (if applicable).
Please check the document version above.

Dynamics of the Caribbean

Ocean Eddies and Thermohaline Staircases

Carine van der Boog

Dynamics of the Caribbean

Ocean Eddies and Thermohaline Staircases

PROEFSCHRIFT

ter verkrijging van de graad van doctor
aan de Technische Universiteit Delft,
op gezag van de Rector Magnificus prof. dr. ir. T.H.J.J. van der
Hagen
voorzitter van het College voor Promoties,
in het openbaar te verdedigen op donderdag 18 maart 2021 om 10:00

door

Catharina Geertruida VAN DER BOOG

Waterbouwkundig Ingenieur,
Technische Universiteit Delft, Nederland
geboren te Nieuwegein.

Dit proefschrift is goedgekeurd door de promotors en de copromotor.

Samenstelling promotiecommissie:

Rector Magnificus,	voorzitter
Prof. dr. J.D. Pietrzak	Technische Universiteit Delft, promotor
Prof. dr. ir. H.A. Dijkstra	Universiteit Utrecht, promotor
Dr. C.A. Katsman	Technische Universiteit Delft, copromotor

Onafhankelijke leden:

Prof. dr. P.M.J. Herman	Technische Universiteit Delft
Prof. dr. L.R.M. Maas	Universiteit Utrecht
Prof. dr. S.S. Drijfhout	University of Southampton
Prof. dr. S. Speich	Ecole Normale Supérieure
Prof. dr. ir. M. Verlaan	Technische Universiteit Delft, reservelid

Typeset by the author with the LaTeX Documentation System.

Preface

On my first day on the job, I spent my morning on Google Maps to look up where the Caribbean Sea actually was. This indicates how little I knew about this subject when I started this project. At that time, I would never have guessed that this thesis would be its result. This thesis wouldn't be possible without the help of many wonderful people who provided me a helping hand whenever I needed one. I'd like to thank you all for that, as now I'm convinced that I know much more about the Caribbean Sea and the oceans in general than at my first day.

First of all, many thanks to my supervisors Caroline, Julie and Henk. I always enjoy our discussions and appreciate your ways to give feedback a positive twist. You are a great team, and hope you will bundle your forces again in the future! Caroline, as my daily supervisor, your role started off as my 'translator' for all the difficult oceanographic terms. At the same time, you always ensured that I got the most out of my PhD: visits to UCLA, summer schools, conferences, and of course the whale-watching trip in San Diego. Everything was possible, and without your support, I probably would not have finished this thesis on time, and you know that that means a lot to me. Julie, thank you so much for your guidance and enthusiasm! At every conference you made sure that my posters and presentations attracted large crowds. You introduced me to your seemingly endless network, and convinced me that scientists can be very friendly people! I also enjoyed our walks along the Oude Delft. Henk, I am still surprised how you manage to always think five steps ahead. This motivated me to try the same, and has definitely accelerated my progress. I also really appreciate the way you advocated for women in science when I mentioned that some others didn't.

Outside my supervisory team, more people have helped me with all my plans and answered all my oceanography questions. Jeroen, thank you for welcoming me at UCLA and starting an opportunistic project with me. At the start, I think we both had absolutely no clue what would come out of it, and I might have surprised you with all the fundamental questions I asked along the way. Thank you for your patience in answering them, and I'll admit it: Chapter 3 turned out to be one of the nicest chapters in this thesis. Let's hope the reviewers think so too.

Femke, our collaboration had a quick start with only a few months between writing the proposal and sailing out. Not only did the Caribbean cruise result in my first publication, but the staircases we observed form the basis of Chapters 5, 6, and 7 of this thesis. Thank you for showing me how nice observational oceanography is! I would also like to thank the Netherlands Initiative Changing

Oceans, who made this all possible. Also many thanks to Anneke, Dick, Kirstin, Mardik, Meike, Ophélie, Sander, Steve, Tolga, and the Pelagia crew for the great time on board. Mardik, I haven't forgotten our bet on who will publish the first cruise results. Unfortunately, I cannot offer you bubbels at my defense, but I won't forget about them!

I appreciated the meetings with the SCENES group (Adam, Caroline, Cornelis, Henk, Julie, Marcel, Olga, Rebecca, René, Riccardo, Roland and Tjeerd). It was nice to talk only about the Caribbean (and forgetting about all the other parts of the ocean) once in a while.

And then there's of course the physical oceanography group in Delft. Adam, Caroline, Juanma, Julie, Lennart, Nils, Olga, Sabine Steffie and Tim, thank you for welcoming me at the start of my master thesis project and the company throughout my PhD. Nils, your knowledge of models, equations and your endless patience while explaining them to me gave my projects a flying start. Sotiria, both as my supervisor and as a colleague, it was a pleasure to have you around. Every group should have someone like you! I appreciated our group discussions, which have more than once helped me further. I enjoyed the presence of the bachelor and master students in this group. Their commitment and enthusiasm are contagious.

Furthermore, I was lucky to be surrounded by colleagues who were always willing to take a break from our daily struggles. The countless number of times we went to the dean's coffee machine, the lunches in the most inspiring cafeteria of the country, and our walks in the Mekelpark have made my days. I will miss the geintjes van Floris and het nuchtere commentaar van Lennart that always followed. Adam, Alejandra, Dirk, Erik, Floris, Gal, Irene, James, Juanma, Lennart, Marion, Nils, Olga, Otti, Sabine, Said, Silke, Sotiria, Steffie, Stuart, Xuexue, and of course everyone else at EFM and the Lab thank you for providing such a great atmosphere!

Buiten het werk om wil ik al mijn vrienden en familie bedanken die hebben bijgedragen aan dit proefschrift. Sommigen hadden een heel praktische bijdrage door hun hulp bij het maken van mijn stellingen en de omslag van dit boekje. Anderen waren er op momenten waarop ik mijn werk even kon vergeten (ook heel belangrijk!). In het bijzonder wil ik hier mijn paranimfen Nicole en Saskia, en Lisette, Pieter en Johan noemen, die altijd aanwezig zijn op alle belangrijke en onbelangrijke momenten in mijn leven. Ondanks dat dit inmiddels al bijna als vanzelfsprekend voelt, blijft dat toch heel fijn en bijzonder. Met diezelfde vanzelfsprekendheid staan ook mijn ouders altijd voor me klaar. Of het nou is om samen te klussen, schaatsen, wandelen, een hapje te eten of om gewoon even te praten, jullie maken er direct tijd voor vrij. Dankjulliewel!

Thomas, als laatste wil ik jou bedanken. Jouw talent om mij altijd aan het lachen te maken, had ik voor geen goud willen missen! Toen ik vier jaar geleden met mijn promotieonderzoek begon, voorzag je me van advies ('wie schrijft die blijft, wie print die wint') en waarschuwde jij me voor de valkuilen van de Graduate School. Eigenwijs als ik was, wilde ik jou bewijzen dat de Graduate School

uitsluitend nuttige vakken geeft. Helaas moest ik, tot jouw grote plezier, al na een half jaar toegeven dat dat niet het geval was. Jouw advies heb daarna toch maar wel opgevolgd. 🦞

In the previous paragraphs, I've written many words to get a simple message across: I had a great time, thanks to all of you. I hope we meet again soon!

Carine van der Boog
Delft, February 2021

Contents

Summary

The Caribbean Sea is a marginal sea of the North Atlantic Ocean. It is characterized by a large through-flow, which is part of the subtropical gyre and in that form contributes to the upper branch of the Atlantic Meridional Overturning Circulation (Johns et al., 2002). Along this through-flow, the characteristics of the basin affect the variability and structure of the surface and subsurface water masses.

At the surface of the Caribbean Sea, the variability of the flow is dominated by mesoscale anticyclonic eddies (Molinari et al., 1981; Centurioni and Niiler, 2003; Richardson, 2005). These anticyclones are formed in the eastern part of the basin and intensify on their path westward. Similar anticyclones can be found in every ocean basin (e.g., Chelton et al., 2007, 2011b; Gaube et al., 2019). In combination with cyclonic eddies, they account for more than half of the surface variability in the ocean (Chelton et al., 2007). Besides the ecological and climatological impact of mesoscale eddies through the redistribution of fundamental tracers (e.g., Wunsch, 2017), these mesoscale eddies have very interesting dynamics. In the case of Caribbean anticyclones, the processes responsible for their formation and intensification are still a topic for discussion.

At intermediate water depths, the Caribbean waters are susceptible to double-diffusive mixing, which leads to the formation of thermohaline staircases (e.g., Schmitt et al., 1987; Merryfield, 2000; Radko, 2013). Similar staircases have been observed in different areas that contain the right stratification, in for example the Arctic Ocean (Shibley et al., 2017) and Mediterranean Sea (Zodiatis and Gasparini, 1996; Bryden et al., 2014). In the latter, double-diffusive fluxes dominate the vertical transport of heat and salt into Mediterranean Deep Water (Zodiatis and Gasparini, 1996). It is unclear whether the double-diffusive mixing in the Caribbean Sea affects the properties of the underlying water masses as well.

While the dynamics of anticyclones and double-diffusive mixing in other regions has been thoroughly discussed, this thesis investigates them in the Caribbean Sea. The aim is to study the anticyclones as well as the double-diffusive mixing to increase our understanding of the dynamics in this basin and to gain insight in their impacts. To that end, we first performed a hydrographic survey of a Caribbean anticyclone to obtain its vertical structure and origin, and studied the formation and intensification of the anticyclones with two numerical models. Because we deployed Argo floats with a high sampling frequency during the survey, we could use this data to increase our understanding of the regional impact of

double-diffusive mixing on the properties of the lower-lying water masses. In combination with the data from other Argo floats and Ice-Tethered Profilers, we also developed a dataset of thermohaline staircases that we used to assess their global impact on the ocean circulation. A brief summary of each chapter is given in the following paragraphs.

Hydrographic survey of a Caribbean anticyclone

To study the vertical structure and ecological impact of anticyclones in the Caribbean Sea, we performed a combined hydrographic and biological survey of a mesoscale anticyclone in the Caribbean Sea between 4 and 11 February 2018. During this survey, we collected vertical profiles of temperature, salinity, oxygen, chlorophyll and turbidity at 15 CTD (conductivity, temperature, depth) stations. The stations were placed on a line across an anticyclone. At these stations, nutrient samples of phosphate, silicate, nitrate and nitrite were collected. Between the stations, measurements of upper ocean velocity, surface temperature and salinity were taken and visual survey of birds and pelagic megafauna were conducted. By using temperature and salinity profiles in combination with velocity measurements we showed that the anticyclone was surface intensified in the upper 150 m of the water column and had a radius of 90 km. Silicate measurements and chlorophyll concentrations indicated that the core of the anticyclone entrained waters from the Orinoco River plume. The visual survey showed that, while higher densities of flying fish were observed at the edge of the anticyclone, there were no increased densities of predators. Below the surface, we observed a barrier layer with strong temperature inversion. Furthermore, the survey confirmed the formation of thermohaline staircases in the Caribbean Sea, as we detected these structures at 12 out of 15 stations.

The origin of Caribbean anticyclones

Despite the fact that the hydrographic survey indicated that the anticyclone originated near the mouth of the Orinoco River, the source of its anticyclonic vorticity remains unknown. To gain insight into this source of, we analyzed the vorticity fluxes in the eastern part of the Caribbean Sea in more detail. To that end, we performed a high-resolution numerical simulation of the eastern Caribbean Sea using the regional ocean model system (ROMS). Based on this simulation, we concluded that the bulk of the inflowing vorticity in the eastern Caribbean Sea is generated at the Lesser Antilles. We found that during the collision of an anticyclonic North Brazil Current (NBC) ring with the Lesser Antilles, the vorticity inflow into the eastern Caribbean increased. The bulk of this increase was generated locally near the topography of the islands. Especially the islands of St. Lucia and Grenada appeared to be hotspots for vorticity generation, where the vorticity generation was triggered by enhanced transport through the passages at these islands. While these enhanced transports were induced by the collision

of upstream NBC rings with the Lesser Antilles, the vorticity of the NBC rings themselves only slightly enhanced the vorticity flux into the Caribbean Sea.

Westward intensification of Caribbean anticyclones

After their formation, Caribbean anticyclones intensify on their path westward (Carton and Chao, 1999; Pauluhn and Chao, 1999; Andrade and Barton, 2000; Richardson, 2005). During this intensification, they propagate along the up-welling region that is located in the southern part of the basin (Astor et al., 2003). To study the impact of the upwelling on the intensification of the anticyclones, we developed a regional setup of the Caribbean Sea with the Massachusetts Institute of Technology general circulation model (MITgcm). With this setup, we per-formed a set of five simulations in which we step by step altered the upwelling strength by adjusting the magnitude of the zonal wind stress. We found that eddy kinetic energy in the Caribbean Sea was dominated by the anticyclones that intensify. The simulations showed that these anticyclones advect upwelling fila-ments offshore. Therefore, we argued that the westward intensification is driven by the advection of cold upwelling filaments, where the advection increases the horizontal density gradients of the anticyclones and directly strengthens their vertical shear. This behavior was confirmed by the different simulations. More-over, we found that the strength of the wind stress, which regulates the north-ward Ekman transport, affected the advection of the Amazon and Orinoco River plume as well: A weaker wind stress resulted in less wind-driven mixing of the river plume and a farther advection into the basin. This led to a strengthening of the salinity gradients of the anticyclones compared to the temperature gradi-ents. Because the density components of the temperature and salinity gradients were of a similar order of magnitude, these results could be used to explain parts of the seasonal and interannual variability of the anticyclones in the Caribbean Sea. Therefore, we concluded that the intensification of Caribbean anticyclones is affected by both upwelling and the river plumes.

A global dataset of thermohaline staircases

Below the surface of the Caribbean Sea, which is dominated by the presence of anticyclonic eddies, the subsurface waters are susceptible to double-diffusive mixing. To assess the impact of double-diffusive mixing on the properties of wa-ter masses in the Caribbean Sea, we analyzed thermohaline staircases that arise from double diffusion. Because these staircases are visually striking structures in the vertical profiles of both temperature and salinity, we developed an algorithm to automatically detect thermohaline staircases based on their vertical structure. The advantage of using the structure of the thermohaline staircases over assump-tions based on the Turner angle is that we can this to assess the performance the algorithm. The algorithm first identifies subsurface mixed layers. Next, the in-terfaces in between the mixed layers are assessed to determine whether they

contain temperature and salinity gradients and whether they are thin compared to the mixed layers. As a final step, the algorithm locates sequences of interfaces, which are labeled as thermohaline staircases. We applied this algorithm on 487,493 temperature and salinity profiles and obtained a global dataset of the occurrence of thermohaline staircases and their characteristics.

The global impact of double-diffusive mixing

Once we obtained a global dataset of thermohaline staircases, we cannot only assess the impact of thermohaline staircases on the properties of water masses in the Caribbean Sea, but also study their impact on the global ocean circulation. In total, approximately 40 % of the ocean is susceptible to double-diffusive mixing (You, 2002). We found that not all of these regions contain thermohaline staircases as only 14 % of the observational profiles actually contained staircases. Moreover, the staircases with multiple steps were clustered in specific regions. One of this regions was a so-far unknown staircase region in the Great Australian Bight. Although the impact of these staircases on the water masses in this region remains unclear, they might affect the salt content of the Tasman Leakage waters that originate in this region. Because the salt content of the Tasman Leakage waters is considered to affect the stability of the global overturning circulation(Gordon, 2003; Speich et al., 2007), the double-diffusive salt fluxes in this region might impact the stability of this overturning. Furthermore, we estimated the combined contribution of all thermohaline staircases to the global mechanical energy budget. We found that thermohaline staircases contributed 7.5 GW [0.1 GW; 32.8 GW] to the global ocean's mechanical energy budget. This was much less than estimates of the energy required to maintain the observed ocean stratification (roughly 2 TW, Munk, 1966). Therefore, we concluded that the impact of thermohaline staircases on the global mechanical energy budget is very limited.

Double-diffusive mixing in the Caribbean Sea

Previous studies speculated that double-diffusive mixing in thermohaline staircases can impact the properties of the underlying Antarctic Intermediate Water (AAIW) in the Caribbean Sea through the vertical salt flux (You, 1999; St. Laurent and Schmitt, 1999; Schmitt, 2005). However, this effect has not been quantified. Therefore, we explored whether the time-averaged spatial variations seen in the properties of AAIW along its mean propagation path could be explained by vertical fluxes resulting from double-diffusive mixing. To that end, we used the global dataset of thermohaline staircases. We found that 7 % of the Caribbean profiles contains staircases. In the staircase layer, we detected a density flux ratio of 0.8, which indicated that the density component of the salt flux exceeds the density component of the heat flux. We found that the time-averaged temperature and salinity of AAIW increased along its path and that the

density component of the salinity increase exceeded the temperature increase. More specifically, we showed that the spatial variation of AAIW can be explained by the double-diffusive fluxes out of the staircase layers by using a steady-state advection-diffusion equation.

Samenvatting

De Caribische Zee is een randzee van de noordelijke Atlantische Oceaan. Dit bekken wordt gekenmerkt door een grote doorstroom die onderdeel is van de subtropische gyre en daarmee bijdraagt aan de bovenste tak van de zogenaamde *Atlantic Meridional Overturning Circulation* (Johns et al., 2002). Tijdens deze doorstroom beïnvloeden de eigenschappen van het bekken de variabiliteit en de structuur van de stroming.

Aan het oppervlak van de Caribische Zee wordt variabiliteit van de stroming op de meso-schaal gedomineerd door anticyclonale wervels (Molinari et al., 1981; Centurioni and Niiler, 2003; Richardson, 2005). Deze anticyclonen ontstaan in het oostelijk deel van het bekken en versterken op hun pad westwaarts. Vergelijkbare anticyclonen komen voor in elk oceaanbekken (e.g., Chelton et al., 2007, 2011b; Gaube et al., 2019). Samen met cyclonale wervels, nemen deze wervels meer dan de helft van de oceaan's oppervlaktevariabiliteit voor hun rekening (Chelton et al., 2007). Naast de ecologische en klimatologische invloed van deze wervels door middel van de herverdeling van fundamentele tracers (e.g., Wunsch, 2017), is de dynamica van deze wervels ook erg interessant. In het geval van de Caribische anticyclonen is hun origine en versterking nog onderwerp van discussie.

Op grotere diepten is het water van de Caribische Zee vatbaar voor dubbele diffusie wat zich uit in het ontstaan van thermohaliene trappen (e.g., Schmitt et al., 1987; Merryfield, 2000; Radko, 2013). Zulke trappen worden over de hele wereld waargenomen, zoals bijvoorbeeld in de Noordelijke IJszee (Shibley et al., 2017) en in de Middellandse Zee (Zodiatis and Gasparini, 1996; Bryden et al., 2014). In dit laatste geval domineert dubbele diffusie het verticale warmte- en zouttransport naar Middellands Diep Water (Zodiatis and Gasparini, 1996).

Terwijl de dynamica van de anticyclonen en van de dubbele diffusie grondig is onderzocht in andere regio's, focust het onderzoek in dit proefschrift zich op de Caribische Zee. Het doel hiervan is om de anticyclonen en dubbele diffusie te bestuderen om ons begrip van de dynamica van dit bekken te vergroten en om inzicht te verkrijgen in hun invloed. We hebben de Caribische anticyclonen onderzocht met behulp van een hydrografisch onderzoek. Dit gaf ons inzicht in de oorsprong en structuur van een wervel. Vervolgens hebben we de formatie en versterking onderzocht met twee numerieke modellen. De dubbele diffusie hebben we bestudeerd met Argo boeien die we hebben uitgezet tijdens het hydrografische onderzoek. We hebben de data van deze boeien gebruikt om de regionale invloed van dubbele diffusie op de eigenschappen van de lagergelegen

watermassa's te begrijpen. In combinatie met de data van andere Argo boeien en de zogenaamde met-ijs-verbonden boeien, hebben we een wereldwijde dataset van thermohaliene trappen gemaakt die we vervolgens gebruikt hebben om hun mondiale effect te schatten. Een korte samenvatting van elk deelonderzoek wordt gegeven in de volgende alinea's.

Hydrografisch onderzoek van een Caribische anticycloon

Om de verticale structuur en invloed van anticyclonale wervels op de verspreiding van nutriënten in de Caribische Zee te bestuderen, hebben we een gecombineerde hydrografische en biologisch metingen van een anticyclonale wervel in de Caribische Zee genomen tussen 4 en 11 februari 2018. Tijdens dit onderzoek, hebben we verticale profielen van de temperatuur, het zoutgehalte, het zuurstofgehalte, het chlorofyl en de troebelheid genomen op 15 stopplaatsen. Op deze stopplaatsen hebben we ook monsters genomen van voedingsstoffen (fosfaat, silicaat, nitraat en nitriet). Tussen de stations, zijn metingen gedaan van de ondiepe snelheden, de oppervlaktetemperatuur en -zoutgehalte. Daarnaast zijn visuele tellingen van vogels en van pelagische megafauna uitgevoerd. Met behulp van de profielen van de temperatuur, het zoutgehalte en de snelheidsmetingen hebben we aangetoond dat de anticycloon versterkt was in de bovenste 150 m van de waterkolom en een straal van 90 km had. De silicaatmetingen en chlorofylconcentraties geven aan dat de kern van de anticycloon water van de rivierpluim van de Orinoco bevat. De visuele metingen laten zien dat, ondanks dat er wel hogere dichtheden van vliegende vissen zijn geobserveerd, er geen toename van roofdieren was. Onder het oppervlak hebben we een barrièrelaag met een sterke temperatuurinversie gesignaleerd. Daarnaast heeft dit onderzoek bevestigd dat in de Caribische Zee thermohaliene trappen kunnen ontstaan; we hebben deze trappen gedetecteerd bij 12 van de 15 stopplaatsen.

De oorsprong van Caribische anticyclonen

Ondanks dat het hydrografisch onderzoek heeft aangeduid dat Caribische anticyclonen ontstaan in het oostelijk deel van het bekken, blijft het onduidelijk waar de draaiing van deze anticyclonen vandaan komt. Om inzicht te krijgen in de bron van deze draaiing, gebruiken we de vorticiteit dat is gedefinieerd als de rotatie van het snelheidsveld. We analyseren de anticyclonale vorticiteit en vorticiteitsstromen naar de Caribische Zee in detail met behulp van een numerieke simulatie. Deze simulatie met een hoge resolutie omvatte het oostelijk deel van de Caribische en is uitgevoerd met het regionaal oceaan modelleer systeem (ROMS). Gebaseerd op deze simulatie, concluderen wij dat het merendeel van de vorticiteit die het oostelijk deel van de Caribische Zee binnenstroomt wordt gegenereerd bij de Kleine Antillen. In totaal betreft dit 67 % van de anticyclonale vorticiteitsstroom en 57 % van de binnenkomende cyclonale vorticiteitsstroom. We signaleren dat tijdens de botsing van een Noord-Braziliaanse stromingsring

(NBC ring) op de Kleine Antillen de vorticiteitsstromen toenemen, en dat wederom hiervan de meeste vorticiteit bij de Kleine Antillen gegenereerd is. Met name rondom St. Lucia en Grenada wordt veel vorticiteit gegenereerd. Op die plekken wordt de vorticiteitsgeneratie veroorzaakt door een toename in het transport door de passages tussen de eilanden. Het is belangrijk om te realiseren dat ondanks dat deze verhoogde transporten veroorzaakt worden door de botsing van NBC ringen met de Kleine Antillen, de vorticiteit van de NBC ringen zelf maar een klein deel van toename in de vorticiteitsstroming kunnen verklaren.

Westwaartse versterking van Caribische anticyclonen

Nadat Caribische anticyclonen zijn ontstaan, hebben deze de neiging om te versterken op hun pad westwaarts (Carton and Chao, 1999; Pauluhn and Chao, 1999; Andrade and Barton, 2000; Richardson, 2005). Deze versterking vindt plaats terwijl ze langs een regio met windgedreven opwelling komen die het zuidelijk deel van het bekken kenmerkt (Astor et al., 2003). Om te begrijpen hoe de opwelling de versterking van de anticyclonen beïnvloedt, hebben we een regionale opstelling van de Caribische Zee met het Massachusetts Institute of Technology algemeen circulatie model (MITgcm) gemaakt. Met deze opstelling hebben we vijf numerieke simulaties gedaan waarin we de sterkte van de opwelling hebben gereguleerd door de zonale windbelasting te variëren. We hebben ontdekt dat de kinetische energie van alle wervels wordt gedomineerd door een klein aantal anticyclonen per jaar. Deze anticyclonen adverteren filamenten met water uit de wind-gedreven opwelling regio's van de kust af. Daarom stellen wij dat de westwaartse versterking gestuurd wordt door de advectie van deze filamenten. Deze advectie zorgt voor een versterking van de horizontale dichtheidsgradiënten van de wervels, wat ervoor zorgt dat de verticale snelheidsgradiënten toenemen. De werking van dit mechanisme is bevestigd aan de hand van de resultaten van de verschillende simulaties. Deze simulaties hebben daarnaast laten zien dat de sterkte van de zonale windbelasting, die het noordwaartse Ekmantransport reguleert, ook de spreiding van de rivierpluimen van de Amazone en Orinoco beïnvloedt: Een zwakker Ekmantransport resulteert in minder windgedreven menging van de rivierpluim en een verdere spreiding van de rivierpluim in de Caribische Zee. Dit leidt tot een relatief grotere invloed van de horizontale gradiënten in zoutgehalte ten opzichte van de horizontale temperatuursgradiënten. Daarom concluderen wij dat de versterking van Caribische anticyclonen beïnvloed wordt door een samenspel van opwelling en de rivierpluimen.

Mondiale dataset van thermohaliene trappen

Onder het oppervlak dat gedomineerd wordt door anticyclonale wervels, zijn de wateren van de Caribische Zee vatbaar voor dubbele diffusie. Om de invloed van dubbele diffusie in de Caribische Zee te kunnen schatten, analyseren we de kenmerken van thermohaliene trappen die door dubbele diffusie ontstaan. Omdat

dat deze trappen duidelijk zichtbare structuren zijn in verticale profielen, hebben we een algoritme ontwikkeld dat thermohaliene trappen detecteert op basis van hun verticale structuur. Het voordeel van het gebruik van de structuur in plaats van aannames op basis van de fysica, is dat we de kenmerkende fysische eigenschappen van thermohaliene trappen, zoals de Turnerhoek, kunnen gebruiken om de resultaten te verifiëren. In het algoritme, identificeren we eerst de menglagen onder het oppervlak. Vervolgens analyseren we de lagen tussen de menglagen om vast te stellen of er grote verticale gradiënten in temperatuur en zoutgehalte zijn en of de tussenlaag dunner is dan de aangrenzende menglagen. Als dat het geval is, zoekt het algoritme naar reeksen van smalle tussenlagen. Deze reeksen worden vervolgens gelabeld als thermohaliene trappen. We hebben dit algoritme toegepast op 487.493 verticale profielen van de temperatuur en het zoutgehalte. Het resultaat is een mondiale dataset van thermohaliene trappen.

Het mondiale effect van dubbele diffusie

Nadat we een mondiale dataset van thermohaliene trappen hadden gemaakt, kunnen we niet alleen de invloed van thermohaliene trappen in de Caribische Zee onderzoeken, maar ook wat hun mondiale invloed is. In totaal is 40 % van de oceaan vatbaar voor dubbele diffusie (You, 2002). Wij constateren dat niet al deze regio's thermohaliene trappen bevatten, omdat maar 14 % van alle profielen in de dataset trappen vertonen. Daarnaast zijn deze thermohaliene trappen voornamelijk geconcentreerd in specifieke regio's. Een van deze regio's is een tot-nu-toe onbekende regio in de Grote Australische Golf. Ondanks dat de invloed van de thermohaliene trappen op de watermassa's in deze regio onbekend is, is het niet ondenkbaar dat ze het zoutgehalte van de Tasmaanse Lekkage beïnvloeden. Bovendien hebben we ook een schatting van de totale bijdrage van alle thermohaliene trappen aan de mondiale mechanische energiebalans gemaakt. We schatten dat deze een totale bijdrage van 7,5 GW [0,1 GW; 32,8 GW] hebben. Omdat dit is veel minder dan het budget van deze balans (ongeveer 2 TW, Munk, 1966), concluderen we dat de invloed van thermohaliene trappen op de mondiale mechanische energiebalans zeer beperkt is.

Dubbele diffusie in de Caribische Zee

Ondanks dat verschillende studies hebben gespeculeerd dat dubbele diffusie in thermohaliene trappen de temperatuur en zoutgehalte van Antarctisch Tussenwater (AAIW) in de Caribische Zee beïnvloeden (You, 1999; St. Laurent and Schmitt, 1999; Schmitt, 2005), is dit effect nog niet gekwantificeerd. Daarom hebben we bestudeerd of de verticale transporten gestuurd door dubbele diffusie de tijdgemiddelde ruimtelijke variatie van AAIW kunnen verklaren. Gebruik makend van de mondiale dataset, vinden we dat 7 % van de profielen in de Caribische Zee thermohaliene trappen heeft. In deze laag met trappen vin-

den we een verhouding van de dichtheidstransporten van 0,8. Dit geeft aan dat de dichtheidscomponent van het zouttransport de dichtheidscomponent van het warmtetransport overschrijdt. We vinden dat de tijdsgemiddelde temperatuur en zoutgehalte van AAIW langs het pad van propagatie toenemen en dat de dichtheidscomponent van het zoutgehalte deze van het temperatuur overschrijdt. We laten zien dat deze waargenomen ruimtelijke variatie van AAIW verklaard kan worden met een advectie-diffusie vergelijking die dubbele diffusie representeert.

Chapter 1

Introduction

1.1   Mixing in the ocean

The dynamics of the ocean are to a large extent determined by mixing processes (Wunsch, 2017). These mixing processes regulate the storage and redistribution of fundamental tracers such as heat, fresh water, carbon and oxygen (Wunsch, 2017). There are two major types of mixing: turbulent mixing and double-diffusive mixing (Thorpe, 2005; Radko, 2013). In this thesis, these two types of mixing are studied with a special focus on the Caribbean Sea with the aim to gain insight into the dynamics and mixing of this basin. The surface flow in the Caribbean Sea is dominated by large turbulent structures, referred to as eddies, while the deep flow is dominated by double-diffusive mixing that leads to the formation of thermohaline staircases. In the following sections, both types of mixing are introduced separately.

1.2   The turbulent ocean

Ocean currents flow through every ocean basin. These currents are turbulent on many scales ranging from small scales of millimeters up to large scales that have dimensions of hundreds of kilometers, referred to as the mesoscale. In general, the mesoscale turbulent structures extract energy from the mean flow and feed the smaller-scale turbulent structures, which is referred to as the energy cascade process (e.g., Nieuwstadt, 1998). The mesoscale structures have a total kinetic energy that is an order of magnitude larger than the kinetic energy of the mean flow (Gill et al., 1974; Wyrtki et al., 1976; Richardson, 1983; Danabasoglu et al., 1994; Fu et al., 2010). This makes the mesoscale structures the most energetic turbulent structures in the ocean (Fu et al., 2010).

The mesoscale turbulent structures are rotating due to the contribution of the rotation of the Earth to the momentum balance (Talley et al., 2011). These rotating structures, referred to as eddies, are visible as positive and negative anomalies in the sea level (Fig. 1.1). Mesoscale eddies with a high density compared to their surroundings are visible as negative anomalies in sea level
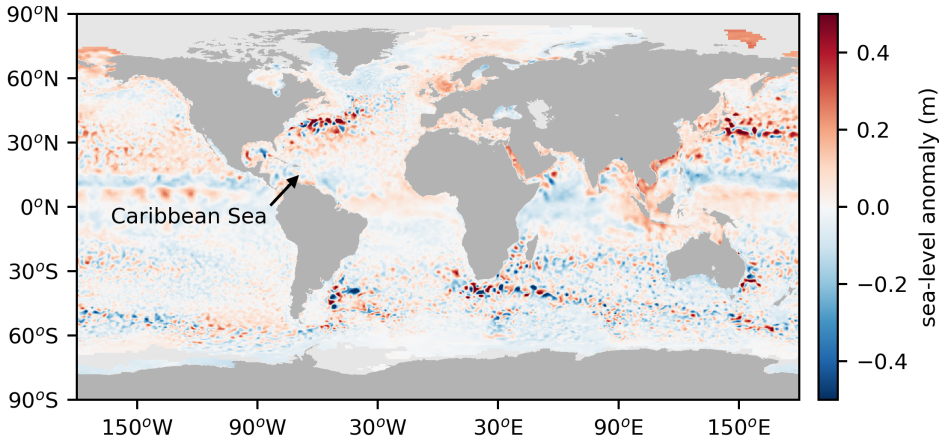
Figure 1.1: Sea-level anomaly with respect to the global mean sea level at the start of my PhD project (1 December 2016). Blue and red anomalies correspond to cyclonic and anticyclonic eddies, respectively. Data is computed from multi-mission altimeter satellite gridded sea surface heights and downloaded from the Copernicus Marine Environment Monitoring Service (http://marine.copernicus.eu).

(blue in Fig. 1.1). They rotate in the same direction as the Earth and are referred to as cyclones. Positive sea-level anomalies correspond to anticyclones that have a negative density anomaly with respect to their surroundings and rotate in the opposite direction to the Earth's rotation (Fig. 1.1).

At any given time, mesoscale eddies cover nearly a third of the ocean's surface (Gaube et al., 2019). More specifically, eddies with amplitudes of 5-25 cm and diameters of 100-200 km account for more than 50 % of the ocean's variability (Chelton et al., 2007). They originate from time variations in the atmospheric forcing, meandering movements of the currents, interaction with topography or from other instabilities of the flow and fulfill an essential role in the mixing and transport of fluids (e.g., Stammer and Wunsch, 1999).

The impact of the these mesoscale eddies is diverse, but they mainly disperse particles and mix tracers in horizontal and vertical directions. In the horizontal, eddies contribute to the observed time-mean heat transport (Wunsch, 1999; Jayne and Marotzke, 2002; Ni et al., 2020), and can play a dominant role in the advection of river plumes and other nutrient-rich waters (Oschlies, 2002; Stramma et al., 2013; Coles et al., 2013; Fournier et al., 2017). In the vertical, eddies may alter the mixed layer depth (Klein et al., 1998; Gaube et al., 2019) and entrain nutrients from below the mixed layer (Falkowski et al., 1991; Zhang et al., 2014; Gaube, 2015).

Mesoscale eddies can in principle originate everywhere (Chelton et al., 2007, 2011b), but regions with higher eddy kinetic energy are located near flows with a strong velocity shear (Wyrtki et al., 1976; Zhang and Qiu, 2018). The cyclones and anticyclones in these regions are visible as the strong blue and red anomalies
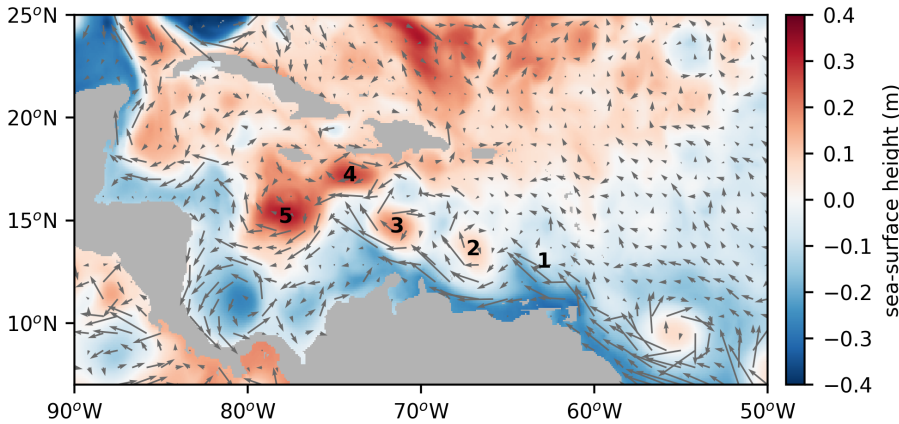
Figure 1.2: Sea-surface height with respect to the mean sea level in the Caribbean Sea (50°W-90°W, 8°N-25°N) on 4 January 2018. Arrows indicate direction of the flow. Numbers 1-5 indicate anticyclonic eddies present at that time in this domain. Numbers increase along the direction of the mean flow. Data is taken from the GLORYS Ocean Reanalysis model, and downloaded from the Copernicus Marine Environment Monitoring Service (http://marine.copernicus.eu).

in Figure 1.1 and have, on average, larger density anomalies with respect to their surroundings. Averaged over the whole world, there is a slight preference for the formation of cyclones (Chelton et al., 2011b). However, anticyclones tend to have a longer life time and are able to propagate further (Chelton et al., 2011b). Surprisingly, these long-lived anticyclones also have the tendency to intensify over time (Dewar and Killworth, 1995; Yavneh et al., 1997; Koszalka et al., 2009; Chen and Han, 2019).

A clear example of anticyclones that intensify over time are Caribbean anticyclones. As the aim of this thesis is to gain insight into the dynamics and mixing in the Caribbean, we will study the life cycle of these anticyclones in more detail in this thesis. The different stages of the intensification of Caribbean anticyclones are visible in Figure 1.2. The weakest anticyclones (number 1 and 2 in Fig. 1.2) are found in the eastern part of the basin where most Caribbean anticyclones are formed (Richardson, 2005). The sea-level anomaly of the anticyclones increases when following the mean flow towards the west (number 3-5 in Fig. 1.2). This spatial variation in sea-surface anomalies of anticyclones is also visible in the sea-surface variance (Fig. 1.3, Andrade and Barton, 2000; Bosch et al., 2002; Oey et al., 2003; Chelton et al., 2011b), which suggests that it is a typical behavior of Caribbean anticyclones. Because mesoscale turbulent features extract energy from the mean flow, it is necessary to first have a clear view of the mean flow and characteristics before turning to this spatial pattern.
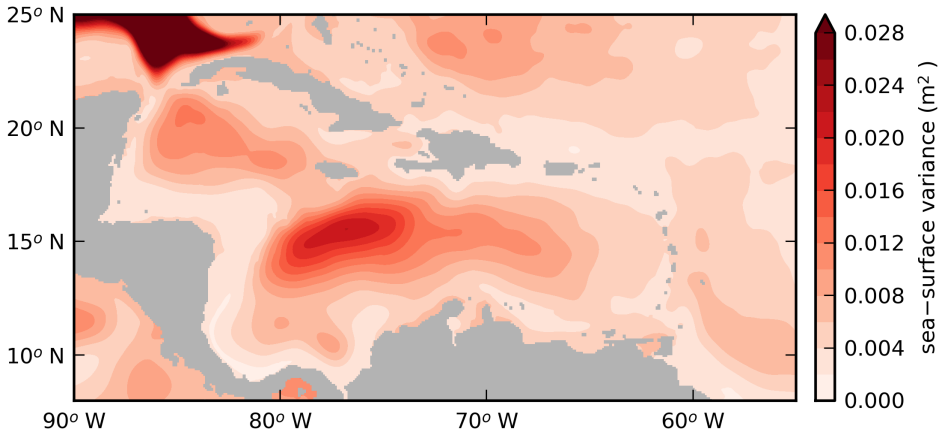
Figure 1.3: Sea-level variance (m²) computed from daily fields sea-level anomalies with respect to the mean sea level in this domain (50°W-90°W, 8°N-25°N) from 1 January 2008 to 31 December 2017. Data is taken from the GLORYS Ocean Re-analysis model, and downloaded from the Copernicus Marine Environment Monitoring Service (http://marine.copernicus.eu).

1.2.1   The mean flow and water masses in the Caribbean Sea

The Caribbean Sea is a highly stratified marginal sea of the North Atlantic Ocean that contains six distinctive water masses. Water masses are bodies of water that have distinctive physical properties, which can be traced back to a specific formation region (Talley et al., 2011). In the Caribbean Sea, these water masses have a combined transport of approximately 25 Sv (1 Sv = 10^6 m³ s^{-1} Johns et al., 2002; Casanova-Masjoan et al., 2018) and they enter the basin along the eastern boundaries through the Lesser Antilles (Fig. 1.4).

The main part of the flow in the Caribbean Sea is transported by Caribbean Surface Water (CSW) and the Subtropical Underwater (STUW) that are located in the upper 200 meter of the water column (Morrison and Nowlin, 1982; Hernández–Guerra and Joyce, 2000; Joyce et al., 2001). These two water masses contain relatively warm and saline waters. The salinity of CSW is lower than the salinity of the lower-lying STUW, because it contains river outflow from the Amazon and Orinoco River (Fig. 1.5, Froelich Jr. et al., 1978; Morrison and Nowlin, 1982). The subsurface salinity maximum of STUW, located at approximately 150 m depth, can be traced back to regions with high evaporation in the central tropical Atlantic (Wüst, 1964; Morrison and Nowlin, 1982; Montes et al., 2016).

Below these water masses, patches of Sargasso Sea Water (SSW) have been identified at roughly 300 m depth (Kinard et al., 1974; Morrison and Nowlin, 1982). These patches enter the Caribbean Sea through the northeastern passages of the Lesser Antilles (Fig. 1.4). Slightly deeper at approximately 400-500 m depth, Tropical Atlantic Central Water (TACW) enters the basin through the southeastern passages of the Lesser Antilles (Fig. 1.4, Carrillo et al., 2016). Through these same passages, Antarctic Intermediate Water (AAIW) also enters

the Caribbean Sea between 500 and 1000 m depth (Tsuchiya, 1989). AAIW originates near Antarctica and contains relatively fresh and cold characteristics compared to the other water masses (Tsuchiya, 1989).

Only a small part of the transport is accounted for by the deepest water mass, North Atlantic Deep Water (NADW), which enters the Caribbean in the northeastern part of the basin (Fig. 1.4, Hernández–Guerra and Joyce, 2000; Joyce et al., 2001). Because the bulk of NADW in the Caribbean Sea is located below 1800 m, which is deeper than the deepest passage, it has a long residence time of approximately 150 years (Joyce et al., 1999). This long residence time decreases its decadal variability, which makes the Caribbean a reliable location to monitor possible changes of this water mass on climatic time scales (Joyce et al., 1999).

Once the flow has entered the Caribbean Sea, the surface waters encounter an upwelling region (Fig. 1.5, Gordon, 1967). This upwelling results from the interaction of the wind forcing with the apparent forces due to the rotation of the Earth, which drives the surface waters offshore with the so-called Ekman transport. Following the conservation of mass, deeper waters move upward near the coast. These waters, consisting mostly of STUW, are colder, more saline and contain more nutrients than the surface waters (Muller–Karger et al., 1989; Rueda–Roa and Muller–Karger, 2013; Rueda-Roa et al., 2018). The result is a horizontal density gradient that strengthens the westward flow (Rueda-Roa et al., 2018).

After the surface flow passed the upwelling region, it continues westward towards the Nicaraguan Rise (NR in Fig. 1.5). There, the main part of the flow deflects northwards and continues towards the Gulf of Mexico (GoM in Fig. 1.5). Another part of the flow continues southward and recirculates in the Panama-Colombia gyre (PCG in Fig. 1.5, Andrade and Barton, 2000).

The mean flow in the Caribbean Sea is part of the subtropical gyre in the North Atlantic, which is a system of wind-driven ocean currents circulating in an anticyclonic direction that spans the entire North Atlantic Ocean at mid latitudes. The gyre contributes to the Atlantic Meridional Overturning Circulation (AMOC), which is defined as the zonal integral of the flow in the Atlantic Ocean (e.g., Zhang et al., 2019; Bower et al., 2019). The AMOC describes the inter-hemispheric volume transport by the oceans and consists of a northward-flowing upper limb and a southward-flowing lower limb. At high latitudes, the relatively warm waters of the northward flowing upper limb cool and sink along the boundaries of the subpolar gyre, before they return southward as part of the lower limb (Spall and Pickart, 2001; Sayol et al., 2019; Georgiou et al., 2020).

The waters in the Caribbean Sea contribute to the upper limb of the AMOC as they enter the basin in the east and they exit the basin in the north. Variations in this flow that originate in the Caribbean Sea can thus modify the flow farther northward. Evidence for this effect has been suggested by Oey et al. (2003) and van Westen et al. (2018), who both showed that the variability in the Caribbean Sea directly affects the downstream variability in the Gulf of Mexico and beyond.
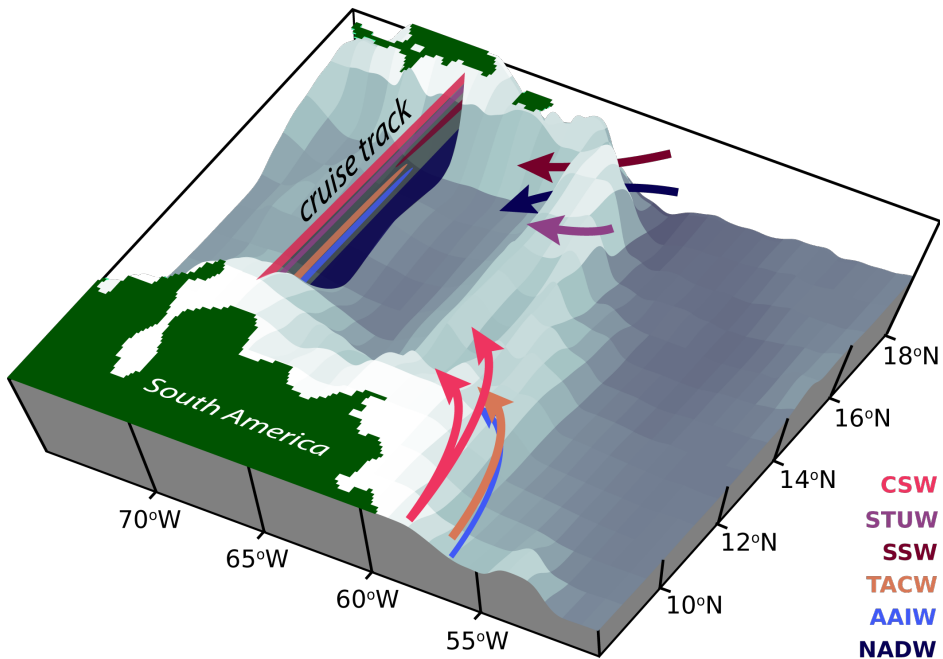
Figure 1.4: 3D Schematic of how water masses enter the eastern Caribbean Sea. Indicated water masses are AAIW = Antarctic Intermediate Water, CSW = Caribbean Surface Water, NADW = North Atlantic Deep Water, SSW = Sargasso Sea Water, STUW = Subtropical Underwater, TACW = Tropical Atlantic Central Water.

1.2.2   Caribbean anticyclones

Compared to eddies in other ocean basins, the Caribbean anticyclones occur frequently and have large diameters (> 200 km Chelton et al., 2007, 2011b). They originate in the eastern part of the basin, where the flow is variable due to a wide range of processes (Fig. 1.5). For example, the outflow of the Orinoco River (Chérubin and Richardson, 2007), the strong winds (Oey et al., 2003), the interaction of the flow with the Lesser Antilles (Molinari et al., 1981), and the variability of the upstream flow itself (Jochumsen et al., 2010) could all trigger the formation of anticyclones. Each of these mechanisms is discussed in more detail in the following paragraphs.

First of all, the fresh water of the Orinoco river outflow is located near the eastern boundary of the Caribbean Sea (Fig. 1.5). The Orinoco River is the third largest river in the world with an average discharge of 33,000 m^3 s^{-1} (Vizy and Cook, 2010). In combination with the fresh water in the Amazon River plume, which is advected towards the Caribbean Sea, these large river plumes dominate the surface salinity in the Caribbean Sea (Froelich Jr. et al., 1978). Chérubin and Richardson (2007) found that, at the arrival of the combined Amazon-Orinoco
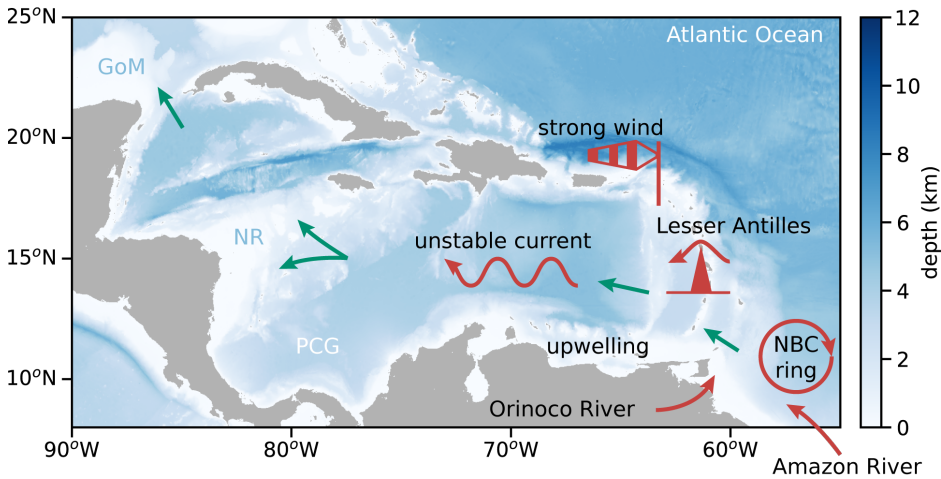
Figure 1.5: Bathymetry of the Caribbean Sea. The green arrows indicate the direction of the mean surface currents. The red icons show the mechanisms that have been suggested as potential formation mechanisms of Caribbean anticyclones. NR = Nicaraguan Rise, GoM = Gulf of Mexico, PCG = Panama Colombia Gyre

River plume in summer, the salinity fronts became stronger, and that this coincided with an increase of the eddy kinetic energy. In combination with a higher number of observations of anticyclones during this period, Chérubin and Richardson (2007) argued that there is a dynamical link between the presence of freshwater plume and the formation of anticyclones.

Second, the wind forcing could also trigger the formation of anticyclones. The mean wind forcing in the Caribbean consists of easterlies that persist year-round (Mo et al., 2005; Muñoz et al., 2008). The spatial variation of these easterlies, in combination with topography, could generate anticyclones in the northern part of the basin (Oey et al., 2003). However, the majority of the Caribbean anticyclones do not originate in this region (Fig. 1.3), which suggests that other effects play a role as well.

These other effects could be the upstream variability, which encompasses both the variability of the flow upstream and as well as the interaction of that flow with the Lesser Antilles. It has been suggested that the collision of upstream North Brazil Current (NBC) rings with the Lesser Antilles could trigger the formation of Caribbean anticyclones (Fratantoni and Glickson, 2002; Goni and Johns, 2003; Jochumsen et al., 2010). Laboratory experiments and idealized numerical studies suggested that the NBC rings can squeeze through the passages between the Lesser Antilles (Simmons and Nof, 2002; Cenedese et al., 2005; Klapp, 2013). However, more realistic numerical modeling studies do not agree on whether Caribbean anticyclones are formed as remnants of NBC rings (Fratantoni and Glickson, 2002; Goni and Johns, 2003; Jochumsen et al., 2010; van Westen et al., 2018) or not (Chérubin and Richardson, 2007; Jouanno et al.,

2008, 2009).

Although it remains unclear what triggers the formation of the anticyclones, it is clear that the anticyclones become more energetic after formation (Andrade and Barton, 2000; Centurioni and Niiler, 2003; Richardson, 2005). In general, the anticyclones intensify on their path westward before they dissipate over the Nicaraguan Rise (Fig. 1.3, Molinari et al., 1981). This intensification has been identified with both surface drifters and sea-surface height anomalies from satellite altimetry (Carton and Chao, 1999; Pauluhn and Chao, 1999; Andrade and Barton, 2000; Centurioni and Niiler, 2003; Richardson, 2005). Despite the fact that this intensification of Caribbean anticyclones is clearly visible in observational data, only a few studies so far have explored the governing dynamics.

Based on satellite altimetry, Andrade and Barton (2000) show that the location of the maximum eddy kinetic energy is located near the maximum anticyclonic wind stress curl in the basin. Therefore, they argue that the intensification is mainly wind-driven. However, Richardson (2005) links the westward intensification of the anticyclones to the anticyclonic shear of the mean flow. To clarify this contradiction, Jouanno et al. (2009) studied the westward intensification in more detail. They show that Caribbean anticyclones extract energy from the mean flow through instabilities of the vertical shear. Although this is in line with the suggestions of Richardson (2005), the question remains what triggers these shear instabilities.

One possible energy source could be provided by the upwelling in the southern part of the basin. The upwelling induces not only horizontal density gradients in the meridional direction, but it also creates a zonal density gradient that is driven by the offshore advection of upwelling filaments by the anticyclones (Jouanno and Sheinbaum, 2013). The result is that the density of the surface waters increases from east to west (Jouanno and Sheinbaum, 2013). Assuming that the relatively light anticyclones maintain their density along their propagation, their density difference with the surrounding waters would increase. This might explain their westward intensification.

It is not only interesting from a dynamical point of view to understand which processes affect the formation and intensification of Caribbean anticyclones, but also from an ecological point of view. More specifically, the Caribbean surface waters are oligotrophic, which means that they contain a limited nutrient supply (Muller–Karger et al., 1989; Muller–Karger and Castro, 1994). The advected upwelling filaments increase the nutrient concentrations offshore (Ezer et al., 2005). In turn, this leads to considerable variability in the regional ecosystem (Rueda–Roa and Muller–Karger, 2013). Besides the advection of upwelling filaments, the anticyclones advect patches of nutrient-rich river water through the basin (Molleri et al., 2010). These patches of river water contain water originating from the Amazon River (Rudzin et al., 2017), which is associated with the inundation of Sargassum algae on Caribbean beaches that have been appearing since 2011 (Gower et al., 2013; Wang and Hu, 2017; Putman et al., 2018; Johns et al., 2020). A recent study suggest that the path of these algae is steered
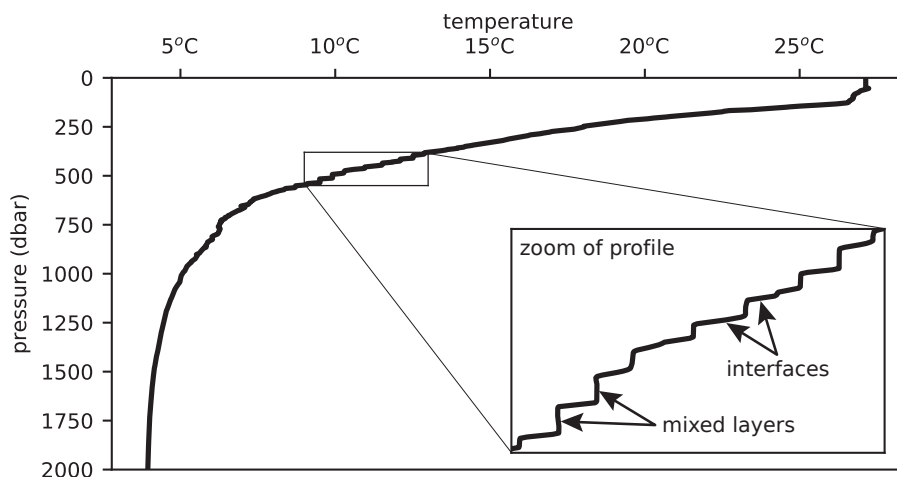
Figure 1.6: Temperature profile as observed during a hydrographic survey on 6 February 2018 at 14.7°N, 69.8°W (see Chapter 2 of this thesis). The inlay shows a zoom of the thermohaline staircase.

by the anticyclones (Brooks et al., 2019). Understanding the dynamics of the anticyclones thus also increases the understanding of the ecological variability.

1.3 The double-diffusive ocean

While the surface in the Caribbean Sea is dominated by turbulent mesoscale anticyclones, at depth the mixing is characterized by double-diffusive mixing (Fig. 1.4, Lambert and Sturges, 1977; Morell et al., 2006). This double-diffusive mixing results in the formation of thermohaline staircases within TACW (Schmitt, 1981). These staircases consist of subsurface mixed layers that are separated from each other by thin interfaces (Fig. 1.6). A tracer release experiment located just east of the Caribbean showed that inside these staircases there is a downward directed salt and heat flux (Schmitt, 2005). Also, characteristic for these thermohaline staircases the resulting buoyancy flux was counter-gradient, which means that the vertical buoyancy flux inside TACW strengthens the stratification (Schmitt, 2005; Radko, 2013). This vertical flux could potentially modulate the properties of the lower-lying AAIW (Fig. 1.4, Schmitt, 2005; Radko, 2013).

To understand how thermohaline staircases modulate the vertical heat and salt fluxes, it is important to gain insight in double-diffusive mixing and how it leads to the formation of the staircase structures. So far, multiple theories for the formation of thermohaline staircases have been proposed: small-scale mixing processes that trigger the formation of internal waves (Stern, 1969); variations in the turbulent heat and salt fluxes (Radko, 2003); counter-gradient buoy-

ancy fluxes that sharpen density gradients (Schmitt, 1994); and lateral intrusions (Merryfield, 2000). Although it remains unclear how these staircases arise, they are a good indicator for the occurrence of double-diffusive mixing (Radko, 2013). The latter occurs when the water column has the right type of stratification (Ruddick, 1983).

Overall, four different types of stratification can be distinguished based on the temperature and salinity variations over depth (middle panel in Fig. 1.7, Ruddick, 1983). The water column has a double stable stratification whenever the temperature decreases with depth and the salinity increases with depth. In this case, both temperature and salinity contribute to a density increase with depth. The opposite holds for the second type of stratification. In this type, the water column is gravitationally unstable, which means that the density decreases with depth. This is an unstable situation that results in convective mixing. This occurs, for example, in the subpolar North Atlantic (Marshall and Schott, 1999). Note that a gravitationally unstable water column does not only occur when the density components of both temperature and salinity decrease with depth, but also when the decrease due to one of these components is strong enough to compensate for the other component that has an increasing density with depth (Fig. 1.7).

The two remaining types of stratification arise when the density components of the temperature and salinity stratification have opposite signs, but the density stratification remains stable (Fig. 1.7). Both types are susceptible to double-diffusive mixing. If the salinity component of the density stratification is unstable and is compensated by the density component of temperature, it is unstable to double diffusion in the salt-finger regime. This type of stratification is also characteristic for the Caribbean Sea, where the warm and saline STUW overly the colder and fresher AAIW (Fig. 1.4, Schmitt, 1981). As a result, the staircases are formed in the layer in between (TACW). In the other type of stratification, referred to as diffusive convection, cold and fresh waters overly warm and saline waters. This predominantly occurs at higher latitudes, such as in the Arctic Ocean (e.g., Shibley et al., 2017). To understand how these two types of stratification induce mixing, we will conduct a thought experiment (e.g., Radko, 2013).

Imagine a water parcel in the ocean that is disturbed upward or downward: its heat and salt content adjusts to its new environment through molecular diffusion. These adjustments do not happen at the same rate: the adjustment of the heat content is much faster than the adjustment of the salt content, because the molecular diffusivity of heat is two orders of magnitude larger than the molecular diffusivity of salt. Depending on the ratio between the stratification of temperature and salinity, the different rates of diffusion can either dampen or enhance the movement of the disturbed water parcel. The enhanced movement is double-diffusive mixing (Fig. 1.7). The mechanism through which this movement is enhanced depends on the regime of double diffusion: salt fingering or diffusive convection.

In the salt-finger regime, warm and saline waters are overlying cold and fresh
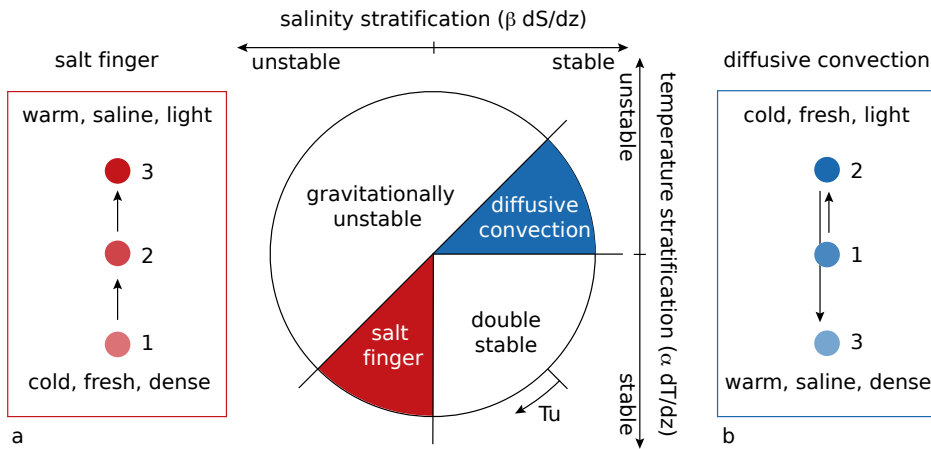
Figure 1.7: Schematic of double-diffusive convection in the (a) salt-finger regime and (b) diffusive-convective regime. The shading of the water parcels indicates the density. The middle panel is modified from Ruddick (1983), and indicates the types of stratification that result in double-diffusive mixing as a function of the Turner angle (Tu, Ruddick, 1983).

waters. If a cold and fresh water parcel (1. in Fig. 1.7a) is disturbed upwards, molecular diffusion will adjust the temperature of the particle towards its new background temperature (2. in Fig. 1.7a). At the same time, the salt content of the water parcel adjusts much slower, which leads to a density decrease of the water parcel. Consequently, the water parcel becomes buoyant with respect to its surroundings and will move further upwards (3. Fig. 1.7a). This enhanced movement results in fingerlike structures that effectively transport salt downward.

In contrast to this effective salt transport in the salt-finger regime, the diffusive-convection regime has a more effective heat transport than salt transport (Fig. 1.7b). In this regime, cold and fresh waters overly the warm and saline waters (Fig. 1.7b). A warm and saline water parcel that is displaced upwards (1. in Fig. 1.7b) will move towards colder and fresher surroundings. There, the water parcel loses heat relatively quickly through molecular diffusion, while it slowly adjusts its salt content (2. in Fig. 1.7b). As a result, the water parcel is more saline than its surroundings. This implies that the water parcel is also denser than its surroundings and will move further downward than its original position (3. in Fig. 1.7b).

The similarity between the two regimes is that both are driven by the release of potential energy that was stored in the unstable component of the stratification (e.g., Radko, 2013): In the salt-finger regime, the potential energy stored in the salinity stratification is released; in the diffusive-convection regime the potential energy stored in the temperature stratification is released. Note that this is fundamentally different from turbulent mixing, which is driven by the dissipation of kinetic energy (e.g., Osborn, 1980). Furthermore, it results in a counter-gradient

buoyancy flux that strengthens the stratification of the water column.

The counter-gradient buoyancy flux arises from a difference in vertical fluxes of heat and salt. In the salt-finger regime, the vertical salt flux exceeds the heat flux, and in the diffusive-convective regime the heat flux exceeds the salt flux. The combination of this difference in the fluxes and the counter-gradient buoyancy flux implies that double-diffusive mixing can also modulate the properties of the water masses directly above and below the double-diffusive layer. Although these fluxes have been observed within the staircase layer itself (Schmitt, 2005), it remains unclear to how far these fluxes extend.

Besides this ability to adjust the properties of water masses locally, the double-diffusive mixing also contributes to the global mechanical energy budget. The global mechanical energy budget describes the energy required to mix the dense waters of the lower limb of the AMOC (Munk, 1966), which decreases their density and allows them to move upward again. Estimates indicate that approximately 2 TW of turbulent mixing is required (Munk, 1966). Averaged over all oceans, this would require an average effective diffusivity of 10^{-4} m^2 s^{-1}. However, the mixing is not distributed evenly over the ocean (Munk, 1966; Munk and Wunsch, 1998; Ferrari and Wunsch, 2009), and the major part of the open ocean displays little mixing with effective diffusivities of approximately 10^{-5} m^2 s^{-1}. To compensate for this little mixing in the open ocean, mixing hotspots with high diffusivities exist at the ocean's boundaries (e.g., Ferrari and Wunsch, 2009).

Double diffusion contributes to the global mechanical energy budget in the open ocean. Note that double diffusion affects the global mechanical energy budget differently than down-gradient turbulent fluxes: the double-diffusive buoyancy flux is counter gradient which implies that it strengthens the stratification. Consequently, more turbulent fluxes are required to compensate for double-diffusive mixing. Taking into account that almost 40 percent of the ocean is susceptible to double-diffusive mixing (You, 2002), the contribution of double-diffusive mixing to the mechanical energy budget might not be negligible. On the other hand, the fact that 40 percent of the oceans contains the right type of stratification does not directly imply that double-diffusive mixing dominates over turbulent mixing.

A good indicator for the occurrence of double-diffusive mixing is the presence of thermohaline staircases (Radko, 2013). This implies that knowledge of the occurrence and characteristics of thermohaline staircases can give insight in the role of double diffusion in the global ocean. First, their global occurrence in combination with estimates of the effective diffusivities can be used to estimate the contribution of double diffusion to the global mechanical energy budget. Second, analysis of individual staircases and water mass properties in regional hotspots with a frequent occurrence of thermohaline staircases, such as the Caribbean Sea, can give insight in the capability of double diffusion to modulate water masses.

1.4   Research questions and outline

The aim of this thesis is to gain insight into the dynamics and mixing in the Caribbean Sea with the focus on two phenomena: turbulent mesoscale anticyclonic eddies at the surface and double-diffusive mixing in deeper parts of the basin. To study the vertical structure and intensification of Caribbean anticyclones three research questions are formulated:

- What is the vertical structure of Caribbean anticyclones and where do they originate?

- Are Caribbean anticyclones remnants of NBC rings?

- Is the westward intensification of Caribbean anticyclones governed by upwelling?

The role of double-diffusive mixing in the Caribbean and global ocean will be assessed in three additional research questions:

- Which characteristics and properties of thermohaline staircases can be used to automatically detect them from observations?

- What is the contribution of double diffusion to the global mechanical energy budget?

- Can double-diffusive fluxes explain the observed variations of the properties of AAIW in the Caribbean Sea?

A brief motivation and approach to each question is given in the following paragraphs. The research questions will be answered in Chapters 2-7. Finally, an overview and discussion of the results is presented in Chapter 8.

What is the vertical structure of Caribbean anticyclones and where do they originate?

The life cycle of Caribbean anticyclones can be divided into three parts: their formation, intensification and dissipation. The anticyclones dissipate over the Nicaraguan Rise, but it remains unknown which mechanisms leads to their formation and intensification. To study the formation and intensification of Caribbean anticyclones in more detail, dedicated eddy surveys of the vertical structure and properties of Caribbean anticyclones are necessary. Most dedicated eddy surveys in the Caribbean Sea have mainly focussed on cyclonic eddies. Two exceptions are the surveys of Silander (2005) and Rudzin et al. (2017). Unfortunately, these studies either measured only the upper part of the anticyclone or did not use the biogeochemical properties to detect the origin of the core waters.

To gain insight in its origin and to capture the full depth of a Caribbean anticyclone, we performed an additional hydrographic survey of such an anticyclone (Chapter 2). We analyze vertical temperature and salinity profiles inside and outside the anticyclone and combine it with samples of the biogeochemical properties. With these observations, we can deduce the origin and describe the vertical structure of an example of a Caribbean anticyclone.

Are Caribbean anticyclones remnants of NBC rings?

The flow that enters the Caribbean Sea is highly variable (Johns et al., 2002). This variability originates from interactions of the flow with the Lesser Antilles and from anticyclonic NBC rings that are formed upstream. Approximately 3-7 NBC rings approach the Lesser Antilles every year (Goni and Johns, 2003; Mélice and Arnault, 2017). Some of these NBC rings dissipate before they reach the islands, while other NBC rings collide with the island chain (Fratantoni and Richardson, 2006; Cruz-Gómez and Vazquez, 2018). So far, it remains unknown what happens during such a collision. Some studies suggested that filaments of the NBC rings can enter the Caribbean Sea (Fratantoni and Glickson, 2002; Goni and Johns, 2003; Jochumsen et al., 2010; van Westen et al., 2018), while others suggested that the collision only acts as a trigger to form new anticyclones on the other side of the island chain (Chérubin and Richardson, 2007; Jouanno et al., 2008, 2009).

In Chapter 3, we study the collision of an NBC ring with the Lesser Antilles to clarify the origin of anticyclonic vorticity of Caribbean anticyclones. To that end, we use a high-resolution model simulation that is able to accurately represent the eastern Caribbean and Lesser Antilles. In this model, we analyze the transports and vorticity fluxes at both sides of the Lesser Antilles.

Is the westward intensification of Caribbean anticyclones governed by upwelling?

One aspect of Caribbean anticyclones that is particularly interesting is that they intensify after their formation. Previous modeling studies have suggested that this intensification is either related to the wind forcing (Andrade and Barton, 2000) or that it is driven by instabilities in the vertical shear of the mean flow (Richardson, 2005; Jouanno et al., 2009). However, it remains unclear how these two processes are related and which mechanism drives the westward intensification. We formulated a new hypothesis in Section 1.2.2 that relates the wind-driven upwelling to the westward intensification. The anticyclones advect upwelled waters offshore, which results in an offshore cooling of the surface waters. It is hypothesized that this increases the horizontal density difference between the anticyclones and their surroundings. In turn, this can be the energy source necessary to intensify the anticyclones.

To test this hypothesis, we use a numerical model with an idealized setup

of the Caribbean Sea. We vary the upwelling strength in different simulations by adjusting the zonal wind forcing. The analysis of the eddy fields in these simulations is discussed in Chapter 4.

Which characteristics and properties of thermohaline staircases can be used to automatically detect them from observations?

Another interesting aspect of the dynamics in the Caribbean Sea is that thermohaline staircases are frequently observed (Merryfield, 2000; Silander, 2005; Morell et al., 2006). Their frequent occurrence within the TACW layer suggests that the vertical mixing is characterized by double diffusion in this layer. Such staircases arise from double-diffusive mixing and can influence the mixing in two ways. First of all, the vertical fluxes of heat and salt inside the staircase layer might modify the properties of AAIW (You, 1999; St. Laurent and Schmitt, 1999; Schmitt, 2005). Second, the diapycnal mixing contributes to the global mechanical energy budget. To study these impacts, it is necessary to quantify the double-diffusive fluxes. However, microstructure measurements of the double-diffusive mixing are scarce, which makes it difficult to obtain a global dataset of direct flux measurements.

Fortunately, the thermohaline staircases are large enough to be captured by Conductivity, Temperature and Depth (CTD) measurements from, for example, hydrographic surveys, Argo floats and Ice Tethered Profilers. Both Argo floats and Ice-Tethered profilers are robotic oceanographic instruments that sample vertical profiles of temperature and salinity (Krishfield et al., 2008; Toole et al., 2011; Argo, 2020). The introduction of the Argo floats in 2000 and the Ice-Tethered Profilers in 2008, resulted in an enormous increase of subsurface oceanic observations covering the full ocean (Roemmich et al., 2009). These observations have increased the knowledge about the role of double diffusion in regions with frequent occurrences of staircases (e.g., Timmermans et al., 2008; Shibley et al., 2017).

In Chapter 5, we explore the possibility to automatically detect thermohaline staircases from vertical temperature and salinity profiles. We identify unique characteristics of thermohaline staircases and use that to develop a detection algorithm. We apply this algorithm on profiles of Argo floats and Ice-Tethered Profilers to obtain a global dataset of thermohaline staircases that can be used to study the regional and global impact of thermohaline staircases on the properties of water masses and the global ocean circulation.

What is the contribution of double diffusion to the global mechanical energy budget?

Modeling studies have shown that ocean general circulation models that incorporate parameterizations of double-diffusive mixing indicate a weakening of the AMOC (Gargett and Holloway, 1992; Merryfield et al., 1999; Oschlies et al.,

2003). Although these ocean models contain many parameterizations, these results indicate that double-diffusive mixing could impact the global ocean circulation. For example, double diffusion can impact the strength and stability of the AMOC through its contribution to the global mechanical energy budget.

In Chapter 6, we use the global dataset of thermohaline staircases from Chapter 5 and estimate the contribution of double diffusion to the global mechanical energy budget. Because thermohaline staircases are an indicator of double-diffusive mixing, we use their global occurrence to quantity the contribution of double-diffusive mixing on the global mechanical energy budget. We compute the effective diffusivity of density in each staircase using the flux laws from Kelley (1990) and empirical estimates from Radko and Smith (2012). The combination of the effective diffusivity and the occurrence of the staircases leads to the first ever estimate based on in-situ ocean observations of how much double diffusion contributes to the global mechanical energy budget.

Can double-diffusive fluxes explain the observed variations of the properties of AAIW in the Caribbean Sea?

In the Caribbean Sea, TACW is susceptible to double-diffusive mixing due to its placement between the warm and saline STUW and cold and fresh AAIW. The thermohaline staircases that arise as a result of this mixing induce a downward heat and salt flux. Although a tracer release experiment confirmed the presence of these downward fluxes (Schmitt, 2005), it remains unknown whether these fluxes actually reach the AAIW layer.

In Chapter 7, we analyze the thermohaline staircases in the Caribbean Sea and compare their characteristics to the variations in properties of AAIW. In particular, we use the data from Argo floats that observations in the Caribbean Sea. We analyze the temperature and salinity characteristics of the mixed layers to identify whether the vertical fluxes arising from the presence of staircases can affect the property variations in AAIW. Using these results, we estimate the magnitude of the double-diffusive fluxes using a set of steady-state advection-diffusion equations.

Chapter 2

Hydrographic and biological survey of a surface-intensified anticyclonic eddy in the Caribbean Sea

Abstract

In the Caribbean Sea, mesoscale anticyclonic ocean eddies impact the local ecosystem by mixing of low salinity river outflow with the nutrient-rich waters upwelling along the Venezuelan and Colombian coast. To gain insight into the physics and the ecological impact of these anticyclones, we performed a combined hydrographic and biological survey of one Caribbean anticyclone in February 2018. We found that the anticyclone had a radius of 90 km and was surface intensified with the strongest velocities (0.72 m s^{-1}) in the upper 150 m of the water column. Below, isopycnal displacements were found down to 700 dbar. The core of the anticyclone entrained waters from the Orinoco River plume, and contained slightly elevated chlorophyll concentrations compared to the surroundings. At the edge of the anticyclone we observed higher densities of flying fish, but not higher densities of predators like seabirds and cetaceans. Below the surface, a strong temperature inversion (0.98 °C) was present within a barrier layer. In addition, we found thermohaline staircases that originated from double diffusion processes within Tropical Atlantic Central Water.

2.1   Introduction

In the Caribbean Sea, two major nutrient sources are available: the wind-driven upwelling along the Venezuelan and Colombian coast and the plumes of the Amazon and Orinoco River that are advected into the basin (Bidigare et al., 1993; Morell and Corredor, 2001; Gilbes and Armstrong, 2004; Molleri et al., 2010; Rueda–Roa and Muller–Karger, 2013). These two nutrient sources are mixed with the oligotrophic surrounding waters by mesoscale eddy activity (Corredor et al., 2004; Hu et al., 2004; Alvera-Azcárate et al., 2009). The eddies in the Caribbean Sea are predominantly anticyclonic and have diameters ranging from 50-200 km (Andrade and Barton, 2000; Gaube, 2015). They are generated in the eastern part of the basin, where the river plumes form strong fronts (Corredor et al., 2003). The anticyclones intensify on their path westward, while passing the upwelling region. There, the anticyclones advect cold filaments of nutrient-rich upwelled waters northwards. Ocean circulation models have been used to show that this advection results in the offshore cooling of Caribbean surface waters (Jouanno and Sheinbaum, 2013).

The anticyclones alter the ecosystem by the advection and dispersal of biota (Ezer et al., 2005) and by the advection of patches containing water from the river plumes (Corredor et al., 2004). Based on ocean color images, Chérubin and Richardson (2007) showed that after the river plume arrives the eddy kinetic energy increases, and they concluded that this enhancement results in considerable flow variability in the Caribbean coastal ecosystems. At greater depths, the flow is less variable and susceptible to the formation of thermohaline staircases, which form from double diffusive processes (Merryfield, 2000). Morell et al. (2006) suggest that Caribbean eddies, both cyclones and anticyclones, could alter these staircase structures. Farther downstream, anticyclones influence the frequency of the shedding of large Loop Current Rings (Oey et al., 2003), a pronounced oceanic feature in the Gulf of Mexico (Oey et al., 2005).

Despite this impact of the Caribbean anticyclones on the local ecosystem, the physical processes governing the origin and development of the anticyclones remain unclear. Some modeling studies suggest that wind is the dominant driver (Oey et al., 2003; Chang and Oey, 2013), while others argue, based on idealized models and surface drifters, that Caribbean anticyclones are formed of remnants of North-Brazil Current (NBC) Rings (Simmons and Nof, 2002; Richardson, 2005). Furthermore, modeling studies show that mixed barotropic-baroclinic instabilities of the Caribbean Current can generate and intensify the anticyclones (Jouanno et al., 2008, 2009).

Additional observations are necessary to clarify the origin and physics of the development of the Caribbean anticyclones. Until now, observations were based on surface drifter data (Molinari et al., 1981; Centurioni and Niiler, 2003; Richardson, 2005) and satellite altimetry (e.g. Nystuen and Andrade, 1993; Alvera-Azcárate et al., 2009). Although these studies provide valuable information about the size and surface properties of the anticyclones, they do not provide details on

their vertical structure. These can be obtained from dedicated surveys of eddies in the Caribbean Sea (Corredor et al., 2004; Silander, 2005; Morell et al., 2006; Rudzin et al., 2017). Rudzin et al. (2017) performed upper ocean observations of a Caribbean anticyclone, and showed that the anticyclone contained a barrier layer, which is the layer between a shallow halocline and deeper thermocline. Barrier layers store heat below the mixed layer and affect the local weather when this heat is released (Rudzin et al., 2017). In the other surveys (Corredor et al., 2004; Silander, 2005; Morell et al., 2006), the emphasis is on the biogeochemical properties of cyclones. Although the eddies in the Caribbean Sea are predominantly anticyclonic, their biogeochemical properties have not been studied before.

To study the origin, vertical structure and ecological impact of Caribbean anticyclones, we performed a combined biological and hydrographic survey of a Caribbean anticyclone in February 2018. With these observations, we can deduce the origin of this anticyclone and its impact on the local ecosystem. We provide details on the survey in Section 2.2 and describe the evolution and vertical structure of the targeted anticyclone in Section 2.3. Afterwards, the upper ocean characteristics (mixed layer, the barrier layer and the thermohaline staircases) of the observations are discussed. The effects of hydrodynamic features on biological processes are investigated in Section 2.4. The results are summarized and discussed in Section 2.5. An overview of the subsurface hydrographic properties, including a water mass analysis is given in the Section 2.A.

2.2 Materials and methods

2.2.1 In-situ measurements

Figure 2.1 shows the track of the survey performed between 4 and 11 February 2018 on the RV Pelagia, which started on Aruba and ended in St. Maarten. The hydrographic data consists of 15 CTD (conductivity, temperature, depth) stations that were located between the islands Aruba and Hispaniola and underway data from an aquaflow system. In addition, upper ocean current velocities were obtained with a Vessel-mounted Acoustic Doppler Current Profiler (VMADCP). Visual surveys of birds and pelagic megafauna were conducted during daylight hours along the cruise track. The locations of survey stations were chosen based on the altimetric signature of an anticyclone in the weeks leading up to the cruise. Based on these analyses, the center of this 180-km wide anticyclone was expected north of Aruba at the start of the cruise. Four Argo floats were deployed during the survey to gain insight on the evolution of the temperature and salinity of Caribbean waters.

The 75 kHz VMADCP mounted under the RV Pelagia collected flow velocity data along the transect. While drifting at stations, the VMADCP was turned off to limit interference with acoustic monitoring of the pelagic fauna. For the
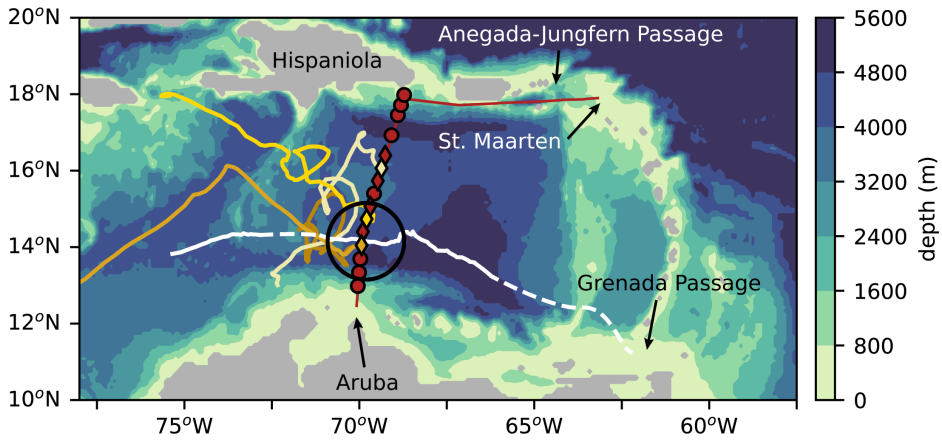
Figure 2.1: Bathymetry (m) of the eastern Caribbean Sea showing the cruise track (red line) and track of the center of the eddy (white line). The black circle indicates the location of the anticyclone, estimated from satellite altimetry, at the time of the survey. The track is obtained with the py-eddy tracker of Mason et al. (2014, white solid line) and extended with visual tracking of sea-level anomalies (white dashed line). Hydrographic stations along the cruise track that were sampled down to the bottom and down to 2000 m are shown with dots and diamonds, respectively. Red markers indicate a hydrographic stations, yellow markers indicate hydrographic stations where also Argo floats were deployed. The tracks of the Argo floats from February 2018 to September 2018 are shown with the yellow solid lines.

results of the acoustic monitoring we refer to de Jong (2018). The VMADCP provided horizontal current velocities below the vessel down to approximately 600-m depth with a vertical resolution of 16 m. The blanking distance below the vessel was 25 m. The temporal resolution of the ensembles is 10 min and each ensemble was averaged over 150 pings. Tidal velocities were estimated with the TPXO9 model (Egbert and Erofeeva, 2002) and removed from the VMADCP data with Cascade V7.2 (Kermabon et al., 2018). Furthermore, a quality check of the VMADCP data was performed by using Cascade V7.2 (Kermabon et al., 2018).

Stations were planned on a line across the anticyclone and continued to the north outside the eddy to observe the background hydrography of the Caribbean Sea (Fig. 2.1). The distance between the stations across the eddy is 38.9 km, which is less than half the radius of the eddy ($R = 90$ km). North of the eddy the stations are separated farther apart with a station distance of 61.4 km over the deep basin. The station distance was smaller (30 km) over the continental slope close to Hispaniola. Stations 1, 2, 3, 8, 12, 13, 14 and 15 were sampled down to the bottom. Stations 4, 5, 6, 7, 9, 10 and 11 were sampled down to 2000 m to save time needed for horizontal resolution.

At each station, vertical profiles of temperature, salinity, oxygen, chlorophyll and turbidity were obtained with a CTD system. Physical parameters and oxygen were measured with a SeaBird Electronics 911 system, Wetlabs and Chelsea

Aqua sensors provided measurements of turbidity and chlorophyll (for further details see de Jong, 2018). At each station, water samples were taken for salinity calibration. The calibrated CTD data were averaged to vertical bins of 1 dbar. In addition, nutrients samples for phosphate, silicate, nitrate and nitrite were collected from all 15 stations with the CTD-rosette with a vertical spacing of 25 dbar in the upper 100 dbar. The vertical spacing increased to 50 dbar down to 250 dbar. Below 250 dbar, nutrient samples were taken every 250 dbar. At each station, the sample depth closest to the chlorophyll maximum was adjusted slightly to specifically sample the chlorophyll maximum. The depth of this maximum was determined from the downcast of the CTD. Unfortunately, it was not possible during this cruise to perform water sample analysis of oxygen and chlorophyll. We therefore focus on relative differences within and between profiles, rather than absolute values. Two Argo floats were deployed at station four and single Argo floats were deployed at stations six and ten (yellow dots in Fig. 2.1). These Argo floats sampled temperature and conductivity every 3 days from the surface down to 2000 dbar to gain insight in the variability of these properties within the Caribbean Sea. During these 3 days, the floats had a parking depth of 500 dbar to avoid grounding on shallow topography downstream.

Surveys of pelagic megafauna took place during daylight hours whenever RV Pelagia was sailing. The observation platform is located on top of the bridge, at 9 m above sea level. Seabirds, marine mammals and flying fish (when visible) were recorded by a team of 2-4 observers, within a 300 m wide strip on the side of the vessel that offered the best viewing conditions. In addition to these strip counts, all animals seen within a 180° scan ahead (port to starboard) were recorded (Tasker et al., 1984). All animals seen were logged per 10-minute counts. The behavior of observed birds and marine mammals was noted according to the standardized coding method described in Camphuysen and Garthe (2004). In addition, the central position and time, as well as environmental conditions were recorded for each 10-minute count.

2.2.2   Complementary data

Prior to, during and following the survey, the evolution of the anticyclone was studied with gridded sea-level anomaly fields from satellite altimetry. These fields with a resolution of 0.25° were downloaded from the Copernicus Marine Environment Monitoring Service (CMEMS, http://marine.copernicus.eu). The track of the anticyclone was obtained from the gridded sea-level anomaly (SLA) fields with the py-eddy tracker of Mason et al. (2014) that identified circular SLAs as eddies. Negative anomalies were identified as cyclones, positive anomalies as anticyclones. If a SLA signal was not sufficiently circular in shape, it was not considered an eddy. To detect the origin of the disturbance, the track obtained with the py-eddy tracker was extended by visual analysis of the altimetry product.

In addition to the gridded sea-level anomaly fields, we applied the py-eddy tracker to daily fields of the global forecast available from CMEMS. The forecast-

ing model, referred to as Mercator, is based on NEMO (Madec et al., 2015). In this model, the sea-level anomaly fields of the satellite altimetry and in-situ temperature and salinity profiles of the Argo floats are assimilated. The model has a spatial resolution of 1/12°.

Globcolour images were used to analyze the spatial distribution of surface chlorophyll (Bertrand et al., 2009). These gridded images are a merged product from multiple satellite missions and have a spatial resolution of 4.63 km (4.63×4.63 km^2) and temporal resolution of one day. The images were generated using CMEMS products at the production centre ACRI-ST. The salinity anomaly of the surveyed anticyclone was analyzed with the along-track salinity observations from the Level 2 Ocean Salinity Output from the Soil Moisture and Ocean Salinity (SMOS) satellite obtained from the European Space Agency (http://earth.esa.int).

2.3   Upper ocean characteristics

2.3.1   Eddy characteristics

The targeted anticyclone was first detected by the py-eddy tracker as a coherent structure on 28 December 2017. At that time, the Mercator model indicated that the anticyclone had a surface salinity of 34.6 psu and temperature of 28.6 °C. The anticyclone became more saline and colder on its path westward which can be attributed to mixing with the surrounding (colder and more saline) waters and to interaction with the atmosphere. The visual analysis of the altimetry data suggested that the anticyclone originated from a disturbance which could be traced back to Grenada Passage on 11 September 2017 (Fig. 2.1). On average, the anticyclone had a westward propagation velocity of 0.1 m s^{-1}, which is in the order of the mean zonal velocity of the Caribbean Current (Richardson, 2005).

At the time of the survey, the center of the anticyclone was located at 14.1°N and 69.8°W. The SLA and geostrophic velocities from altimetry data show that the center of the anticyclone was captured by our observations (Fig. 2.2). The near surface velocity field obtained from the ADCP is similar to that derived from satellite altimetry, and it suggests that the eddy was close to geostrophic balance. This is confirmed by the low Rossby and Burger numbers of the anticyclone (Table 2.1). The largest surface speed (0.72 m s^{-1}) was found 90 km south of the center of the anticyclone, while the flow 90 km north of the anticyclone was weaker (0.41 m s^{-1}). This difference in surface velocity was induced by the Caribbean Current, which interacted with the southern part of the anticyclone at that moment. The diameter of the anticyclone was 180 km.

Satellite altimetry indicated that the anticyclone had a SLA of 0.20 m during the survey (Fig 2.3a). The VMADCP velocities show that the anticyclone was surface-intensified, with the strongest velocities (>0.5 m s^{-1}) in the upper 150 m of the eddy (Fig. 2.3b). Below that depth, the swirl velocities were smaller

Table 2.1: Eddy characteristics at 5 February 2018. The amplitude is obtained from altimetry. The velocity, depth scale and radius are obtained from the VMADCP. The vertical stratification is taken from the CTD measurements. The minimal and maximum Brunt-Väisälä frequency, Burger number are both indicated. Other parameters used to estimate the variables are $f_0 = 1.4 \times 10^{-4}$ s^{-1}, g = 9.81 m s^{-2} and $\rho_0 = 1028$ kg m^{-3}.

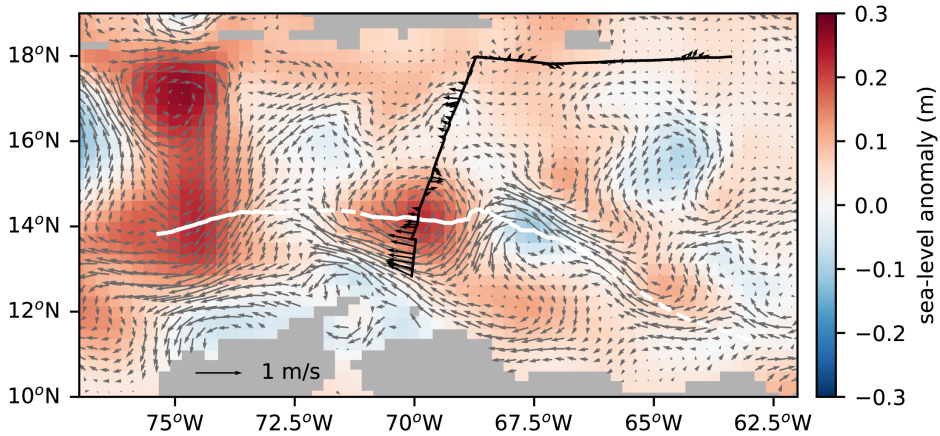|		
sea-surface height amplitude	A	0.20 m
swirl velocity	U	0.41-0.72 m s^{-1}
depth scale	D	$\mathcal{O}(150$ m$)$
radius	R	90 km
Rossby number	$Ro = \frac{U}{f_0 R}$	0.03-0.06
Brunt-Väisälä frequency	$N = \sqrt{-\frac{g}{\rho_0}\frac{\partial \rho}{\partial z}}$	0 - 0.03 s^{-1}
Burger number	$Bu = \frac{N^2 D^2}{f_0^2 R^2}$	0 - 0.12

Figure 2.2: Gridded sea-level anomaly (m) on 5 February 2018 with the geostrophic surface velocities (grey vectors) obtained from gridded altimetry from E.U. Copernicus Marine Service Information. The cruise track is indicated by the solid black line. The black arrows show the velocities of the ADCP, averaged over the upper 25-35 m (below the blanking distance). The white line indicates the track of the anticyclone.

than 0.1 m s^{-1}. The weak velocities were induced by small isopycnal displacements, which were found down to 700 dbar. This implies that the anticyclone was baroclinic and had a relatively weak barotropic component. It is plausible that the weak isopycnal displacements were induced by the mass of the anticyclone above, meaning that only the surface waters were advected with the anticyclone. This view is supported by the path of the Argo floats, which were deployed in the core of the anticyclone. These Argo floats had a parking depth of 500 dbar and diverted from the path of the anticyclone after deployment (Fig. 2.1).

The surface-intensified velocity structure of the anticyclone is clearly visible in the vertical shear of the anticyclone (Fig. 2.3c). The shear is strongest at the flanks of the anticyclone between 13°N and 15°N below the thermocline (red line in Fig. 2.3c), which indicates that the strongest velocities of the anticyclone are confined to the isothermal layer. In line with Mignot et al. (2012), we defined the depth of the thermocline ($D_{T^*-0.2}$) as the depth where the temperature decreased by 0.2 °C compared to the temperature of the mixed layer. The depth of the halocline ($D_{S^*\pm0.06}$) was defined as the depth where the salinity deviates from the salinity of the mixed layer (S^*) by $\Delta S_A = 0.06$ g kg^{-1}. Interestingly, the strongest shear was not found at the bottom of the mixed layer, but it was found deeper below the thermocline.

The surface of the anticyclone was less saline ($\Delta S_A = -0.2$ g kg^{-1}) and warmer ($\Delta T = +0.2$ °C) than the surrounding waters (Fig. 2.3d,e). The combined temperature and salinity difference of the anticyclone corresponds to a surface density difference of $\Delta \rho = -0.46$ kg m^{-3} between the core of the anticyclone and the surface waters to the north. The maximum temperature of the anticyclone was 28.0 °C and was located at approximately 90 dbar (Fig 2.3d). This subsurface maximum reflects a temperature inversion and is discussed in Section 2.3.3.

The combination of the salinity anomaly of the anticyclone and the slightly (but significant) elevated silicate levels (Supplementary Fig. 2.9e), suggested that the anticyclone entrained river outflow. Apparently, the anticyclone originated at Grenada Passage close to the outflow of the Orinoco River in September 2017. At that time, the discharge of the Orinoco River was high (Fig. 2.4a), while the plume of the Amazon River had not yet arrive at this location. This made it plausible that the anticyclone entrained water from the Orinoco River plume and propagated westward with the mean flow. We found in sea-surface salinity observations from the 'Soil Moisture and Ocean Salinity' satellite that a few days prior to the cruise, on 29 January 2018, the core of the anticyclone contained a low salinity anomaly (Fig. 2.4b), of which a weak signal was still observed at the time of the cruise (Fig. 2.3e). This view is in line with the results of the Mercator model, where the salinity of the anticyclone was relatively low at the start of the track (34.6 psu) and increased on its path westward.

The evolution of the anticyclone after the survey was analyzed with gridded SLA obtained from satellite altimetry and from the output of the Mercator model. This analysis showed that the surveyed anticyclone interacted with a
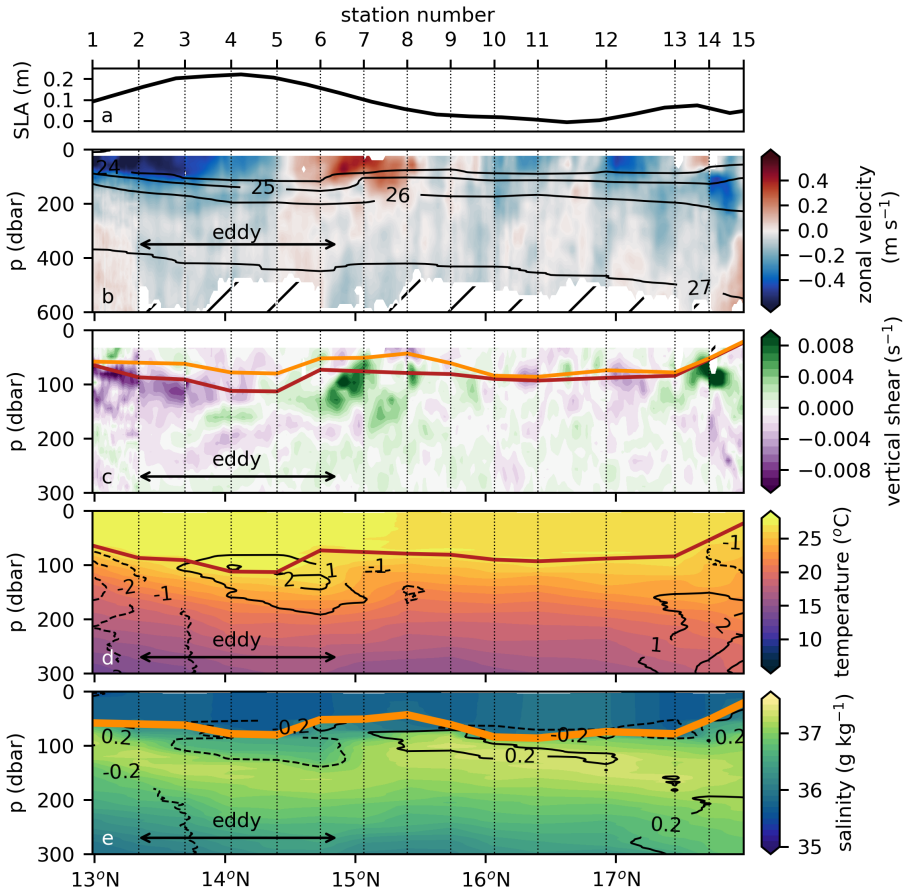
Figure 2.3: (a) Sea-level anomaly (cm) at 5 February 2018 from satellite gridded altimetry obtained from CMEMS. (b) Zonal velocity (m s^{-1}) along the cruise track. Positive velocities are in eastward direction. The hatched regions indicate where VMADCP data were rejected due to poor backscatter. The black contour lines show the isopycnals. (c) Vertical shear of zonal velocity (s^{-1}) along the cruise track. (d) Conservative temperature (°C) obtained from CTD profiles. The black contour lines show temperature deviations from the mean temperature profile. (e) Absolute salinity (g kg^{-1}). The black contour lines show salinity deviations from the mean salinity profile. Both temperature and salinity are interpolated along the survey from the profiles obtained at the stations. The thermocline and halocline, indicated with the red and orange line respectively, were computed following Mignot et al. (2012).
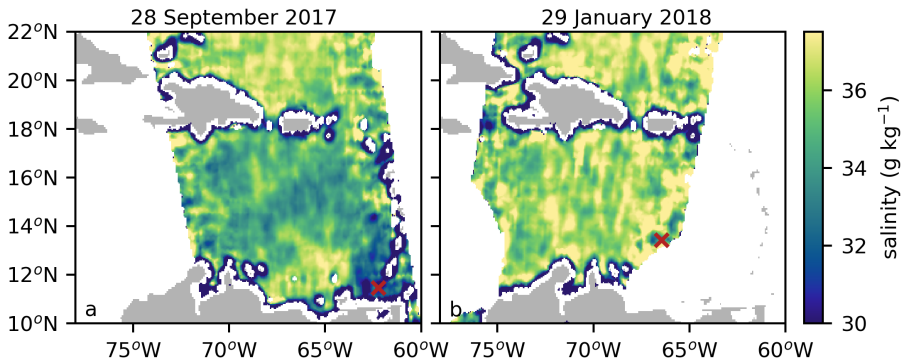
Figure 2.4: Sea-surface salinity from the 'Soil Moisture and Ocean Salinity' satellite at (a) 28 September 2017 and (b) 29 January 2018. The approximate formation region of the anticyclone is indicated with the red cross. The location of the anticyclone at 29 January 2018 was obtained from satellite altimetry with the py-eddy tracker and is indicated with the red cross.

second anticyclone (SLA = +0.29 m) that was located at 16.6°N and 75.4°W during the survey (Fig. 2.2). This first resulted in a small weakening of the sea-level anomaly signal of the surveyed anticyclone (SLA = +0.18 m). On 13 March 2018, the two anticyclones merged into one anticyclone with a maximum sea-level anomaly of SLA = +0.30 m that propagated farther westward. Previous modeling studies suggested that Caribbean anticyclones get more energetic on their path westwards through baroclinic instabilities (Carton and Chao, 1999; Jouanno et al., 2009). More specifically, as discussed in Chapter 4 of this thesis, the westward growth of the anticyclones is thought to be related to the upwelling along the South-American coast. However, the merging process of this particular anticyclone illustrates that anticyclones can also get more energetic through merging and indicates that not all anticyclones develop in the same manner.

2.3.2   Mixed-layer depth and chlorophyll

The Caribbean Sea has a seasonal cycle in mixed layer depths driven by the north-south movement of the Intertropical Convergence Zone and the associated intensification of the northeasterly trade winds over the basin during boreal winter (Taylor and Alfaro, 2005). Montoya–Sánchez et al. (2018) determined a climatology of air-sea heat exchange and mixed layer depth using atmosphere and ocean reanalyses. They conclude that surface cooling and mixed layer deepening is predominantly caused by the latent heat loss caused by the trade winds. Winter mixed layer depths are typically around 50 m depth, with slightly shallower depths ($\approx$ 30 m) in the Southern Caribbean due to upwelling induced shoaling of isopycnals and slightly deeper (> 60 m) towards the north. Maximum mixed layer depths are typically reached in February, at the end of the cooling season (Montoya–Sánchez et al., 2018).
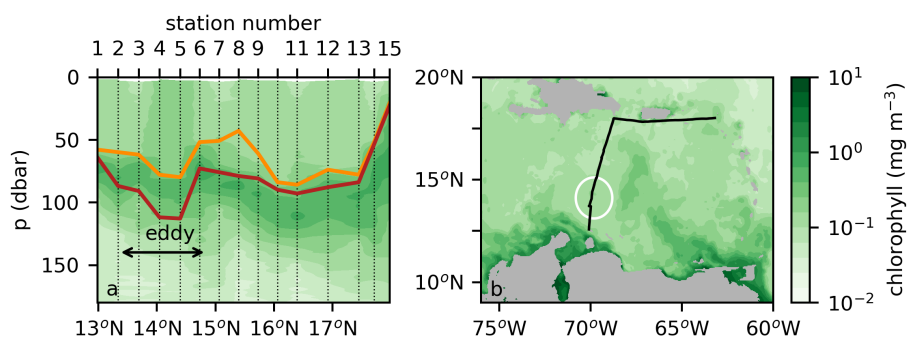
Figure 2.5: (a) Chlorophyll-a fluorescence concentrations (mg m^{-3}) along the hydrographic section. The thermocline and halocline, indicated with the red and orange lines respectively, were computed following Mignot et al. (2012). (b) Surface chlorophyll concentrations from merged satellite products at 5 February 2018 obtained from E.U. Copernicus Marine Service Information. The cruise track is shown by the black line and the location of the eddy is indicated by the white circle. Note the logarithmic color scale.

Our survey coincided with this cooling season. During the survey, winds measured and recorded by the underway logging system were consistently from the northeast with speeds of 10.0 ± 1.7 m s^{-1}. The mixed layer at the CTD stations was confined by the halocline that separated the relatively fresh Caribbean surface waters from the saline subtropical underwater (see Section 1.5). The mixed layers depth was between 40 and 80 dbar, with the deeper mixed layers located in the center of the anticyclone and on the northern side of the section (Fig. 2.5a).

The mixed layer itself was depleted of nutrients, with PO_4 and $NO_3 + NO_2$ concentrations below 0.1 μmol l^{-1} and silicate concentration around 2 μmol l^{-1}, and low values for near-surface chlorophyll concentration (Supplementary Fig. 2.9). Below the mixed layer, concentrations increased sharply (Fig. 2.5a). This sharp increase, which was still in the photic zone, coincided with a maximum in nutrients. At the core of the anticyclone, the deep chlorophyll maximum was found inside the barrier layer (outlined by the red and orange lines in Fig. 2.5a), while it was located below the barrier layer outside the anticyclone.

In general, the Caribbean Sea is considered as an oligotrophic region, where the main region of productivity is found along the southern boundary (Muller–Karger et al., 1989; Muller–Karger and Castro, 1994), which is sustained by upwelling along the Venezuelan coast (Rueda–Roa and Muller–Karger, 2013). Farther north, increases in plankton are attributed to the more nutrient rich inflow from the Amazon and Orinoco rivers (Muller–Karger et al., 1989; Hu et al., 2004).

The spatial gradient, seen in the chlorophyll data from the merged satellite product (Fig. 2.5b), highlights lower concentrations chlorophyll north of the position of the anticyclone, which is similar as observed during the survey (Fig.

2.5a). These weak spatial changes at the surface were in strong contrast to the much higher subsurface chlorophyll signal (Fig. 2.5a). Higher surface concentrations were found south of the anticyclone, where strong trade winds forced coastal upwelling (Fig. 2.5b).

At the core of the anticyclone, the observed surface chlorophyll concentration was enhanced (doubled in fact) compared to surrounding surface waters, although it was still quite low (Fig. 2.5). Mesoscale eddies are known to alter the chlorophyll concentrations in various ways. The dominant mechanism is the horizontal advection of phytoplankton in the periphery of eddies (Chelton et al., 2011a; Gaube et al., 2014). Chlorophyll anomalies can also be trapped in the core of the eddies (Early et al., 2011), of which the properties are altered by eddy-induced upwelling or downwelling (Gaube et al., 2013). In general, cyclones are considered more productive than anticyclones (Falkowski et al., 1991), but recently Dufois et al. (2016) showed that during winter anticyclones can be more productive than cyclones due to winter mixing in some parts of the Caribbean.

The elevated surface chlorophyll concentration inside the anticyclone implies that the anticyclone was more productive than its surroundings (Fig 2.5a). As we did not observe elevated levels of $NO_3 + NO_2$ concentrations in the core of the anticyclone (Supplementary Fig. 2.9f), it is unlikely that the observed enhancement is due to increased winter mixing. However, we found that these higher values coincide with slightly elevated silicate concentrations (Supplementary Fig. 2.9e), which we associated with the advection of the Orinoco River plume. Eastwards of the anticyclone, surface chlorophyll values were higher compared to those in the anticyclone (Fig. 2.5a). This offshore local maximum in surface chlorophyll east of the surveyed anticyclone was due to the offshore advection of nutrient-rich filaments of upwelled waters (Fig. 2.5b). At that location, a cyclone and anticyclone were present (Fig. 2.2). Apparently, these eddies (67°W, 14°N) trapped positive chlorophyll anomalies and advected these to the north.

2.3.3   Barrier layer and temperature inversion

In the previous section, it was shown that the low salinity in the core of the anticyclone and the elevated productivity suggests that the anticyclone entrained waters from the Orinoco River plume. In combination with the larger mixed layer depth inside the anticyclone, the anticyclone became more susceptible for the formation of a thick barrier layer. Previous studies showed indeed that the surface waters in the Caribbean Sea are susceptible to the formation of barrier layers (Mignot et al., 2007; Rudzin et al., 2017). A barrier layer, defined as the layer between the top of the halocline and the top of the thermocline (Pailler et al., 1999), forms as a result of specific thermal and haline forcing (de Boyer Montégut et al., 2004). In general, heat is trapped in the barrier layer, which is released once the barrier layer gets eroded by intense atmospheric forcing (de Boyer Montégut et al., 2004). This heat release affects the heat transfer between the ocean and atmosphere, which has a potential important climatic impact (de
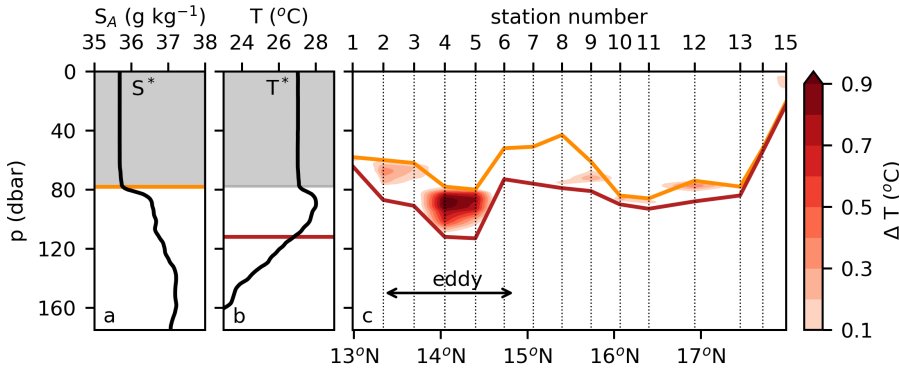
Figure 2.6: (a) Absolute salinity profile of the upper 180 dbar of the water column at station 4. The orange solid line shows the depth of the halocline at that location. The grey shaded area indicates the depth over which the mixed layer salinity (S^*) is determined. (b) Conservative temperature profile at station 4. The red solid line shows the depth of the thermocline, which was defined as the depth where the temperature decreased with 0.2 °C compared to the temperature of the mixed layer. The grey shaded area indicates the depth over which the mixed layer temperature (T^*) is determined. (c) Magnitude of the temperature inversion, defined as the temperature of the barrier layer minus the temperature of the mixed layer along the hydrographic section. The depth of the halocline and thermocline are indicated by the orange and red lines, respectively.

Boyer Montégut et al., 2004). For example, in the Caribbean Sea, this release of heat might enhance the growth of tropical cyclones (Balaguru et al., 2012).

The barrier layer thickness (BLT) is used as a proxy for the effects and strengths of the barrier layer (McPhaden and Foltz, 2013). During the hydrographic survey, a barrier layer was present in the southern part of the basin (Fig. 2.6a). The thickest layers were observed within the core and at the periphery of the anticyclone (BLT $= 35 \pm 1$ dbar). This is in line with observations of Rudzin et al. (2017), who found thicker barrier layers inside than outside their surveyed anticyclone.

In general, a strong halocline allows for the formation of temperature inversions inside barrier layers (Mignot et al., 2012). These temperature inversions have a strong seasonal cycle. The barrier layer warms due to solar radiation in summer (Masson and Delecluse, 2001). This heat is trapped in fall, when the mixed layer becomes less saline due to the river outflow (Mignot et al., 2007). During winter months, the mixed layer is cooled by the atmosphere, which leads to convective mixing (Montoya–Sánchez et al., 2018). This mixing tends to erode the top of the barrier layer, and is limited by a strong halocline, allowing summer temperatures to be maintained in the barrier layer, and creating a temperature inversion (Mignot et al., 2012).

During the survey, several temperature inversions were observed, which shows that the halocline was sufficiently strong to maintain a stable density stratifica-

tion (Fig. 2.6c). The strongest temperature inversion (+0.96 °C) was found in the thickest (≈35 dbar) and deepest (≈90 dbar) barrier layer. This is in line with Girishkumar et al. (2013) who showed that the magnitude of the temperature inversion correlates with the thickness of the barrier layer. The strongest temperature inversion was located at the core of the anticyclone, where low salinity anomalies in the mixed layer strengthened the salinity stratification. Furthermore, the barrier layer was located deeper in the water column due to the low density of the anticyclones. Both the salinity stratification and the deeper placement of the barrier layer are favorable conditions for the formation of temperature inversions (Mignot et al., 2007; Girishkumar et al., 2013).

2.3.4   Thermohaline Staircases

Below the mixed layer and barrier layer, a layer of strong vertical shear separated the surface-intensified flow from the weak flow below (Fig. 2.3b,c). At the depth of these weak velocities, the temperature and salinity profiles obtained with the CTD clearly displayed thermohaline staircases (Fig. 2.7a,b). Similar staircase structures have been found before in this region (e.g. Lambert and Sturges, 1977; Morell et al., 2006). They are formed by double diffusive mixing (salt fingers) between a warm and saline layer and a colder and fresher layer below. Double diffusive mixing occurs when the amount of turbulent mixing is low and the water mass has a low density ratio (R_ρ, Merryfield, 2000), defined as:

$$R_\rho = \frac{\alpha T_z}{\beta S_z},$$
(2.1)

where T_z and S_z are the vertical gradients of potential temperature and absolute salinity, respectively. Here, α is the thermal expansion coefficient and β the haline contraction coefficient. If the density ratio is lower than 4, staircases may be observed in the ocean (Merryfield, 2000).

During the survey, staircases were present between 250 and 600 dbar in the density range of 26.6-27.2 kg m^{-3} with a density ratio of $R_\rho = 1.7 \pm 0.2$ at $\sigma_0 = 27$ kg m^{-3}. Due to the meridional slope of the isopycnals, the staircases are found slightly higher in the water column in the south (Fig. 2.7). Below the anticyclone, staircases were observed slightly deeper in the water column due to the eddy-induced isopycnal displacement. The staircases consisted of homogeneous layers with a thickness of 2-31 dbar. Most staircases were found within Tropical Atlantic Central Water (TACW, see Section 2.A), where the temperature and salinity both decreased with depth, from the warm and saline STUW above towards the cold and less saline Antarctic Intermediate Water (AAIW) underneath. Staircase structures were weaker outside the TACW layer (Fig. 2.7c), where the deep salinity minimum was slightly higher (Supplementary Fig. 2.9b).

The four Argo floats that were deployed have a parking depth of 500 dbar, so at the depth of the staircase structures. As a result, the floats were advected with the staircases. Their profiles revealed that the staircases were persistent, and
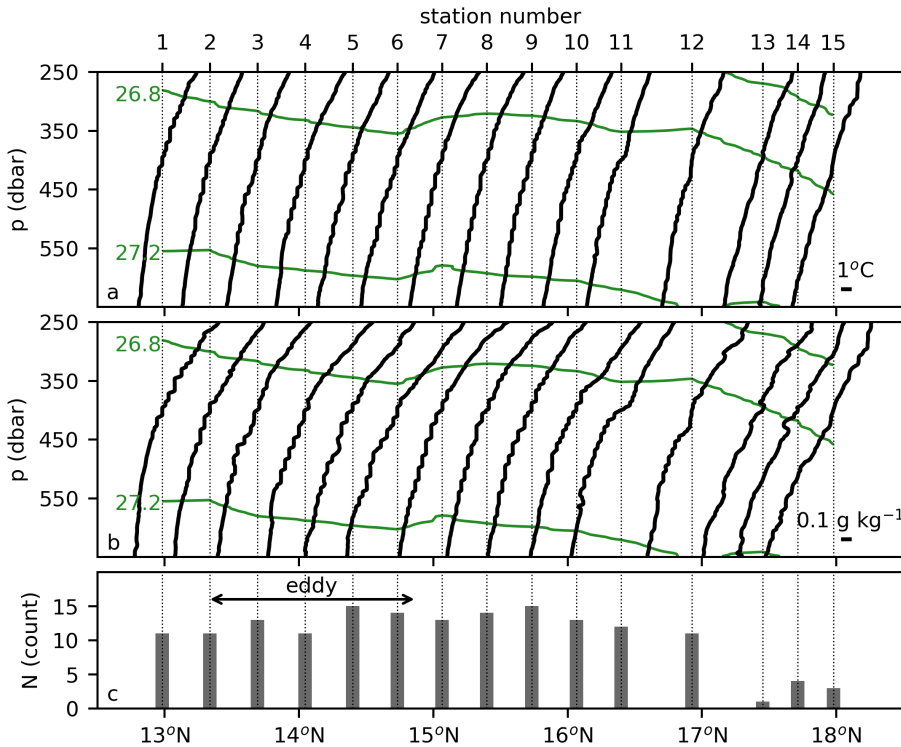
Figure 2.7: (a) Conservative temperature (°C) profiles and (b) absolute salinity (g kg^{-1}) profiles obtained with the CTD, between 250 and 650 dbar. σ-contours are indicated. Each profile is projected upon the latitude of the station, indicated with the dashed black lines. The green lines show to the density contours along the track. (c) The number of staircases that were found in each profile.

that most staircases remained coherent structures for several weeks to several months. From deployment until September 2018, staircases were present at $\sigma_0 = 26.6 - 27.2$ kg m^{-3}. Within this layer, the average value of the density ratio was $R_\rho = 2.5 \pm 1.3$ at $\sigma_0 = 27.0$ kg m^{-3}. A more detailed analysis of the thermohaline staircases in the Caribbean Sea is presented in Chapter 7 of this thesis.

2.4   Ecological implication

The ecological impact of the surveyed anticyclone on the higher trophic levels was studied with a survey of the pelagic megafauna. The Caribbean Sea is known to be a global-scale hot spot for marine biodiversity (Roberts et al., 2002), but the marine biodiversity in the offshore and deep parts of the basin is under-sampled (Miloslavich et al., 2010). In general, the coastal regions have a higher primary production (Andrade and Barton, 2005), and are more biodiverse than the
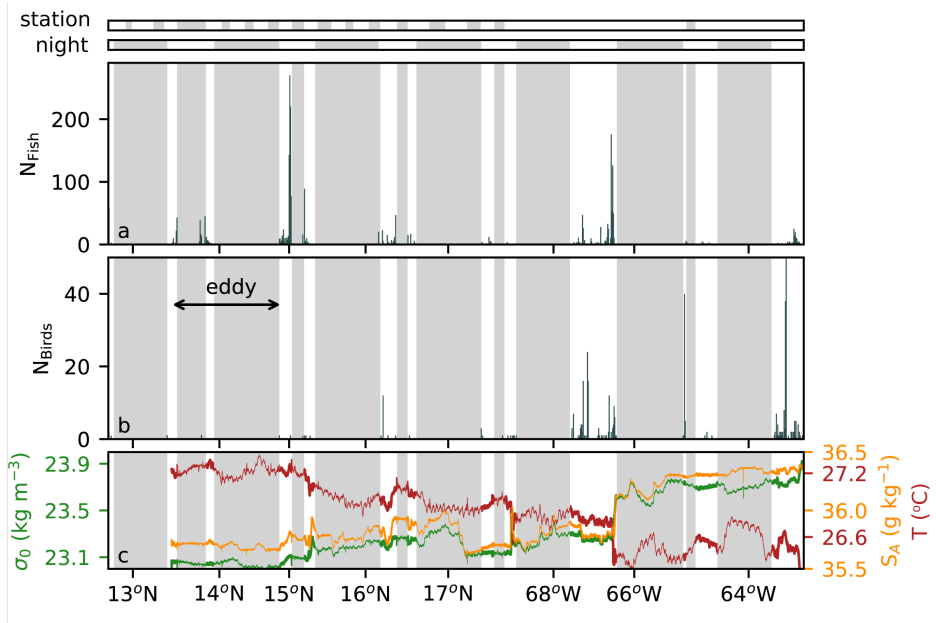
Figure 2.8: (a) Number of flying fish (N_{Fish}) observed along the track per 10-minute count. (b) Number of birds (N_{Birds}) observed per 10-minute count. (c) Surface temperature (T), salinity (S_A) and density anomaly (σ_0) as observed with the ship-board thermo-salinograph. The shaded grey regions indicate locations without observations during stations (top bar) and during nights (2nd bar). These periods without observations are also indicated by the shaded grey in panels a, b and c. The dark grey solid line distinguishes the first part of the track (northward; hydrographic survey) from the second part (eastward en route to St. Maarten).

oligotrophic offshore waters (Miloslavich et al., 2010). However, the dispersal of nutrient-rich upwelled waters and the advection of the river plumes by mesoscale anticyclones locally increase the productivity offshore.

In general, fish are known to be concentrated at fronts (Paramo et al., 2003; Wells et al., 2017), and the fronts of anticyclones are associated with upwelling (Seki et al., 2001; Bakun, 2006; Gaube et al., 2013). We observed a relatively high number of flying fish in coastal areas (Fig. 2.8a), and a peak of flying fish was observed at 15°N (Fig. 2.8a) that coincided with the northern front of the anticyclone (Fig 2.8c). Note that this front was observed with the thermo-salinograph short after station 7, while the peak of flying fish was observed before station 7. Shortly after station 7, the sea-surface salinity increased with approximately 0.2 g kg^{-1}, and sea-surface temperature decreased with 0.3 °C from south to north. At the northern front, the depth of the mixed layer was slightly shallower (40 dbar), which might be related to frontal upwelling (Fig. 2.5a). At the southern front of the anticyclone, we did not observe a similar peak of flying fish. The southern front of the anticyclone coincided with a strong coastal jet, and the depth of the mixed layer was slightly deeper (60 dbar). Also, small positive

anomalies of $NO_3 + NO_2$ at both fronts suggests frontal upwelling (Supplementary Fig. 2.9f). Note that we do not have observations of fauna near the center of the eddy as these parts were surveyed during the night.

Along the 542 km that could be surveyed during daylight hours, we recorded in total 15 birds species, of which Brown Booby was the most abundant (n = 276; 62 % of all birds recorded). It was seen throughout the whole survey area, but numbers were low during the northbound transects from Aruba to Hispaniola, i.e., in the region of the eddy studied. We found very low bird densities in the central Caribbean and along the northern front of the anticyclone (Fig. 2.8b), while potential prey (flying fish) seemed abundantly present (Fig. 2.8a). That seabirds were largely absent from the central Caribbean may be explained by the generally low numbers of birds remaining in the Caribbean, due to loss of breeding habitat during the last century (Van Halewijn and Norton, 1984; Lowrie et al., 2012; Leopold et al., 2019). The remaining birds might not need to venture far offshore from their breeding colonies around the Caribbean Sea, since there is less competition today for prey closer to the breeding colonies, as seabird have been depleted (Ashmole, 1963). In addition, the availability of prey far offshore might be unpredictable, so that other parts of the Caribbean might offer more predictable feeding opportunities, such as the coastal upwelling zones in the south of the basin. Far offshore, seabirds may have to rely on other predators that drive fish to the surface, such as large fish or cetaceans. Very few of these were seen during the survey.

2.5   Summary, discussion and conclusions

We conducted a hydrographic and biological survey of a Caribbean anticyclone to gain insight into its origin, vertical structure and ecological impact. The 180-km wide anticyclone was surface intensified with the highest velocities located in the upper 150 m and along the southern perimeter of the anticyclone. Below 150 m, weaker velocities were observed, which might be caused by the passage of the shallow anticyclone above.

The anticyclone originated near Grenada Passage, which is similar to the anticyclone surveyed by Rudzin et al. (2017). Based on the low salinity and elevated silicate concentrations in the core of the anticyclone, we suggest that the anticyclone entrained surface waters originating from the Orinoco River. This is another source of salinity anomalies than suggested by Rudzin et al. (2017), who suspected that these anomalies originated from an NBC Ring. Ffield (2005) showed that the salinity of NBC Rings depends on the position of the Amazon River plume. The salinity anomalies found in this study as well as in the study of Rudzin et al. (2017) therefore highlight the importance of the Amazon and Orinoco River plumes on the formation and properties of Caribbean anticyclones.

The elevated silicate levels in the anticyclone coincided with an elevated chlorophyll concentration. This surface chlorophyll concentration in the cen-

ter of the anticyclone was much lower than that in the nutrient-rich upwelling regions, and lower than that at the deep chlorophyll maximum. This is in agreement with previous observations that the offshore regions in the Caribbean Sea are oligotrophic (Muller–Karger et al., 1989; Muller–Karger and Castro, 1994). However, the small surface increase in chlorophyll concentration compared to the surroundings was significant and highlights that Caribbean anticyclones can be productive, and thus can transport isolated ecosystems from the eastern to the western part of the basin.

The deep chlorophyll maximum was located below the mixed layer inside the barrier layer. The thickest barrier layers, which also contained a strong temperature inversion, were located in the core of the anticyclone. Based on Argo float profiles, de Boyer Montégut et al. (2007) found that maximum temperature inversions (0.6 °C in the Caribbean) occur in November and December. Although our survey took place in February, we observed much stronger temperature inversions (up to 0.98 °C) than found by de Boyer Montégut et al. (2007). Because temperature inversions form in winter as the mixed layer cools, we suggest that the expected magnitude of temperature inversions can be larger in late winter (February) than in early winter (November/December) if the barrier layer is located deep enough. This implies that previous estimates might have underestimated the magnitude of temperature inversions, and that the heat trapped in the barrier layer is higher than expected. This could have important consequences, as this heat can be released during intense atmospheric forcing (de Boyer Montégut et al., 2007) and might be an additional energy source for developing hurricanes in this region.

Below the barrier layer, weak velocities due to isopycnal displacement were found. Because the sea-level signature of the anticyclone and the tracks of the Argo floats that were deployed in the core of the anticyclone did not follow similar paths, it is plausible that waters at 500 dbar were not advected with the anticyclone. Therefore, we approximated the depth of the anticyclone to be 150 m, at the lower bound where we observed the highest velocities and where the shear decreases to the background value. This is shallower than the two estimates from previous observations of Caribbean anticyclones, where Rudzin et al. (2017) and Silander (2005) estimated depths of 500 m and 1400 m, respectively. Although these differences seem large, the anticyclone observed by Silander (2005) had a similar surface-intensified flow structure. Also the velocities of the anticyclone observed by Rudzin et al. (2017) have a surface-intensified pattern, which reveals the possibility that all three anticyclones were shallow and the weak isopycnal displacement at depth was induced by the anticyclone above. Therefore, we think that most Caribbean anticyclones transport only water in the upper layer, while the passage of the shallow anticyclone induces a weak depression of the isopycnals at larger depths.

Below the anticyclone, we observed thermohaline staircases in the TACW layer. Based on the tracks of the deployed Argo floats, we showed that the thermohaline staircases were not advected with the anticyclone. This is in line with

the observation that the anticyclone was shallow and that the weak isopycnal displacements in this layer were induced by the presence of the anticyclone above. This might also explain why we did not find a clear difference in staircase presence between the core and the periphery of the anticyclone, in contrast to previous studies (Silander, 2005; Morell et al., 2006; Bebieva and Timmermans, 2016).

The presence of the anticyclone altered the local ecology slightly, as shown by elevated chlorophyll concentrations in the core. The anticyclone contained a source of nutrients (Si) and a peak of flying fish was observed at its northern front. However, it seemed to be too far offshore to attract birds. The low densities of birds that were observed are a matter of concern and could be related to the loss of breeding habitat offshore (Van Halewijn and Norton, 1984; Lowrie et al., 2012; Leopold et al., 2019).

2.A   Distribution of water masses

The Caribbean Sea is highly stratified, and contains six water masses with distinctive properties (Morrison and Nowlin, 1982; Hernández–Guerra and Joyce, 2000). The surface waters of much of the Caribbean Sea consist of Caribbean Surface Water (CSW) that is characterized by salinities below 36 psu (Morrison and Nowlin, 1982). In general, marine nutrients are limited in CSW (Hansell and Follows, 2008), except during periods of maximum river discharge of the Amazon and Orinoco Rivers when CSW is mixed with the silicate-rich river outflow (Froelich Jr. et al., 1978; Corredor and Morell, 2001). This mixing results in the dispersal of patches of low salinity anomalies that can be found up to several hundreds of kilometers from the river outflow and can be identified by an elevated silicate concentrations (Morell and Corredor, 2001; Corredor and Morell, 2001). In our observations, CSW had an average temperature and salinity of $T = 26.9 \pm 0.2$ °C and $S_A = 35.8 \pm 0.1$ g kg^{-1}, respectively (Supplementary Fig 2.9a,b).

A strong halocline separates CSW from the saline Subtropical Underwater (STUW) (Morrison and Nowlin, 1982; O'Connor et al., 2005). STUW is characterized by salinities (S_P) exceeding 37 psu. It originates from regions with high evaporation in the central tropical Atlantic Ocean and enters the Caribbean Sea in the northeast (Fig. 1.4, Wüst, 1964; Morrison and Nowlin, 1982; Montes et al., 2016). The depth at which STUW is found decreases towards the Venezuelan coast, where it is upwelled and transports nutrients towards the surface (Rueda–Roa and Muller–Karger, 2013; Montes et al., 2016). In line with Morrison and Nowlin (1982) and Hernández–Guerra and Joyce (2000), we found the highest salinities in the northern part of the basin where the STUW is less diluted (Supplementary Fig. 2.9b). In addition, we found that the core of the STUW followed the $\sigma_0 = 25.2$ kg m^{-3} isopycnal and varied in depth over the hydrographic section between 100 and 150 dbar.

Small patches of Sargasso Sea Water (SSW) enter the Caribbean Sea through the Anegada-Jungfern Passage at approximately 300 dbar (Fig. 1.4,aging Morrison and Nowlin, 1982). SSW can be identified by (slightly) elevated levels of oxygen concentrations. The signal weakens along its path towards the southern part of the basin, because of the aging of this water mass (Kinard et al., 1974). We identified patches of SSW by oxygen concentrations that were approximately 10 μmol l^{-1} higher than the surrounding values (Supplementary Fig. 2.9c). These patches followed the $\sigma_0 = 26.4$ kg m^{-3} isopycnal, which sloped upward towards 150 dbar near the Venezuelan coast.

Below the patches of SSW, an oxygen minimum indicated the presence of Tropical Atlantic Central Water (TACW, Supplementary Fig 2.9c). TACW originates in the tropical Atlantic Ocean and enters the Caribbean Sea through the southeastern passages (Fig. 1.4, Kinard et al., 1974; Morrison and Nowlin, 1982). Although the origin of this oxygen depletion in this layer remains unclear, the mean current pattern suggest that TACW originates near Angola (Portela
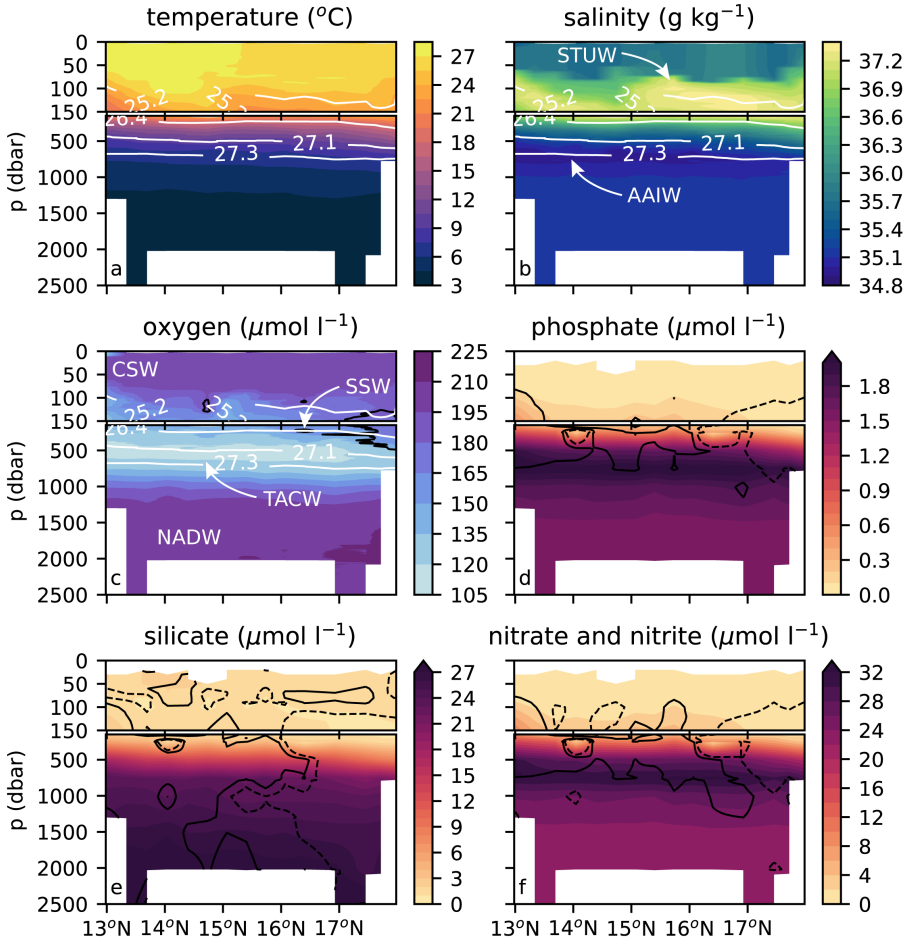
Supplementary Figure 2.9: Section of conservative temperature (T), absolute salinity (S_A), oxygen (O_2), phosphate (PO_4), silicate (Si) and combined nitrate and nitrite ($NO_3 + NO_2$) along the cruise track. Indicated water masses are AAIW = Antarctic Intermediate Water, CSW = Caribbean Surface Water, NADW = North Atlantic Deep Water, SSW = Sargasso Sea Water, STUW = Subtropical Underwater, TACW = Tropical Atlantic Central Water. The white contour line indicate the isopycnals in the core of a water mass. The black contour lines show positive (solid) and negative (dashed) anomalies from the depth-averaged mean for O_2 (contour drawn at 15 μmol l^{-1}), PO_4 (contour drawn at -0.05 and 0.05 μmol l^{-1}), Si (contour drawn at -0.2 and 0.2 μmol l^{-1}) and $NO_3 + NO2$ (contour drawn at -0.5 and 0.5 μmol l^{-1})

et al., 2018). We found that the core of TACW ($O_2 < 120$ μmol l^{-1}) was located at the $\sigma_0 = 27.1$ kg m^{-3}-isopycnal at approximately 500 dbar and had a temperature of 9.3 ± 1.2 °C and a salinity of 35.2 ± 0.2 g kg^{-1}.

Antarctic Intermediate Water (AAIW) enters the Caribbean Sea through the same passages as TACW, but at greater depths (Fig. 1.4). AAIW can be identified by a salinity minimum and a phosphate and nitrate maximum (Morrison and Nowlin, 1982). This water mass originates from the Southern Ocean and propagates northward into the Atlantic Ocean at depths ranging between 500 and 1000 m (Tsuchiya, 1989). Supplementary Figure 2.9b,d,f shows that the core of AAIW was located at approximately 700 dbar. The core had an average salinity of 35.0 ± 0.02 g kg^{-1} and a temperature of 6.6 ± 0.4 °C.

The deep waters of the Caribbean Sea consist of strongly diluted North Atlantic Deep Water (NADW, Joyce et al., 1999). This water mass originates from the North Atlantic Ocean and enters the Caribbean Sea through Anegada-Jungfern Passage in the northeast of the Caribbean Sea (Fig. 1.4, Morrison and Nowlin, 1982). Because this deep passage is shallower than the depth of the Caribbean Sea, the deeper parts of the Caribbean Sea are not in contact with the rest of the Atlantic Ocean. In line with previous observations (Morrison and Nowlin, 1982; Joyce et al., 1999), we found that NADW was vertically homogeneous below 1800 dbar (Supplementary Fig. 2.9) and had an average temperature of 3.91 ± 0.03 °C and an average salinity of 35.2 ± 10^{-3} g kg^{-1}.

Chapter 3

Generation of vorticity by flow-topography interaction: Anticyclones in the Caribbean Sea

Abstract

Mesoscale anticyclonic eddies dominate the sea-surface height variability in the Caribbean Sea. Although it is well established that these anticyclones are formed near the eastern boundary of the Caribbean Sea, which is demarcated by the Lesser Antilles, the source of their anticyclonic vorticity remains unclear. To gain insight into this source, we analyze the fluxes of vorticity into the Caribbean at its eastern boundary using a high-resolution numerical model. We find that the anticyclonic vorticity in the eastern Caribbean Sea predominantly results from the interaction of ocean currents with the topography around the Lesser Antilles. More specifically, St. Lucia and Grenada are hotspots for vorticity generation. The local generation scales with the amplitude of the volume transport through the passages between these islands. This finding is in contrast with the view that anticyclonic North Brazil Current (NBC) rings in the Atlantic Ocean are the main source of anticyclonic vorticity in the eastern Caribbean Sea. Our analyses reveal that the direct contribution of the vorticity of the NBC rings is of lesser importance than the local generation. However, the collision of upstream NBC rings with the Lesser Antilles increases the volume transport through the passages into the Caribbean Sea, so that their presence indirectly leads to enhanced local production of anticyclonic vorticity. This process is an example of the importance of vorticity generation by means of flow-topography interactions, which is ubiquitous in the oceans, and expected to be important whenever currents and steep topography meet.
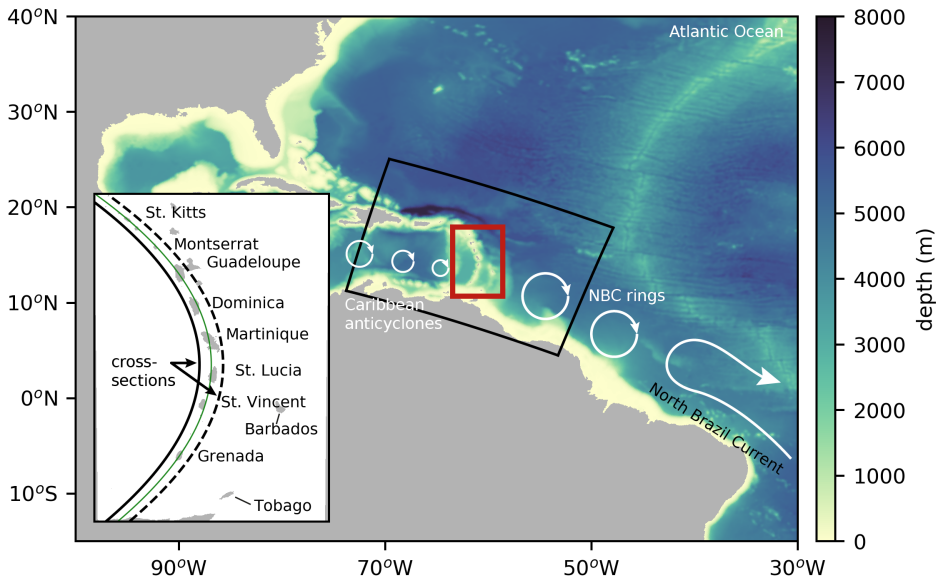
Figure 3.1: Map of the bathymetry of the Caribbean Sea, used in the numerical simulations. The black box indicates the domain of the first nested grid (*CS-nest*), the red box indicates the second nested grid (*LA-nest*). Typical locations and size of Caribbean anticyclones, North Brazil Current rings and the North Brazil Current are sketched in white. The inlay zooms in on the islands of the Lesser Antilles, and indicates the locations of the eastern (dashed line), middle (green line) and western (solid line) cross sections used in the analyses.

3.1   Introduction

Nearly a third of the ocean's surface is, at any given time, covered by mesoscale eddies (Gaube et al., 2019). These eddies dominate the surface variability, and they redistribute fundamental tracers along their path of propagation (Richardson, 1983; Wunsch, 1999; Chelton et al., 2007; Fu et al., 2010). Along these paths, which can be hundreds of kilometers long (Chelton et al., 2007, 2011b), mesoscale eddies can collide with the steep topography of island arcs. Well-known examples of such collisions are the North Brazil Current (NBC) rings that encounter the Lesser Antilles in the Atlantic Ocean (Fig. 3.1; e.g., Didden and Schott, 1993; Fratantoni and Richardson, 2006; Jochumsen et al., 2010) and the eddies that collide with the Kuril Islands in the Pacific Ocean (Rabinovich et al., 2002; Itoh and Yasuda, 2010; Prants et al., 2016).

When a mesoscale eddy collides with an island arc, the eddy can either squeeze through the passages (Goni and Johns, 2001), split into smaller eddies (Richardson and Tychensky, 1998; Richardson, 2005; Cardoso et al., 2020), or completely disintegrate (Jochumsen et al., 2010). Idealized models (Simmons and Nof, 2002; Duran-Matute and Fuentes, 2008) and laboratory experiments

(Cenedese et al., 2005; Tanabe and Cenedese, 2008) indicate that the response of the eddies depends on multiple factors, such as the size of the eddy, the angle of approach and the width of the gaps between the islands. While these different responses imply that not all eddies will continue their path after a collision, it is possible that filaments of their vorticity are advected downstream of the islands (Shi and Nof, 1994; Simmons and Nof, 2002). For example, Goni and Johns (2001, 2003) and Richardson (2005) suggested that vorticity filaments of NBC rings feed the formation of anticyclones directly downstream of the Lesser Antilles. However, others (Chapter 4 of this thesis, Chérubin and Richardson, 2007; Jouanno et al., 2009) suggested that these filaments of NBC rings are not necessary to obtain a realistic eddy field in the Caribbean Sea. Consequently, the source of the vorticity of Caribbean anticyclones remains unclear.

Another process that needs to be taken into account is the generation of vorticity near steep topography (Deremble et al., 2016; Srinivasan et al., 2019). Multiple studies have shown that such local generation of vorticity can result in the formation of eddies downstream (Jiménez et al., 2008; Gula et al., 2015; Molemaker et al., 2015; Johnston et al., 2019). In particular, Jiménez et al. (2008) found that the eddy generation depends on the flow velocities near the topography. Despite that these studies all focussed on other regions than the Lesser Antilles, this type of vorticity generation is generic and expected to be relevant here, because the topography is steep and the volume transport through the narrow passages is large (Johns et al., 2002). It is therefore necessary to account for this process when studying the potential link between NBC rings in the Atlantic Ocean and anticyclones in the Caribbean Sea.

In this study, we quantify both the generation of vorticity near the Lesser Antilles and the advection of vorticity filaments from NBC rings to gain insight into the origin of Caribbean anticyclones. For this, we use a regional model with a high resolution to accurately represent the eastern Caribbean Sea (Sections 3.2 and 3.3). First, we quantify both the time-averaged and the time-varying vorticity fluxes near the Lesser Antilles to assess the relative contribution of the advected and locally generated vorticity near the Lesser Antilles (Section 3.4). To assess the contribution of the anticyclonic vorticity of NBC rings to the anticyclonic vorticity in the eastern Caribbean Sea, we study a collision event of one NBC ring in detail in Section 3.6. The implications of our main result, namely that the bulk of vorticity flux into the eastern Caribbean Sea is locally generated, are discussed in Section 3.7.

3.2 Model configuration and methods

3.2.1 Model configuration

We performed a simulation of the eastern Caribbean Sea using the Regional Oceanic Modeling System (Shchepetkin and McWilliams, 2005, ROMS,). The

Table 3.1: Grid settings of simulations used in this study: the nominal horizontal grid resolution (Δx, Δy) and number of vertical levels (N). The minimum and maximum vertical grid size (Δz) in a water column of 2000 m are shown in the right column.

domain	Δx, Δy (km)	N	Δz (m)
Atlantic Ocean (*parent*)	7	50	5.2; 106.8
Caribbean Sea (*CS-nest*)	2	100	2.7 ; 42.2
Lesser Antilles (*LA-nest*)	0.7	100	2.7 ; 42.2

ROMS model uses terrain-following σ-coordinates to solve the primitive equations with a full equation of state (Shchepetkin and McWilliams, 2011). We applied a one-way nesting procedure to force higher resolution regional computational domains (see Mason et al., 2010). As a parent simulation, we used the simulation with a nominal resolution of 7 km that covers most of the Atlantic Ocean (Table 3.1) described in Mason et al. (2011). We refer to that paper for further details. The first nested grid covered the eastern part of the Caribbean Sea and had a nominal resolution of 2 km (*CS-nest*, black box in Fig. 3.1, Table 3.1). This simulation was run for 720 days (2 model years). The second nested grid, referred to as *LA-nest*, was located inside the *CS-nest* around the Lesser Antilles (red box in Fig. 3.1), and had a nominal horizontal resolution of 700 m. This configuration was run for 54 days to study a single collision event of an NBC ring with the Lesser Antilles in detail (Table 3.1).

The bathymetry of both nests was constructed with the SRTM30-plus dataset[1]. The minimum depth was restricted to 5 m, and land areas were masked using the coastlines obtained from the GSHHS dataset[2]. At these land points, the velocities were set to zero, which is equivalent to applying a no-slip boundary condition.

It is well known that in models with terrain-following coordinates pressure gradient errors arise near steep topography, such as near the Lesser Antilles (Fig. 3.2). To mitigate these pressure-gradient errors that are associated with the terrain-following coordinates of the ROMS, the raw bathymetry data was adjusted. First, the raw bathymetry data was smoothed with a Gaussian smoothing kernel that had a width of 6 times the horizontal grid resolution. Next, the steepness of the slopes was limited by setting the slope-parameter, r, which performs a logarithmic smoothing to the topography, to $r = 0.2$ (for further details see Lemarié et al., 2012). As a final step, the near-surface layers of both nested grids were flattened over 300 m during the stretching procedure that was applied to better resolve the surface and bottom boundary layers (Table 3.1).

Besides this adjustment of the bathymetry, the numerical schemes implemented in the ROMS are designed to mitigate the pressure-gradient error as well (detailed description in Shchepetkin and McWilliams, 2003). In short, two important steps are taken in the numerics. First, the density and depth are treated as continuously differentiable polynomial functions in the computation of the

---

[1] http://www.topex.ucsd.edu/WWW_html/srtm30_plus.html
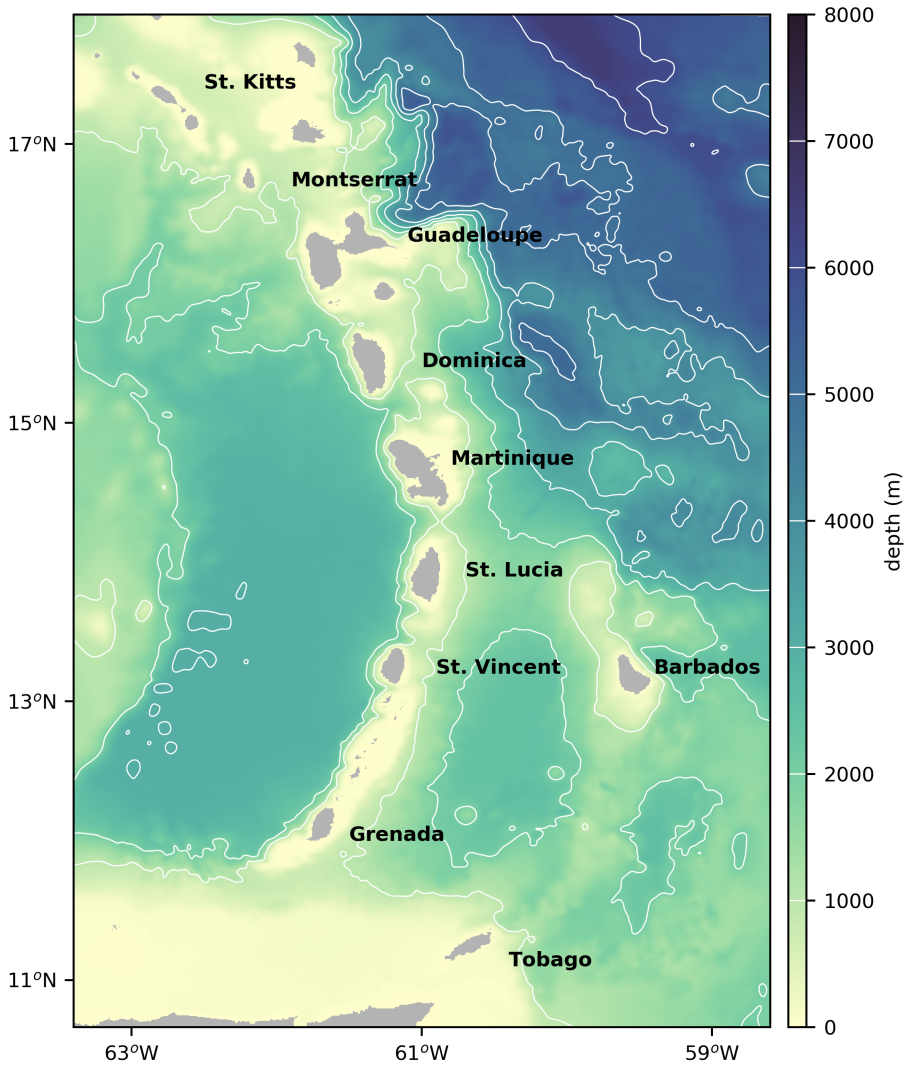[2] http://www.soest.hawaii.edu/pwessel/gshhg/

Figure 3.2: Bathymetry used in the nested grid of the Lesser Antilles (*LA-nest*). The white contour lines corresponds to the isobaths between 0 and 8000 meter at intervals of 1000 m.

pressure gradient force. In contrast to previous methods with a second order accuracy, this results in a 4th-order accurate function where special attention is payed to spatially non-uniform grids. Second, Shchepetkin and McWilliams (2003) showed that disregarding the compressibility of sea water results in significant errors that can even be larger than the classical pressure-gradient errors due to the hydrostatic inconsistency associated with the terrain-following grids. These errors are mitigated by accounting for the compressibility of sea water.

At the surface, a climatological forcing of a normal year similar to that applied by Lemarié et al. (2012) was used. The daily wind stresses were computed with the QuickSCAT-based daily product of scatterometer wind stresses (Risien and Chelton, 2008). Monthly-averaged surface heat fluxes were constructed with CORE (Large and Yeager, 2009). We applied an idealized diurnal cycle to the incoming shortwave radiation. Monthly-averaged precipitation and evaporation were obtained from HOAPS (Andersson et al., 2010). The outflow of rivers was implemented using climatological discharges obtained from Dai and Trenberth (2002). Different from Lemarié et al. (2012), the discharge of each river was prescribed by means of an array of point sources near the river mouth. At these point sources, monthly discharges were prescribed over the full water column with a salinity of 1 psu and an idealized seasonally varying temperature that varied with an amplitude of 1°C around a mean of 28°C. The velocity imposed at the river outflow was scaled with the total area of the outflow to get a volume transport that matched the observed discharges.

At the lateral boundaries of both nested grids, a sponge layer with a width of 1/12 of the domain size was defined to smoothly connect the nested-grid solutions to the prescribed boundary conditions. This sponge layer was implemented as an explicit lateral viscosity that increased from 0 near the interior to 5 m^2 s^{-1} and 0.1 m^2 s^{-1} at the boundary of the *CS-nest* and *LA-nest*, respectively. We applied the K-profile parameterization (KPP, Large et al., 1994) to parameterize the vertical mixing of tracers and momentum, and parameterized bottom friction, using the logarithmic law with a roughness length of 0.01 m. Horizontal mixing was implicitly parameterized by using a third-order horizontal upstream-biased advection scheme and a vertical semi-implicit advection scheme (for further details, see Shchepetkin, 2015). To limit spurious diapycnal mixing, isoneutral diffusion was applied in the both nested grids (Lemarié et al., 2012).

3.2.2   Methods

For both nests, snapshots of the velocity, temperature, salinity, and sea-surface height anomalies were saved every 6 hours. The temperature and salinity fields were converted to conservative temperature and absolute salinity, respectively, using the TEOS-10 software (McDougall and Barker, 2011) to allow for comparison with data from the World Ocean Atlas 2018 (WOA2018, Locarnini et al., 2019; Zweng et al., 2019). To validate the magnitude of the volume transports into the eastern Caribbean Sea against observations from Johns et al. (2002)

and Kirchner et al. (2008), we defined a cross section through the Lesser An-
tilles (green line in the inlay of Fig. 3.1) and computed the volume transports
perpendicular to this cross section.

   We determined the source of the anticyclonic vorticity in the eastern Caribbean
Sea with a computation of the flux of the relative vorticity from the 6-hourly snap-
shots. The relative vorticity, simply referred to as vorticity in the remainder of
this study, was defined as:

$$\zeta = \frac{\partial v}{\partial x} - \frac{\partial u}{\partial y}, \tag{3.1}$$

where u and v are the velocities in zonal (x-direction) and meridional (y-direction)
direction, respectively. The terms on the right-hand-side were computed from
snapshots of the 3-dimensional velocities fields on the terrain-following coordi-
nates:

$$\left[\frac{\partial v}{\partial x}\right]_z = \left[\frac{\partial v}{\partial x}\right]_\sigma - \left[\frac{\partial z}{\partial x}\right]_\sigma \frac{\partial v}{\partial z}; \tag{3.2a}$$

$$\left[\frac{\partial u}{\partial y}\right]_z = \left[\frac{\partial u}{\partial y}\right]_\sigma - \left[\frac{\partial z}{\partial y}\right]_\sigma \frac{\partial u}{\partial z}; \tag{3.2b}$$

where the subscripts z and σ indicate the direction along horizontal surfaces
and along the terrain-following surfaces, respectively. In these computations, we
ignored sea-level variations. The resulting 3-dimensional vorticity fields were
used to compute the fluxes of vorticity, where we distinguished between fluxes
of anticyclonic and cyclonic vorticity. The fluxes of anticyclonic vorticity in zonal
and meridional direction were defined as:

$$F_x^{\text{AC}} = \int_0^{300m} u\zeta H(-\zeta)\,dz, \tag{3.3a}$$

$$F_y^{\text{AC}} = \int_0^{300m} v\zeta H(-\zeta)\,dz, \tag{3.3b}$$

respectively, where the superscript AC indicates that only the anticyclonic vortic-
ity is considered and H is the Heaviside function. The fluxes were only integrated
to a depth of 300 m, because the Caribbean anticyclones have a strong baroclinic
structure (Chapter 2 of this thesis, Rudzin et al., 2017). The flux of cyclonic vor-
ticity was computed in a similar way, but then conditionally sampled for $\zeta > 0$.

   The fluxes of vorticity were used to separate the generation of vorticity at the
Lesser Antilles from the vorticity advected from the Atlantic Ocean. To that end,
we shifted the cross section along the Lesser Antilles eastward and westward by
0.25° (dashed and solid line in the inlay of Fig. 3.1). The fluxes were computed
perpendicular to these cross sections, where positive values correspond to fluxes
into the Caribbean Sea. In Section 3.4, we will show that the volume transport
through these two cross sections is similar, implying that the divergence of the
volume transport between these cross sections is small. Hence, the difference

Table 3.2: 2-year averaged volume transports in Sv (1 Sv = 10^6 m^3 s^{-1}) through the passages between the Lesser Antilles in the model (*CS-nest*, second column) and in available observations Johns et al. (2002); Kirchner et al. (2008). Standard errors of the mean are indicated at the cross section along the Lesser Antilles (the green line in Figure 3.1). Positive numbers correspond to transports into the Caribbean Sea.

Section	*CS-nest*	Johns et al. (2002)	Kirchner et al. (2008)
Montserrat - St. Kitts	0.30 ± 0.02		
Guadeloupe - Montserrat	0.83 ± 0.03	1.1 ± 1.1	
Dominica - Guadeloupe	1.43 ± 0.03	1.6 ± 1.2	0.7 ± 0.5
Martinique - Dominica	1.04 ± 0.06	1.6 ± 1.2	1.6 ± 0.5
St. Lucia - Martinique	2.74 ± 0.04	1.5 ± 2.4	1.2 ± 0.5
St. Vincent - St. Lucia	3.62 ± 0.05	2.9 ± 2.2	3.6 ± 0.5
Grenada - St. Vincent	1.03 ± 0.01		
Venezuela - Grenada	4.60 ± 0.06	5.7 ± 2.4	
66°W	21.12 ± 0.54	18.4 ± 4.7	

between fluxes of vorticity east and west of the Lesser Antilles can be used as a measure for the local generation and dissipation of vorticity at the island arc.

3.3   Model validation

3.3.1   Mean flow

The mean flow in the Caribbean Sea is part of the subtropical gyre in the North Atlantic Ocean and enters the basin through the Lesser Antilles (Johns et al., 2002). In line with observations (Johns et al., 2002; Kirchner et al., 2008), we find that the bulk of the modeled flow enters the basin through the passages between the southern islands (Table 3.2). A smaller fraction of the flow enters the basin through the northern passages (Table 3.2). The modeled volume transport through all passages adds up to 21.12 ± 0.54 Sv at 66°W, which is in line with to the volume transport of 18.4 ± 4.7 Sv estimated from observations (Johns et al., 2002).

Also in line with observations (Johns et al., 2002; Kirchner et al., 2008), we find that the flow into the Caribbean is highly variable (Table 3.2). Previous observations indicated that part of this variability is driven by the 2 to 7 NBC rings that propagate towards the Caribbean Sea each year (Goni and Johns, 2003; Mertens et al., 2009; Mélice and Arnault, 2017). More specifically, Mertens et al. (2009) showed that, before they reach the Lesser Antilles, the NBC rings decrease the volume transport into the Caribbean, while they increase the volume transport during the actual collision.

To identify whether the flow into the Caribbean Sea contains a realistic representation of the water masses, we analyze the time-averaged properties of the water masses in the model (Fig. 3.3). Because, the Caribbean anticyclones are
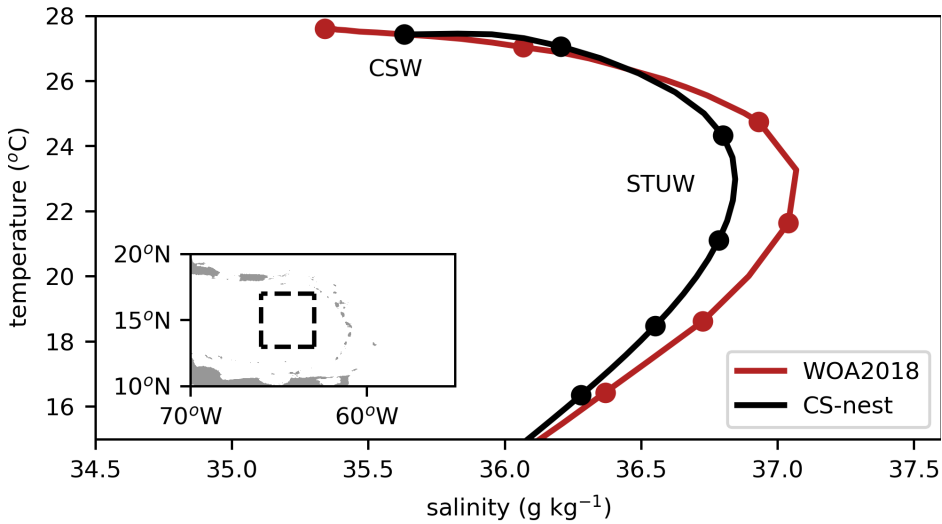
Figure 3.3: Temperature-Salinity diagram of the time-mean conservative temperature and absolute salinity in the eastern Caribbean Sea (63°W-66°W, 13°N-17°N, see dashed box in inlay) for the simulations with the *CS-nest* (black) and WOA2018 (red). Dots correspond to depth levels from 0 m to 250 m with intervals of 50 m. The approximate locations of Caribbean Surface Water (CSW) and Subtropical Underwater (STUW) are indicated.

shallow, and the vorticity fluxes are analysed to a depth of 300 m, we limit ourselves to the validation of the characteristics of the upper-ocean water masses. The model contains the two distinctive water masses that are characteristic for the upper Caribbean Sea: the subsurface properties (i.e. the salinity maximum) of Subtropical Underwater (STUW) and the surface properties of Caribbean Surface Water (CSW, Morrison and Nowlin, 1982; Hernández–Guerra and Joyce, 2000). A comparison to data from the WOA2018 in the eastern Caribbean Sea (63°W-66°W, 13°N-17°N, Fig. 3.3) indicates that the model underestimates the salinity of the STUW. We find a salinity maximum of S = 36.8 g kg^{-1} in the model compared to S = 37.1 g kg^{-1} in the WOA2018. This underestimation is seen in both the Atlantic Ocean and the Caribbean Sea. Taking the relatively long travel distance of STUW from its formation region in the central tropical Atlantic to the Caribbean Sea into account (Qu et al., 2013; Montes et al., 2016), this underestimation is likely the result of too much diapycnal mixing in the parent simulation.

In contrast, the temperature distribution of STUW is adequately modeled and the surface properties of the CSW are also well represented in the model (Fig. 3.3). The adequate representation of these surface properties implies that the surface forcing is well captured by the model and that the model is able to represent the time-averaged temperature and salinity in this basin.
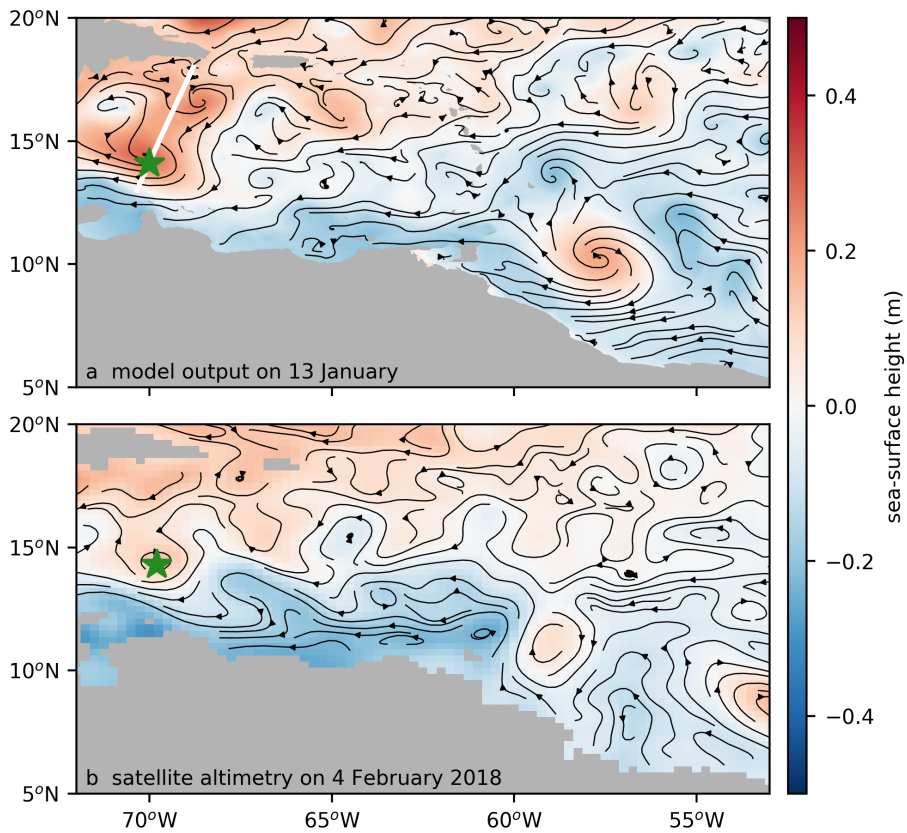
Figure 3.4: Sea-surface height (a) in the *CS-nest* simulation on 13 January and (b) from satellite altimetry on 4 February 2018. Streamlines of the flow are indicated with black curves. Green stars highlight the location of anticyclones discussed in Section 3.3.2. The white line indicates the location of the cross sections depicted in Fig. 3.5. The sea-surface height from satellite altimetry in (b) is computed from multi-mission altimeter satellite grid-ded sea-surface heights, downloaded from the Copernicus Marine Environment Monitoring Service (http://marine.copernicus.eu).

3.3.2   Caribbean anticyclones

To assess that the vorticity in the eastern Caribbean Sea is accurately represented in the model, we analyze the properties of the simulated Caribbean anticyclones and their vertical structure. Caribbean anticyclones are known to dominate the sea-surface variability in the Caribbean basin (e.g., Centurioni and Niiler, 2003; Richardson, 2005), and surface drifter data indicates that approximately 4-8 anticyclones are formed each year (Richardson, 2005). In line with these observations, we find that 13 anticyclones are formed in the vicinity of the Lesser Antilles during the 2 years of the simulation. Based on their vertical structure, we can distinguish two types of Caribbean anticyclones in the model: shallow and deep anticyclones. The shallow anticyclones have a strong surface-intensified character with weak velocities below the pycnocline $|u| < 0.1$ m s^{-1} as defined in Chapter 2 of this thesis. The deep anticyclones display stronger velocities below the pycnocline.

Because the modeled shallow anticyclones have a similar velocity structure as the in-situ observations that were described in Chapter 2 of this thesis, we compare these observations to a simulated shallow anticyclone near the location of this hydrographic survey in the central Caribbean (green stars in Fig. 3.4). As expected, we find that both anticyclones are intensified at the surface and have a weak velocity shear below the main thermocline (compare Fig. 2.3b,c and Fig. 3.5a,b). Furthermore, the mixed layer depth of the modeled anticyclone (MLD = 80 m) is about equal to the mixed layer depth of the observed anticyclone, and the mixed layers in both anticyclones are limited by the halocline (orange lines in Fig. 2.3d,e and Fig. 3.5c,d). This is typical for the Caribbean Sea in winter, and indicates the presence of a barrier layer, which is defined as the layer between the halocline and thermocline (de Boyer Montégut et al., 2004; Mignot et al., 2007; Rudzin et al., 2017). The fact that the model captures such a barrier layer suggests that it has a realistic representation of the mixed-layer dynamics.

The deep anticyclones have a similar structure as previously observed by Rudzin et al. (2017), who performed upper-ocean measurements of a Caribbean anticyclone and concluded that this example was a coherent vortex down to at least 500 m depth. These anticyclones have, similar to the shallow anticyclones, a baroclinic structure, but display stronger velocities below the pycnocline. One example of a modeled deep anticyclone that was present in summer is shown in Figure 3.6. During this season, the sea-surface height gradients in the Caribbean basin are stronger. A comparison to a sea-surface height field obtained from satellite altimetry indicates that this is also the case for observations (compare Fig. 3.4b and Fig. 3.6). This is expected, as Caribbean anticyclones tend to be more energetic in summer than in winter (Jouanno et al., 2012).

The vertical structure of the modeled deep anticyclone is shown in Figure 3.7, and strong velocities are found below the thermocline (red line in Fig. 3.7a). The structure of the vertical shear suggests that this anticyclone is deeper than 300 m (Fig. 3.7b). While the observations of Rudzin et al. (2017) did not capture the
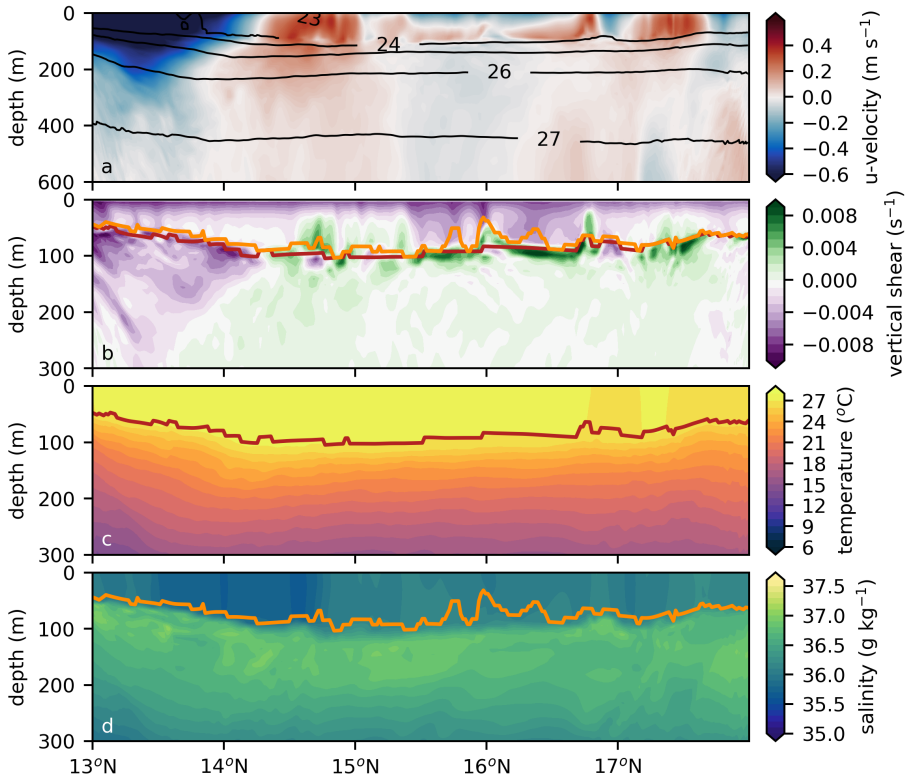
Figure 3.5: Characteristics of a modeled shallow anticyclone in the Caribbean Sea in winter, by means of cross sections of the (a) velocity perpendicular to the cross section (m s^{-1}), (b) vertical shear of this velocity (s^{-1}), (c) conservative temperature (°C) and (d) absolute salinity (g kg^{-1}) on 13 January. Contour lines in panel (a) show the isopycnals. The thermocline and halocline, indicated with the red and orange curve respectively, were computed following Mignot et al. (2012).

full depth of the anticyclone, their findings indicate that not all Caribbean anticyclones are as shallow as the one described in Chapter 2 of this thesis. Not only does this imply that the vertical structure of Caribbean anticyclones is diverse, it also indicates that the model generates anticyclones with realistic characteristics.

3.4   Advective vorticity flux

3.4.1   Mean fluxes

To quantify the fluxes of vorticity into the eastern Caribbean Sea, we compute the 2-year averaged zonal flux of anticyclonic vorticity (Fig. 3.8, equation 3.3a). This computation indicates that two different sources of anticyclonic vorticity are
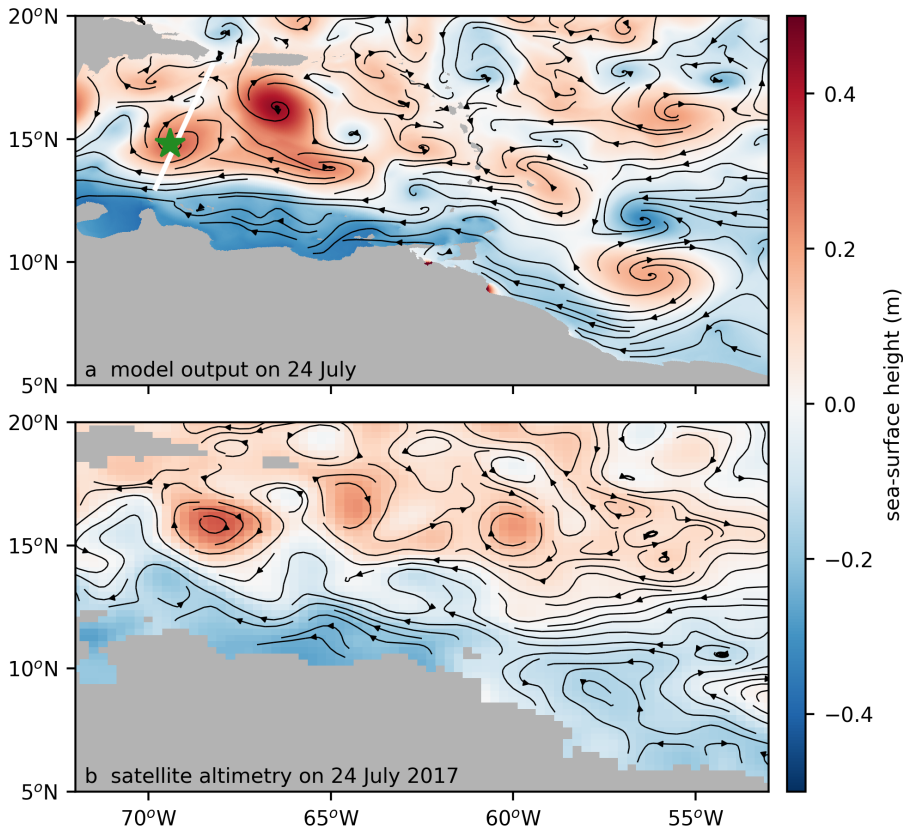
Figure 3.6: Sea-surface height (m) in the (a) *CS-nest* on 24 July of year 6 and (b) from satellite altimetry on 24 July 2017. Streamlines of the flow are indicated with black curves. The green star highlights the location of anticyclones discussed in Section 3.3.2. The white line indicates location of cross section of Fig. 3.7. The sea-surface height from satellite altimetry is computed from multi-mission altimeter satellite gridded sea-surface heights, downloaded from the Copernicus Marine Environment Monitoring Service (http://marine.copernicus.eu).

Figure 3.7: Characteristics of a modeled deep anticyclone in summer, by means of cross sections of the (a) u-component of the velocity (m s^{-1}), (b) vertical shear of the u-component of the velocity (s^{-1}), taken at the location indicated in Fig. 3.6 on 24 July year 6. Contour lines in panel (a) show the isopycnals. The thermocline and halocline, indicated with the red and orange line respectively, were com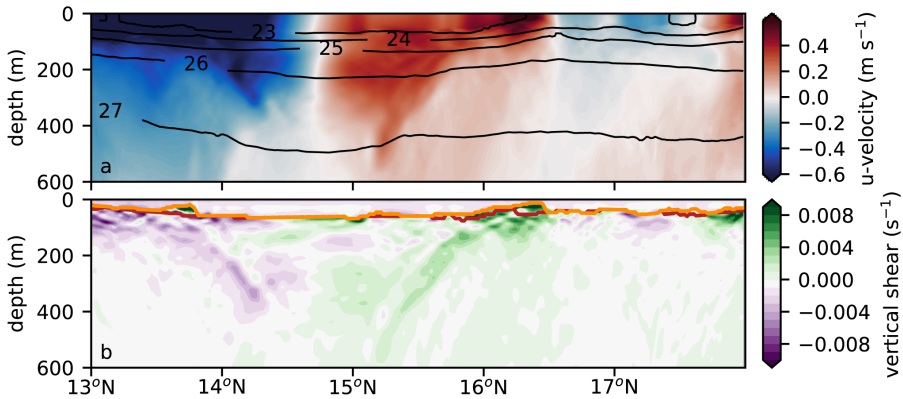puted following Mignot et al. (2012). Note that the vertical axis of panel (b) extends deeper than the one in Figure 3.5b.

present in the eastern Caribbean Sea: the advection of vorticity from the Atlantic Ocean, and the generation of vorticity near the Lesser Antilles. The advection of anticyclonic vorticity includes the westward propagation of anticyclonic NBC rings, and is visible as a coherent (i.e., westward) flux of anticyclonic vorticity path from the Atlantic towards the Lesser Antilles (Fig. 3.8). The magnitude of the flux decreases between Tobago (T) and Barbados (B), which indicates that part of this anticyclonic vorticity flux is dissipated or redirected in meridional direction there. West of the Lesser Antilles, extreme values (dark blue) are visible that are not connected to the vorticity fluxes in the Atlantic Ocean. These values have the largest magnitude near the southern boundaries of the islands, which is indicative for the local generation of vorticity (dark blue in Fig. 3.8). Especially near Grenada (G) and St. Lucia (L), we find a clear signal that vorticity is generated locally (arrows in Fig. 3.8).

Next, we quantify the relative contribution of both sources of vorticity to the total influx of vorticity. This can be obtained by comparing the vorticity fluxes on the eastern and western side of the Lesser Antilles. Note that we can use the difference in vorticity flux as a measure for the generation of the vorticity, because the volume transport in the eastern and western cross section in Fig. 3.8 is similar (Fig. 3.9a). West of the Lesser Antilles, a total section-integrated flux of 165 m^3 s^{-2} of anticyclonic vorticity is transported into the Caribbean Sea (solid line in Fig. 3.9b). Of this flux, 54 m^3 s^{-2} can be attributed to the advection of anticyclonic vorticity towards the Lesser Antilles from thee east (dashed line in Fig. 3.9b). The difference of 111 m^3 s^{-2} between these cross sections reflects the local generation of vorticity between the cross sections (grey shading in Fig.
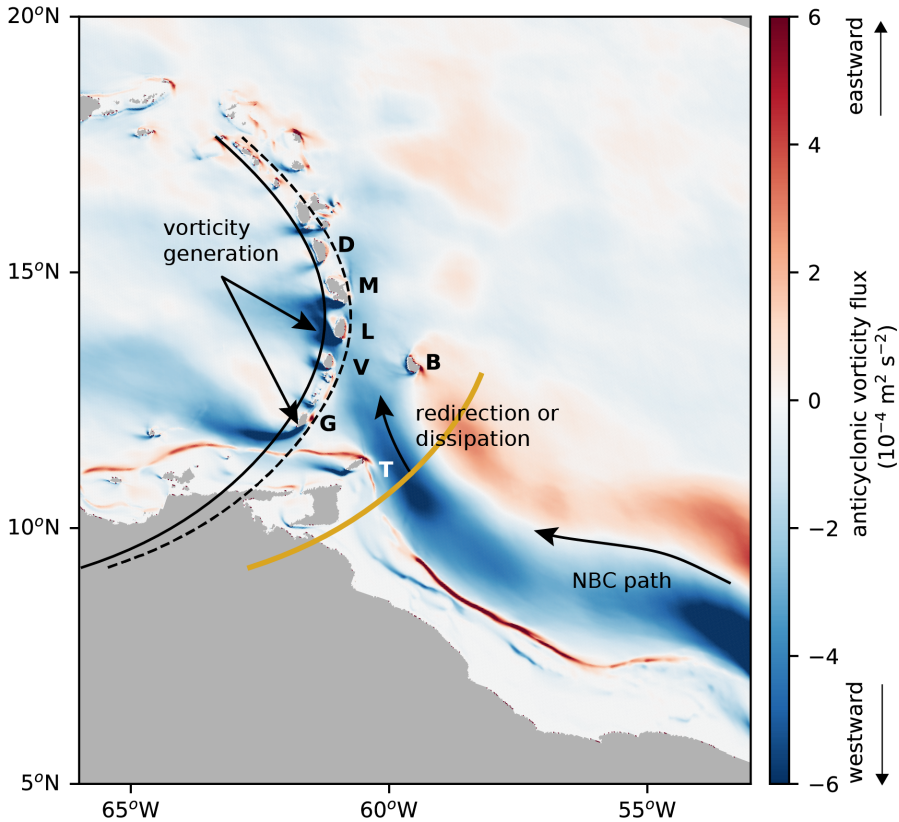
Figure 3.8: Zonal component of the anticyclonic vorticity flux integrated over the upper 300 m of the water column and averaged over 2 years model data from *CS-nest*. Negative values correspond to a flux in westward direction. Dashed and solid lines indicate the locations of the cross sections east and west of the Lesser Antilles, respectively. Letters are placed east of the islands to indicate their location: D = Dominica, M = Martinique, L = St. Lucia, V = St. Vincent, G = Grenada, T = Tobago, B = Barbados. The yellow curve indicates the location of the cross section along which the maximum sea-level anomaly is obtained that is used to gain insight into the passage of NBC rings in Section 3.5 (Fig. 3.10d).

Figure 3.9: Total (a) volume transport (b) anticyclonic vorticity flux and (c) cyclonic vorticity flux at the Lesser Antilles integrated along the eastern (dashed lines) and western (black solid line) cross section (Fig. 3.1) integrated over the upper 300 m of the water column. The grey shaded area indicates the generation of vorticity between the cross sections. (d) Maximum sea-level anomaly between Barbados and Tobago along the yellow curve in Fig. 3.8. The blue shading indicates the collision of an NBC ring with the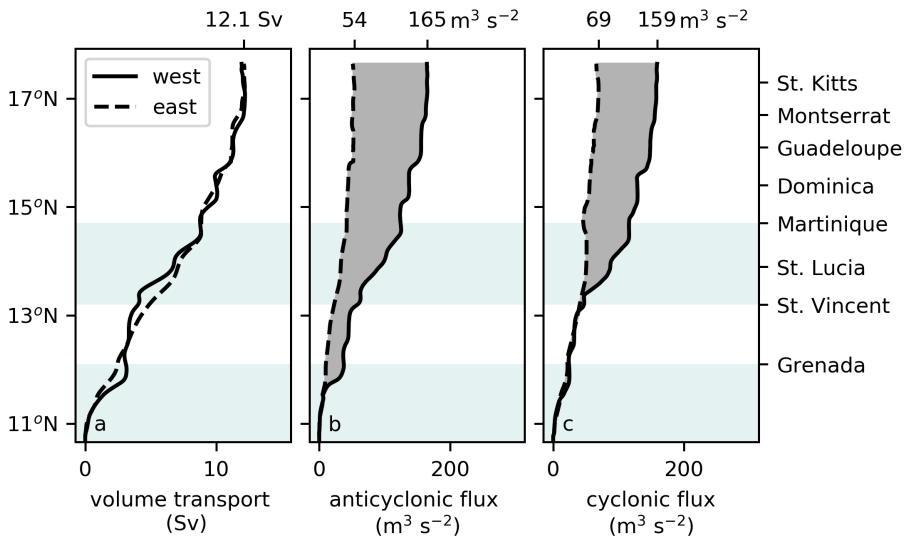 Lesser Antilles that is described in Section 3.6. The data is smoothed with a Hanning function with a window of 30 days. 5 October and 19 June indicate the times of minimum and maximum volume transport through the Lesser Antilles.

3.8b), which comprises 67 % of the total anticyclonic vorticity flux into the eastern Caribbean Sea. This is much larger than the contribution of the vorticity that is advected from the Atlantic Ocean and contains the vorticity of the NBC rings (33 %).

Similar to what we find for the anticyclonic vorticity flux, the cyclonic vorticity flux into the eastern Caribbean Sea is also dominated by the local generation of vorticity near the Lesser Antilles (grey shading in Fig. 3.9c). The magnitude of the cyclonic vorticity flux west of the Lesser Antilles is 159 m^3 s^{-2}, of which 69 m^3 s^{-2} is attributed to advection of cyclonic vorticity from the Atlantic Ocean (solid and dashed lines in Fig. 3.9c, respectively). This implies that 57 % of the cyclonic vorticity flowing into the Caribbean Sea is generated between the two cross sections.

Besides quantifying the relative contributions of the advected and generation of vorticity near the Lesser Antilles, Figure 3.9 also shows that the generation of vorticity varies latitudinally as is reflected by a strong difference in meridional gradients between the cross sections. From Figure 3.9b, two regions with enhanced local generation of anticyclonic vorticity can be identified (blue shad-

ing): south of Grenada and between St. Vincent and Martinique. In contrast, at latitudes where the meridional gradients in the eastern cross section are similar to the western cross section, the vorticity flux into the Caribbean Sea is predominantly advected from the Atlantic Ocean. This occurs, for example, between Grenada and St. Vincent and north of Martinique.

Following Jiménez et al. (2008), we expect that the magnitude of the vorticity generation is related to the flow speed and thus to the magnitude of the volume transport through the passages. Indeed, passages with a strong volume transport also have enhanced generation of anticyclonic vorticity (blue shading in Fig. 3.9a,b). For example, the passages south of Grenada and between St. Vincent and Martinique contain 67 % of the total volume transport into the eastern Caribbean Sea, and approximately 69 % of the anticyclonic vorticity is generated here. The volume transport through the other passages (between Grenada and St. Vincent and north of Martinique), where little anticyclonic vorticity is generated, is much weaker (4.1 Sv, Fig. 3.9a). Overall, these findings suggest that the bulk of the anticyclonic vorticity that enters the Caribbean Sea is generated between the two cross section s. Moreover, these results also indicate that the local generation of vorticity is regulated by the magnitude of the volume transport through the passages.

3.5   Temporal variability of the vorticity flux

To determine the link between the magnitude of the volume transport and vorticity generation in more detail, we analyze the temporal variations of the vorticity fluxes in this section. Similar to observations of Johns et al. (2002) and Rhein et al. (2005), we find highly-varying volume transports through the passages of Lesser Antilles with a minimum modeled volume transport of 3.2 Sv in the upper 300 m of the water column and a maximum of 19.7 Sv (Fig 3.10a). A comparison of these volume transports to the vorticity fluxes at the western side of the Lesser Antilles confirms that there is a close relation between the magnitude of the volume transport and the magnitude of the anticyclonic and cyclonic vorticity fluxes (solid lines in Fig. 3.10b,c). More specifically, the peaks in volume transport coincide with peaks in the anticyclonic and cyclonic vorticity flux into the eastern Caribbean Sea (solid line in Fig. 3.10b,c). For example, during maximum inflow on 19 June, the anticyclonic vorticity flux has a maximum of 358 m^3 s^{-2}, while it was much smaller on 5 October (57 m^3 s^{-2}), when the volume transport was weak (2.6 Sv, solid line in Fig. 3.10b). The vorticity flux east of the Lesser Antilles is at all times smaller than the flux on the western side of the islands. This shows that anticyclonic vorticity is continuously generated at the Lesser Antilles (grey shading in Fig. 3.10b). The same is found for the cyclonic vorticity flux, of which the magnitude also has a strong connection to the magnitude of the volume transport.

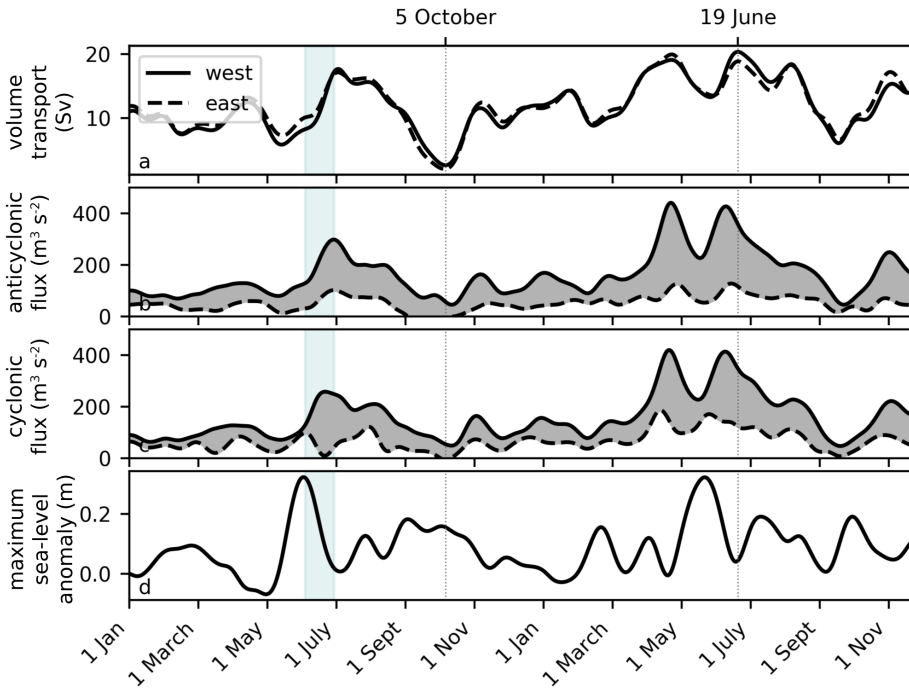Figure 3.11 shows a more detailed relation between the total volume trans-

Figure 3.10: Total (a) transport (b) anticyclonic vorticity flux and (c) cyclonic vorticity flux at the Lesser Antilles integrated along the eastern (dashed lines) and western (black solid line) cross section (Fig. 3.1) and over the upper 300 m of the water column. (d) Maximum sea-level anomaly between Barbados and Tobago along the yellow line in Fig. 3.8. Red lines indicate the percentage of generated vorticity compared to total vorticity flux into the Caribbean computed at the western cross section. The grey shaded area corresponds to the vorticity flux that is generated between the cross sections. The light blue shading indicates the collision studied in Figures 3.12-3.15. The data is from *CS-nest* and smoothed with a Hanning window of 30 days.

port through the Lesser Antilles and the generation and advection of vorticity. The advection, which is defined as the 6-hourly snapshots of vorticity flux through the eastern cross section, scales about linearly with the transport. This implies that, on average, with stronger volume transport more anticyclonic vorticity is transported into the eastern Caribbean Sea. Similar to the advection, the generation of vorticity, defined as the difference between the 6-hourly snapshots west and east of the Lesser Antilles, also depends on the magnitude of the transport. Overall, this figure shows that both the advection and generation of vorticity are proportional to the transport. As expected from Fig. 3.10b,c, the vorticity flux into the Caribbean Sea is dominated by the locally generated vorticity.
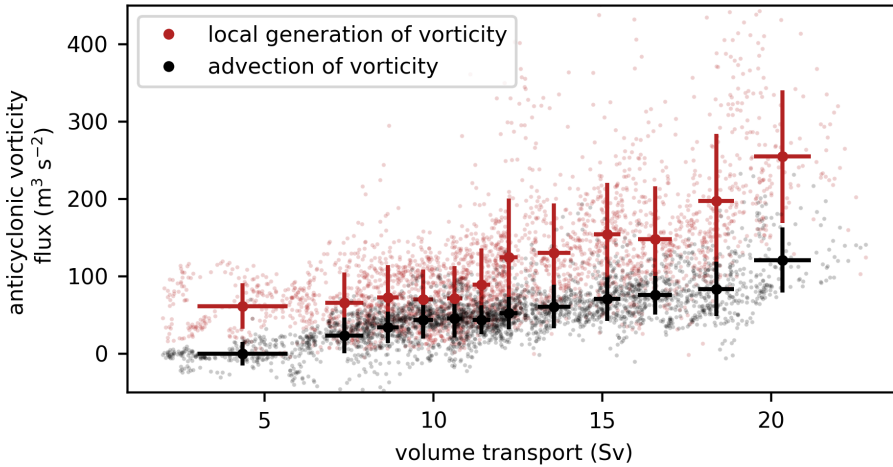
Figure 3.11: Relation between the total volume transport and the anticyclonic vorticity flux into the Caribbean Sea, distinguishing the local generation of vorticity (red symbols) and the advection of vorticity from the Atlantic Ocean (black dots). The local generation of vorticity is defined as the difference between the 6-hourly snapshots of the vorticity flux west and east of the Lesser Antilles (similar to grey shading in Fig. 3.10b). The advection of vorticity corresponds to the anticyclonic vorticity flux east of the Lesser Antilles (similar to Fig. 3.10b). The thick dots indicate average values per 250 data points, where the error bars correspond to one standard deviation.

3.6 Event study of the collision of a NBC ring with the Lesser Antilles

Previous studies suggested that the volume transport into the Caribbean Sea is regulated by NBC rings (Mertens et al., 2009). These rings are visible as positive sea-level anomalies. We extract these sea-level anomalies by taking the maximum sea-level anomaly (max $(\eta - \overline{\eta})$, where $\overline{\eta}$ is the mean dynamic topography) along the yellow curve in Fig. 3.8. During the 2-year *CS-nest* model simulation, approximately 10 rings propagate towards the Lesser Antilles. To investigate if their presence affects the generation and advection of vorticity, we study a collision of an NBC ring with the Lesser Antilles in more detail (period indicated by blue shading in Figure 3.10).

The start of the collision event is defined as the moment when the NBC ring passes between Tobago and Barbados (peak in sea level in Fig. 3.10d). At that time, the volume transport into the Caribbean is already increasing (Fig. 3.10a). This coincides with an increase of the anticyclonic and cyclonic vorticity flux on the western side of the Lesser Antilles (solid lines in Fig. 3.10b,c). The end of the collision event is defined as when the anticyclonic vorticity of the NBC ring has diminished east of the Lesser Antilles. This occurs approximately 25 days later.
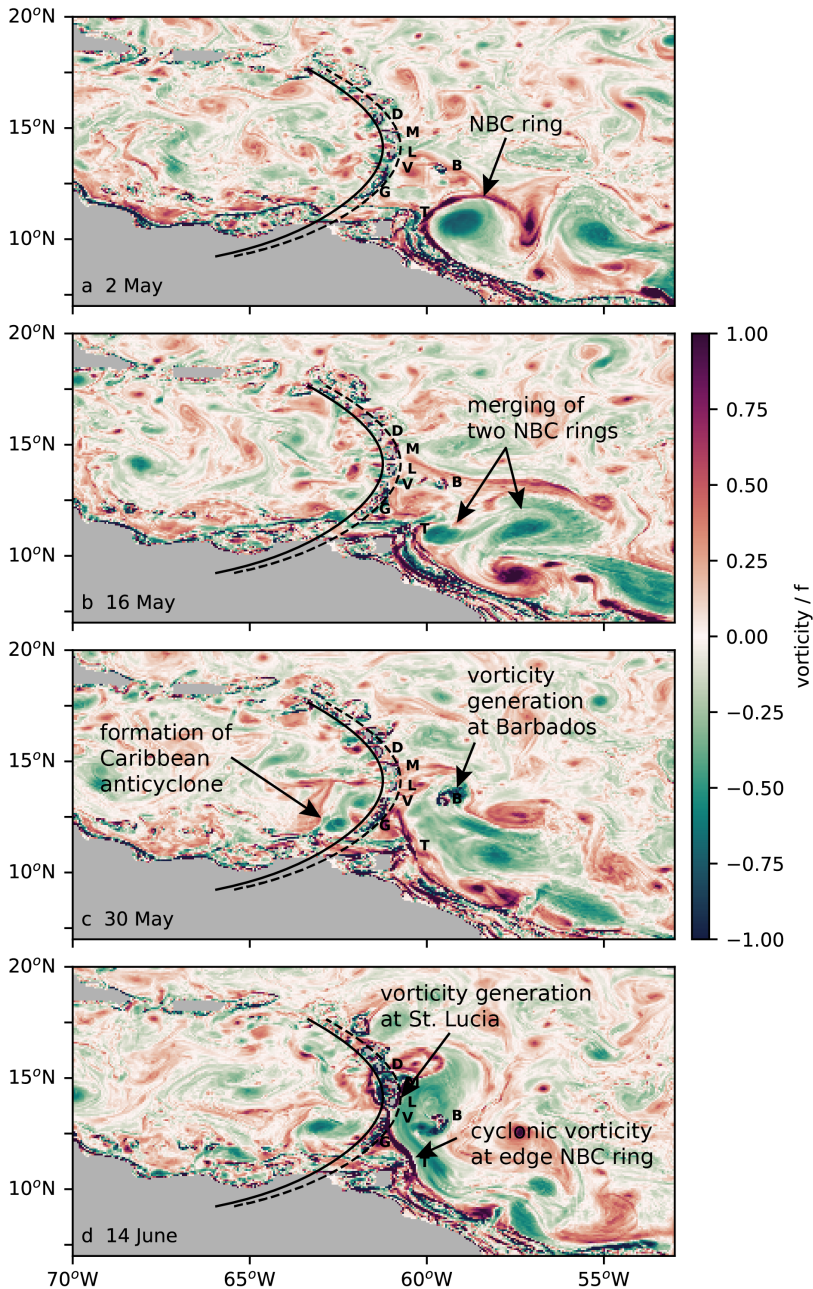
Figure 3.12: Vorticity averaged over the upper 300 m modeled using the *CS-nest*, scaled with the local Coriolis parameter ($f = 2\Omega \sin \phi$) during a collision event of an NBC ring with the Lesser Antilles on (a) 2 May, (b) 16 May, (c) 20 May, (d) 14 June. Dashed and solid lines indicate the locations of the cross sections east and west of the Lesser Antilles, respectively. Letters are placed east of the islands to indicate their location: D = Dominica, M = Martinique, L = St. Lucia, V = St. Vincent, G = Grenada, T = Tobago, B = Barbados.
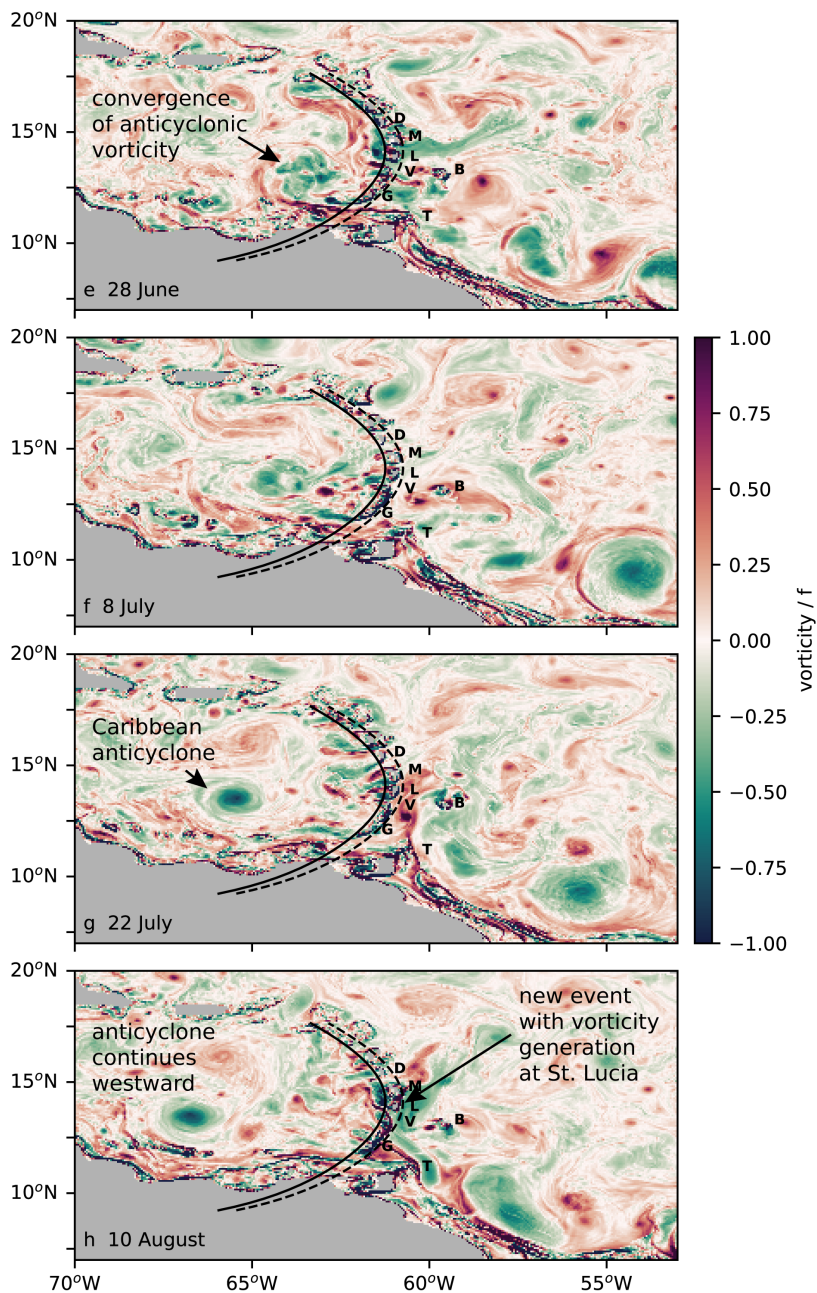
Figure 3.12: (continued) (e) 28 June, (f) 8 July, (g) 22 July, (h) 10 August.

To determine how the presence of the NBC ring affects the fluxes of vorticity, we first describe the collision event in Section 3.6.1 using the 6-hourly snapshots of the vorticity fields. The description starts 40 days before the collision event with snapshots from the *CS-nest* (Fig. 3.12a-d). Before the description continues to approximately 40 days after the event (Fig. 3.12e-h), the collision itself is described using snapshots from the *LA-nest* (Fig. 3.13). Subsequently, we analyze the time-averaged vorticity fluxes of this collision in Section 3.6.2.

3.6.1   Descriptive analysis

Vorticity snapshots of the collision event obtained from the *CS-nest* are displayed in Figure 3.12. On 2 May, which is approximately 40 days before the collision, two NBC rings are present in the Atlantic Ocean (Fig. 3.12a). Both rings have an anticyclonic core (green shading in Fig. 3.12), of which one has a cyclonic edge (red shading). Similar to observations of Cruz-Gómez and Vazquez (2018), we find that the NBC ring with a cyclonic edge stalls south of Barbados (B). Fourteen days later on 16 May, the two rings merge (Fig. 3.12b). On 30 May, the merged NBC ring approaches the Lesser Antilles and passes the first ridge between Barbados (B) and Tobago (T, Fig. 3.12c). During this passage, anticyclonic vorticity is generated near Barbados in the wake of the island. At the same time, the cyclonic edge of the NBC ring separates the anticyclonic core from the Lesser Antilles. This effect is still visible between Tobago (T) and St. Vincent (V) 14 days later on 14 June (Fig. 3.12d).

To study the interaction between the NBC ring and the Lesser Antilles in even more detail, we analyze vorticity snapshots from the *LA-nest* simulation with a 700 m horizontal resolution (Fig. 3.13). On 14 June, a patch of anticyclonic vorticity, which appears to be generated in the wake of Tobago (T), flows into the Caribbean Sea (Fig. 3.13a). Similarly, a patch of anticyclonic vorticity develops farther northward at St. Lucia (L). This patch of anticyclonic vorticity enters the Caribbean Sea on 19 June (Fig. 3.13b).

The cyclonic vorticity that originates from St. Lucia as well is generated at the eastern side of this island. Besides the local generation of vorticity near St. Lucia (L) and Tobago (T), there is also a flux of anticyclonic vorticity into the Caribbean Sea south of Grenada (G). This flux is clearly visible on 24 June as a maximum in anticyclonic vorticity in the wake of Grenada (G, Fig. 3.13c). This patch of vorticity is advected into the Caribbean Sea together with some remaining anticyclonic vorticity of the NBC ring (Fig. 3.13d).

Because only small remnants of the NBC ring can be found on the eastern side of the Lesser Antilles on 29 June (Fig. 3.13d), we resume with the snapshots from the *CS-nest* (zoomed out map in Fig. 3.12e). At that time, an anticyclone forms on the Caribbean side of the Lesser Antilles (Fig. 3.12e-f). This anticyclone consists of merged submesoscale filaments of vorticity that can be traced back to Grenada (G) and to St. Lucia (L, Fig.3.12c,g). After formation, this anticyclone propagates along the mean flow in westward direction (Fig. 3.12h).

3.6.2 Vorticity generation

The snapshots of the vorticity field highlight the two different sources of anticyclonic vorticity that flow into the eastern Caribbean Sea during the NBC ring-island collision event: advection of vorticity from the Atlantic Ocean and the local generation of vorticity near the Lesser Antilles. To analyze the contribution of these sources, we compute the time-averaged vorticity fluxes during the collision event (Fig. 3.14). For completeness, we show the fluxes of both anticyclonic (Fig. 3.14a,b) and cyclonic vorticity (Fig. 3.14c,d).

The advection of anticyclonic vorticity from the NBC ring into the eastern Caribbean Sea is visible on the Atlantic side of the Lesser Antilles. This westward advection of anticyclonic vorticity from the eastern boundary of the domain towards the Caribbean is minor as, judging from the spatial pattern (blue shading in Fig. 3.14a), most anticyclonic vorticity appears to be generated at the islands. At the southern boundaries of Tobago (T) and Barbados (B) we find clear maximums of the flux of anticyclonic vorticity, which shows that vorticity is locally generated there.

Similar to its westward advection, the northward advection of anticyclonic vorticity indicates locations with enhanced local generation of vorticity (red shading in Fig. 3.14b). One of these locations is the passage south of St. Lucia (L), where also some of the anticyclonic vorticity of the NBC rings is advected. Also part of the cyclonic edge of the NBC ring is advected through this passage, which is visible by a maximum that extends from the southern boundary towards St. Lucia (L, Fig. 3.14c,d). Northward of St. Lucia, it splits into an Atlantic branch and a Caribbean branch.

To quantify the relative contributions of the advection and generation of vorticity, we compute the 25-days averaged volume transport and vorticity fluxes through the previously defined cross sections during this event (Fig. 3.15). Compared to the time-averaged fluxes (Fig. 3.9), the anticyclonic and cyclonic vorticity flux into the eastern Caribbean are relatively high during the event (Fig. 3.15b,c). These anomalously high fluxes of vorticity coincide with a relatively high volume transport and are both due to increased advection of vorticity and enhanced generation of vorticity. Consequently, only 29 % of the vorticity flux into the Caribbean Sea can be attributed vorticity from the Atlantic Ocean. Recall that east of the most eastern cross section also vorticity is generated at Tobago and Barbados (Fig. 3.15). Consequently, the contribution of the vorticity of NBC rings is at most 29 %.

During the collision event, we obtain a similar latitudinal variation in the generation of vorticity as found in the two-year averaged fluxes (Fig. 3.9, Fig. 3.15b). Most anticyclonic vorticity is generated locally south of Grenada and near St. Lucia (light blue shading in Fig. 3.15b). Most cyclonic vorticity is generated near St. Lucia (Fig. 3.15c). Overall, these results show that also during the collision of an NBC ring with the Lesser Antilles the bulk of the vorticity flux into the Caribbean Sea is generated near the topography.
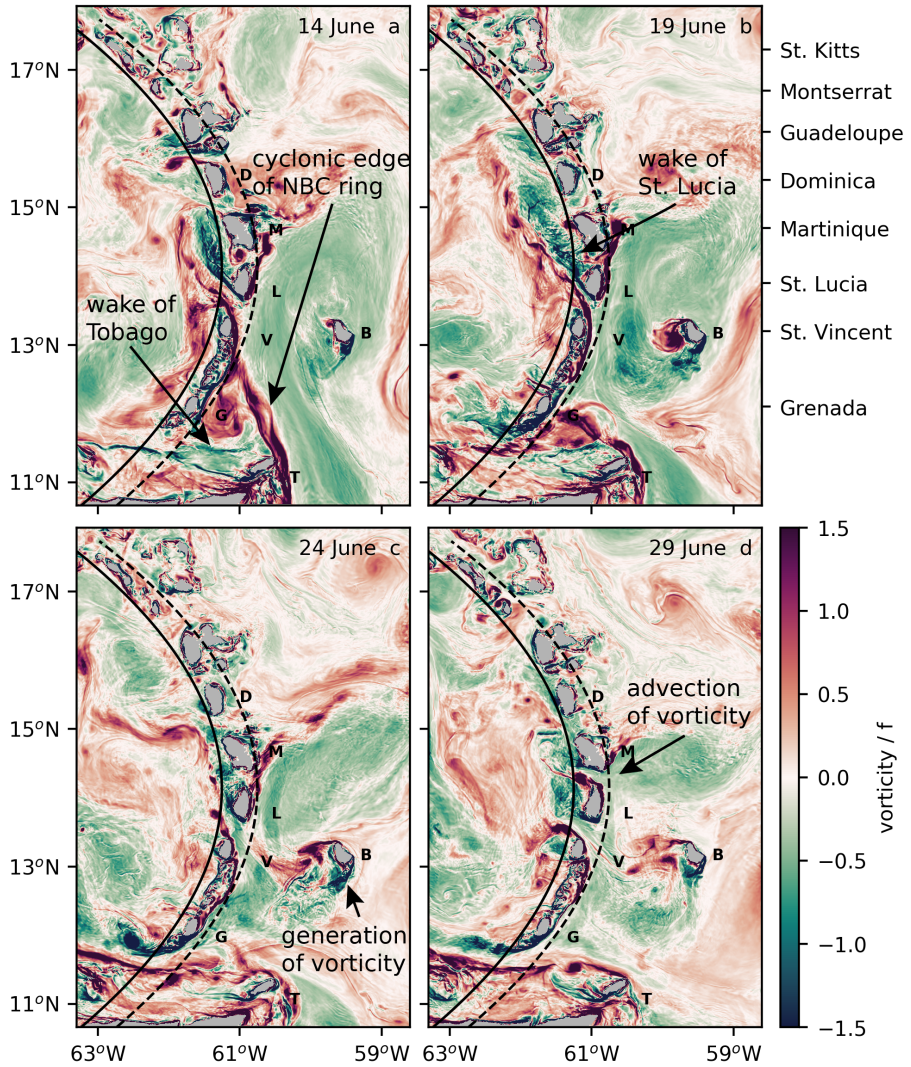
Figure 3.13: Similar as Figure 3.12, but then for the *LA-nest* simulation on (a) 14 June, (b) 19 June, (c) 24 June, (d) 29 June.
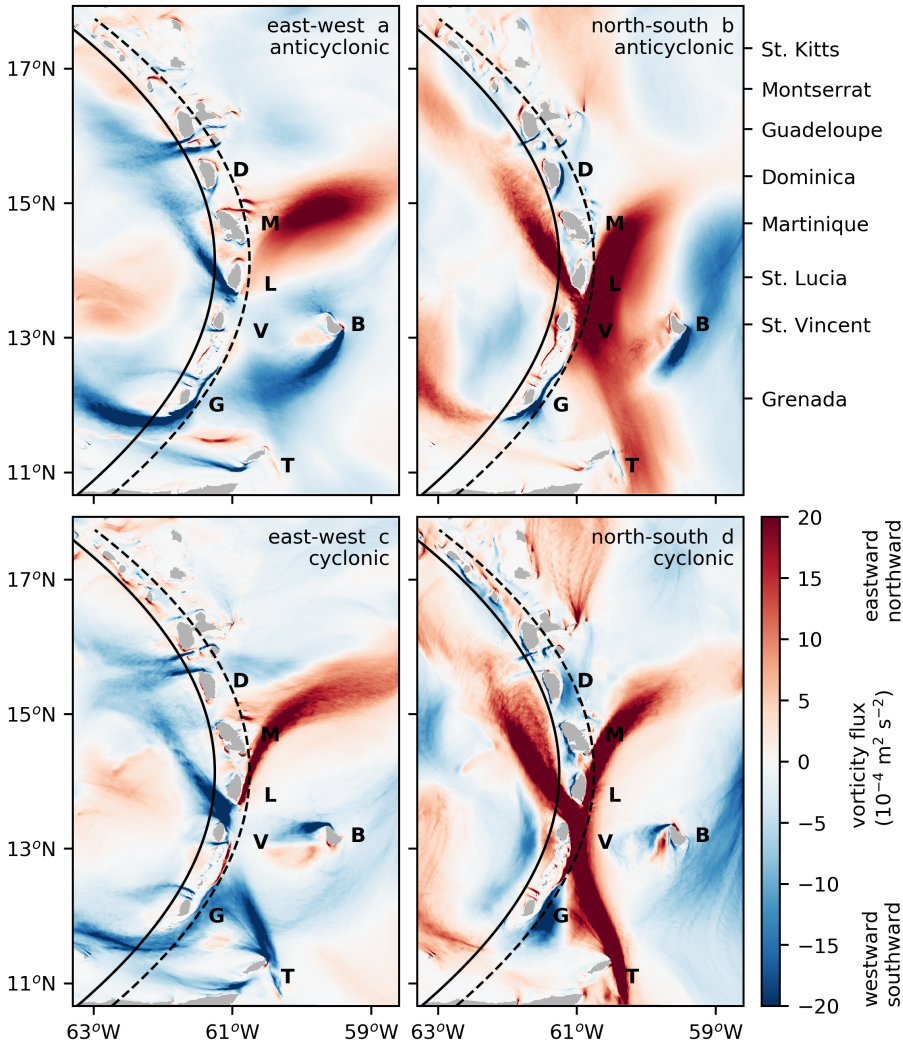
Figure 3.14: Directional vorticity flux integrated over the upper 300 m of the water column and averaged between 3 June and 28 June (*LA-nest*). (a,b) Anticyclonic vorticity flux in (a) eastward and (b) northward direction; (c,d) Cyclonic vorticity flux in (c) eastward and (d) northward direction. Dashed and solid lines indicate the locations of the cross sections east and west of the Lesser Antilles, respectively. Letters are placed east of the islands to indicate their location: D = Dominica, M = Martinique, L = St. Lucia, V = St. Vincent, G = Grenada, T = Tobago, B = Barbados.
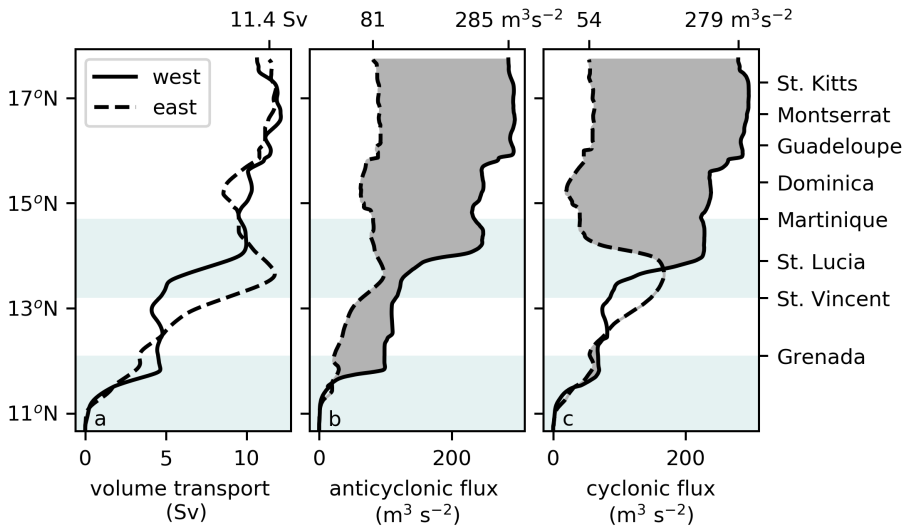
Figure 3.15: Same as Fig. 3.9, but then during the collision of an NBC ring with the Lesser Antilles (3 June to 28 June, as simulated by the *LA-nest* configuration).

3.7   Discussion and conclusions

In this study, we analyzed the local generation of vorticity near steep topography of the Lesser Antilles island arc, which separates the Atlantic Ocean from the Caribbean Sea, with a high-resolution numerical model. On the Atlantic side of the Lesser Antilles, the flow is dominated by anticyclonic North Brazil Current (NBC) rings that collide with this island arc. The flow in the Caribbean Sea is characterized by the formation of mesoscale anticyclonic eddies in the vicinity of the islands. Our model results indicate that the vertical structure of these anti-cyclonic eddies is diverse. Some anticyclones have a strong baroclinic structure similar to the observations in Chapter 2 of this thesis, while other anticyclones displayed stronger flow velocities below the thermocline, as was previously observed by Rudzin et al. (2017). We speculate that these different vertical structures may result from variations in the vorticity flux directly downstream of the steep topography. However, further research is necessary to clarify what sets the velocity structure of these anticyclones.

To analyze the local generation of vorticity near the steep topography, we computed the fluxes of vorticity east and west of the Lesser Antilles. This allowed us to quantify the relative contributions of the vorticity advected from the Atlantic Ocean (containing the vorticity of the NBC rings) and the vorticity that is locally generated. We found that, during the two years of the model simulation, 67 % of the anticyclonic vorticity flux is generated locally. The remaining 33 % of the vorticity flux is advected from the Atlantic Ocean. The latter contribution

contains both the vorticity generated locally at the easternmost islands of the Lesser Antilles (Tobago and Barbados) and the anticyclonic vorticity filaments of North Brazil Current rings that collide with the islands.

We showed that the local generation of vorticity depends on the magnitude of the volume transport from the Atlantic Ocean to the Caribbean Sea. In particular, the passages with the strongest volume transport also contain the strongest local generation of vorticity. The passages south of Grenada and between St. Vincent and Martinique, which are known for their strong volume transport (Johns et al., 2002; Rhein et al., 2005), show this enhanced generation and the bulk of the locally generated vorticity originates in these regions. These results are supported by observations (Andrade and Barton, 2000; Richardson, 2005) that show that most Caribbean anticyclones are formed directly downstream of these passages.

Mertens et al. (2009) showed that the volume transport through the Lesser Antilles is regulated by the passage of NBC rings. Before a collision event, the NBC rings first decrease the volume transport, after which they enhance it. In line with these results, we obtained an enhanced volume transport through passages of the Lesser Antilles during the collision of an NBC ring. At the same time, both the vorticity flux from the Atlantic Ocean and the local generation of vorticity increased. This enhanced inflow resulted in the formation of a Caribbean anticyclone downstream. While this anticyclone confirms the presence of a connection between the presence of NBC rings and the formation of Caribbean anticyclones as was previously observed (Goni and Johns, 2001, 2003; Richardson, 2005; Rudzin et al., 2017; van Westen et al., 2018), our model results show that this connection is indirect, and that Caribbean anticyclones are predominantly generated in response to the increase in volume transport into the Caribbean Sea.

Overall, the results of this study show that local generation of vorticity near the steep topography of the Lesser Antilles is a crucial part in the vorticity budget of the Caribbean Sea. This vorticity is most likely generated by frictional processes that takes place in the bottom boundary layer (e.g., Dong and McWilliams, 2007; Vic et al., 2015; Srinivasan et al., 2017). Idealized modeling studies showed that these frictional processes significantly contribute to the vorticity budget through the bottom pressure torque (Srinivasan et al., 2019; Jagannathan et al., 2021). In particular, the no-slip boundary condition generates horizontal and vertical shear layers in the bottom boundary layer when a flow encounters a sloping topography (Srinivasan et al., 2019). In turn, these shear layers can lead to the formation of vortices downstream by a combination of barotropic and centrifugal instabilities (Molemaker et al., 2015; Gula et al., 2015; Srinivasan et al., 2019). In this study, we showed that even in an eddy-dominated flow, the vorticity downstream of steep topography is predominantly locally generated. Therefore, this study highlights the importance of vorticity generation by means of flow-topography interactions. Because these interactions are ubiquitous in the ocean, they are expected to be important whenever currents and steep topography meet.

Chapter 4

The impact of upwelling on the intensification of anticyclonic eddies in the Caribbean Sea

Abstract

The mesoscale variability in the Caribbean Sea is dominated by anticyclonic eddies that are formed in the eastern part of the basin. These anticyclones intensify on their path westward while they pass the coastal upwelling region along the Venezuelan and Colombian coast. In this study, we used a regional model to show that this westward intensification of Caribbean anticyclones is steered by the advection of cold upwelling filaments. Following the thermal wind balance, the increased horizontal density gradients result in an increase of the vertical shear of the anticyclones and of their westward intensification. To assess the impact of variations in upwelling on the anticyclones, several simulations were performed in which the northward Ekman transport (and thus the upwelling strength) is altered. As expected, stronger (weaker) upwelling is associated with stronger (weaker) offshore cooling and a stronger (weaker) westward intensification of the anticyclones. Moreover, the simulations with weaker upwelling show farther advection of the Amazon and Orinoco River plumes into the basin. As a result, in these simulations the horizontal density gradients were predominantly set by horizontal salinity gradients. The importance of the horizontal density gradients driven by temperature, which are associated with the upwelling, increased with increasing upwelling strength. The results of this study highlight that both upwelling and the advection of the river plumes affect the life cycle of mesoscale eddies in the Caribbean Sea.

4.1   Introduction

The circulation in the Caribbean Sea is characterized by the through-flow of the wind-driven subtropical North-Atlantic gyre (Gordon, 1967), known as the Caribbean Current. This flow is part of the upper branch of the Meridional Overturning Circulation (Johns et al., 2002), and is highly variable, which manifests itself in meanders and mesoscale eddies. The temporal and spatial variability of the Caribbean Current is influenced by regional differences in wind (Nystuen and Andrade, 1993; Andrade and Barton, 2000; Chang and Oey, 2013; de Jong, Maria, 2017), fresh water inflow from the Amazon and Orinoco River plumes (Chérubin and Richardson, 2007; Beier et al., 2017), resonating Rossby waves (Hughes et al., 2016) and, at interannual time scales, by the El Niño Southern Oscillation (Alvera-Azcárate et al., 2009; Beier et al., 2017).

Surface drifter data show that the mesoscale variability in this region is dominated by anticyclonic eddies (Molinari et al., 1981; Centurioni and Niiler, 2003; Richardson, 2005). These anticyclones are formed in the eastern part of the basin and transport low salinity anomalies originating from the Amazon and Orinoco river plumes westward (Chapter 2 of this thesis, Silander, 2005; Rudzin et al., 2017). They can be generated from the interaction of the flow with the topography (Molinari et al., 1981; Andrade and Barton, 2000), from the meandering current (Andrade and Barton, 2000), from instabilities due to the presence of the river plume (Chérubin and Richardson, 2007), and from perturbations caused by the interaction of North Brazil Current Rings (NBC Rings) with topography (e.g., Simmons and Nof, 2002; Goni and Johns, 2003; Jochumsen et al., 2010). Jouanno et al. (2009) used a model to clarify the dominant generation mechanism, and concluded that the mean flow in the Caribbean Sea is intrinsically unstable, which means that any perturbation could trigger the formation of Caribbean anticyclones.

After formation, the Caribbean anticyclones are advected westward with the mean flow (Gordon, 1967; Andrade and Barton, 2000), and propagate along the wind-driven upwelling regions at the South-American coast. Based on a hydrographic time series of the upwelling in Cariaco Basin, Astor et al. (2003) found that the interannual variability of temperatures in the upwelling region is affected by the anticyclones that advect cold filaments of upwelled waters offshore. This advection affects the ecosystem as it transports larvae and nutrients offshore (Andrade and Barton, 2005; Baums et al., 2006). The advection of these cold filaments also leads to cooling of the interior of the Caribbean Sea (Jouanno and Sheinbaum, 2013). The anticyclones leave the Caribbean Sea through Yucatan Channel. Model studies examining the Yucatan Channel region have shown that Caribbean anticyclones could influence eddy-shedding events of the Loop Current (Murphy et al., 1999; Carton and Chao, 1999; Oey et al., 2005; Candela, 2003; van Westen et al., 2018).

During their propagation, the anticyclones become more energetic (Carton and Chao, 1999; Pauluhn and Chao, 1999; Andrade and Barton, 2000; Richard-

son, 2005). Although this intensification is clearly present in observations (Carton and Chao, 1999; Pauluhn and Chao, 1999; Andrade and Barton, 2000; Richardson, 2005), only a few studies elaborate (briefly) upon the dynamics of this intensification. Based on surface drifter data, Richardson (2005) suggested that the anticyclonic shear of the Caribbean Current could amplify the anticyclones. In contrast, Andrade and Barton (2000) found, based on satellite altimetry data, a direct relationship between the maximum curl of the wind stress and the westward intensification of anticyclones. This relationship highlights that wind stress alters the life cycle of the anticyclones. Jouanno et al. (2009) used a regional model to study the life cycle of Caribbean anticyclones and computed the mechanical energy balance of the flow in this region. Although this balance shows that baroclinic instabilities provide the energy necessary for the westward intensification of the anticyclones, it does not explain what drives the westward intensification of the anticyclones.

In this study, we hypothesize that this intensification is steered by the offshore advection of cold upwelling filaments that cool the interior of the basin. The advection of the filaments results in denser surface waters in the western part of the basin compared to the eastern part of the basin, suggesting that the density difference between the relatively light anticyclones and the surrounding waters will increase. Following the thermal wind balance, it can be expected that the vertical shear of the anticyclone will increase, and consequently its strength.

To test this hypothesis, we use a regional model in which we only vary the upwelling strength. To isolate the impact of upwelling on the life cycle of the anticyclones, we kept all other forcing parameters constant. The coastal upwelling is adjusted by altering the magnitude of the zonal wind stress with a constant. The curl of the wind stress is kept constant by applying the adjustment over the full model domain. A description of the model is provided in Section 4.2, and is followed by a comparison between the modeled flow and observations (Section 4.3). Section 4.4 and 4.5 contain the analysis of the westward intensification of the anticyclone and how this is related to the advection of upwelling filaments. The sensitivity of the mean flow and eddy variability to changes in upwelling strength are discussed in Section 4.6. The results are summarized and discussed in Section 4.7.

4.2   Model configuration and methods

4.2.1   Model configuration

The numerical simulations were performed with the hydrostatic configuration of the Massachusetts Institute of Technology (MIT) primitive equation model (Marshall et al., 1997). The computational domain extended from 99°W to 55°W and from 6°N to 33°N (Fig. 4.1a), and was set up with a horizontal resolution of 1/12°, which is well below the internal Rossby radius of deformation in this re-

gion (60-80 km, Chelton et al., 1998). The same topography as the Operational Mercator global ocean analysis (Mercator) of the E.U. Copernicus Marine Service Information was used, where the topography is based on ETOPO1 for the deep ocean and near the coast on GEBCO8 for the coast and slopes. In this topographic setup, the majority of the islands of the Lesser Antilles are represented (Fig. 4.1). The islands that are too small to be captured are modeled as shallow ridges. In the vertical, the model contained 50 levels in z-coordinates, increasing in depth from 1 m at the surface towards 459 m at the lower levels.

The time step was 240 s. All simulations had a total duration of 25 years, of which the first five years were considered as spin-up and were excluded from the analysis. The model output was saved as 5-day averaged fields. The simulations were initialized with time-averaged fields for sea-surface height, temperature, salinity and velocity. These fields were obtained from the years 2007-2017 of Mercator. The vertical diffusion of tracers was parameterized with the GGL90 mixed layer parameterization (Gaspar et al., 1990). The horizontal diffusion was parameterized with the Redi-scheme (diffusion coefficient of 125 m^2 s^{-1}, Redi, 1982). The sub-grid scale mixing was parameterized with Smagorinsky viscosities (Smagorinsky et al., 1993).

All simulations were forced with time-averaged surface and lateral boundary conditions. A sponge layer with a meridional width of 1.25° (15 grid cells) was applied at the lateral boundaries. There, the velocity fields were relaxed towards the time-averaged fields of Mercator (years 2007-2017) with a relaxation time that varied linearly from a month at the offshore side of the domain towards a day at the domain boundary. At these boundaries, temperature, salinity, and velocities in zonal and meridional directions were prescribed. At the surface, a fresh-water flux, temperature restoring and a wind stress were applied (Fig. 4.1b-d). The temperature was restored towards sea-surface temperature (SST) averaged over the years 2007-2017 of Mercator with a relaxation time scale of one month. The surface fresh-water flux was obtained from the diagnosed fresh-water flux of a 250-year simulation described in Le Bars et al. (2016). The Orinoco River, Magdalena River and Mississippi River are prescribed as stationary fresh water fluxes at the open boundaries with discharges based on Fekete et al. (2000).

The reference simulation (Ekman100) is forced by a time-averaged zonal wind forcing, computed from the wind fields of years 2007-2017 of ERA-Interim (Dee et al., 2011). Prescribing stationary values implied that the NBC Rings, which can trigger the formation of the anticyclones (Goni and Johns, 2003; Richardson, 2005), were not represented at the boundaries. However, Jouanno et al. (2009) and Lin et al. (2012) showed that a realistic eddy field in the Caribbean Sea can be obtained without the presence of NBC Rings. Moreover, in Section 3 we will show that a realistic eddy field is obtained with these boundary conditions. Therefore, we considered these boundary conditions sufficient for the purpose of this study.

To investigate the effect of wind-driven upwelling on the westward intensification of anticyclones, only this zonal wind forcing (τ_x) was altered between

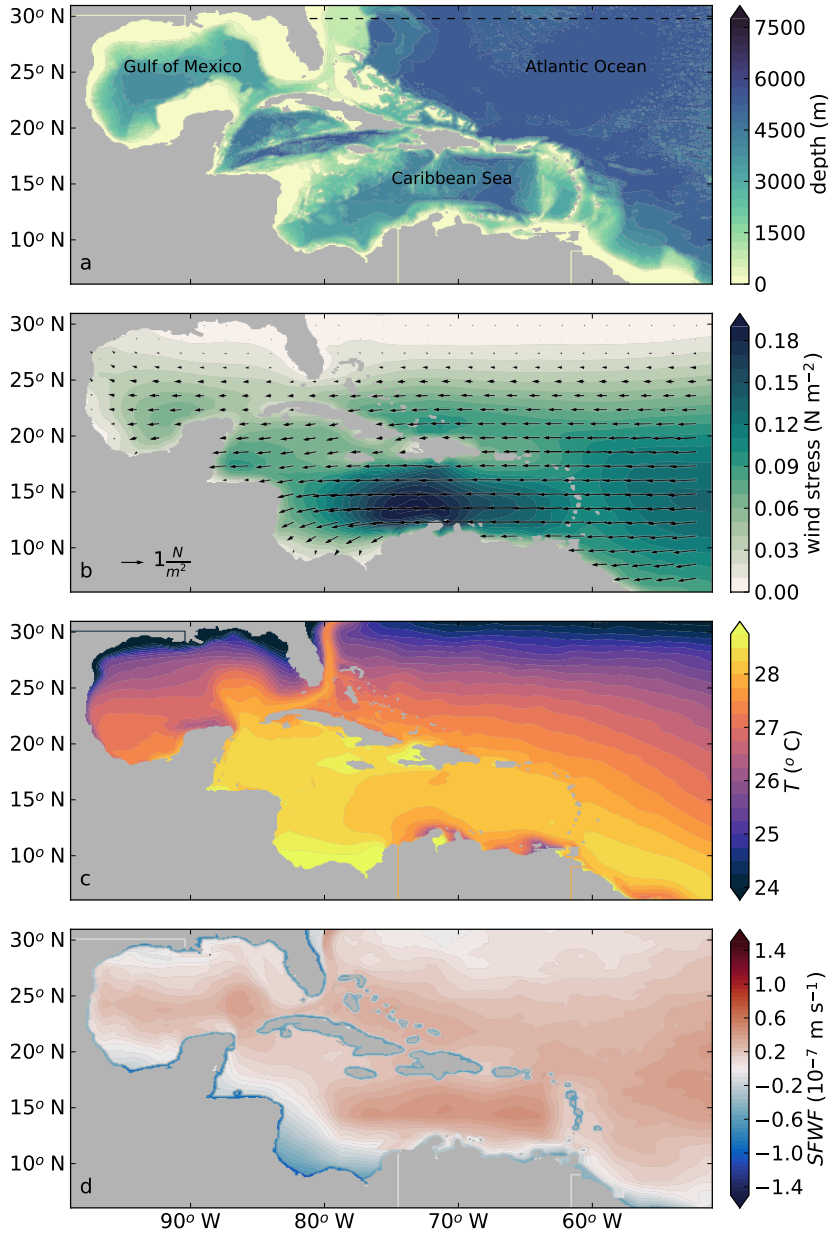Figure 4.1: Setup of the regional model in MITgcm. (a) Bathymetry in m. The sponge layer is indicated with the dashed line. (b) Magnitude of the wind stress. The direction in indicated with the vectors. Not all velocity vectors are shown for clarity purposes. (c) Surface temperature field in °C used for restoring. (d) Surface fresh water flux in m s^{-1}. Positive values correspond to a net surface buoyancy loss.

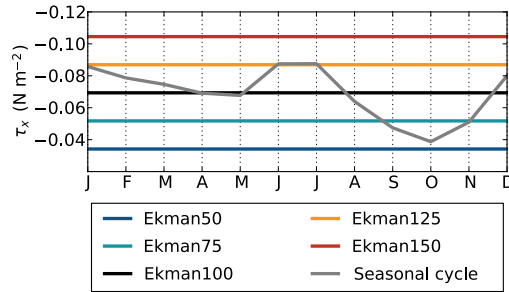Figure 4.2: Average zonal wind stress in N m^{-2} in the southern Caribbean Sea (10.5°N-12.5°N, 65°W-70°W) in the simulations. The seasonal variation of the zonal wind stress at this location, obtained from ERA-Interim (Dee et al., 2011), is shown for reference. Negative values correspond to easterly winds.

simulations. The magnitude of the zonal wind stress was reduced or increased in each simulation by the same constant over the entire domain (Fig. 4.2). With this approach, we ensured that we only change the upwelling strength and not the curl of the wind stress. The magnitude of the reduction or increase was determined based on the zonal wind stress in the upwelling region in Ekman100. In Ekman150, the zonal wind stress in the upwelling region was 50 % stronger than the wind stress in Ekman100, resulting in a theoretical increase of the northward Ekman transport of 50 %. The wind stress along the coast was weaker in the Ekman50, leading to a theoretical weaker upwelling (50 %) in this simulation compared to Ekman100. The same principle was applied in Ekman75 and Ekman125.

The adjustment of the zonal wind forcing resulted in changes in mesoscale variability over the full domain. Because the applied constant was optimized to alter the northward Ekman transport in the Cariaco and Guajira upwelling regions, it resulted in unrealistic magnitudes of the zonal wind stress (and thus of the northward Ekman transport) in some other regions. Therefore, we will only analyze the impact of the changes in wind forcing on the mesoscale variability close to the Cariaco and Guajira upwelling regions (Fig. 4.3c), and disregard other coastal upwelling regions.

The range of τ_x applied in the simulations covers the seasonal variations (Fig. 4.2). The magnitude of the stationary zonal wind stress in Ekman50 was similar to the observed zonal wind stress in fall, while the stronger stationary zonal wind stress in Ekman125 was comparable to the wind stress during winter and summer months. The zonal wind stress in Ekman150 was stronger than the seasonal cycle, but was similar to zonal wind stresses that are observed during years with anomalously high wind velocities (Whyte et al., 2008).

4.2.2 Methods

To analyze the behavior of the mesoscale eddies, we analyzed both the eddy kinetic energy (EKE) and the individual eddies. Following Jouanno et al. (2012), we calculated the EKE from 5-day averaged velocity fields that were high-pass filtered with a 125-day running mean. This 125-day period was long enough to capture the variability of the eddies, which have a characteristic period of 50-100 days (Jouanno et al., 2008), but was shorter than the interannual variability.

To gain insight into the westward intensification of Caribbean anticyclones, we used the py-eddy tracker to follow them (Mason et al., 2014). The py-eddy tracker used 5-day averaged sea-level anomaly fields to identify near-circular features. Anomalies were computed with respect to 20-year averaged fields. Negative anomalies were identified as cyclones, and positive anomalies as anticyclones. More detailed information about the numerics of the py-eddy tracker can be found in Mason et al. (2014). We set a minimum life time of 75 days. Taking into account the average westward propagation velocity of 0.13 m s^{-1} (Richardson, 2005), the anticyclones propagate approximately 840 km during this minimum life time.

At the center of the eddies provided by the eddy tracker, we extracted the amplitude (A_{eddy}), swirl velocity (u_{swirl}), radius (R_{eddy}) and properties from the model output to assess their characteristics. The amplitude was defined as sea-surface height difference between the eddy and the 20-year average sea-surface height at the center of the eddy. Since the py-eddy tracker identifies circular anomalies as eddies, we could define the swirl velocity as the average of the maximum northward and maximum southward velocity of the eddy. The location of both velocities was used to obtain a robust estimate of the eddy radius (R_{eddy}), which we defined as half the distance between these locations. To characterize the local properties (T, S, σ) of the background and the eddies, these variables were averaged over the upper 50 m. This depth corresponds to the average depth of the pycnocline in the Caribbean Sea. The latter ensures that these properties not only reflect variations in surface forcing. The background properties were defined as the 125-day averaged values of the upper 50 m at the location of the eddy obtained from the py-eddy tracker. The differences between the properties of the eddies and the background are computed as $\Delta = \text{eddy} - \text{background}$.

To gain insight in the geostrophic part of the westward intensification of the anticyclones in each simulation, we computed the strength of the horizontal density gradients ($|\nabla\sigma|$). These gradients were calculated over the upper 50 m of the water column for 5-day averaged density fields as follows:

$$|\nabla\sigma| = \sqrt{\left(\frac{\partial\sigma}{\partial x}\right)^2 + \left(\frac{\partial\sigma}{\partial y}\right)^2}, \qquad (4.1)$$

where σ corresponds to the density. The contribution of temperature ($|\nabla\sigma_T|$) and salinity ($|\nabla\sigma_S|$) to the horizontal density gradients was computed in a sim-

ilar manner, where the density differences were calculated assuming a linear equation of state as $\Delta\sigma_T = \rho_0\alpha(T_1 - T_0)$ and $\Delta\sigma_S = \rho_0\beta(S_1 - S_0)$, respectively. Here, α, β and ρ_0 are constants; $\alpha = -3.1 \times 10^{-4}\ °C^{-1}$, $\beta = 7.2 \times 10^{-4}\ psu^{-1}$, and $\rho_0 = 999.8\ kg\ m^{-3}$.

Since the focus of this study is to analyze the westward intensification of the anticyclones, we not only calculate the EKE and strength of the horizontal density gradients over the full domain, but we also calculate their contribution associated with the anticyclones only. We estimate the latter by considering the EKE and density gradients around the core of an eddy at each 5-day averaged field over a spatial extend of $1.5 \times R_{eddy}$. This procedure allows us to study only the westward intensification of the anticyclones.

4.3   Performance of the regional model

4.3.1   Mean flow

The modeled surface current in Ekman100 enters the Caribbean Sea through the southern passages of the Lesser Antilles (Fig. 4.3a), which is similar to what is seen in observations (Johns et al., 2002). The flow through the Lesser Antilles is highly variable and depends on variations of the flow upstream and on the wind forcing (Johns et al., 2002). Based on scarce data, Johns et al. (2002) estimated the transport at 66°W at 18.4 ± 4.7 Sv. In our simulation, the transport is more stable due to the stationary forcing and is on average 13.6 Sv at 66°W, which is close to the lower range of the estimate of Johns et al. (2002). Further westward at 80°W, the modeled flow accelerates over shallow topography at 17°N, where it continues northwestward towards Yucatan Channel into the Gulf of Mexico.

In the southwest of the Caribbean Sea, the modeled surface currents displays a cyclonic recirculation (Fig. 4.3a). This recirculation is known as the Panama-Colombia Gyre (PCG) and is wind-driven (Centurioni and Niiler, 2003; Andrade, 2003). Part of the PCG continues as an eastward subsurface countercurrent, which results from the Sverdrup circulation in the North Atlantic tropical cell (Andrade, 2003). The countercurrent flows below the upwelling region, and its depth is related to the wind strength (Andrade, 2003; Andrade and Barton, 2005). The model is able to reproduce the subsurface countercurrent at a depth of approximately 100 m, which is slightly higher in the water column than at the 200 m observed by Andrade (2003) and the 150 m observed by Hernández–Guerra and Joyce (2000); the modeled strength (0.11 m s^{-1}) is comparable to their observations.

Ekman100 displays a strong meridional density gradient in the mixed layer that varies between $\sigma = 25.1$ kg m^{-3} in the south (11°N) and $\sigma = 22.7$ kg m^{-3} in the north (18°N, Fig. 4.3b). The strongest meridional gradients are close to the surface and co-located with the Caribbean Current. The location of the dense waters coincide with the two major upwelling regions: Cariaco and Guajira. The
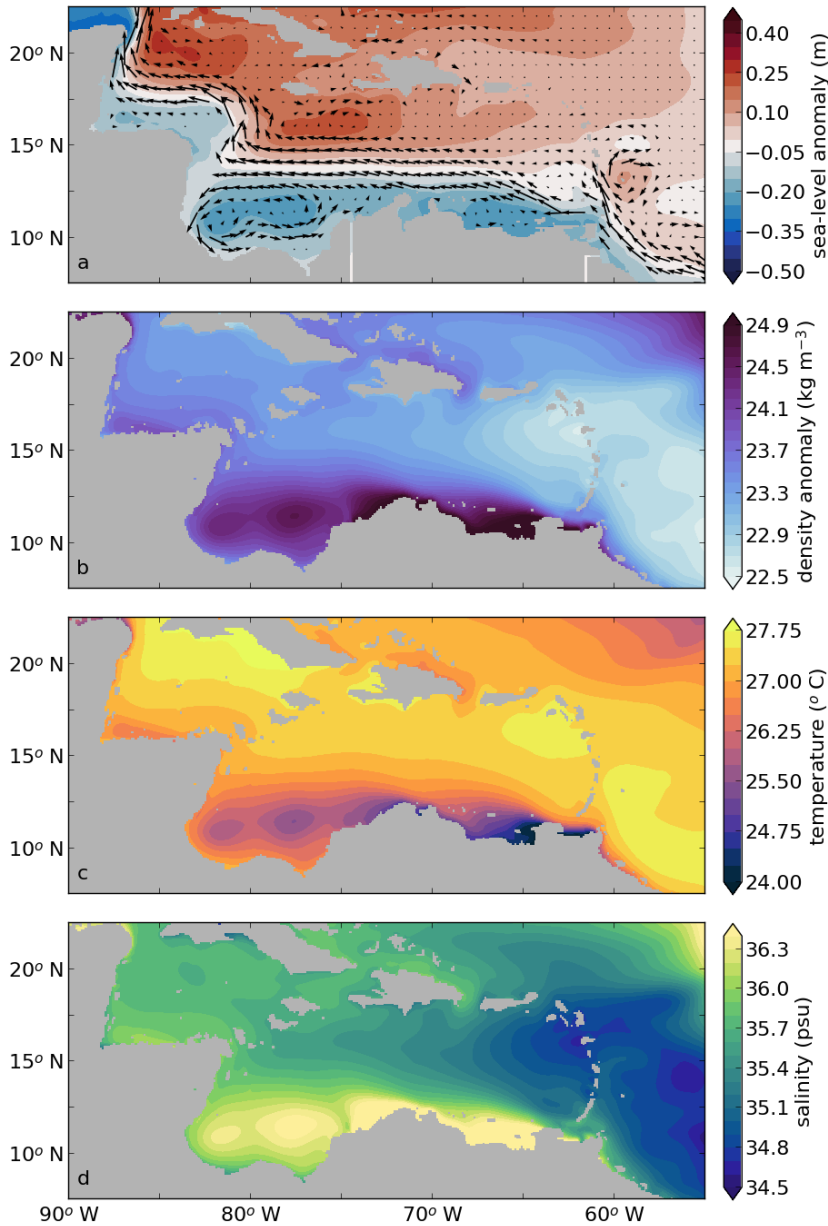
Figure 4.3: 20-year near-surface average properties of the Caribbean Sea in Ekman100. (a) Mean sea-level anomaly (SLA) in m with velocity vectors. Surface current vectors are only shown every eighth grid cells for clarity purposes. (b) Density ($\sigma = \rho - 1000$) in kg m^{-3}, (c) Temperature in °C and (d) Salinity in psu. Properties in panel b-c-d are averages over the upper 50 m.

upwelled waters are colder and more saline than the surrounding surface waters (Fig. 4.3c,d).

The Cariaco upwelling region in the southeast of the Caribbean Sea is located at 63°W-65°W, 10°N-12.5°N (Rueda–Roa and Muller–Karger, 2013). The modeled minimum (24.9 °C) and maximum temperatures (27.4 °C) in Cariaco Basin are less extreme than the observed temperatures (minimum: 20.3 °C, maximum: 30.1 °C, Rueda–Roa and Muller–Karger, 2013). Although the model is not able to capture this seasonal variability, the modeled average SST (25.4 °C) is similar to observations (25.2 °C, Rueda–Roa and Muller–Karger, 2013). Note that these modeled temperatures are lower than the restoring temperature (Fig. 4.1c), which indicates that the model is able to reproduce coastal upwelling. The Guajira upwelling region is located west of the Cariaco upwelling region, between 69°W and 74°W (Andrade and Barton, 2005; Rueda–Roa and Muller–Karger, 2013). Here, the observed average SST is slightly higher (25.5 °C) than in the Cariaco upwelling region (Rueda–Roa and Muller–Karger, 2013). Similar to these observations, the model displays a temperature difference between the two upwelling regions (26.1 °C in Guajira, Fig. 4.3c). Furthermore, the modeled temperatures are in line with Andrade and Barton (2005), who found surface temperatures varying between 25.6°C and 28°C in the Guajira upwelling region.

In addition to the meridional density gradient, the model also displays a clear zonal density gradient in the Caribbean Sea (Fig. 4.3b): the Caribbean Current is relatively light as it enters the Caribbean Sea. This zonal density gradient is mainly due to a zonal salinity gradient, and to a lesser extent to a zonal temperature gradient (Fig. 4.3c-d). As mentioned in the introduction, the zonal temperature and salinity gradients are related to the offshore advection of cold and saline upwelling filaments (Jouanno and Sheinbaum, 2013). The magnitude of the zonal density gradient is largest in the surface mixed layer and decreases rapidly below. According to observations, the zonal salinity gradient is also related to the dispersal of the Amazon and Orinoco River plumes into the basin (e.g., Hu et al., 2004; Chérubin and Richardson, 2007). In the model, the Amazon River plume enters the domain at the southern boundary, while the fresh water of the Orinoco River enters the domain at 61°W, 9°N (Fig. 4.1d). The river plume is advected with the mean flow and becomes more saline through mixing with the saline (upwelled) surface waters in the basin, and through evaporation. Overall, the zonal and meridional gradients of salinity and temperature are similar to observations, indicating that the model is able to capture the upwelling, the advection of the river plume water and the relevant mesoscale processes.

4.3.2   Eddy kinetic energy

In line with observations (Andrade and Barton, 2000; Richardson, 2005; Carton and Chao, 1999), we find that the flow in the Caribbean Sea is highly variable (Fig. 4.4). In the eastern part of the basin, the modeled surface EKE is relatively low (100-300 cm^2 s^{-2}, Fig 4.4a) and similar to observations of Andrade and Bar-
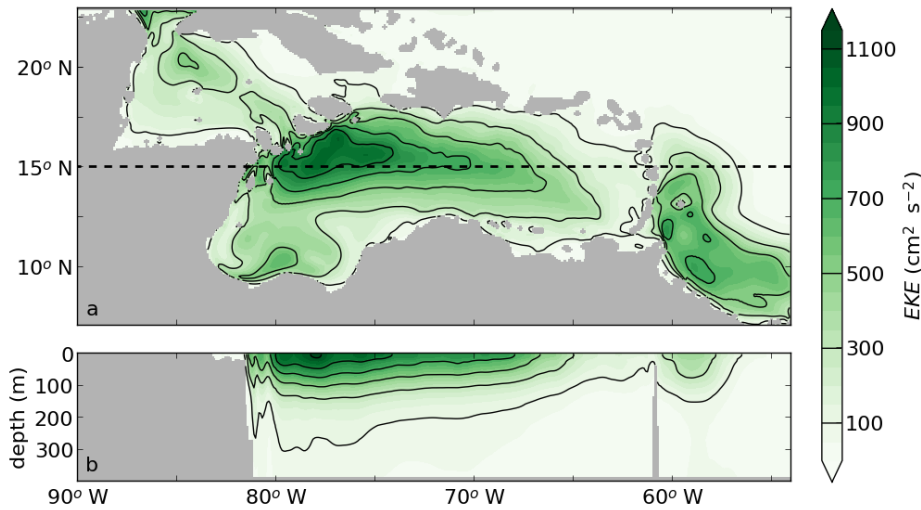
Figure 4.4: Eddy kinetic energy (EKE) in cm^2 s^{-2} of Ekman100 obtained from 5-day averaged velocity fields that are high-passed filtered with a 125-day mean. (a) 20-year average of the EKE in the upper 50 m of the water column and (b) cross section of EKE at 15°N over the upper 400 m.

ton (2000). The EKE increases westward towards a maximum >900 cm^2 s^{-2} at 78°W. The modeled magnitude of EKE is higher than found in satellite altimetry (>600 cm^2 s^{-2}, Andrade and Barton, 2000; Jouanno et al., 2012), but it is more similar to estimates obtained from surface drifters (>900 cm^2 s^{-2}, Richardson, 2005). This is in line with other modeling studies (Jouanno et al., 2008, 2012), and this discrepancy is mainly attributed to the coarse resolution (0.25°) of the gridded altimetry data products (Jouanno et al., 2008). The modeled spatial variability of EKE matches analyses of to satellite altimetry well (Jouanno et al., 2012; Ducet et al., 2000). Corresponding to observations (Silander, 2005, , Chapter 2 of this thesis), we find that the eddy kinetic energy is surface intensified (Fig. 4.4b). In line with the modeling results of Jouanno et al. (2008), the magnitude of EKE at depth also increases towards the west (Fig. 4.4b).

The variability in the Caribbean Sea manifests itself in the presence of mesoscale eddies (Fig. 4.5). In line with observations (Centurioni and Niiler, 2003), the mesoscale eddies are predominantly anticyclonic (Fig. 4.5a). As expected, the surface densities of these anticyclones are lighter than those of the surrounding surface waters (Fig. 4.5b). The density differences are due to both temperature and salinity (Fig. 4.5c,d). Figure 4.5c also displays the northward advection of a cold filament. Similar filaments have been observed, and it is known that these can be advected several hundreds of kilometers from the upwelling region (Andrade and Barton, 2005). This advection results in the offshore cooling of surface waters (Jouanno and Sheinbaum, 2013).
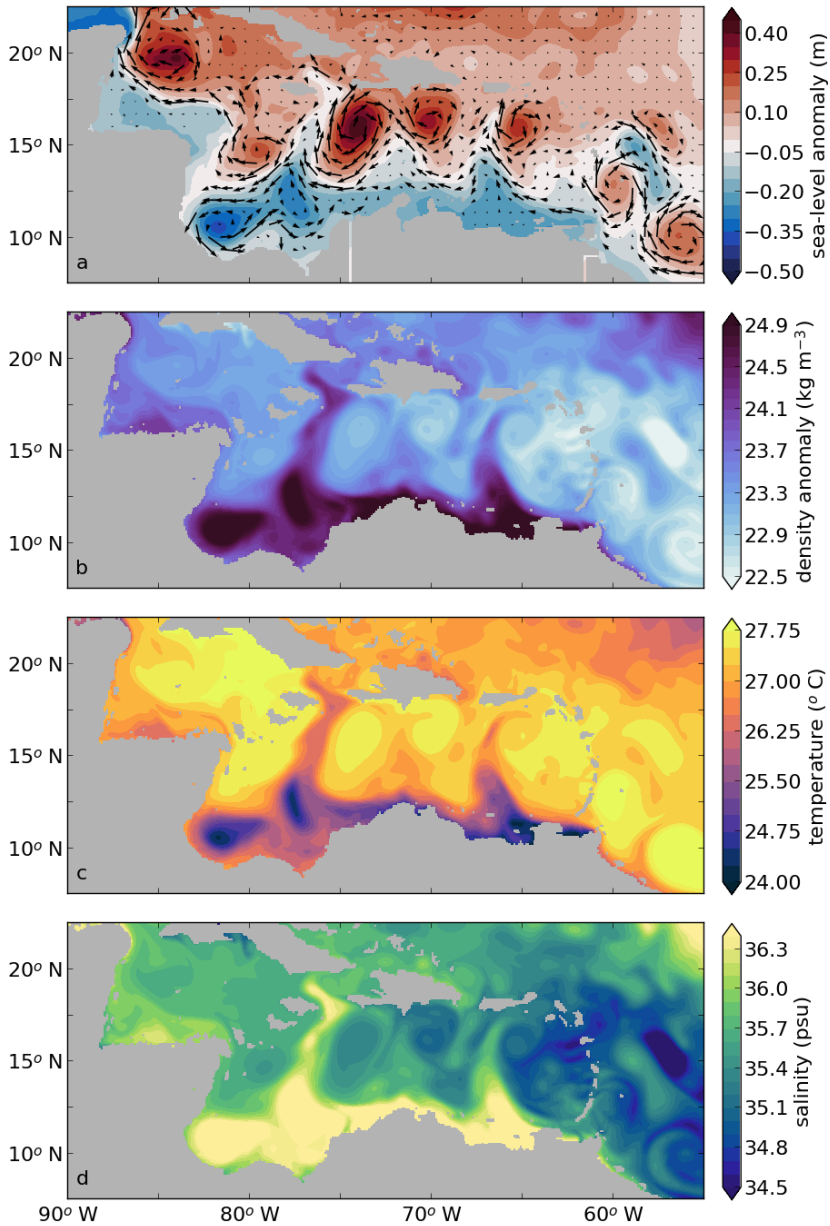
Figure 4.5: Near-surface properties of the Caribbean Sea, averaged over a 5-day period during the final year of the simulation Ekman100. (a) Mean sea-level anomaly (SLA, in m) with velocity vectors. Surface current vectors are only shown every eighth grid cells for clarity purposes. (b) Density ($\sigma = \rho - 1000$) in kg m^{-3}, (c) Temperature in °C and (d) salinity in psu. Properties in panels are averages over the upper 50 m.

4.3.3   Eddy characteristics

From the py-eddy tracker (Mason et al., 2014), we found that on average, 8.55 anticyclones and 5.70 cyclones are formed in the reference simulation Ekman100 east of 75°W, between 12.5°N-17.5°N every year. These numbers are in line with the 8-12 anticyclones per year estimated from surface drifter data (Richardson, 2005). To our knowledge, there are no previous estimates for the formation rate of cyclones in the Caribbean Sea.

The anticyclones have an average amplitude of $A_{\mathrm{eddy}} = 0.17$ m and swirl velocities of $u_{\mathrm{swirl}} = 0.60$ m s^{-1} between 65°W-75°W and 12.5°N-17.5°N (Table 4.1). This amplitude and swirl velocity are similar to those found in hydrographic surveys (Silander, 2005; Rudzin et al., 2017, , Chapter 2 of this thesis), and similar to velocities obtained from surface drifters ($u_{\mathrm{swirl}} = 0.5$ m s^{-1}, Richardson, 2005). In general, the core of the anticyclones is warmer ($\Delta T = +0.15$ °C) and fresher ($\Delta S = -0.18$ psu) than the surrounding surface waters (Fig. 4.5c-d).

In the central Caribbean Sea (65°W-75°W and 12.5°N-17.5°N), the cyclones are less energetic than the anticyclones, and have an average amplitude of $A_{\mathrm{eddy}} = -0.16$ m and swirl velocity of $u_{\mathrm{swirl}} = 0.50$ m s^{-1}. Observations indicate that cyclones are generated near topographic features in the Caribbean Sea (Richardson, 2005), and can contain upwelling waters (Andrade and Barton, 2005). The modeled properties of the cyclones are in agreement with these observations. It appears that the mesoscale eddies are close to geostrophic balance, with an average Rossby number of 0.15±0.01 (anticyclones) and 0.14 ± 0.03 (cyclones), where the Rossby number is calculated as Ro $= u_{\mathrm{swirl}}/(R_{\mathrm{eddy}} \times f)$, in which u_{swirl} is the swirl velocity of the eddy, R_{eddy} is the radius and f the Coriolis parameter.

There is a strong and significant correlation between the amplitude of the tracked mesoscale eddies and the surface EKE. This suggests that the westward increase of EKE is related to the strength of the eddies. We find that 57 of the anticyclones that are formed in the Caribbean Sea during the 20 years of the simulation propagate from a region with weak EKE (<65°W) towards a region with high EKE (>75°W). The paths of these anticyclones are indicated with the black lines in Figure 4.6a. The other 96 anticyclones that are formed in the Caribbean Sea during the 20 years of the simulation are either generated west of 65°W or do not pass 75°W (grey lines in Fig. 4.6a). In contrast to the anticyclones, cyclones display relatively short tracks: Only one cyclone passes both 65°W and 75°W (black line in Fig. 4.6b). This is similar to observations of Richardson (2005) who showed that the cyclones follow a different path than anticyclones.

To assess the contribution of the anticyclones with the long tracks to the total EKE variability, we calculated their EKE from the zonal and meridional velocity fields by taking into account the EKE within a region of $1.5 \times R_{\mathrm{eddy}}$ around each eddy as described in Section 4.2. The spatial distribution of EKE due to these long-lived eddies (Fig. 4.6c) is similar to the spatial distribution of the total EKE (Fig. 4.4a). Notably, the magnitude of the EKE of these selected eddies is approximately 55 % of the total EKE (Fig. 4.4), while it is computed from only 37

Table 4.1: Number of eddies per year and average Rossby number with standard deviations in each simulation between 12.5°N-17.5°N, 65°W-75°W. Amounts are obtained with the py-eddy tracker. The formation rate is computed as the number of eddies that are formed each year east of 75°W. The long tracks represents the percentage of the eddies that were formed east of 65°W and could be tracked west of 75°W. The Rossby number is calculated as $Ro = u_{swirl}/(R_{eddy} \times f)$, where u_{swirl} is the swirl velocity of the eddy, R_{eddy} is the radius and f the Coriolis parameter. Density, temperature and salinity is taken at the core of the anticyclones. One standard deviation is added to indicate the interannual variability.

	Ekman50	Ekman75	Ekman100	Ekman125	Ekman150
Anticyclones					
Formation rate (year⁻¹)	10.85±2.22	9.25±1.76	8.55±1.72	8.65±1.19	9.10± 1.89
Long tracks (<65°W, >75°W)	36 % (71/199)	34 % (57/167)	37 % (57/153)	43 % (70/160)	36 % (59/165)
Rossby number	0.14±0.01	0.14±0.01	0.15±0.01	0.15±0.02	0.15±0.01
Density anomaly (kg m⁻³)	21.94±0.11	22.20±0.12	22.68±0.09	22.90±0.05	23.05±0.06
Temperature (°C)	27.93±0.02	27.79±0.03	27.64±0.05	27.52±0.05	27.39±0.06
Salinity (psu)	34.09±0.14	34.38±0.14	34.96±0.11	35.19±0.05	35.34±0.06
Cyclones					
Formation rate (year⁻¹)	6.15 ± 1.49	5.30 ± 1.62	5.70 ± 1.71	4.90 ± 1.67	4.15 ± 2.06
Long tracks (<65°W, >75°W)	0 % (0/105)	2 % (2/89)	1 % (1/95)	0 % (0/79)	0 % (0/69)
Rossby number	0.11 ± 0.02	0.12 ± 0.02	0.14 ± 0.03	0.15 ± 0.04	0.12 ± 0.03
Density anomaly (kg m⁻³)	23.17±0.15	23.12±0.28	23.44±0.14	23.51±0.25	23.49±0.27
Temperature (°C)	27.49±0.14	27.40±0.24	27.09±0.18	26.94±0.36	26.95±0.40
Salinity (psu)	35.54±0.16	35.44±0.28	35.73±0.11	35.76±0.18	35.74±0.20
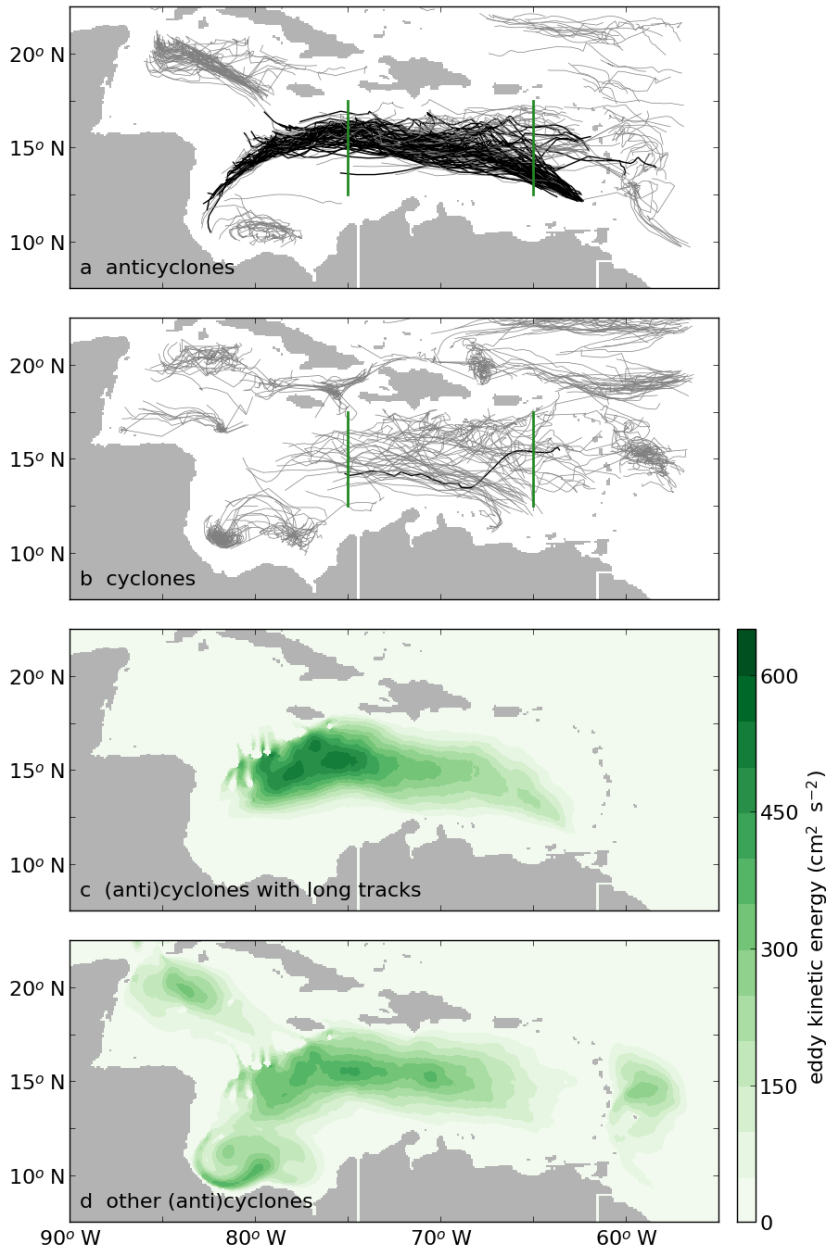
Figure 4.6: Paths of (a) anticyclones, and (b) cyclones that are identified by the py-eddy tracker (Mason et al., 2014) in Ekman100 during 20 years of model simulation. The black lines indicate tracks that pass both cross-sections at 65°W and 75°W (green lines). All other tracks are indicated in grey. (c) Estimate of EKE in cm^2 s^{-2} of the long tracks (black lines in panels a and b). (d) Estimate of EKE of all other tracks (grey lines in panels a and b).

% of the eddies (57/153 anticyclones in 20 years). This shows that the modeled westward increase of EKE is dominated by the westward increase of EKE of a small number of long-lived eddies, which is also confirmed by the weaker eddy kinetic energy of the eddies with shorter tracks (Fig. 4.6d). Because our results show that the eddies with long tracks, dominate the mesoscale variability in the Caribbean Sea, we will focus on these 57 energetic anticyclones in the remainder of this study.

4.4   Westward intensification

Figure 4.6 showed that the EKE of the anticyclones with long tracks increases towards the west. We hypothesized that the intensification of the anticyclones was governed by a westward strengthening of the horizontal density gradients. In this section, we evaluate the evolution of the horizontal density gradients of the anticyclones and the validity of the thermal wind balance.

Figure 4.7 shows the different components of the thermal wind balance ($\frac{\partial V}{\partial z}$, $\frac{g}{\rho_0 f}\nabla\sigma$) computed from high-pass filtered density and velocity fields. As in Fig. 4.6c, only the anticyclones with long tracks are taken into account. The vertical shear of the anticyclones (Fig. 4.7a) increases from the eastern part of the basin towards the west. The horizontal density gradients of the anticyclones (Fig. 4.7b) have a similar magnitude and spatial distribution as the vertical shear (Fig. 4.7a). This indicates that, on average, the anticyclones were close to geostrophy. For this case, the horizontal density gradients due to salinity (Fig. 4.7d) are slightly stronger than the horizontal density gradients due to temperature (Fig. 4.7c).

To gain insight into the westward intensification of the anticyclones, we computed the zonal variation of the EKE, vertical shear, density gradients and properties of the anticyclones (Fig. 4.8). Overall, the meridional maximum of EKE that is contained in the anticyclones increases from approximately 200 cm^2 s^{-2} at 65°W towards 530 cm^2 s^{-2} at 75°W (Fig. 4.8a). These values are similar to those observed in Andrade and Barton (2000).

Similar to the EKE, the horizontal density gradients and vertical shear of the anticyclones increases towards the west (Fig. 4.8b). In line with the low Rossby number of the anticyclones, there is a small difference in magnitude between the vertical shear and density gradients indicating the presence of small ageostrophic velocities. As in Fig. 4.7c and Fig. 4.7d, the horizontal density gradients due to temperature and salinity gradients both increase towards the west. This increase in both temperature and salinity can be explained by the properties of the upwelled waters, which are both colder and more saline than the background environment. Note that the density gradients induced by salinity are stronger than those induced by temperature differences (dashed and dotted lines in Fig. 4.7c-d, respectively). Although the anticyclones become slightly denser on their path westward through mixing with the surrounding waters (dots in Fig. 4.8c), this density increase is much weaker than the westward density increase of the
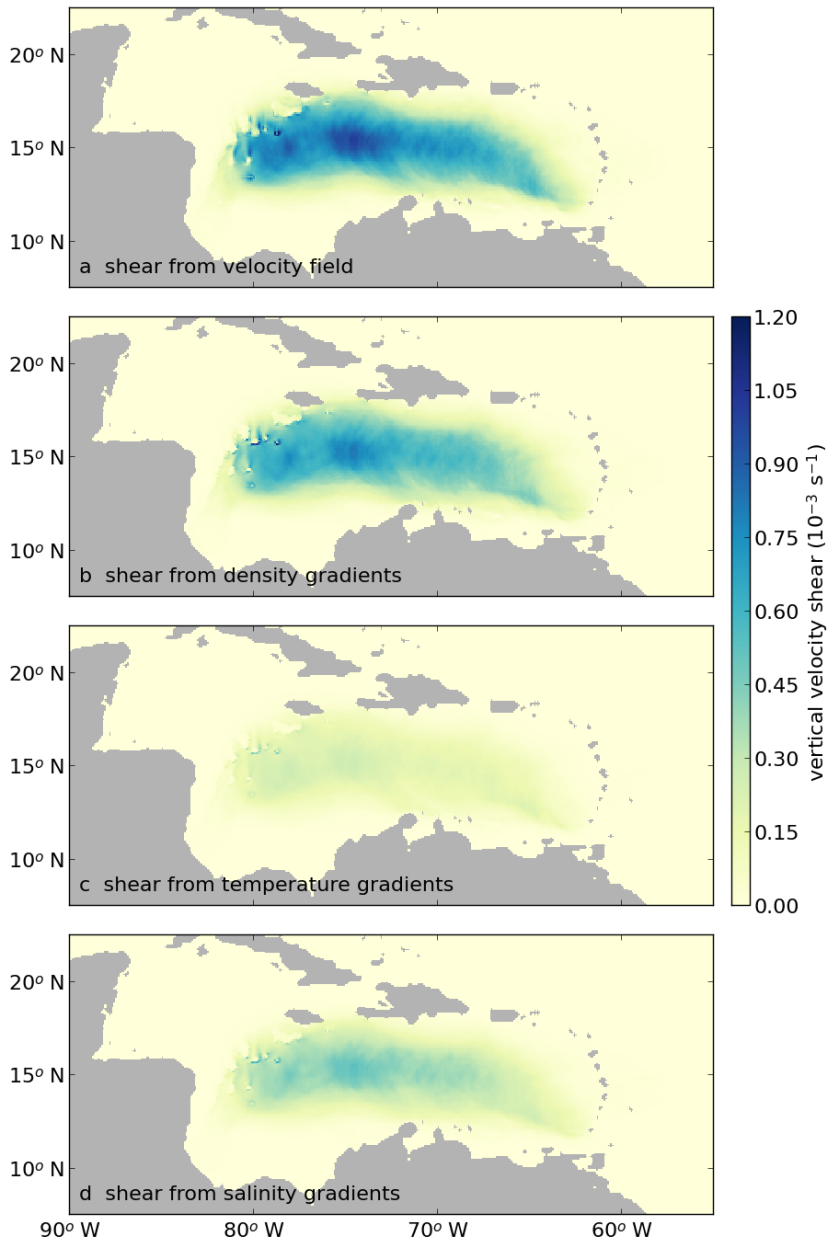
Figure 4.7: (a) Vertical shear of the anticyclones, averaged over the upper 50 m. (b) Horizontal density gradients of the anticyclones, scaled with $g/(\rho_0 f)$ according to the thermal wind equation. Horizontal density gradients due to (c) temperature gradients and (d) salinity gradients of the anticyclones.
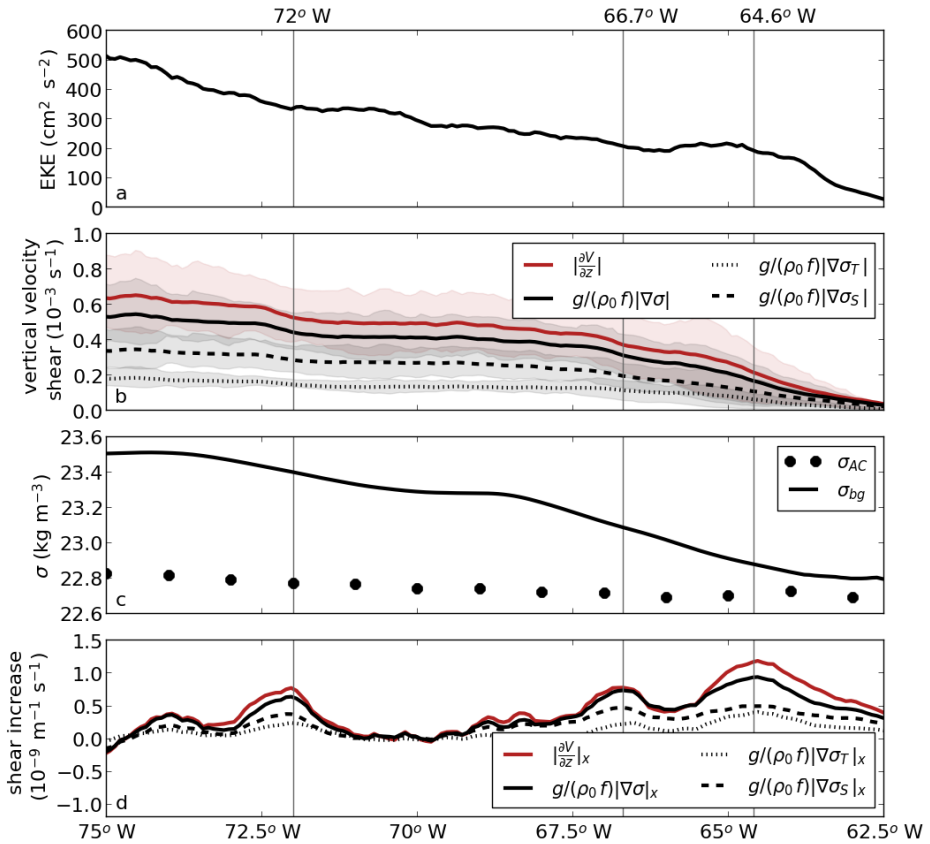
Figure 4.8: (a) Zonal variation of the (a) meridional maximum eddy kinetic energy, and (b) vertical velocity shear and shear computed from horizontal density gradients between 12.5°N and 17.5°N of the anticyclones with long tracks. The shaded regions indicate the 25th and 75th percentile. All properties are averaged over the upper 50 m of the water column. (c) Density anomaly of the background (σ_{bg}) and anticyclones (σ_{AC}), averaged over the upper 50 m. The density anomaly of the anticyclones is averaged per degree longitude. (d) The variations of vertical shear and horizontal density gradients with longitude in westward direction of the anticyclones with long tracks.

surrounding waters (solid line in Fig. 4.8c), suggesting that indeed changes in properties of the background environment are the dominant factor resulting in the westward increase of the horizontal density gradients.

Because the westward increase of the horizontal density gradients and vertical shear of the anticyclones (Fig. 4.8b) is not constant, we computed the variations with longitude in westward direction of these quantities (Fig. 4.8d). From this, three regions can be identified as locations of more rapid intensification (64.6°W, 66.7°W, 72°W). Up to 64.6°W, the westward increase of horizontal density gradients is not fully balanced by the vertical shear, indicating that the westward intensification of the anticyclones is not in geostrophic balance at this stage. The westward intensification becomes more geostrophic towards the second peak of rapid intensification at 66.7°W (Fig. 4.8d). This peak is located near the Cariaco upwelling region. As the anticyclones move closer towards the Guajira upwelling region, they intensify more rapidly again (at 72°W in Fig. 4.8d). Although the third rapid increase is located eastward of the Beata Ridge at 73°W, it is possible that this topographic feature has some impact on the westward intensification, as was previously proposed by Andrade and Barton (2000). However, our model result suggest that all three regions of more rapid increase are located close to preferred locations of the shedding of upwelling filaments (Fig. 4.5c).

4.5   Offshore advection of dense upwelling filaments

Figure 4.8 showed that the westward increase of EKE coincides with a westward increase of the vertical shear and density gradients of the anticyclones. This westward density increase of the surrounding surface waters is possibly governed by the advection of cold upwelling filaments offshore (Jouanno and Sheinbaum, 2013). According to Jouanno and Sheinbaum (2013), these filaments, characterized by strong temperature gradients, are advected by the anticyclones. Since we found regions with a more rapid increase in horizontal density gradients of the anticyclones (Fig. 4.8d), we evaluate in this section whether that increase is related to the advection of cold upwelling filaments.

We defined a measure for the strength of the filaments to study if there is a relation between the filaments and the eddy kinetic energy of the anticyclones. Because of their sense of rotation, the filaments are expected on the western side of the anticyclones, and hence we define this measure as a combination of the asymmetry of the density gradients around the anticyclone and the density gradient (induced by temperature) on the western side of the anticyclone. The asymmetry is defined as the ratio between the strength of the horizontal density gradient on the western and eastern side of the anticyclone ($\frac{|\nabla\sigma_{\text{west}}|}{|\nabla\sigma_{\text{east}}|}$). An asymmetry larger than one corresponds to a situation where the density gradients on the western side of the anticyclone are stronger than on the eastern side, which suggests that an anticyclone advects a filament. Furthermore, we expect that the
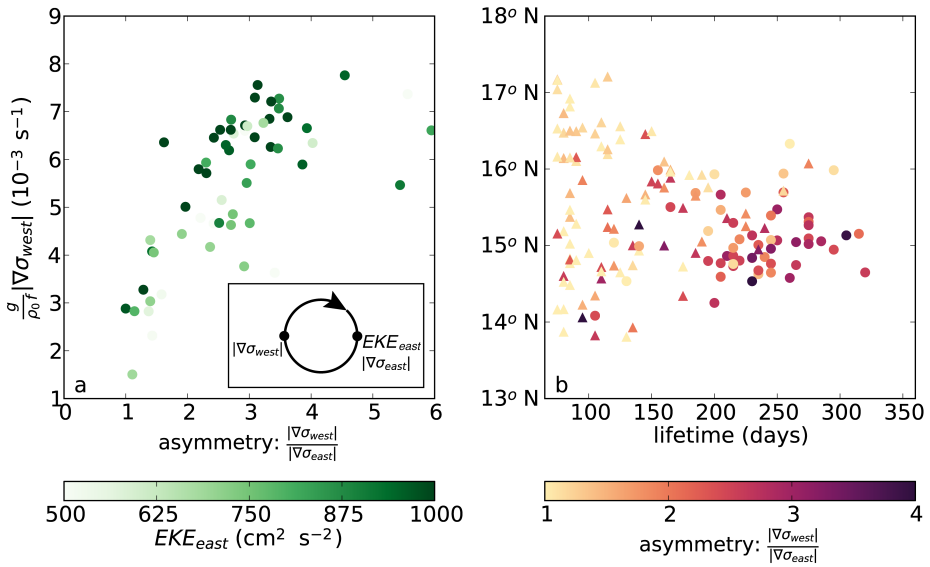
Figure 4.9: (a) Asymmetry of the anticyclones ($\frac{|\nabla\sigma_{\text{west}}|}{|\nabla\sigma_{\text{east}}|}$) versus the strength of the horizontal temperature gradients on the western side of the anticyclones ($|\nabla\sigma_{T,\text{west}}|$) in Ekman100. The asymmetry is defined as the ratio between the strength of the horizontal density gradient on the western and eastern side of the anticyclone between 65°W and 75°W. Colors indicate the EKE of the eastern side of each eddy. Each dot represents one anticyclone, the inlay contains a schematic of the locations where the properties are calculated. (b) The total life time versus latitude of each anticyclone. Anticyclones with long tracks (black lines in Fig. 4.6a) are indicated with dots, anticyclones with short tracks (grey lines in Fig. 4.6a) are indicated with triangles. Colors denote the asymmetry of the anticyclones. All properties are calculated as average values between 65°W and 75°W from individual anticyclones in all simulations.

anticyclones that advect filaments have strong horizontal temperature gradients on the western side. These two properties are shown in Figure 4.9a. It displays a positive correlation between the asymmetry and the strength of the temperature gradients, so that the most asymmetric anticyclones have the strongest temperature gradients on their western side, corresponding to our hypothesis that the anticyclones with strong temperature gradients advect cold upwelling filaments.

The relation between the eddy kinetic energy and the advection of filaments is also shown in Figure 4.9a. The average eddy kinetic energy is computed on the eastern side of the anticyclone to exclude the kinetic energy associated with the filament. The EKE of the anticyclone is positively correlated to the strength of the western temperature gradient of the anticyclone, which denotes that the anticyclones with strong filaments are more energetic than the anticyclones with weaker filaments. This means that the westward intensification of individual anticyclones can be affected by the advection of cold filaments.

To understand this positive correlation between the advection of filaments

and the strength of the anticyclones, we compared the anticyclones with long tracks to the other anticyclones that are present in the Caribbean Sea between 65°W and 75°W (black and grey lines in Fig. 4.6, respectively). This comparison between the asymmetry of the anticyclones, their life time and their meridional location reveals two interesting aspects (Fig. 4.9b). First, the anticyclones with long tracks (dots in Fig. 4.9b) are located in the southern part of the basin (<16°N). Second, the anticyclones with long tracks are in general more asymmetric than the other anticyclones (triangles in Fig. 4.9b).

The combination of these two aspects suggests a relation between the advection of filaments and the lifetime of Caribbean anticyclones: Anticyclones that propagate close to the upwelling region are more likely to advect a cold filament that increases their western horizontal temperature gradients. Such offshore advection of dense filaments increases the horizontal density gradients leading to the westward intensification of the anticyclones. Consequently, these anticyclones become more energetic and their lifetime increases. In contrast to the anticyclones with long tracks, the anticyclones with short tracks (triangles in Fig. 4.9b) are in general more symmetric and located farther north, and thus apparently do not advect cold filaments. This suggests that anticyclones that do not advect cold filaments dissipate, deform or merge rather than intensify. This is in line with the earlier result that the anticyclones with long tracks are more energetic than the anticyclones with short tracks (Fig. 4.6c,d).

4.6   Impacts of varying upwelling

In the previous section, we found that the westward intensification of Caribbean anticyclones is characterized by an increase of horizontal density gradients of the anticyclones, due to the advection of cold upwelling filaments by the anticyclones themselves. We expect that changes in upwelling strength result in changes in the properties of the filaments, which would affect the westward intensification of these anticyclones. To study the impacts of upwelling on this westward intensification of the anticyclones, we performed sensitivity simulations in which we altered the upwelling strength (Section 4.2). This resulted in differences in both the mean flow and mesoscale variability.

4.6.1   Changes in upwelling

The zonal wind stress in Ekman50 and Ekman75 was reduced compared to Ekman100, such that the wind stress in the upwelling region was 50 % and 25 % less than Ekman100, respectively. The decrease in zonal wind stress in Ekman50 and Ekman75 results in weaker upwelling and consequently warmer SST in the Cariaco Basin (Fig. 4.10a,b). The highest coastal temperatures are present in Ekman50. Sea-surface salinity decreased in both Ekman75 and Ekman50 compared to Ekman100 (Fig. 4.10a-c). This freshening is related to the presence

of a subsurface salinity maximum in the Caribbean Sea due to the presence of a water mass, referred to as Subtropical Underwater. This water mass is located at approximately 100 m depth and leads to more saline upwelled waters compared to the fresher surface waters (Chapter 2 of this thesis). Weaker upwelling thus results in warmer and fresher surface waters (Fig. 4.10a,b), and stronger upwelling results in colder and more saline surface waters (Fig. 4.10d,e).

Besides differences in the mean properties (σ, T, S), the width of the upwelling region also changes in the simulations: In Ekman125 and Ekman150, the upwelling is confined to a narrower region than in Ekman75 and Ekman50. Moreover, we find that the core of the subsurface countercurrent is displaced upwards in Ekman50 and Ekman75 compared to Ekman100 (red contour in Fig. 4.10). This upward change in line with the observations where the core was also displaced upwards in weaker wind conditions (Andrade, 2003; Andrade and Barton, 2005). The increased northward Ekman transport in Ekman125 and Ekman150 leads to colder and more saline surface waters. In these simulations, the core of the subsurface countercurrent is positioned lower in the water column (red contour in Fig. 4.10). The changing position of the subsurface countercurrent and the changes in sea-surface properties in the upwelling regions indicate that the model is able to reproduce realistic upwelling properties as was also shown in Section 4.3.

4.6.2   Changes in EKE

The upwelling strength impacts the offshore EKE (Fig. 4.11). In the interior of the Caribbean Sea, the surface EKE and subsurface EKE decreases (increases) for weaker (stronger) zonal wind strength. For example, the magnitude of the mean EKE in the interior of the Caribbean Sea decreases by 27 % in Ekman50 compared to Ekman100 (Fig. 4.11a). In Ekman75, a slightly weaker decrease of 15 % is present (Fig. 4.11b). In Ekman125 and Ekman150, the surface EKE increases with 13 % and 28 %, respectively (Fig. 4.11c,d). Overall, the EKE variations indicate a positive correlation between the coastal wind stress and the strength of the mesoscale eddies. A similar correlation is found in the subsurface EKE. This is in line with the finding that the upwelling was shallower in the simulations with weaker upwelling and deeper in simulations with stronger upwelling.

To gain insight into the sensitivity of the westward increase of EKE to variations in upwelling, the maximum of the total EKE between 12.5°N and 17.5°N was computed as a function of longitude (Fig. 4.12a). The largest changes in EKE are seen in the western part of the basin. In Ekman100, the EKE increased by 123 % from 65°W to 75°W, while the weaker upwelling in Ekman50 and Ekman75 resulted in a smaller westward increase of the EKE by 62 % and 97 %, respectively. Ekman125 and Ekman150 have a stronger westward increase in EKE compared to Ekman100. Overall, there is a clear positive correlation between the upwelling strength and the westward increase in EKE.
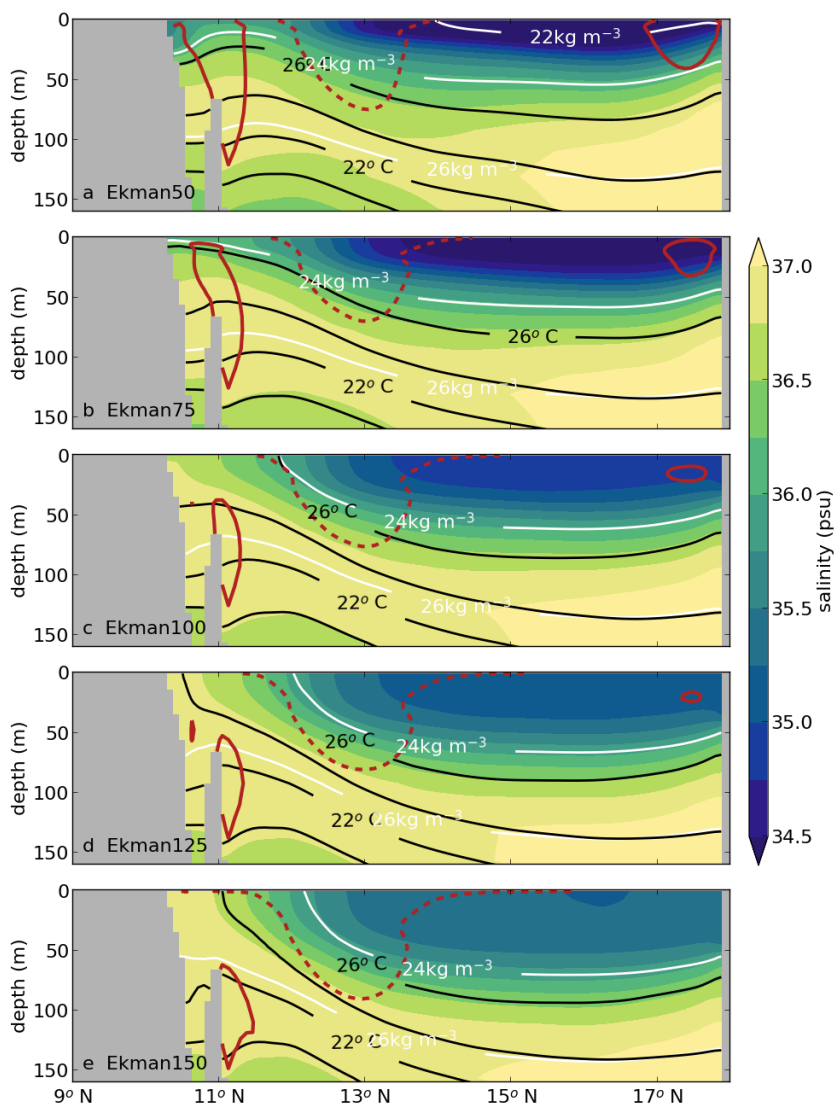
Figure 4.10: Cross-section at 66°W of the 20-year averaged salinity in (a) Ekman100, (b) Ekman50, (c) Ekman75, (d) Ekman125 and (e) Ekman150 (shading). The solid red line indicates the position of the subsurface countercurrent (contour line at an eastward velocity of 0.07 m s^{-1}). The Caribbean Current is indicated with the dashed red line (contour line at westward velocity of 0.2 m s^{-1}). The black contours shows the 20-year average temperature in each simulation; the white contour indicates the 20-year average density in each simulation.
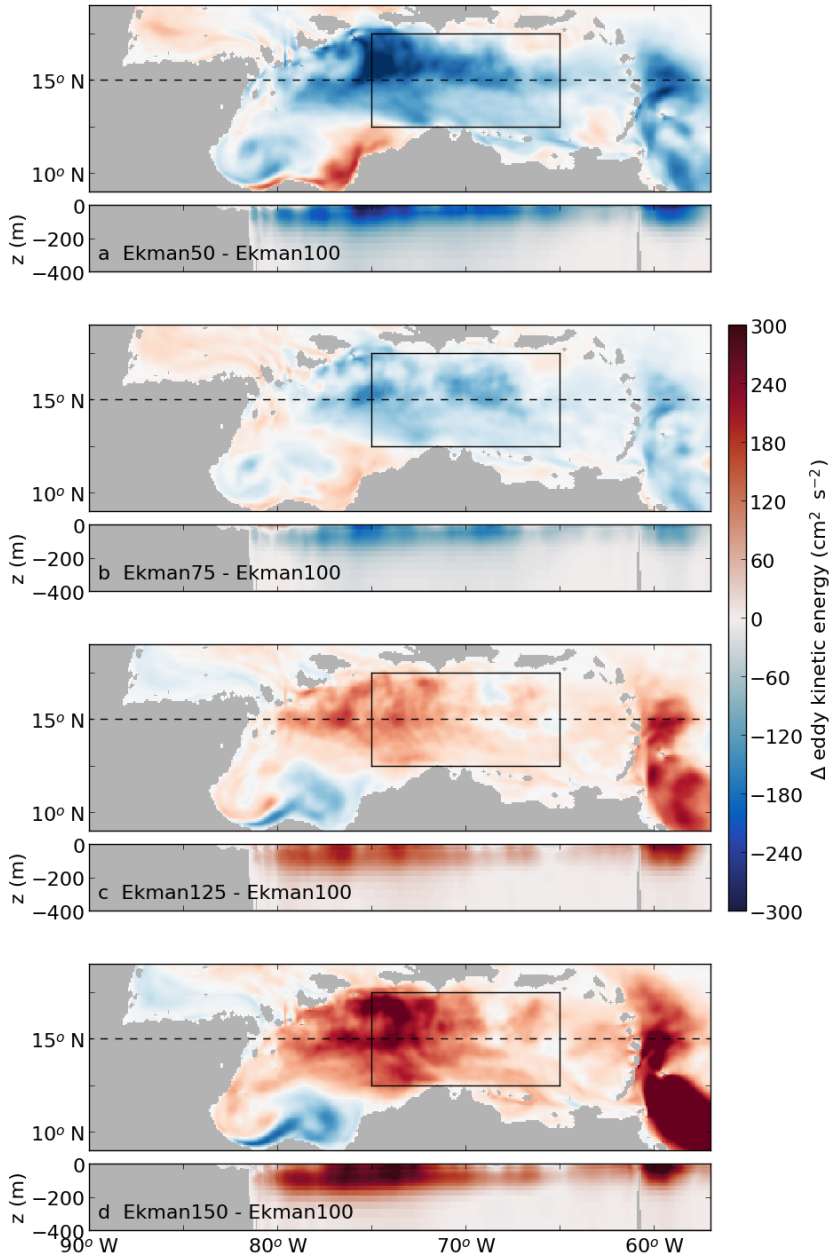
Figure 4.11: EKE anomaly compared to Ekman100 (Fig. 4.4) at the near-surface and at a cross-section at 15°N in (a) Ekman50, (b) Ekman75, (c) Ekman125 and (d) Ekman150. Positive values correspond to enhanced EKE compared to Ekman100. The black box indicates the interior of the Caribbean Sea (12.5°N-17.5°N, 65°W-75°W). The dashed line shows the location of the cross-sections in the lower panels.

Figure 4.12: (a) Zonal variation of the maximum of EKE between 12.5°N-17.5°N, from 65°W to 75°W for each simulation. (b) As (a), but for the anticyclones with long tracks only. The EKE was averaged over the upper 50 m. Note the difference in scale between the two panels.

4.6.3 Changes in eddy characteristics

Next, we assessed whether the changes in the westward increase in EKE can be attributed to changes in the eddy field and to changes in the westward intensification of anticyclones. To this end, we studied the behavior of individual eddies in the each simulation with the py-eddy tracker. The number of anticyclones that are formed each year in the interior of the Caribbean Sea is highly variable and varies between 8.55 year^{-1} (Ekman100) and 10.85 year^{-1} (Ekman50, Table 4.1). These numbers are in line with a formation rate of 8-12 anticyclones per year as observed by Richardson (2005). In all simulations, between 34 % and 43 % of the anticyclones that are formed in the Caribbean Sea have long tracks (Table 4.1). The pat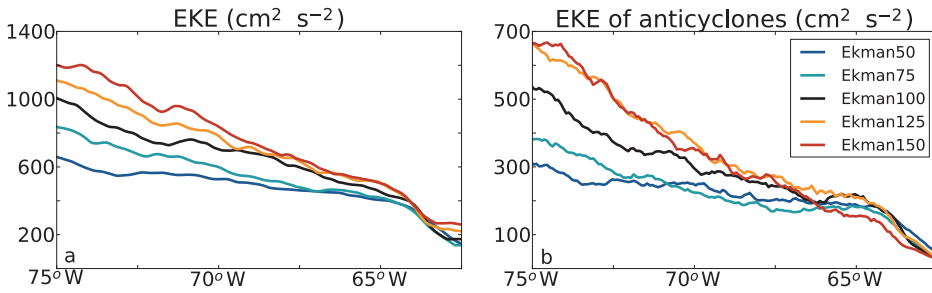hs of these anticyclones with long tracks are, similar to Ekman100 (Fig. 4.6a), located in the southern part of the basin (not shown).

Similar to Ekman100, we computed the EKE associated only with the long-lived anticyclones which were formed in the eastern part of the basin (<65°W) and propagate beyond 75°W (Fig. 4.12b). Similar behavior is visible as for the total EKE in Figure 4.12a: The EKE increases towards the west in all simulations, and stronger (weaker) upwelling correspond to a larger (smaller) westward increase. In the simulations with strong upwelling (Ekman100, Ekman125 and Ekman150), the anticyclones with long tracks (Fig. 4.12b) are responsible for more than half of the total EKE (Fig. 4.12a), even though they constitute only 34-43 % of the total number of anticyclones in this region (Table 4.1). In Ekman50 and Ekman75, the anticyclones with long tracks become less dominant. In these simulations, the westward increase of EKE is also less pronounced than in the stronger wind conditions. Overall, this shows that in all simulations, a substantial part of the EKE and the longitudinal variations therein are governed by the evolution of a small number of anticyclones, and that this effect is stronger in simulations with stronger upwelling.

In general, the anticyclones are fresher and warmer than the surrounding waters in all simulations. The freshest and warmest anticyclones are present in

Ekman50, while the most saline and coldest anticyclones are found in Ekman150 (Table 4.1). It is interesting to note that the variation of the properties of the anticyclones is very small in each simulation (see standard deviation of the anticyclone properties in Table 4.1). This suggests that, like shown for Ekman100 in Fig. 4.8c, also for the simulations in which the upwelling was varied the properties of the anticyclones remain approximately constant during their propagation westward.

In line with observations of Centurioni and Niiler (2003), we found less cyclones than anticyclones in each simulation (Table 4.1). The lowest average formation rate of cyclones is found in Ekman150 with 4.15 cyclones per year, and the highest average formation rate is present in Ekman50 with 6.15 cyclones per year. These formation rates were highly variable, and differences in formation rates between simulations were not significant. In none of the simulations, the py-eddy tracker was able to track multiple cyclones from east to west (65°W-75°W). This implies that the cyclones are either deformed or dissipated too much, such that the py-eddy tracker could not track their sea-level anomaly. Overall, the behavior of the mesoscale eddies is similar in all simulations and the spatial pattern and magnitude of the surface EKE is governed by the anticyclones with long tracks. The westward intensification of these anticyclones is discussed in the next section.

4.6.4   Westward intensification

We showed in Section 4 that the westward increase of EKE in Ekman100 coincided with a westward strengthening of the vertical shear of the long-lived anticyclones (Fig. 4.6c, Fig.4.7a). This increase in vertical shear was related via the thermal wind relation to the strengthening of the horizontal density gradients at the western edge of the anticyclone caused by the advection of upwelling filaments (Fig. 4.9a). Here, we analyze the thermal wind relation in the sensitivity simulations and its relation to the westward intensification of the anticyclones (Fig. 4.13).

In all simulations, the vertical shear of the anticyclones increases from east to west (Fig 4.13a). This westward increase in vertical shear is similar to the westward strengthening of the horizontal density gradients (Fig. 4.13b). Similar to Ekman100, the magnitude of the horizontal density gradients is slightly smaller than the vertical shear in all simulations, but their variation is similar. In combination with the low Rossby number of the anticyclones (Table 4.1), this implies that the anticyclones are in near-geostrophic balance during their evolution.

The anticyclones display the strongest westward intensification in the simulations with stronger upwelling (orange and red lines in Fig. 4.13a,b). These simulations have relatively low vertical shear at 65°W. In the simulations with weaker upwelling, Ekman50 and Ekman75, the anticyclones intensify less than in Ekman100. Moreover, in Ekman50, the vertical shear even weakens between 70°W and 73°W. At the same location, the EKE also does not increase in Ekman50
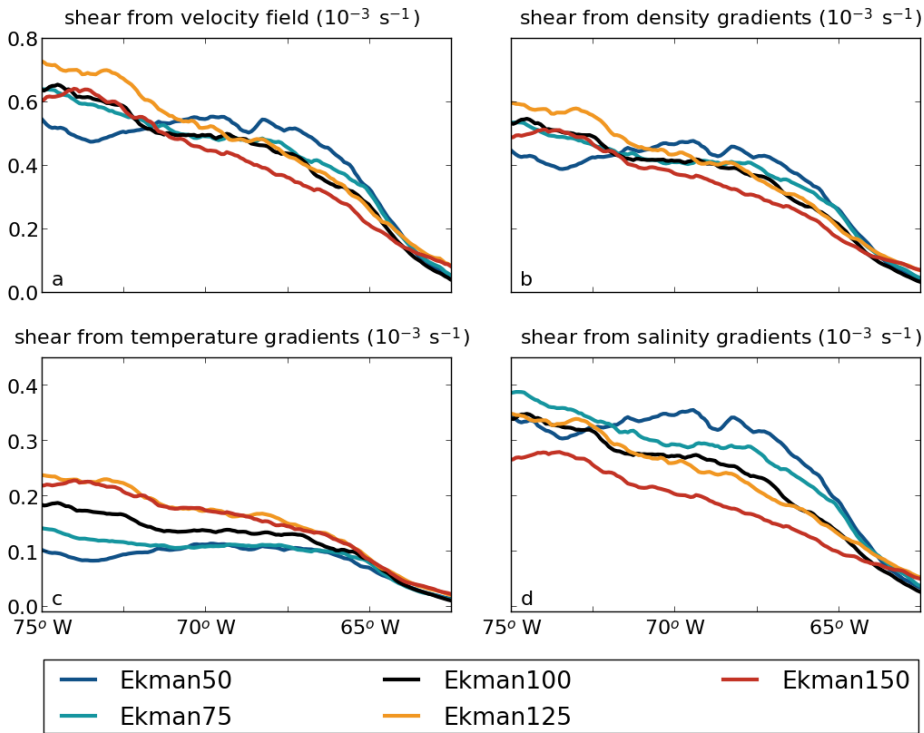
Figure 4.13: Zonal variation of the meridional average (12.5°N-17.5°N) of the (a) average vertical shear of the anticyclones, (b) horizontal density gradients, (c) horizontal density gradients induced by temperature gradients and (d) horizontal density gradients induced by salinity gradients. All properties are computed over the upper 50 m of the water column.

(Fig. 4.12b).

It is remarkable that, at 65°W, the strongest vertical shear and density gradients of the anticyclones are present in Ekman50, while the weakest gradients were located in Ekman150 (compare the blue and red lines in Fig. 4.13a,b). This suggests that the early development (east of 65°W) of the anticyclones differs between the simulations. The strong gradients in Ekman50 at 65°W are surprising, because we expected stronger gradients in simulations with stronger upwelling. An explanation for the strong horizontal density gradients at 65°W in Ekman50 can be found after separating the total horizontal density gradients into density gradients induced by temperature and salinity (Fig. 4.13c,d). While the density gradients driven by temperature gradients have a similar magnitude in each simulation in the eastern part of the basin (Fig. 4.13c), the density gradients driven by salinity gradients differ substantially between the simulations at 65°W (Fig. 4.13d) and are negatively correlated to the upwelling strength.

To understand why the salinity gradients in the eastern part of the basin are stronger for weaker upwelling, we analyzed the average spatial variation

of the total density gradients. Figure 4.14 shows the magnitude of the time-averaged horizontal density gradients $|\nabla \sigma|$ of Ekman100 (middle column), and the strengthening or weakening of these gradients in Ekman50 (right column) and Ekman150 (left column) compared to Ekman100. The strongest horizontal density gradients are located at the Guajira and Cariaco upwelling regions (Fig. 4.14b). These density gradients are weaker in Ekman50 than in Ekman100 (Fig. 4.14a), and stronger in Ekman150 (Fig. 4.14c).

The horizontal density gradients at the upwelling region are due to both horizontal temperature and salinity gradients (Fig. 4.14e-h). Because upwelling brings relatively cold and saline waters towards the surface (Fig. 4.10), the strength of these density gradients increase for stronger upwelling (Fig. 4.14c) and decrease for weaker upwelling (Fig. 4.14a). In Ekman150, the strengthening of the horizontal density gradients is mainly due to temperature induced density gradients in the upwelling region (Fig. 4.14f,i). In contrast, in Ekman50, the weakening of the temperature gradients (Fig. 4.14d) and salinity gradients (Fig. 4.14g) contribute roughly equally to the weakening of the total horizontal density gradients (Fig. 4.14a).

In the interior of the basin, the horizontal density gradients strengthen in Ekman50 compared to Ekman100 (Fig. 4.14a), while they are weaker in Ekman150 compared to Ekman100 (Fig. 4.14c). It appears that this response results from the increasing importance of the Amazon and Orinoco River plumes for weaker wind conditions. The wind affects both the propagation and spreading of the river plume. First of all, the northward Ekman transport advects the river plumes towards the north as previously observed by Molleri et al. (2010). This northward Ekman transport is weaker in Ekman50, and consequently the river plumes follows the mean flow towards the west (Fig.4.14g). The stronger Ekman transport in Ekman150 results in a more northward path of the river plumes (Fig.4.14i). The second consequence of changing wind conditions is the impact of the wind-driven vertical mixing. The strong zonal winds in Ekman150 induce more wind-driven mixing of the surface waters than the winds in Ekman50. As a result, salinity anomalies propagate less far westward in Ekman150 than in Ekman50. The farther advection of the river plume in Ekman50 explains why the anticyclones have stronger salinity gradients in Ekman50 than in the other simulations (Fig. 4.13d).

From this analysis we conclude that a weakening of the zonal wind in Ekman50 leads to an increased influence of the Amazon and Orinoco River plume compared to the other simulations. More specifically, in Ekman50, the upper ocean density gradients in the interior of the Caribbean Sea are dominated by salinity gradients (Fig. 4.14j), while the density gradients are predominantly temperature driven in Ekman150 (Fig. 4.14l). So, depending on the zonal wind strength, the total horizontal density gradients in the Caribbean Sea are either driven by temperature or salinity gradients, which suggests that both the river plumes as well and the upwelling affect the variability in the basin.
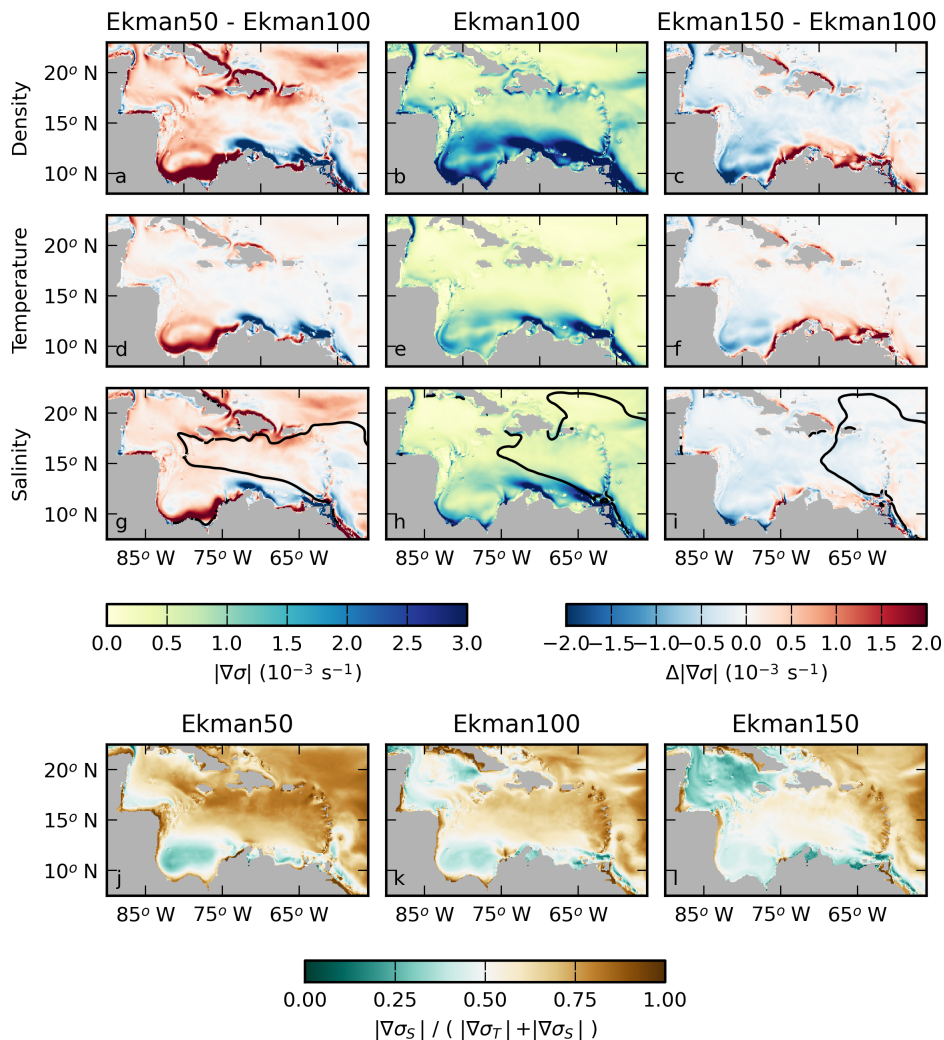
Figure 4.14: (a-c) Average strength of the horizontal density gradients ($|\nabla\sigma|$) in Ekman50, Ekman100, Ekman150 (see Section 4.2). The middle column shows the magnitude of the density gradients in Ekman100. Left and right columns contain the difference between Ekman50 and Ekman150 and Ekman100, respectively. Red colors indicate an increase of the horizontal density gradient. (d-f) Average strength of the horizontal density gradients due to temperature variations ($|\nabla\sigma_T|$). (g-i) Average strength of horizontal density gradients due to salinity variations ($|\nabla\sigma_S|$). The solid black line indicates where $S = 35.5$ psu. (j-l) Relative magnitude of density gradients due to salinity compared to density gradients due to temperature ($\frac{|\nabla\sigma_S|}{|\nabla\sigma_T|+|\nabla\sigma_S|}$). All properties are averaged over 20-years and over the upper 50 m of the water column.

4.7   Summary and discussion

In this study, we used a regional model of the Caribbean Sea to investigate the interaction between mesoscale anticyclones and the wind-driven coastal upwelling along the South-American coast. We showed that the westward intensification of Caribbean anticyclones is driven by an increase in the horizontal density gradient between their cores and their surroundings (Fig. 4.7). Notably, the increase is governed by density changes of the surroundings; not by density changes within the anticyclone (Table 4.1). More specifically, the density of the surroundings increases through the offshore advection of cold filaments of upwelled water by the anticyclones, which in turn is governed by the passage of the anticyclones themselves. This increases the horizontal density gradient between the anticyclone and the surroundings on the western side of the anticyclone (Fig. 4.9a). As a result, its vertical shear increases, and the anticyclone becomes more energetic. Approximately 2-4 anticyclones per year showed this behavior. The anticyclones that are not associated with the advection of cold filaments, strengthen this view that the westward intensification of Caribbean anticyclones is facilitated by the advection of filaments of upwelled water. These anticyclones were less energetic and had shorter life spans than the anticyclones that intensified towards the west.

Further support for this view is obtained from the series of simulations in which the strength of the upwelling was altered by adjusting the zonal wind stress (and thus the northward Ekman transport). Stronger upwelling leads to an increase in offshore cooling, and thus to a stronger increase in the horizontal density gradient between the anticyclones and their surroundings. As a result, the anticyclones intensify more on their path westward compared to the case of weaker upwelling. We also found that a decrease of the northward Ekman transport in the basin allows the river plumes to advect further into the basin. This influences the early development of the anticyclones. This non-linear response of the evolution of anticyclones to changes in upwelling highlights the fact that the horizontal density gradients in the Caribbean Sea are predominantly set by salinity gradients in case of weak wind forcing and by temperature gradients in case of strong wind forcing.

Previous studies in the Caribbean Sea mainly focussed on either the influence of the river plumes (e.g., Hu et al., 2004; Chérubin and Richardson, 2007), or on the influence of the wind (e.g., Oey et al., 2005; Astor et al., 2003; Jouanno et al., 2009). However, based on our results, we argue that it is important to take the interaction between the pathway of the river plume and the upwelling into account when studying mesoscale variability in the Caribbean Sea.

Based on the different wind forcing in the simulations, we can speculate on the seasonal eddy variability in the Caribbean Sea: the strong zonal wind stress in winter is similar to Ekman125, and the weaker winds in fall are represented by Ekman50 and Ekman75. In Ekman150, the anticyclones intensified more than in Ekman50. This implies that during the strong wind forcing in winter the anticyclones intensify more. Furthermore, during weak wind forcing, we expect that
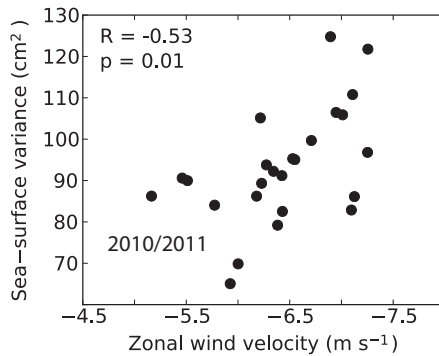
Figure 4.15: Year-averaged sea-level variance and coastal zonal wind velocities. Sea-surface spatial variance is obtained from daily sea-level anomaly fields from years 1993-2017 from satellite altimetry (CMEMS) and averaged over the interior of the Caribbean Sea (12.5°N - 17.5°N, 65°W - 75°W). Coastal zonal winds in the upwelling region (10°N -12.5°N, 65°W - 75°W) are obtained from years 1993-2017 from ECMWF (ERA-Interim, Dee et al., 2011). Each dot represents one year.

the salinity gradients of the river plume will become dominant. However, the dispersal of the Amazon and Orinoco River plumes also has a distinct seasonal cycle (Hellweger and Gordon, 2002; Chérubin and Richardson, 2007), which is absent in our model and would be an interesting topic for further study.

The results of this study also highlight some aspects of the interannual variability of the eddy field in the Caribbean Sea. In our simulations, stronger wind forcing resulted in a higher EKE in the center of the Caribbean Sea. Assuming that this relation holds on interannual time scales as well, these results suggest a positive correlation between the wind forcing and eddy variability in the interior of the basin. Jouanno and Sheinbaum (2013) used a model with seasonally varying boundary conditions and identified a similar relationship. This is also found in observations (Fig. 4.15), which show that sea-surface variance is higher in years with stronger zonal winds. Figure 4.15 also suggests that the response of the sea-surface variance to the wind stress is non linear: Although 2010 and 2011 were years with weak zonal winds, the sea-surface variance was relatively high. It is interesting to note that the salinity in the Cariaco Basin was anomalously low in these years (CARIACO–project, 2018). Taking into account the shallow depth of this salinity anomaly, it is plausible that it is related to the farther westward propagation of the river plumes as seen in Ekman50. This supports our view that both upwelling and the dispersal of the river plumes affect the mesoscale eddy field in the Caribbean Sea.

Over the past two decades, a weak decreasing trend has been observed in the coastal wind stress and upwelling strength (Campbell et al., 2011; Lima and Wethey, 2012; Torres and Tsimplis, 2013). Not only did this have severe ecological impacts (Villamizar G. and Cervigón, 2017), it also impacts the mesoscale variability. Our results suggest that weaker upwelling will lead to less westward

intensification of Caribbean anticyclones and less mesoscale variability in the interior of the basin. Furthermore, in weaker wind conditions the offshore advection of (nutrient-rich) cold filaments is weaker, which results in less offshore advection of nutrients and biota.

Overall, in this study we showed how the strength of the zonal wind stress in the Caribbean Sea impact the eddy variability in this basin. We showed how two processes induced by the northward Ekman transport impact the development of the most energetic anticyclones. First, the river plume sets the properties of the anticyclones during their early development in the eastern Caribbean Sea. Second, the anticyclones intensify themselves by the advection of cold and saline upwelling filaments. Together these two processes explain some key aspects of the mesoscale variability in the Caribbean Sea.

Chapter 5

Global dataset of thermohaline staircases obtained from Argo floats and Ice-Tethered Profilers

Abstract

Thermohaline staircases are associated with double-diffusive mixing. They are characterized by stepped structures consisting of mixed layers of typically tens of meters thick that are separated by much thinner interfaces. Through these interfaces enhanced diapycnal salt and heat transport take place. In this study, we present a global dataset of thermohaline staircases derived from observations of Argo profiling floats and Ice-Tethered Profilers using a novel detection algorithm. To establish the presence of thermohaline staircases, the algorithm detects subsurface mixed layers and analyses the interfaces in between. Of each detected staircase, the conservative temperature, absolute salinity, depth and height, as well as some other properties of the mixed layers and interfaces are computed. The algorithm is applied to 487,493 quality-controlled temperature and salinity profiles to obtain a global dataset. The performance of the algorithm is verified through an analysis of independent regional observations.

5.1   Introduction

Thermohaline staircases consist of subsurface mixed layers that are separated by thin interfaces. They are associated with double-diffusive processes, which in turn result from a two orders of magnitude difference between the molecular diffusivity of heat and that of salt (Stern, 1960). Whenever the vertical gradients of temperature- and salinity-induced stratification have the same sign, these differences in molecular diffusivity can enhance the vertical mixing through double-diffusive convection, leading to effective diffusivities of the order of 10^{-4} m^{-2} s^{-1} (Radko, 2013, and references therein).

It is still a topic of discussion how double-diffusive convection leads to the formation of thermohaline staircases in oceanic environments (Merryfield, 2000). For example, Stern (1969) argued that small-scale mixing processes trigger the formation of internal waves. On the other hand, variations in the turbulent heat and salt fluxes (Radko, 2003) or in the counter-gradient buoyancy fluxes that sharpen density gradients (Schmitt, 1994) could also lead to the formation of thermohaline staircases. Lastly, subsurface mixed layers can also arise from thermohaline intrusions (Merryfield, 2000). Although it remains unclear how these staircases arise, these studies agree that the formation of these subsurface mixed layers are related to double-diffusive processes.

Based on the Turner angle (Tu), which compares the density component of the temperature distribution with the density component of the salinity distribution, two regimes of double diffusion can be distinguished (Ruddick, 1983). Waters with $-90° < $ Tu $ < -45°$ correspond to a stratification where both temperature and salinity increase with depth and belong to the diffusive-convective regime (DC). Those with $45° < $ Tu $ < 90°$ correspond to a stratification where temperature and salinity decrease with depth and belong to the salt-finger regime (SF).

Theoretical and laboratory studies have indicated that diapycnal fluxes of heat and salt in thermohaline staircases are elevated compared to the background turbulence (e.g., Schmitt, 1981; Kelley, 1990; Radko and Smith, 2012; Garaud, 2018). These results were confirmed by a tracer release experiment in the western tropical Atlantic Ocean (Schmitt, 2005). Although these enhanced fluxes were observed, the importance of these fluxes for the global mechanical energy budget remain unknown. Moreover, the vertical heat and salt fluxes in thermohaline staircases can also affect water-mass properties. In some regions, persistent thermohaline staircases with layers stretching over a few hundred kilometers have been observed (Schmitt et al., 1987; Timmermans et al., 2008; Shibley et al., 2017), which could result in significant diapycnal fluxes between water masses. For example, the double-diffusive diapycnal fluxes in the Mediterranean Sea dominate the transport between the deep water masses (Zodiatis and Gasparini, 1996; Bryden et al., 2014; Schroeder et al., 2016), and in the Arctic Ocean and Southern Ocean, an upward heat flux has been observed through staircase interfaces (Timmermans et al., 2008; Shibley et al., 2017; Polyakov et al., 2012;

Bebieva and Speer, 2019).

Modeling studies that incorporated parameterizations of double-diffusive fluxes, indicated that the associated double-diffusive diapycnal fluxes can reduce the strength of the global overturning circulation (Gargett and Holloway, 1992; Merryfield et al., 1999; Oschlies et al., 2003). To be able to study this with observations, we present a global dataset of the occurrence of thermohaline staircases and their properties. The dataset is based on observations from Argo floats and Ice-Tethered Profilers. In the following sections we briefly describe the raw data used to extract the dataset (Section 5.2) and the algorithm we designed to detect staircase structures (Section 5.3). The sensitivity of this detection algorithm to the chosen input parameters is assessed in Section 5.4. The dataset is verified in Section 5.5, followed by some guidelines for the use of the dataset in Section 5.6.

5.2 Data preparation

The dataset contains observations of autonomous Argo floats and autonomous Ice-Tethered Profilers (ITP). The data of all active and inactive profilers is obtained from http://www.argo.ucsd.edu and http://www.whoi.edu/itp from 13 November 2001 to 14 May 2020. Details on the profilers are described in Krishfield et al. (2008) and Toole et al. (2011) for the ITP and in Argo (2020) for the Argo floats. First a quality check is performed, where a profile is excluded from analysis if it was taken by an Argo float mentioned on the grey list. This grey list contains floats that may have problems with at least one of the sensors[3] . As thermohaline staircases consist of mixed layers with depths of tens of meters, we also require that profiles have continuous data up to 500 dbar with an average resolution finer than 5 dbar. Details on the origin and vertical resolution of the profiles are depicted in Table 5.1 and Figure 5.1, in which Figure 5.1b confirms that all profiles have observations deeper than 500 dbar. Furthermore, the average vertical resolution of the profiles indicates the average resolution is well below the 5 dbar that was used as a threshold (Fig. 5.1c). After this quality control, 487,493 vertical temperature and salinity profiles remain. Their global distribution is shown in Figure 5.2.

Next, the profiles of the Argo floats and ITP were linearly interpolated to a vertical resolution of 1 dbar from the surface to 2000 dbar so that their data could be analyzed in a consistent manner. As a result, the small steps in, for example, Arctic staircases might be missed (see Section 5.5). From these interpolated profiles we calculate several variables. Absolute salinity (S) in g kg^{-1} and conservative temperature (T) in °C are computed with the TEOS-10 software (McDougall and Barker, 2011). Note that we use conservative temperature as this is more accurate than potential temperature in computations concerning heat fluxes and heat content (Graham and McDougall, 2013). We apply a moving average of 200 dbar (Table 5.2) to obtain the background conservative

---

[3] https://www.nodc.noaa.gov/argo/grey_floats.htm
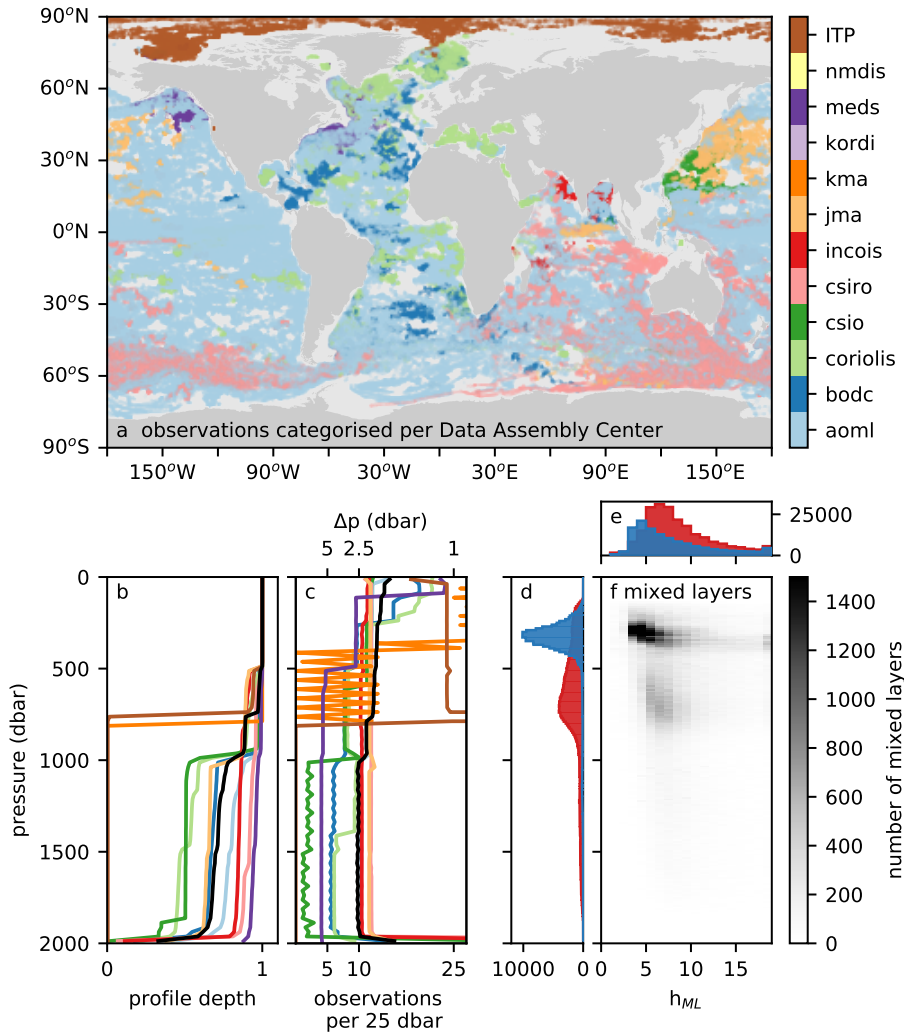
Figure 5.1: (a) Locations of observations categorized by Data Assembly Centers (DAC) when obtained by an Argo float. Profiles obtained with Ice-Tethered Profilers are indicated with ITP. (b) Cumulative fraction of profiles that reached a given pressure in 25-dbar intervals from 0 to 2,000 dbar per DAC. (c) Average number of observations in 25-dbar intervals from 0 to 2,000 dbar. (d) Distribution of detected mixed layer pressures in the salt-finger (red histogram) or diffusive-convective (blue histogram) regime. (e) Number of detected mixed layers height in the salt-finger (red histogram) or diffusive-convective (blue histogram) regime. (f) Distribution of detected mixed layer heights in thermohaline staircases per pressure level. Panels (b) and (c) were obtained following Wong et al. (2020). Black lines indicate the averages in total global dataset. More details on abbreviations of DAC can be found in Argo (2019)

Table 5.1: Number of floats and profiles in the global dataset. Profiles taken with Argo floats are categorized by the Data Assembly Center (DAC). Profiles taken with Ice-Tethered Profilers are categorized as ITP. The percentage between brackets indicates the relative contribution to the total number of profiles in the global dataset (487,493 profiles). More details on abbreviations of DAC can be found in Argo (2019)

DAC / ITP	number of floats	profiles
aoml	2,692	312,285 (64.1 %)
bodc	93	11,092 (2.3 %)
coriolis	347	27,134 (5.6 %)
csio	81	15,099 (3.1 %)
csiro	378	42,942 (8.8 %)
incois	65	4,363 (0.9 %)
jma	205	22,919 (4.7 %)
kma	1	1 (0.0 %)
kordi	0	0 (0.0 %)
meds	145	9,285 (1.9 %)
nmdis	0	0 (0.0 %)
ITP	82	42,373 (8.7 %)
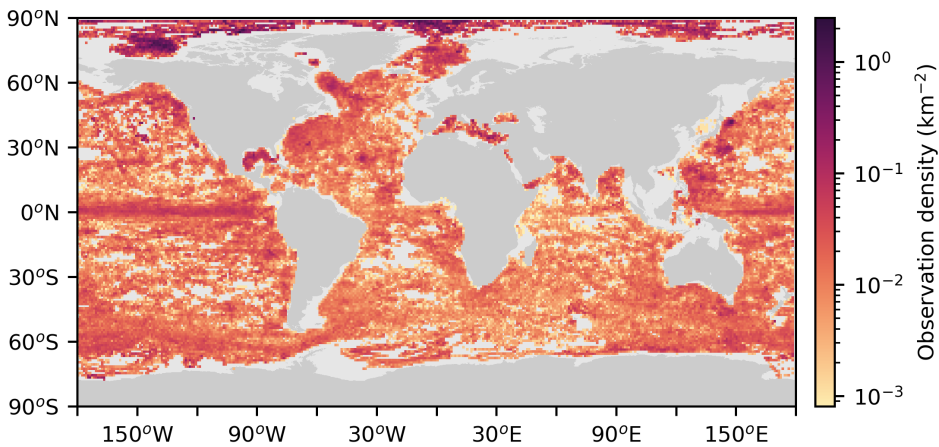
Figure 5.2: Observation density of the number of profiles obtained from the Argo floats and Ice-Tethered Profilers after quality control (in km^{-2}). Observation density is binned per degree longitude and degree latitude. Empty bins indicate that no data was available at that location.

Table 5.2: Input parameters of the data preparation and the algorithm as used in this study. The sensitivity of the algorithm to the input variables can be found in the Section 5.5. MAW is moving average window.

| parameter	description	value
MAW	chosen to obtain background profiles	200 dbar
$\partial \sigma_1 / \partial p_{max}$	density gradient threshold for detection mixed layer	0.0005 kg m^{-3} dbar^{-1}
$\Delta \sigma_{1,ML,max}$	maximum density gradient within mixed layer	0.005 kg m^{-3}
$h_{IF,max}$	maximum interface height	30 dbar

temperature and absolute salinity profiles of the water column and to compute the thermal expansion coefficient (α in °C^{-1}) and the haline contraction coefficient (β in kg g^{-1}). A consequence of the moving average of 200 dbar is that the upper 100 dbar and lower 100 dbar of each profile is omitted in the remainder of the analysis. The Turner angle is computed using profiles that were smoothed with a moving average of 50 dbar instead of 200 dbar, which is similar to Shibley et al. (2017), following Ruddick (1983), from

$$\text{Tu} = \tan^{-1}\left(\alpha \frac{\partial T}{\partial p} - \beta \frac{\partial S}{\partial p}, \alpha \frac{\partial T}{\partial p} + \beta \frac{\partial S}{\partial p} \right), \tag{5.1}$$

where the vertical gradients are approximated with a central differences scheme.

5.3   Detection algorithm

After the data pre-processing, we apply a detection algorithm that exploits the vertical structure of staircase profiles (Fig. 5.3). The benefit of using the vertical structure, instead of using assumptions based on the Turner angle, is that we can use this angle to verify the results. The detection algorithm consists of five steps. First the algorithm detects all data points that are located in the subsurface mixed layers (ML, green dots in Fig. 5.3) by identifying weak vertical density gradients in conservative temperature and absolute salinity. Next, the properties of any layer lying between the mixed layers (the interfaces, IF, orange dots in Fig. 5.3) are assessed by applying a minimum in temperature and salinity variations. Third, the height of the interface and variations within the interface are limited. The fourth step determines the regime of double diffusion (diffusive convection or salt fingers), and the fifth step is the identification of sequences of interfaces, which eventually characterizes the thermohaline staircases. The different steps of the algorithm applied to three example profiles are shown in Supplementary Figures 5.9-5.11. In the following subsections, each algorithm step is described in more detail.
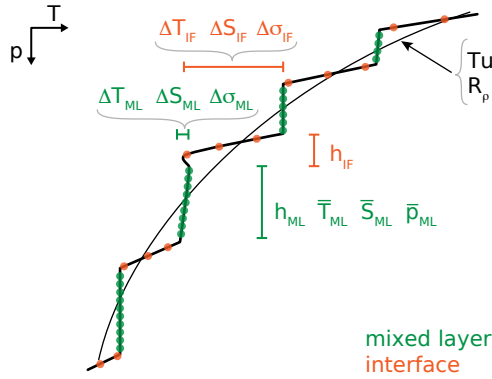
Figure 5.3: Schematic of a typical temperature profile with staircases, indicating the definitions of the quantities used to detect the thermohaline staircases (green: mixed layer; orange: interface). The overbar indicates layer-averaged properties.

5.3.1 Mixed layers

The first step of the detection algorithm is the identification of the mixed layers. Preferably, this is done by assessing a density difference relative to a reference pressure, which is the most reliable method to detect a mixed layer (Holte et al., 2017). However, in the case of a thermohaline staircase it is necessary to detect subsurface mixed layers, because the reference pressure is unknown beforehand. To determine this reference pressure, a threshold gradient criterium is applied first (Dong et al., 2008). In this criterium, vertical density gradients are identified as a mixed layer whenever the gradients are below a certain threshold.

We apply the gradient criterium on the vertical gradients of the potential density anomaly at a reference pressure of 1000 dbar (σ_1). We used a threshold of $\partial \sigma_1 / \partial p_{\max} = 0.0005$ kg m^{-3} dbar^{-1} (Table 5.2), which is similar to mixed layer gradients used by Bryden et al. (2014). Furthermore, this threshold gradient is slightly larger than the threshold used by Timmermans et al. (2008), who used 0.005°C m^{-1} (which corresponds to $\partial \sigma_1 / \partial p_{\max} = 0.00036$ kg m^{-3} dbar^{-1}). The threshold gradient method is applied on both conservative temperature and absolute salinity profiles, i.e.,

$$\left| \alpha \rho_0 \frac{\partial T}{\partial p} \right| \leq 0.0005 \text{ kg m}^{-3}\text{dbar}^{-1},$$
$$\left| \beta \rho_0 \frac{\partial S}{\partial p} \right| \leq 0.0005 \text{ kg m}^{-3}\text{dbar}^{-1}. \tag{5.2}$$

Also the vertical density gradients from the combined temperature and salinity effects must satisfy this condition:

$$\left| \frac{\partial \sigma_1}{\partial p} \right| \leq 0.0005 \text{ kg m}^{-3}\text{dbar}^{-1}. \tag{5.3}$$

These three conditions ensure that the vertical conservative temperature, absolute salinity and potential density gradients are all below the threshold value. At each pressure level where all three conditions are met the datapoint is identified as a mixed layer. Next, for each continuous sequence of data points, the algorithm computes the average pressure. This is then used as a reference pressure, which is required to be able to apply the mixed layer detection.

At every reference pressure, a maximum density range is required within the mixed layers to identify the full vertical extent of each mixed layer. To allow for small variations of conservative temperature and absolute salinity in the mixed layer, but to exclude variations in the interface, we use a threshold of $\Delta\sigma_{1,\text{ML,max}}$ =0.005 kg m^{-3} for density variations within each mixed layer (Table 5.2). This density range corresponds to the density range used by Holte et al. (2017) for the detection of surface mixed layers. The applied density range allows for mixed layers with heights of the order of 10 m assuming gradients of $\partial\sigma_1/\partial p_{\text{max}}$ =0.0005 kg m^{-3} dbar^{-1}. To ensure separation between individual mixed layers, the upper and lower datapoint of each mixed layer are removed. Note that this results in a minimum interface height of 2 dbar, which could result in false negatives in for example the Arctic Ocean (Section 5.5)

After applying the threshold for density range, the algorithm defines each continuous set of data points as a mixed layer and computes the average pressure ($\overline{p}_{\text{ML}}$), average conservative temperature ($\overline{T}_{\text{ML}}$), average absolute salinity ($\overline{S}_{\text{ML}}$), mixed layer density ratio ($\overline{R}_\rho = \alpha\frac{\partial\overline{T}}{\partial p}/\left(\beta\frac{\partial\overline{S}}{\partial p}\right)$), average Turner angle ($\overline{\text{Tu}}_{\text{ML}}$) and height ($h_{\text{ML}}$) for each mixed layer.

5.3.2   Interfaces: conservative temperature and absolute salinity variations

The algorithm defines an interface as the part of the water column between two mixed layers. In addition, to ensure a stepped structure the algorithm requires that the conservative temperature, absolute salinity and potential density variations within each mixed layer should be smaller than the variations in the interface (Fig. 5.3):

$$\max\left(\left|\Delta T_{\text{ML,1}}\right|,\left|\Delta T_{\text{ML,2}}\right|\right) < \left|\Delta T_{\text{IF}}\right|;$$
$$\max\left(\left|\Delta S_{\text{ML,1}}\right|,\left|\Delta S_{\text{ML,2}}\right|\right) < \left|\Delta S_{\text{IF}}\right|; \quad (5.4)$$
$$\max\left(\left|\Delta\sigma_{1,\text{ML,1}}\right|,\left|\Delta\sigma_{1,\text{ML,2}}\right|\right) < \left|\Delta\sigma_{1,\text{IF}}\right|;$$

where the subscripts 1 and 2 correspond to the mixed layer directly above and below an interface, respectively. It appears that most data points that meet these requirements (orange histograms in Fig. 5.4a-c) have Turner angles in the two double-diffusive regimes. This dependence of the variations in the interfaces on the Turner angle is in line with expectations that staircase-like structures are mostly found within double-diffusive regimes. In total, 28 % of all detected interfaces meet all three requirements (Fig. 5.4d).

Figure 5.4: Histogram of the number of detected interfaces as a function of the Turner angle (Tu) by applying a criterion for (a) conservative temperature, (b) absolute salinity, (c) potential density and (d) all three properties given in equation 6.7 (orange shading). Each panel shows the data remaining compared to the raw interface data (grey). Vertical shaded bands correspond to Turner angles in the diffusive-convective (blue) and salt-finger (red) regime.

5.3.3   Interface: height

The next step in the staircase detection algorithm is to limit the height of the interface to ensure that the mixed layers are separated from each other by a relatively thin interface (Fig. 5.3). We require

$$h_{\text{IF}} < \min\left(h_{\text{ML},1}, h_{\text{ML},2}\right), \tag{5.5}$$

i.e. the interface height is smaller than the height of the mixed layers directly above and below the interface. In total, 27 % of the interfaces that fulfilled the conservative temperature and absolute salinity requirements meet this requirement (Fig. 5.5a). Note that this part of the algorithm defines the top and bottom of a sequence of a staircase in a profile. Furthermore, the tallest observed interfaces are found in the Mediterranean Sea with heights up to $h_{\text{IF}} = 27$ m, where they separate mixed layers of over 100 m (Zodiatis and Gasparini, 1996; Radko, 2013). To prevent false detection of large vertical interfaces of up to hundreds of meters, we limit the interface height to $h_{\text{IF},max} = 30$ dbar (Table 5.2, Fig. 5.5b). This only affects the classification of 1 % of the interfaces (Fig. 5.5b).

To solely detect step-like structures that are associated with the presence of thermohaline staircases, the algorithm also removes all interfaces with conservative temperature or absolute salinity inversions. This is done by limiting the number of local minima and maxima of the conservative temperature and absolute salinity allowed in each interface to two (Fig. 5.5c). The combination of all three interface height requirements is met by 27 % of the interfaces detected based on the conservative temperature and absolute salinity requirements discussed in the previous section (Fig. 5.5d).

5.3.4   Interface: double-diffusive regime

After the algorithm has selected all the interfaces with a step-like structure, the double-diffusive regime of each interface is assessed (Fig. 5.6a). In case both conservative temperature and absolute salinity of the mixed layers above and below the interface increase with pressure, the interface is classified as the diffusive-convective regime. If the conservative temperature and absolute salinity of the mixed layers above and below the interface both decrease with pressure, the interface belongs to the salt-finger regime. The algorithm detects more interfaces in the salt-finger regime (27 %) than in the diffusive-convective regime (11 %, Fig. 5.6a). As expected, most interfaces with diffusive-convective characteristics have Turner angles between $-90° < \text{Tu} < -45°$ (blue histogram in Fig. 5.6a) and most salt-finger interfaces have Turner angles between $45° < \text{Tu} < 90°$ (red histogram in Fig. 5.6a). This implies that these interface properties are consistent with the background stratification.
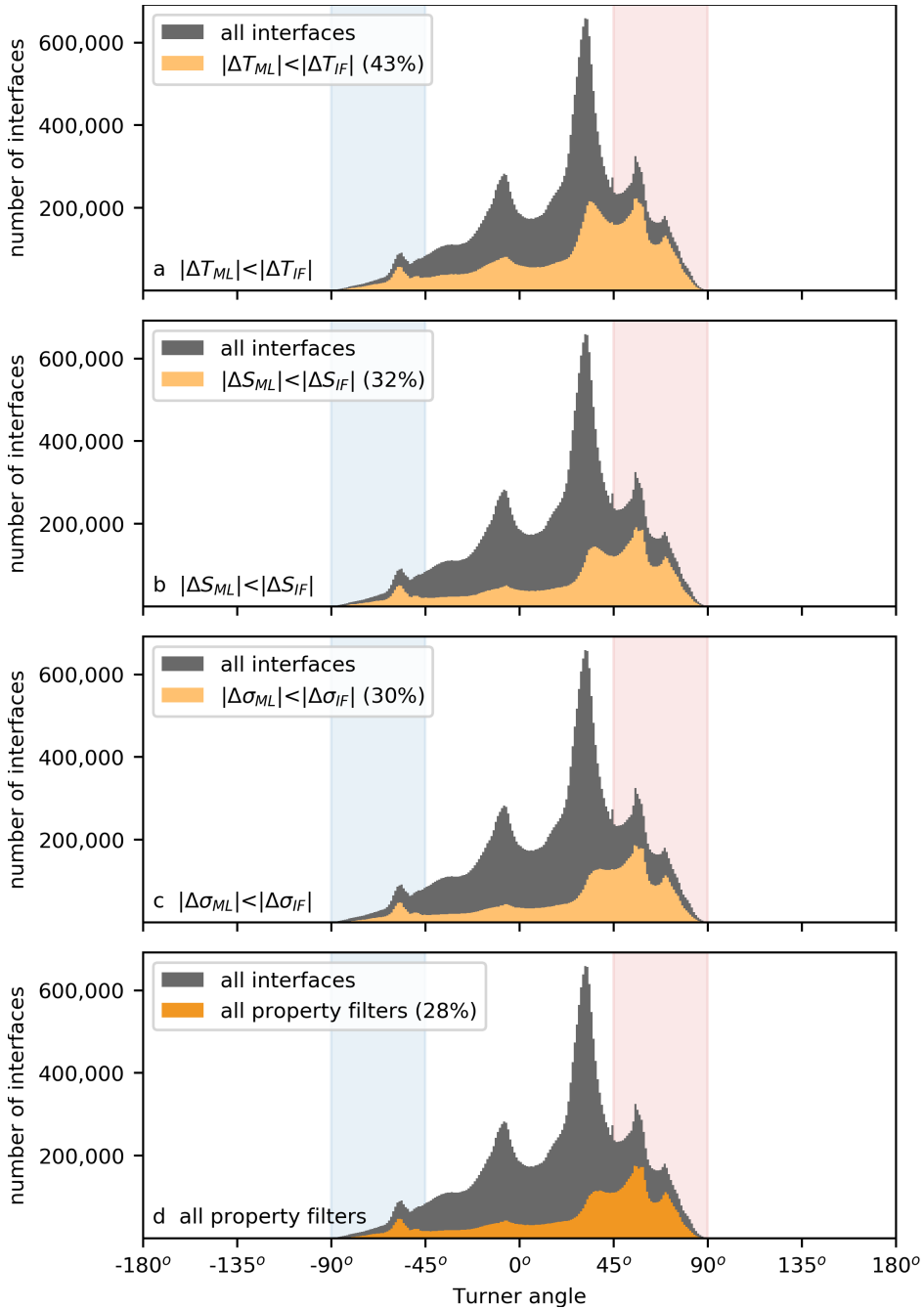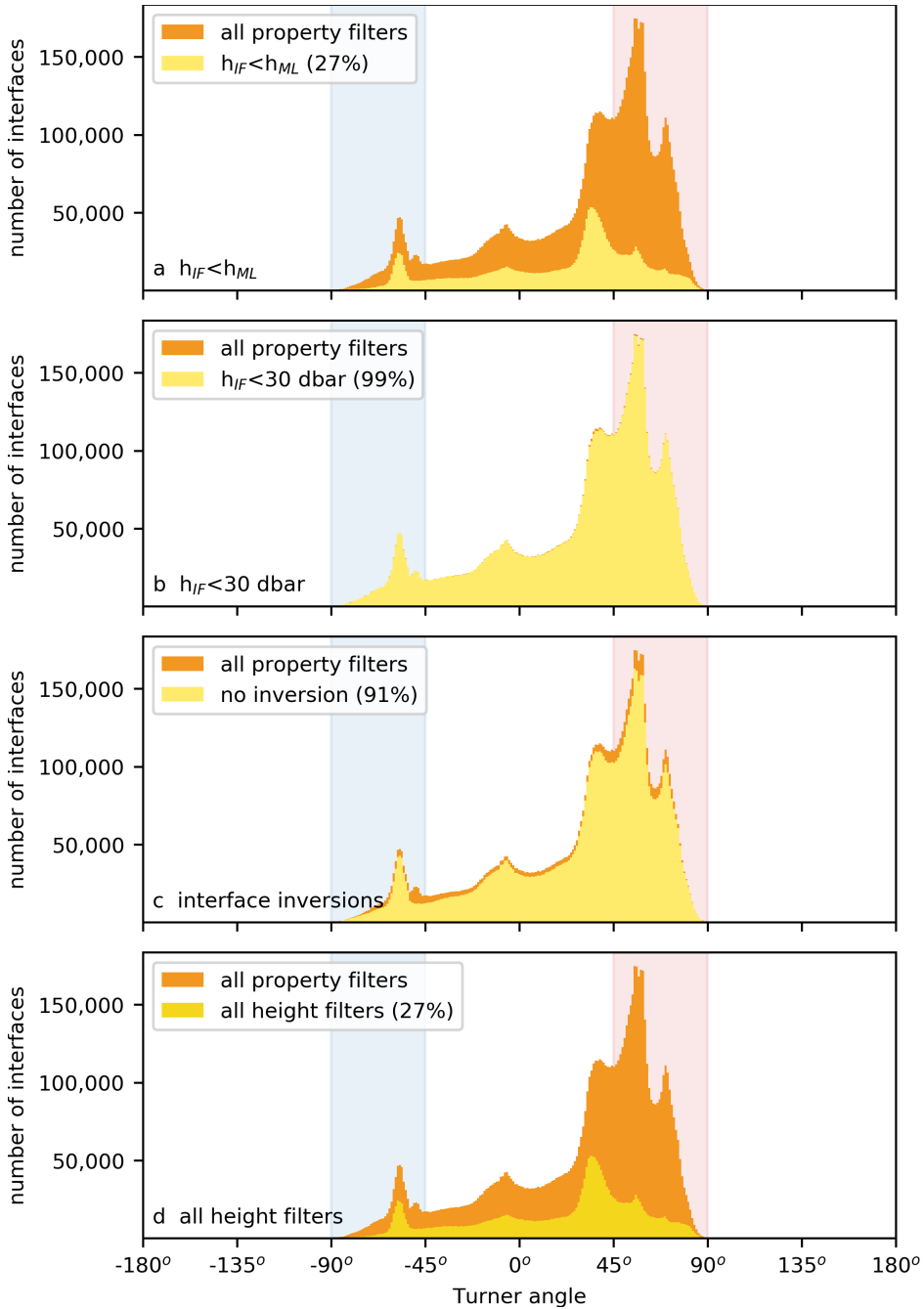
Figure 5.5: Histogram of the number of detected interfaces as a function of the Turner angle (Tu) by applying a criterion for (a) height, (b) maximum height, (c) inversions and (d) all three height limitations (yellow shading). Each panel shows the data remaining compared to the interfaces detected based on the conservative temperature and absolute salinity requirements shown in Fig. 5.4d (orange shading). Vertical shaded bands correspond to Turner angles in the diffusive-convective (blue) and salt-finger (red) regime.

5.3.5   Sequences of interfaces

The final step of the detection algorithm is to only select vertical sequences of at least two interfaces in the same double-diffusive regime that are separated from each other by one mixed layer (Fig. 5.6b). This step removes most thermohaline intrusions, as these are characterized by alternating mixed layers in the diffusive-convective and salt-finger regime (Bebieva and Timmermans, 2017). In this final step, the algorithm also removes also salt-finger interfaces and diffusive-convective interfaces outside their favorable Turner angle (compare Fig. 5.6a and Fig. 5.6b).

After applying this final step of the algorithm, we obtain a global dataset consisting of 166,141 interfaces in the salt-finger regime and 119,619 interfaces in the diffusive-convective regime. The distribution of the pressure levels and height of the mixed layers at these interfaces is displayed in Fig. 5.1. In general, mixed layers in the diffusive-convective regime are found at lower pressure levels than mixed layers in the salt-finger regime (Fig. 5.1d). At the same time, the height of the mixed layers in the diffusive-convective regime are smaller, which is in line with previous observations (Fig. 5.1e, e.g., Radko, 2013). Recall that the algorithm required a minimal interface height of 2 dbar, which implies that, following equation 5.5, the minimal mixed layer height is 3 dbar and that the detection of interfaces is cut off below these limits. Consequently, the interfaces with smaller heights are missed by the algorithm. Figure 5.1e indicates that this is more problematic for interfaces in the diffusive-convective regime than for interfaces in the salt-finger regime.

Examples of thermohaline staircases, which were selected based on their high number of interfaces, are shown in Figure 5.7. In line with previous results (Rudels, 2015), staircases in the diffusive-convective regime (Fig. 5.7a) are mainly detected on the thermocline with the conservative temperature increasing with depth. These staircases are predominantly located in the Arctic Ocean at a depth between 300-400 m, which is between the warm and saline Atlantic Water and cold and fresh surface waters (Rudels, 2015). Figure 5.7a also indicates that the deepest mixed layer of some thermohaline staircases is located at the temperature maximum, which suggests that this lowest layer might be the result of thermohaline intrusions (Ruddick and Kerr, 2003). There, the algorithm identified a mixed layer, because temperature and salinity stratification were weak enough (see Section 5.3.1). Furthermore, both conservative temperature and absolute salinity in this mixed layer are larger than in the mixed layer above. While both are typical for a staircase in the diffusive-convective regime, the algorithm does not detect whether this mixed layer is a temperature maximum, which could indicate that arose from thermohaline intrusions. Note that this only concerns the deepest mixed layers of the staircases, and that only the characteristics of the interfaces in between mixed layers are labelled as part of a staircase by the algorithm.

Thermohaline staircases with a high number of steps in the salt-finger regime
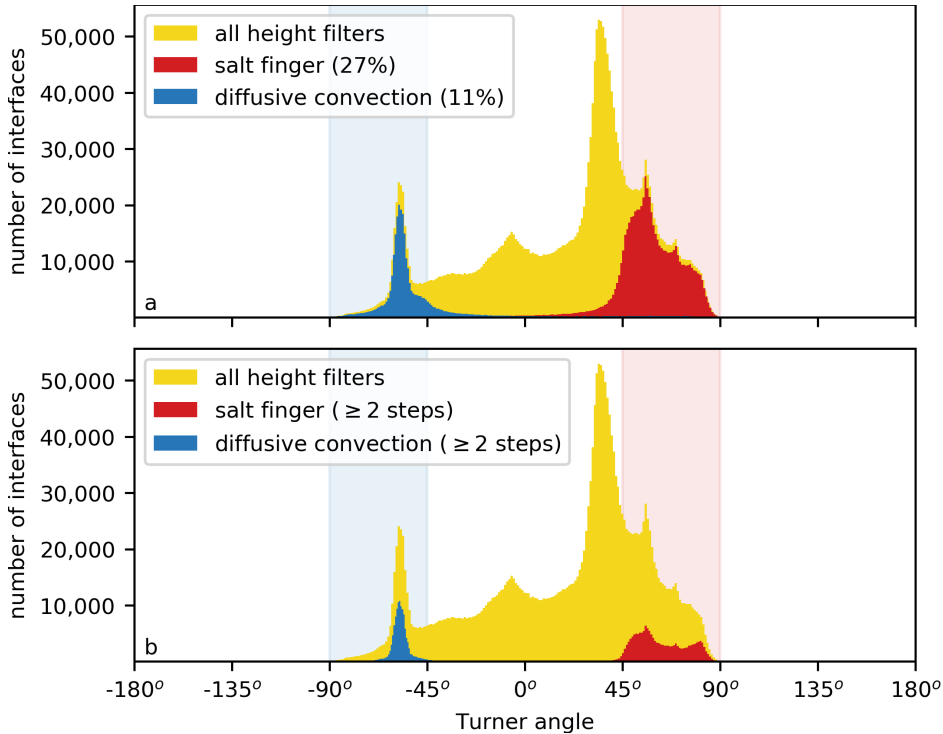
Figure 5.6: Histogram of the number of detected interfaces as a function of the Turner angle (Tu) after (a) classification of the double-diffusive regime and (b) selection of sequences of the interfaces. Each panel shows the data remaining compared to the interfaces detected based interface height requirement shown in Fig. 5.5d (yellow shading). Vertical shaded bands correspond to Turner angles in the diffusive-convective (blue) and salt-finger (red) regime.

are detected on the main thermocline where the conservative temperature decreases with depth (Fig. 5.7b). Compared to the staircases in the diffusive-convective regime, these staircases are located slightly deeper at 400-700 m. While the locations of these staircases vary, they are located above the cold and fresh Antarctic Intermediate Water, which is observed below 700 m (Tsuchiya, 1989; Fine, 1993; Talley, 1996).

For each thermohaline staircase, characteristics of the interfaces and mixed layers, such as their conservative temperature, absolute salinity and height, are available in the dataset. An overview of the provided variables is given in Supplementary Table 5.4. The detection algorithm is verified by comparing our data to independent observations in three regions in Section 5.5.
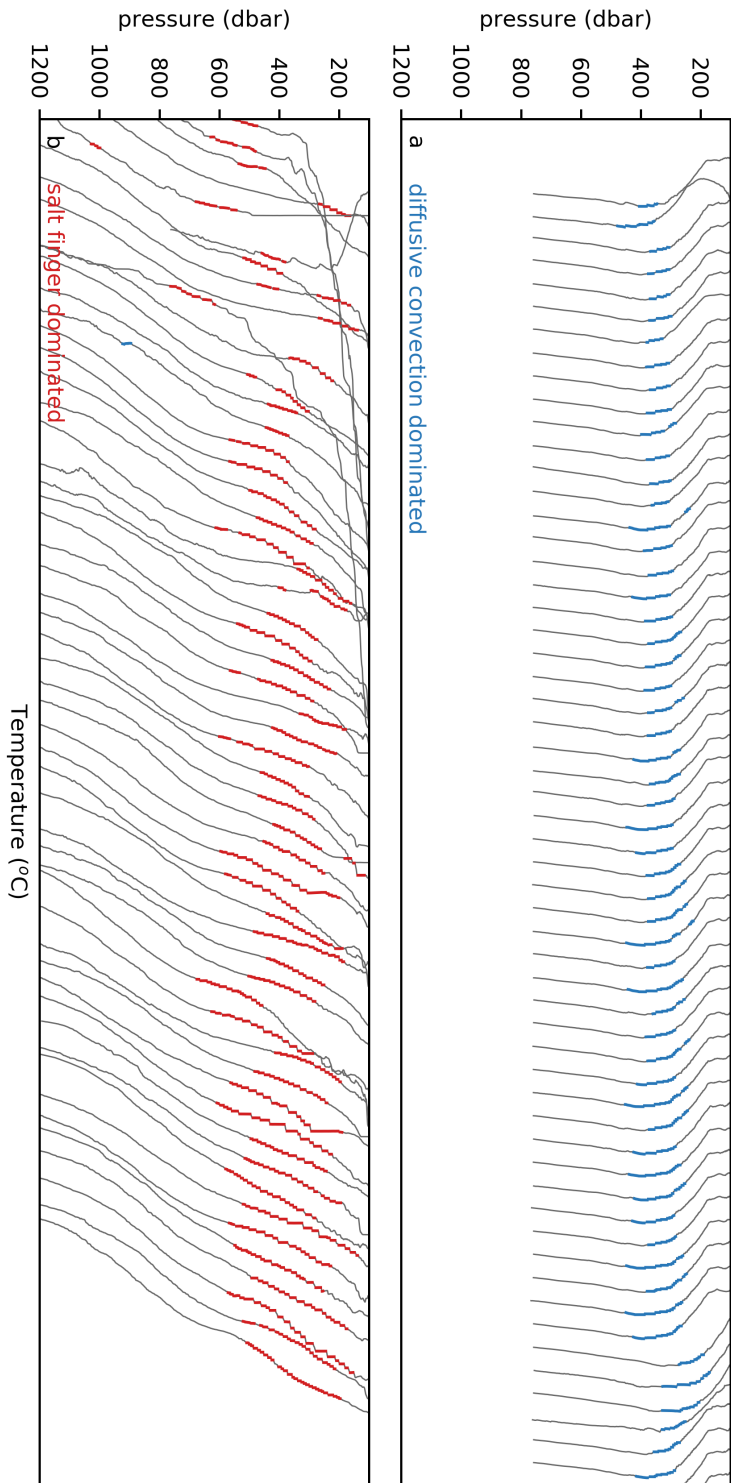
Figure 5.7.: Example conservative temperature profiles selected by the staircase detection algorithm. They are ordered left-right by the number of steps detected. Top panel shows examples of increasing steps of diffusive convection, bottom panel shows examples of the salt-finger regime.

5.4 Robustness of the detection algorithm

The algorithm requires four input parameters: the moving average window, a threshold for the maximum density gradients of the mixed layers, the maximum density difference of the mixed layers and the maximum height of the interface (Table 5.2). In this section, the sensitivity of the algorithm to each input parameter is assessed (Fig. 5.8).

The moving average window is used by the algorithm to compute the thermal expansion coefficient (α), the haline contraction coefficient (β) and the density ratio (R_ρ). We varied the moving average window between 50 dbar and 350 dbar to assess the sensitivity of the outcomes of this choice (Fig. 5.8a). We find that the varying moving average window does not result in large variations in detected mixed layers (Fig. 5.8a).

In contrast to the moving-average window, the detection algorithm is sensitive to the value set for the density gradient threshold of the mixed layer (Fig. 5.8b), which is used to obtain a reference pressure for the sub-surface mixed layers (Section 5.3.1). Not surprisingly, we detect more (less) interfaces when we increase (decrease) the allowed threshold density gradient. A small value allows for only the strongest mixed layers to be detected, which are usually referred to as well-defined staircases, while a large density gradient also allows for the detection of rough staircases (e.g., Durante et al., 2019). Although the number of detected interfaces depends on the value set for this density gradient, the detected interfaces remain confined to the two double-diffusive regimes, indicating a robust outcome of the algorithm for the choice of this input parameter.

Similar to the variations of the maximum density gradient, the variation of the maximum density difference allowed within the mixed layer results in a different number of detected interfaces (Fig. 5.8c). The number of detected mixed layers increases when we decrease the maximum density difference allowed within the mixed layer. This effect is mostly visible in the diffusive-convective regime, as we obtained a decrease of 54 % of detected interfaces in the diffusive-convective regime compared an decrease of 31 % of detected interfaces in the salt-finger regime in case we doubled the density difference in the mixed layer ($\Delta\sigma_{1,\max} = 10 \times 10^{-3}$ kg m^{-3}). This difference between the regimes is due to relatively small interface variations in the diffusive-convective regime compared to the salt-finger regime (Radko, 2013) and can be explained as follows: When a too large density difference is applied, the relatively small density gradients in the interfaces of the diffusive-convective regime are detected as mixed layers by the algorithm. Consequently, multiple mixed layers can be identified as a single mixed layer. However, if the applied density difference is too small, this could result in the detection of multiple mixed layers per staircase step.

The last input parameter of the detection algorithm concerns the interface height (Fig. 5.8d). As expected from Fig. 5.5b, variations of this input parameter do not result in large differences in the number of detected interfaces. If we omit this input parameter by setting it to infinity, we obtain a total increase of detected
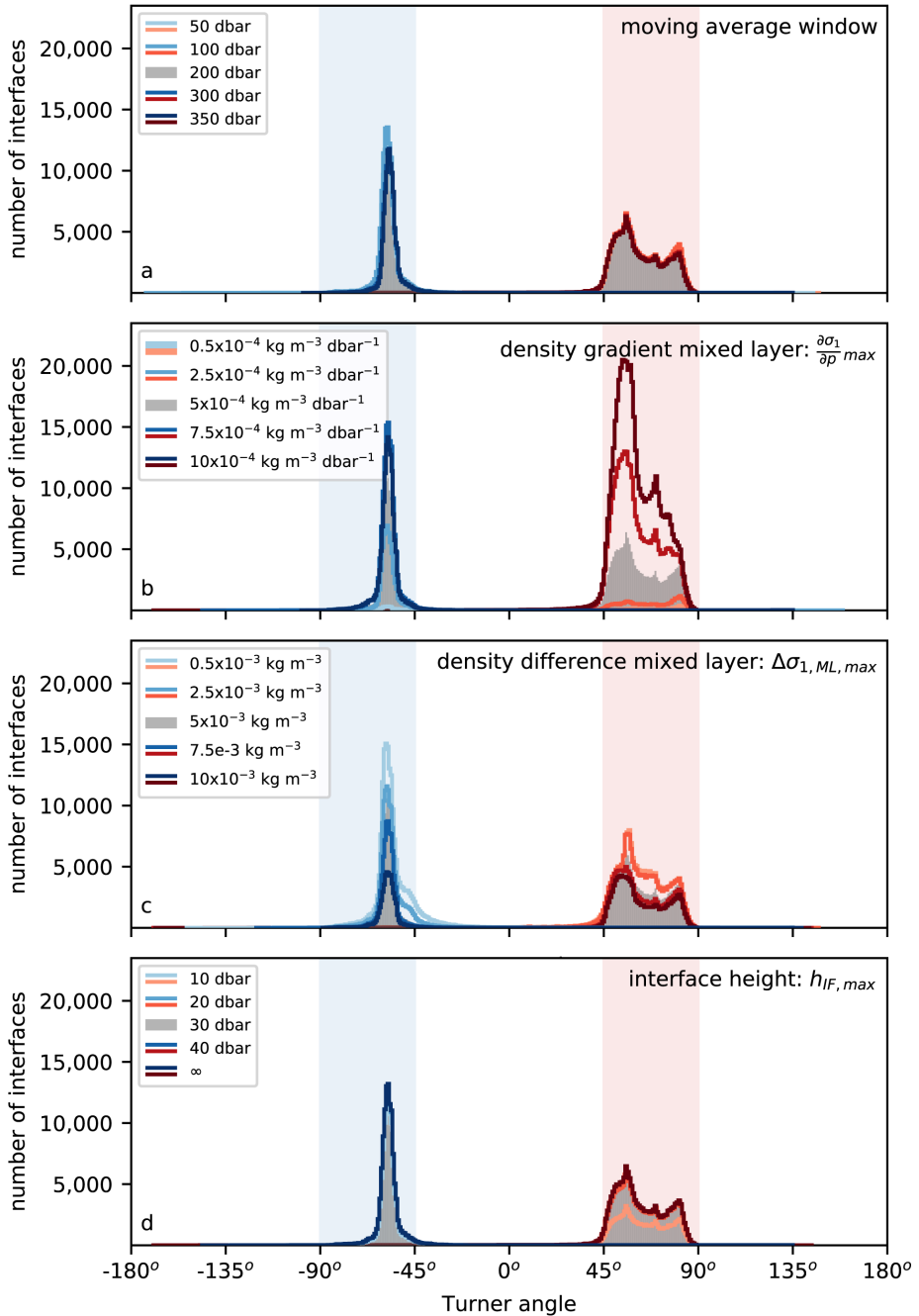
Figure 5.8: Number of detected interfaces obtained with the detection algorithm for different input parameters. Each sub-panel shows the sensitivity of the algorithm to one input parameter: (a) moving average window, (b) density gradient of the mixed layer, (c) density difference within the mixed layer and (d) the maximum height of the interface. The grey histograms correspond to the default parameters (Table 5.2). The colored lines correspond to the varying parameter. Shaded regions indicate Turner angles in the diffusive-convective (blue) and salt-finger (red) regime.

interfaces of 17 %.

Overall, the detection algorithm gives robust results as it predominantly detects interfaces within the double-diffusive regime (Fig. 5.8). In line with expectations, the detection algorithm is most sensitive to the threshold value for the maximum density gradient in the mixed layer and the density variations within the mixed layers. The four input variables allow for optimization of the detection algorithm based on the regime and characteristics of the staircases.

5.5   Regional verification

The characteristics of thermohaline staircases obtained with the detection algorithm are compared to those obtained from previous observational studies for three major staircase regions: the Canada Basin in the Arctic Ocean, the Mediterranean Sea, and the C-SALT region in the tropical Atlantic Ocean. An overview is given in Table 5.3.

In the Canada Basin (135°W-145°W, 75°N-80°N), the algorithm detects thermohaline staircases in the diffusive-convective regime in 90 % of the profiles (Table 5.3). Both the occurrence and depth range are comparable to what was reported by Timmermans et al. (2008) and Shibley et al. (2017), who analyzed thermohaline staircases from several Ice-Tethered Profilers, demonstrating that our detection algorithm indeed detects thermohaline staircases at the right location. Microstructure observations suggested that the thermohaline staircases in Canada Basin have interfaces heights of approximately $h_{IF} = 0.15$ m (Padman and Dillon, 1987; Radko, 2013). Due to the vertical resolution of the profiles and the design of the algorithm (recall that the mixed layers are separated from each other by removing the upper and lower datapoint of the mixed layer, Section 5.3.1), the method is not capable of detecting very thin interfaces (Supplementary Figure 5.9). As expected from these limitations for the detection of the interface heights, the algorithm detects conservative temperature and absolute salinity steps (ΔT_{IF} and ΔS_{IF}, respectively) in the gradients layers that are in the upper ranges of earlier observations (Padman and Dillon, 1987; Timmermans et al., 2003, 2008; Shibley et al., 2017).

In the Mediterranean Sea, thermohaline staircases are characterized by relatively thick mixed layers that are separated by thick interfaces of up to 27 m (Zodiatis and Gasparini, 1996). In this region (0°E-15°E, 30°N-43°N), the detection algorithm detected thermohaline staircases with interfaces up to 21 dbar in 6 % of the profiles, which is comparable to previous observations (Table 5.3). An example of the detection of a Mediterranean staircase is shown in Supplementary Figure 5.10. We find that the depth at which the thermohaline staircases occur is underestimated by the detection algorithm. This could be explained by the fact that most Mediterranean observations are obtained by the Coriolis DAC (Fig. 5.1a). From this DAC, approximately 50 % of the profiles have observations that are deeper than 1000 dbar (Fig. 5.1b), which means that the coverage

Table 5.3: Statistics of thermohaline staircases in Canada Basin (135°W-145°W, 75°N-80°N), Mediterranean Sea (0°E-15°E, 30°N-43°N), North Atlantic Ocean (53°W-58°W, 10°N-15°N). The observations techniques indicate Argo floats (Argo), Ice Tethered Profilers (ITP), Conductivity Temperature Depth measurements (CTD). The regime of the thermohaline staircases is indicated by DC (diffusive convection) and SF (salt finger) with the occurrence between brackets. The obtained variables of the global dataset are indicated with the 2.5 and 97.5-percentile.

	technique	type	depth range (dbar)	ΔT_{IF} (°C)	ΔS_{IF} (g kg^{-1})	h_{IF} (dbar)
Canada Basin:						
global dataset	ITP+Argo	DC (90 %)	263 - 448	0.007 - 0.1	0.003 - 0.04	2 - 9
Padman and Dillon (1987)	CTD+MS (100)	DC (100 %)	320 - 430	0.004 - 0.013	0.0016 - 0.0049	0.15
Timmermans et al. (2003)	CTD (15)	DC	2400-2900	0.001 - 0.005	0.0035 - 0.0045	2 - 16
Timmermans et al. (2008)	ITP (6,400)	DC (96 %)	200 - 300	0.04	0.014	
Shibley et al. (2017)	ITP (15,800)	DC (80 %)		0.04±0.01	0.01 ±0.003	< 1 m
Mediterranean Sea:						
global dataset	ITP+Argo	SF (6 %)	287 - 866	0.0097 - 0.12	0.0017 - 0.031	3 - 21
Zodiatis and Gasparini (1996)	CTD	SF	600 - 2500	0.04 - 0.17	0.01 - 0.04	2 - 27
Bryden et al. (2014)	CTD	SF (32 %)	600 - 1400	0.03 - 0.13	0.009 - 0.03	5 - 16
Buffett et al. (2017)	seismic imaging	SF	550 - 1200			
Durante et al. (2019)	CTD (21 profiles)	SF	500 - 2500	approx. 0.15		4 - 17
North Atlantic Ocean:						
global dataset	ITP + Argo	SF (60 %)	265 - 837	0.019 - 0.97	0.0014 - 0.16	3 - 18
Schmitt et al. (1987)	CTD+MS	SF	180 - 650	0.5 - 0.8	0.1 - 0.2 psu	1 - 10
Schmitt (2005)	CTD+MS	SF	200 - 600	<1		0.5 - 5
Fer et al. (2010)	Seismic imaging	SF	550 - 700			

below 1000 dbar is limited in the Mediterranean Sea. Although the Argo floats, and consequently the detection algorithm, do not cover the full extent of the staircases (Fig. 5.1), the conservative temperature and absolute salinity steps that are found are similar to previous observations (Table 5.3). Note that the conservative temperature and absolute salinity steps of the staircases increase with depth (Zodiatis and Gasparini, 1996), which explains why the conservative temperature and absolute salinity steps detected by the algorithm are slightly smaller than those observed in the deeper observations (Zodiatis and Gasparini, 1996; Durante et al., 2019).

In the C-SALT region in the western tropical North Atlantic Ocean (53°W-58°W, 10°N-15°N), the algorithm detected thermohaline staircases in the salt-finger regime in 60 % of the profiles (Table 5.3). Similar to previous studies (Schmitt et al., 1987; Schmitt, 2005; Fer et al., 2010), the algorithm detected thermohaline staircases on the main thermocline (see example in Supplementary Fig. 5.11). Again, the interface height is slightly overestimated by the detection algorithm, but the algorithm obtained conservative temperature and absolute salinity steps comparable to previous studies.

Overall, the comparison between the outcomes of the detection algorithm with previous studies indicates that the detection algorithm performs well. The small overestimation of the interface height can be attributed to the limited vertical resolution and the limitation imposed by the detection algorithm to avoid detection of false positives. Despite this overestimation, the interfaces are detected at the correct depths with conservative temperature and absolute salinity steps within realistic ranges. Therefore, we conclude that the detection algorithm is very suitable for the automated detection of thermohaline staircases in large and quickly growing datasets like the Argo float and Ice-Tethered Profilers data.

5.6 Conclusions

In this study, we presented an algorithm to automatically detect thermohaline staircases from Argo float profiles and Ice-Tethered Profiles. As these thermohaline staircases have different mixed layer heights and temperature and salinity steps across the interfaces in different staircase regions, the design of the detection algorithm is based on the typical vertical structure and shape of the staircases (Fig. 5.3-5.5). Note that by formulating the algorithm solely on this vertical structure of the staircases, we could use the Turner angle of the detected staircases for verification. Using this Turner angle, we showed that the structures are within the two double-diffusive regimes: the salt-finger regime and the diffusive-convective regime (Fig. 5.6).

We optimized the input of the algorithm such that it provides a global overview and limits the number of detected false positives. As a result, the regional verification in Section 5.5 indicated that the data pre-processing and data analysis have some limitations. For example, the vertical resolution of 1 dbar in the pro-

files is too course to capture all staircase steps in the Arctic Ocean. In the Mediterranean, the Argo floats did not dive deep enough to capture the full depth of the staircase region. However, the fact that (i) the algorithm detects thermohaline staircases at realistic depth ranges, with (ii) conservative temperature and absolute salinity steps across the interfaces, and in (iii) the same double-diffusive regime as previous studies (Table 5.3), indicates that the algorithm itself performs well. Therefore, when considering an individual staircase region, we recommend optimizing the input variables of the algorithm for that specific region and applying the algorithm on additional data, for example high-resolution CTD or microstructure profiles, where available.

A sensitivity analysis to different input parameters showed that the results of the detection algorithm are robust; the detected staircase interfaces are confined to the double-diffusive regimes. Furthermore, the comparison between the detected interface characteristics of thermohaline staircases in three prevailing staircase regions and previous observations, suggested that the detection algorithm accurately captures both double-diffusive regimes. The algorithm detected correct magnitudes of the conservative temperature and absolute salinity steps in the interfaces, which allows for adequate estimates of the effective diffusivity in thermohaline staircases.

The global dataset resulting from the detection algorithm contains properties and characteristics of both mixed layers and interfaces. Combined with their locations, this data allows for a statistical analysis of thermohaline staircases on global scales. For example, the global occurrence of thermohaline staircases could give insight in the contribution of double diffusion to the global mechanical energy budget. Moreover, the interface characteristics can be used to validate model and laboratory results on how double-diffusive mixing impacts the regional ocean circulation.

5.A   Example profiles with steps of the algorithm
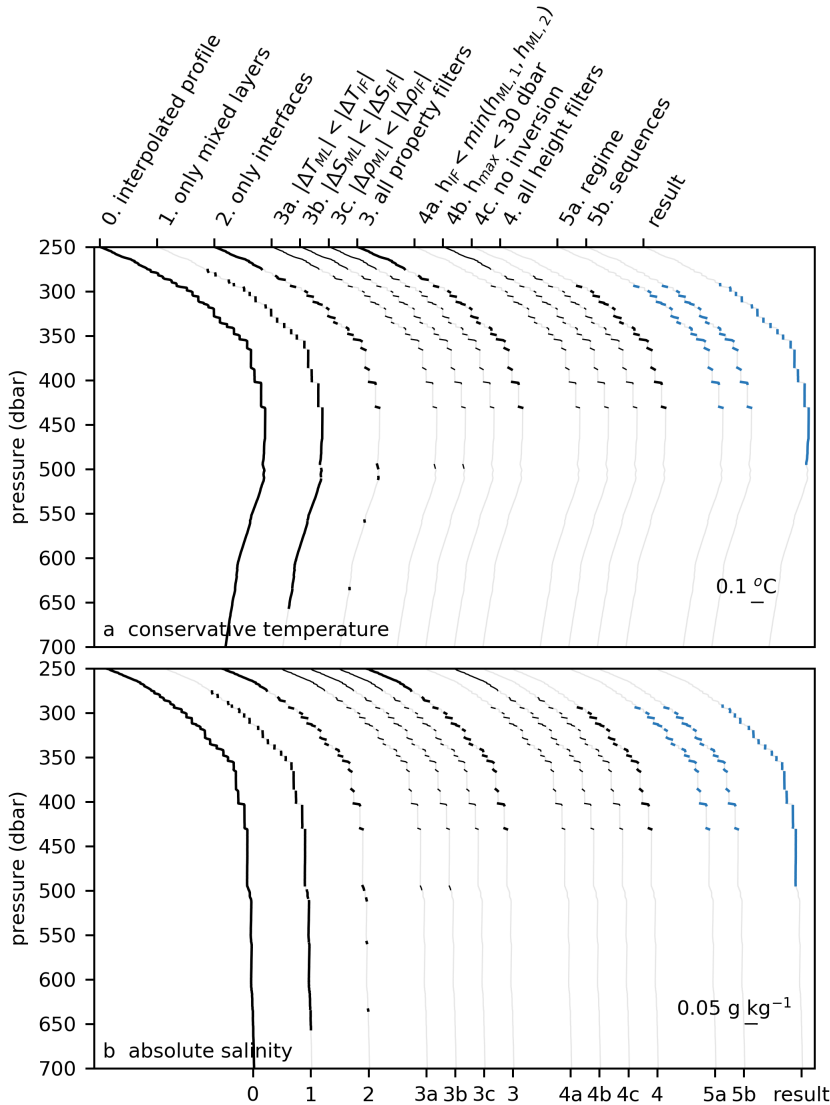
Supplementary Figure 5.9: Steps of the detection algorithm applied on a profile in the Arctic Ocean, where steps are indicated on separate (a) conservative temperature and (b) absolute salinity profiles. Each profile is shifted for clarity. Similar to Figures 5.4-5.6, an interface is not considered by the detection algorithm when the interface characteristics did not meet the requirements of a previous step. Original profile is taken from Ice-Tethered-Profiler ITP64 at 137.8°W and 75.2°N on 29 January 2013. The details of the data preparation and the algorithm steps are discussed in Section 5.2 and Section 5.3, respectively.
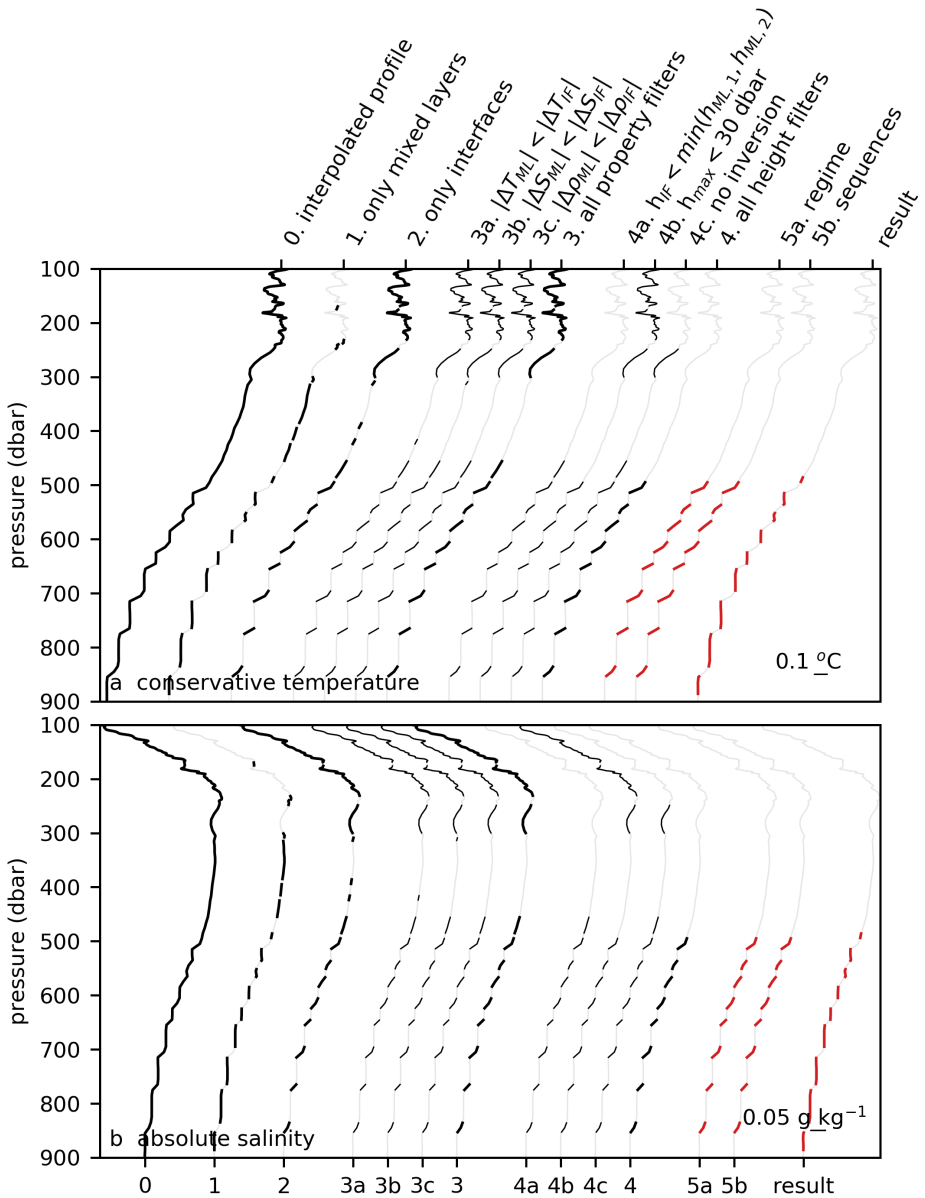
Supplementary Figure 5.10: as Supplementary Figure 5.9, but for a profile in the Mediter-
ranean Sea. Original profile is taken from Argo float 6901769 at 8.9°E and 37.9°N on 31
October 2017.
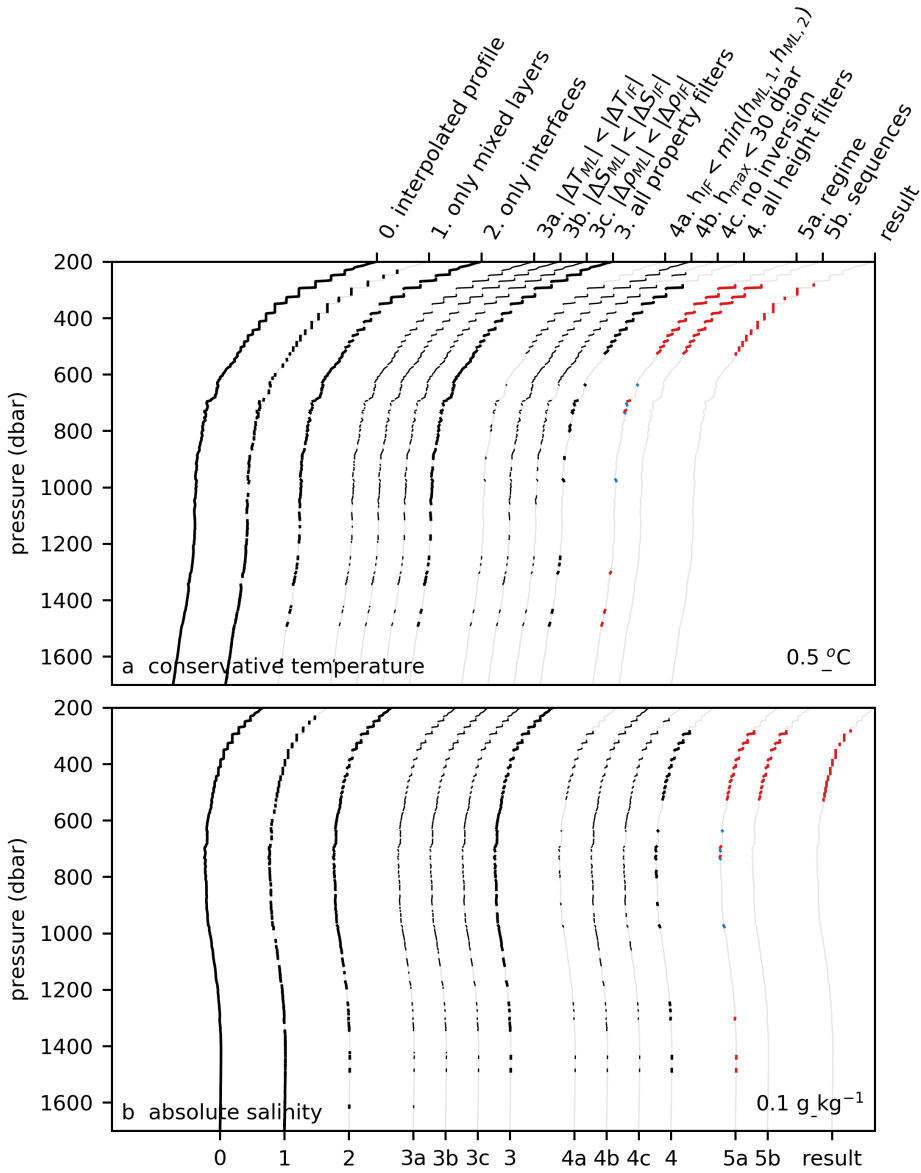
Supplementary Figure 5.11: as Supplementary Figure 5.9, but for a profile in the western tropical North Atlantic. Original profile is taken from Argo float 4901478 at 53.3°W and 11.6°N on 9 August 2014.

Supplementary Table 5.4: Metadata of all variables that are saved in the dataset.

variable	unit	description
floatID		float identification number of ITP or Argo float
lat	°E	latitude of observation
lon	°N	longitude of observation
juld	days	Julian date of observation
ct	°C	conservative temperature (full profile)
sa	g kg^{-1}	absolute salinity (full profile)
ML_{SF}		mask with mixed layers in the salt-finger regime
ML_{DC}		mask with mixed layers in the diffusive-convective regime
p_{ML}	dbar	average pressure of the mixed layer
h_{ML}	dbar	height of the mixed layer
T_{ML}	°C	average conservative temperature of mixed layer
S_{ML}	g kg^{-1}	average absolute salinity of mixed layer
Tu_{ML}	°	average Turner angle of mixed layer
R_{ML}		average density ratio of the mixed layer
h_{IF}	dbar	height of the interface
Tu_{IF}	°	Turner angle at the center of the interface
R_{IF}		density ratio at the center of the interface
ΔT_{IF}	°C	conservative temperature difference within the interface
ΔS_{IF}	g kg^{-1}	absolute salinity difference within the interface

Chapter 6

Double-diffusive mixing makes a small contribution to the global ocean circulation

Abstract

Double-diffusive processes enhance diapycnal mixing of heat and salt in the open ocean. However, observationally-based evidence of the effects of double-diffusive mixing on the global ocean circulation is lacking. Here we analyze the occurrence of double-diffusive thermohaline staircases in a dataset containing over 480,000 temperature and salinity profiles from Argo floats and Ice-Tethered Profilers. We show that about 14 % of all profiles contains thermohaline staircases that appear clustered in specific regions, with one hitherto unknown cluster overlying the westward flowing waters of the Tasman Leakage. We estimate the combined contribution of double-diffusive fluxes in all thermohaline staircases to the global ocean's mechanical energy budget as 7.5 GW [0.1 GW; 32.8 GW]). This is small compared to the estimated energy required to maintain the observed ocean stratification of roughly 2 TW. Nevertheless, we suggest that the regional effects, for example near Australia, could be pronounced.

6.1   Introduction

Double diffusion arises in the ocean when either the temperature- or salinity-induced stratification is statically unstable, while the overall density stratification is statically stable (Stern, 1960). Two regimes of double diffusion are distinguished: the salt-finger regime characterized by a destabilizing salinity stratification, and the diffusive-convective regime with a destabilizing temperature stratification. The release of potential energy stored in the stratification of the unstable component drives the double-diffusive mixing, resulting in a counter-gradient buoyancy flux that restratifies the water column (Radko, 2013). Another aspect typical for double-diffusive mixing is an inequality between the density components of the resulting vertical salt and heat fluxes; the density flux ratio $\gamma = F_T/F_S \neq 1$, where F_T is the vertical heat flux and F_S is the vertical salt flux (Schmitt, 1979).

Ocean general circulation models that incorporate parameterizations of double-diffusive mixing indicate that it induces a weakening of the ocean's meridional overturning circulation (Gargett and Holloway, 1992; Merryfield et al., 1999; Oschlies et al., 2003). This decrease could either arise from the counter-gradient diapycnal mixing or from the modification of water masses through the differential vertical fluxes of heat and salt. First, the diapycnal mixing caused by double diffusion contributes to the mechanical energy budget in the deep ocean. In total, approximately 2 TW is required to maintain the abyssal stratification (Munk, 1966; Munk and Wunsch, 1998; Ferrari and Wunsch, 2009). Double-diffusive mixing can occur in the open ocean and enhances interior mixing locally (Radko, 2013). However, the magnitude of its resulting contribution to the global mechanical energy budget is so far unknown.

Second, observations indicate that the double-diffusive vertical fluxes of heat and salt could modify oceanic properties (Johnson and Kearney, 2009; Schroeder et al., 2016). For example, the waters in the southern Indian Ocean became more susceptible to double diffusion over the last decades (Johnson and Kearney, 2009). Observations (Johnson and Kearney, 2009) indicated that this could lead to stronger double-diffusive fluxes, which in turn provides an explanation for the observed changes in the water masses in this period. Also in the Mediterranean Sea the vertical transport of heat and salt between the Levantine Intermediate Water and Mediterranean Deep Water seems to be dominated by double-diffusive fluxes (Zodiatis and Gasparini, 1996). Over the past decades, these fluxes increased the salinity of the Mediterranean Deep Water, which in turn affected the salt and heat input into the Atlantic Ocean (Schroeder et al., 2016). Furthermore, due to the inequality of the strength of the vertical heat and salt fluxes associated with double diffusion, it is thought to be the major consumer of spiciness in the ocean (Schmitt, 1999; Chassignet and Verron, 1998).

Although many studies have highlighted the importance of double-diffusive mixing in the ocean, an observationally-based analysis of the impact of these processes on the global ocean circulation is lacking. In this study, we analyze the

global distribution of thermohaline staircases, which arise from double-diffusive processes. Thermohaline staircases are stepped structures in the temperature and salinity stratification consisting of a sequence of subsurface mixed layers separated by thin interfaces with sharp temperature and salinity gradients. The mixed-layer heights of thermohaline staircases range from several meters in the Arctic Ocean (Timmermans et al., 2008; Shibley et al., 2017) to several hundreds of meters in the Tyrrhenian Sea and Black Sea (Radko, 2013). In contrast to the microstructure of the double-diffusive mixing itself, the vertical length scales of the mixed layers of thermohaline staircases are larger so that they can be captured by Argo floats and Ice-Tethered Profilers (Schmitt, 2005; Guthrie et al., 2017, see Section 6.2). Based on our global distribution of thermohaline staircases (Chapter 5 of this thesis), we compute the effective diffusivity of heat and salt in each step of a thermohaline staircase and use that to quantify the total contribution of double-diffusive mixing to the global mechanical energy budget.

6.2 Methods

We use the global dataset of thermohaline staircases that is obtained with an algorithm to automatically detect these structures (Chapter 5 of this thesis). In short, the staircase detection algorithm is applied on vertical temperature and salinity profiles obtained from Ice-Tethered Profilers and Argo Floats between 13 November 2001 and 14 May 2020. The data is obtained from http://www.whoi.edu/itp and http://www.argo.ucsd.edu for the Ice-Tethered Profilers and Argo floats, respectively. The average coverage is $1.4{\times}10^{-3}$ observations in km^{-2} ($A_{ocean} \approx 3.6{\times}10^8$ km^{-2}), with the highest observation density of 2.5 km^{-2} in the Arctic Ocean (83°N and 99°W), and smallest observation density in the centers of the subtropical gyres (Fig. 5.2). This variation in data coverage results in a (small) overestimate of the occurrence of diffusive-convective staircases as these predominantly occur at high latitudes. Moreover, the Arctic Ice-Tethered Profilers generally follow the ice floe and not the flow at the depth of the staircase, which results in a randomized field of staircase observations in this region. After a quality control, profiles that have an average resolution exceeding 5 dbar and contain observations below 500 dbar are selected, which results in a dataset consisting of 487,493 profiles. Their average vertical resolution is relatively high (finer than 2.5 dbar) in the upper 1000 m of the water column (Chapter 5 of this thesis), where most thermohaline staircases are found (Radko, 2013). Deeper in the water column, the average vertical resolution of the profiles is approximately 2.5 dbar. Afterwards, the profiles are subsequently linearly interpolated from 0-2000 dbar with a vertical resolution of 1 dbar. The algorithm itself consists of five steps that detect sequences of interfaces in each temperature and salinity profile:

1. Mixed layers are identified by selecting layers with density gradients below $5{\times}10^{-4}$ kg m^{-3} dbar^{-1}. Where this criterion is met, the mixed layers are defined as the layer within a density interval of $5{\times}10^{-3}$ kg m^{-3}.

2. The interfaces, defined as the layers between these mixed layers, should have larger temperature, salinity and density variations than those found within the adjacent mixed layers.

3. The interfaces are required to be thinner than the adjacent mixed layers, and the maximum interface thickness is limited to 30 dbar. Furthermore, interfaces are required to contain no temperature or salinity inversion.

4. The double-diffusive regime of each interface is determined: When the temperature and salinity of a mixed layer below an interface are higher (lower) than the temperature and salinity of the mixed layer directly above, the regime of the interface is classified as diffusive-convective (salt-finger) regime.

5. Sequences of interfaces that are of the same double-diffusive regime are detected; each sequence of interfaces consisting of more than one step (>2 mixed layers) is classified as a thermohaline staircase.

A detailed description of the algorithm to obtain this dataset and tests of its robustness can be found in Chapter 5 of this thesis. A sensitivity test performed for the chosen input parameters of the detection algorithm shows robust results (Chapter 5 of this thesis). As an example, the sensitivity of the occurrence of thermohaline staircases to the value of the mixed layer criterion (step 1 of the algorithm) is shown in Fig. 6.1. It clearly shows that while it affects the number of detected steps, the same spatial pattern emerges. Due to the vertical resolution of the observations and the linear interpolation by the algorithm, it cannot detect very thin interfaces (Chapter 5 of this thesis). This particularly plays a role for staircases in the diffusive-convective regime in the Arctic Ocean, where interfaces can be as thin as 0.1 m (Padman and Dillon, 1987; Radko, 2013). The minimum layer height that can be detected by the algorithm is 2 dbar (Chapter 5 of this thesis). Consequently, the smallest interfaces are missed by the algorithm and the average temperature and salinity steps in the diffusive-convective interfaces are overestimated (Chapter 5 of this thesis). However, the algorithm detects an accurate staircase occurrence for staircases in the diffusive-convective regime (n^{DC}) in this region (Chapter 5 of this thesis). Because thermohaline staircases in the salt-finger regime have larger vertical length scales and are therefore more easily detected by the algorithm, the staircase occurrence for staircases in the salt finger regime (n^{SF}) is also considered reliable.

At each staircase interface, the effective diffusivities of heat (K_T), salt (K_S) and buoyancy (K_ρ) are computed. Taking into account that the detection algorithm mainly detects interfaces that arise from double-diffusive mixing (Chapter 5 of this thesis), we assume that all detected interfaces result from either diffusive convection (DC) or from salt fingering (SF). To limit detection of thermohaline intrusions, the detection algorithm only detects sequences of interfaces within the same regime (step 5 of the algorithm) as intrusions induce interfaces that alternate in both different regimes (Bebieva and Timmermans, 2017). Although it is
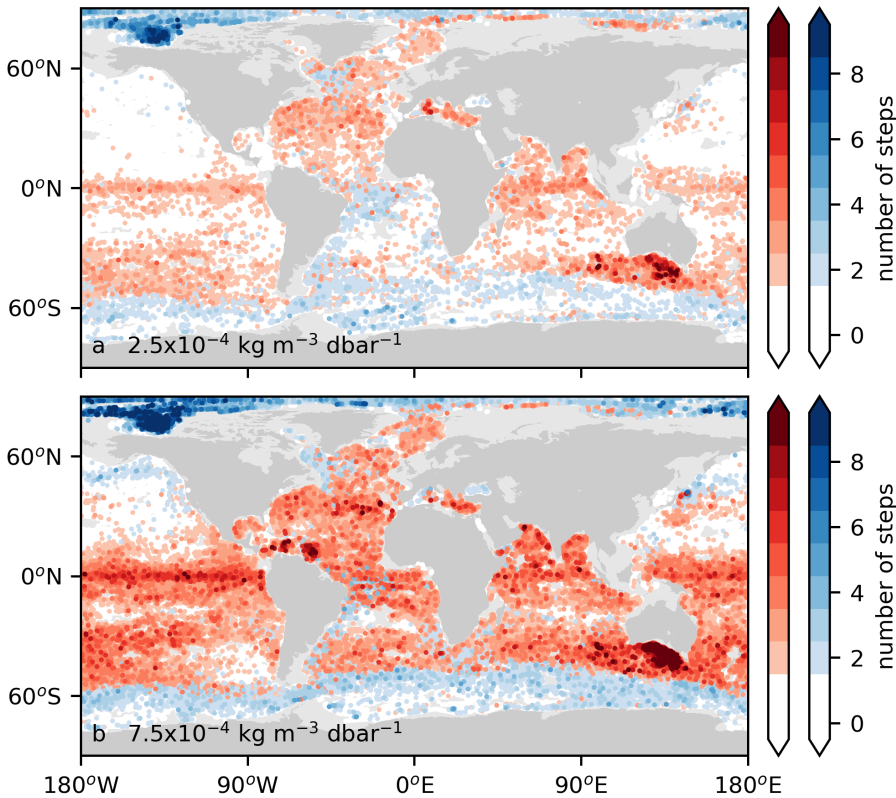
Figure 6.1: Sensitivity of the number of staircases detected resulting for different input parameters of the staircase detection algorithm (Chapter 5 of this thesis). (a) $\partial\sigma_1/\partial p_{max} = 2.5\text{x}10^{-4}$ kg m^{-3} dbar^{-1} (b) $\partial\sigma_1/\partial p_{max} = 7.5\text{x}10^{-4}$ kg m^{-3} dbar^{-1}. For each profile, the number of steps per staircase in the salt-finger regime (red dots) and diffusive-convective regime (blue dots) is plotted. Profiles with the largest numbers are plotted last for clarity. Figure 6.2 shows the same for the standard value of $\partial\sigma_1/\partial p_{max} = 5.0\text{x}10^{-4}$ kg m^{-3} dbar^{-1}

expected that such intrusions have a limited impact on the results, the detection of thermohaline intrusions could result in an underestimation of the computed fluxes through an interface by 50 % (Bebieva and Timmermans, 2017).

To compute the effective diffusivities in the diffusive-convective regime, we apply a similar flux law (Turner, 1965). Although empirical evidence suggests that it is reasonable to extrapolate these flux laws to the oceanic environment, uncertainties do exist about the magnitude of most variables within these flux laws (Kelley et al., 2003). In general, the flux laws proposed by Kelley (1990) agree well with observations (Robertson et al., 1995; Timmermans et al., 2008; Shibley et al., 2017); we therefore choose to apply these in this study. However, it should be noted that there are some indications, mainly from numerical simulations, that fluxes computed with these relations (Kelley, 1990) could un-

derestimate observed heat fluxes by 50 % (Flanagan et al., 2013). Following Kelley (1990), we compute the effective diffusivity of heat:

$$K_T^{\mathrm{DC}} = 0.0032 e^{4.8 R_\rho^{0.72}} \left(\frac{\alpha g \kappa}{Pr} \right)^{\frac{1}{3}} (\Delta T_{\mathrm{IF}})^{\frac{4}{3}} \left(\frac{\partial T}{\partial z} \right)^{-1}, \tag{6.1}$$

where R_ρ is the density ratio ($R_\rho = \left(\alpha \frac{\partial T}{\partial z} \right) \left(\beta \frac{\partial S}{\partial z} \right)^{-1}$, which is limited to $0 < R_\rho < 1$), κ the molecular diffusivity of heat in m^2 s^{-1}, α the thermal expansion coefficient in °C^{-1}, g the gravitational acceleration in m s^{-2}, Pr the Prantle number and ΔT_{IF} the conservative temperature difference across an interface in °C. The vertical gradients of conservative temperature are computed with a central differences scheme from temperature profiles that are smoothed with a 50 dbar moving average. Recall that the average magnitude of the temperature differences across the interfaces is overestimated by the algorithm (Chapter 5 of this thesis). Therefore, the effective diffusivity should be considered as an upper bound. We convert the effective diffusivity of heat to heat fluxes (F_H) as: $F_H = \rho c_p K_T^{\mathrm{DC}} \frac{\partial T}{\partial z}$, where ρ is a reference density and c_p the specific heat of seawater. The effective diffusivity of salt follows from the effective diffusivity of heat in combination with the flux ratio γ:

$$K_S^{\mathrm{DC}} = K_T^{\mathrm{DC}} \frac{R_\rho}{\gamma^{\mathrm{DC}}}, \tag{6.2}$$

where the density flux ratio (γ) computed following Kelley (1990) as:

$$\gamma^{\mathrm{DC}} = \left(\frac{R_\rho^{-1} + 1.4 \left(R_\rho^{-1} - 1 \right)^{\frac{3}{2}}}{1 + 14 \left(R_\rho^{-1} \right)^{\frac{3}{2}}} \right)^{-1}. \tag{6.3}$$

In contrast to the diffusive convection, the flux laws cannot be extrapolated to oceanic environments for thermohaline staircases in the salt-finger regime, as they are known to lead to a significant overestimation of the effective diffusivities (Taylor and Veronis, 1996; Kelley et al., 2003; Radko, 2005, 2013). Therefore, we use an empirical estimate (Radko and Smith, 2012) to compute the effective diffusivities of salt and heat instead:

$$K_S^{\mathrm{SF}} = \left(\frac{135}{\left(R_\rho - 1 \right)^{\frac{1}{2}}} - 62.75 \right) \kappa R_\rho, \tag{6.4}$$

with a density ratio limit of $1 < R_\rho < 10$. The effective diffusivity of heat is computed as follows:

$$K_T^{\mathrm{SF}} = K_S^{\mathrm{SF}} \frac{\gamma^{\mathrm{SF}}}{R_\rho}, \tag{6.5}$$

where γ^{SF} is computed as $\gamma^{\mathrm{SF}} = 2.709 e^{-2.513 R_\rho} + 0.5128$ (Radko and Smith, 2012). Note that, in contrast to the diffusive-convective regime, the effective diffusivi-

ties in the salt-finger regime do not depend on the temperature or salinity jumps across the interfaces. A comparison of our results to tracer-based oceanic observations in the western tropical Atlantic Ocean obtained by Schmitt (2005) indicates that we obtained lower effective diffusivities than found in these observations (Fig. 6.3). However, because these observations most likely also include mixing in the vicinity of topography, these high estimates are most likely a combination of double-diffusive mixing and turbulent mixing. Finally, the effective diffusivity of buoyancy is computed separately for both regimes from the combined effective diffusivities of heat and salt:

$$K_\rho = -K_T \frac{1 - \gamma^{-1}}{R_\rho^{-1} - 1},$$

(6.6)

where γ is the flux ratio.

6.3 Results

6.3.1 The global distribution of thermohaline staircases

The global distribution of thermohaline staircases obtained using the methods outlined in Section 6.2, indicates that thermohaline staircases are formed in specific regions depending on regional water-mass characteristics (Fig. 6.2). In total, the global dataset comprises 39,469 profiles with thermohaline staircases in the salt-finger regime (n^{SF} = 8.1 % of all 487,493 profiles) and 31,053 profiles with thermohaline staircases in the diffusive-convective regime (n^{DC} = 6.4 % of all profiles).

In general, thermohaline staircases in the diffusive-convective regime occur at high latitudes where fresh and cold surface waters overlie warmer and more saline waters. Especially the Canada Basin that is located within the Arctic Ocean is known for its persistent occurrence of thermohaline staircases (Timmermans et al., 2008; Shibley et al., 2017). There, thermohaline staircases with a high number of steps are observed (dark blue areas in Fig. 6.2). Previous studies estimated the double-diffusive upward heat transport at 0.004-0.3 W m^{-2}, which is an order of magnitude smaller than the mean surface mixed layer heat flux (Padman and Dillon, 1989; Timmermans et al., 2008). In line with this estimate, we find an upper bound of the average heat fluxes of 0.5 W m^{-2} (at 135°W-145°W, 75°N-80°N, Fig. 6.3a). Besides the Canada Basin, other regions in the Arctic Ocean and Southern Ocean also reveal the presence of thermohaline staircases in the diffusive-convective regime (Muench et al., 1990; Polyakov et al., 2012; Bebieva and Timmermans, 2019; Bebieva and Speer, 2019).

At lower latitudes, double diffusion is predominantly in the salt-finger regime (red in Fig. 6.2). Using the automated detection algorithm, we identify thermohaline staircases in all well-known formation regions: in the western tropical Atlantic Ocean (Schmitt, 2005; Schmitt et al., 1987), the Caribbean Sea (Merry-
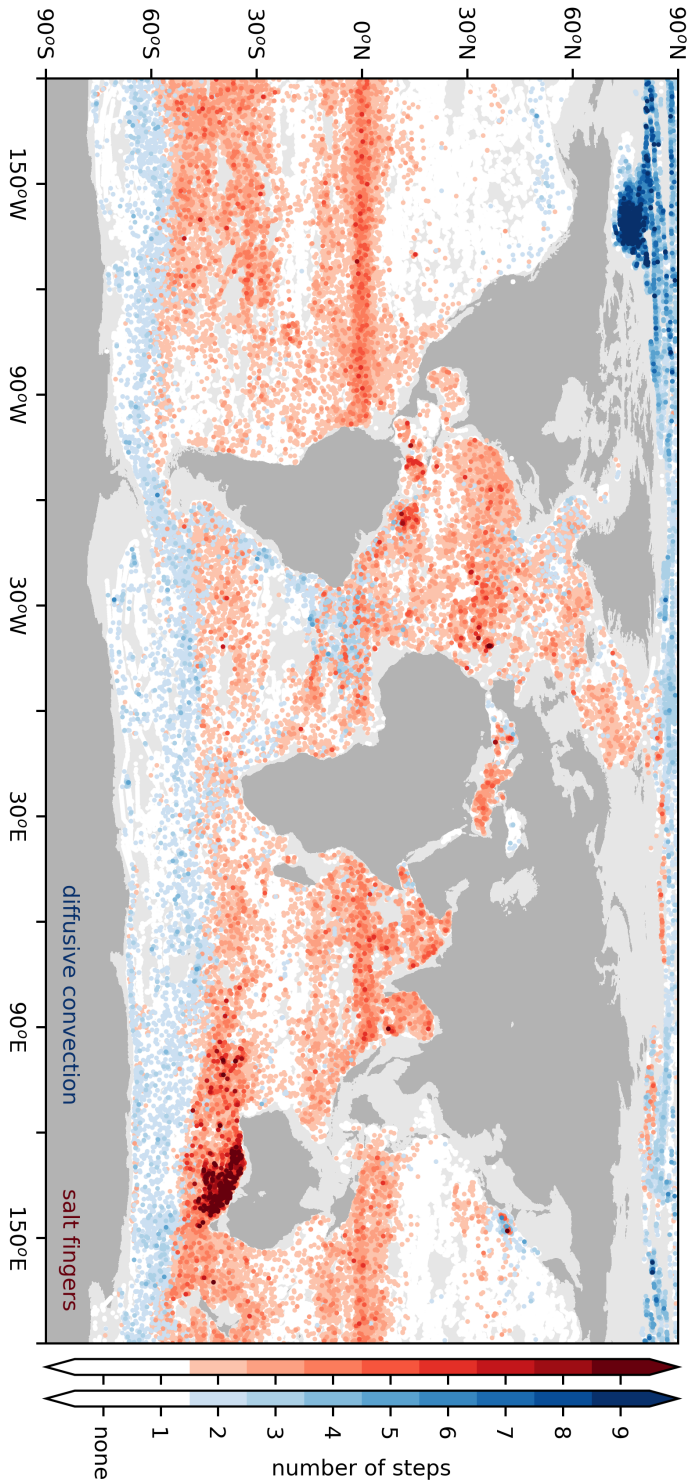
Figure 6.2: Global distribution of the occurrence of thermohaline staircases based on global dataset of Argo floats and Ice-Tethered Profiles using the detection algorithm (Chapter 5 of this thesis). For each profile, the number of steps within thermohaline staircases in the salt-finger regime (red dots) and diffusive-convective regime (blue dots) is plotted. Profiles with the largest numbers of steps are plotted last for clarity.
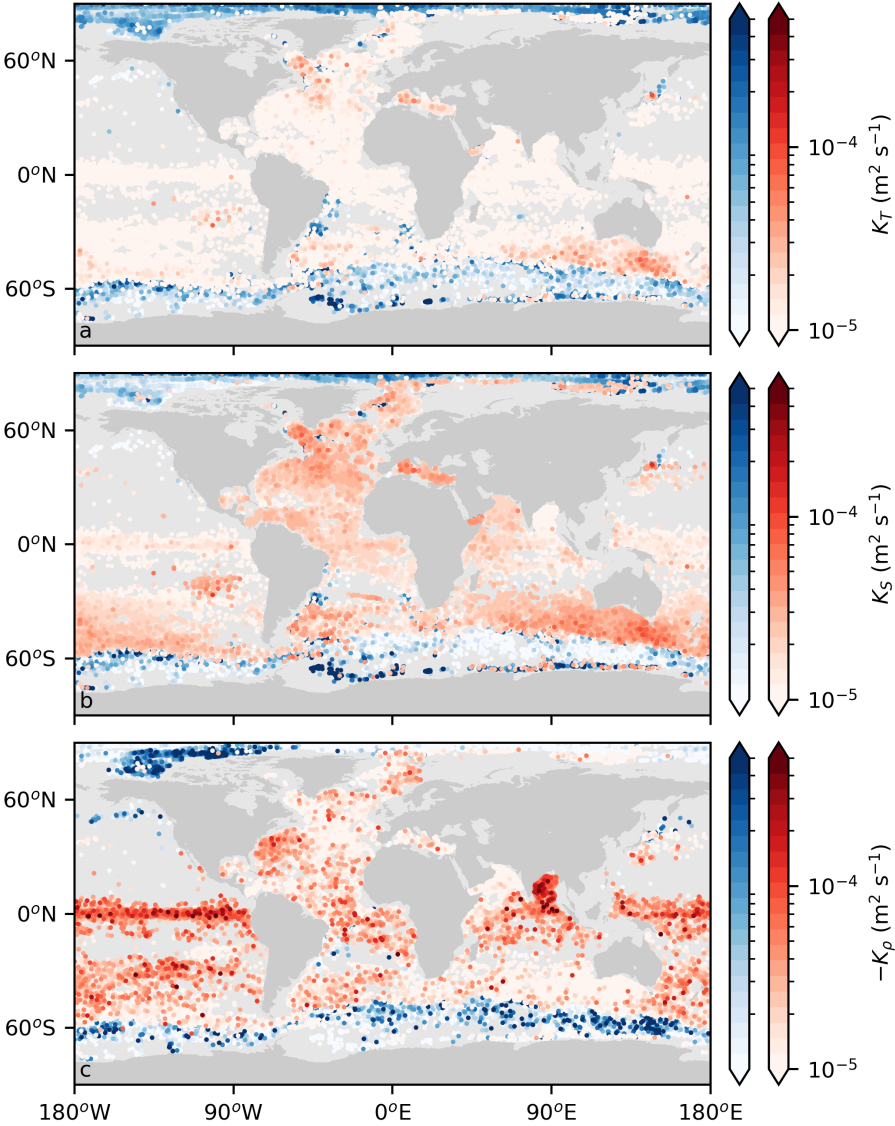
Figure 6.3: Effective diffusivities (per profile) computed in each profile with a thermohaline staircase. For each profile, the average diffusivities per staircase in the salt-finger regime (red dots) and diffusive-convective regime (blue dots) are plotted. Panels show the average effective diffusivity of (a) heat (K_T) and (b) salt (K_S) and (c) buoyancy (K_ρ) per profile.

field, 2000, Chapter 2 of this thesis), below the Mediterranean outflow (Tait and Howe, 1971), within the Mediterranean Sea (Zodiatis and Gasparini, 1996; Durante et al., 2019) and along the equator (Lee et al., 2014). These thermohaline staircases have, in general, thicker mixed layers and interfaces than staircases in the diffusive-convective regime (Radko, 2013), which allows for more accurate estimates of the temperature and salinity steps across interfaces (Chapter 5 of this thesis). Using a previous empirical estimate (Radko and Smith, 2012), we obtain an average effective diffusivity of salt of $K_S^{SF} = 1.92 \times 10^{-5}$ m^2 s^{-1} [2.5×10^{-7} m^2 s^{-1}; 1.0×10^{-4} m^2 s^{-1}], where the values between brackets correspond to the 2.5 and 97.5 percentile ranges (Fig. 6.3b).

Besides these well-known regions with thermohaline staircases, the global analysis presented here also reveals a newly-discovered staircase region in the Great Australian Bight (Fig. 6.2, Fig. 6.4a,b). There, the warm and saline Subtropical Surface Water overlies the cold and fresh Antarctic Intermediate Water (Fig. 6.4a,b). This interface is susceptible to double-diffusive mixing with Turner angles varying between $45° <$Tu$< 90°$ (Ruddick, 1983). As expected the mixed layers of the staircases are located at this interface (Fig. 6.4c). Thermohaline staircases appear abundant in this region (32°S-42°S, 125°E-145°E): in total, 62% of the 2,241 profiles contain staircases (Fig. 6.4d). The alignment of the temperature and salinity data of each mixed layer (alignment in Fig. 6.4e) indicates that the mixed layer properties and vertical structure of the staircases are similar across multiple profiles. To gain insight in the lateral coherence of these similarities of the properties, we quantify using the aligned data points as an example (red dots in Fig. 6.4e). We obtain a lateral coherence over a region of several hundreds of kilometers that persisted for almost 2 years, which is similar to what is seen in other major staircase regions (Schmitt et al., 1987; Timmermans et al., 2008). The slopes of these aligned points correspond to the density flux ratio and confirm a downward salt and heat transport within the thermohaline staircases ($\gamma^{SF} < 1$).

Part of Antarctic Intermediate Water in the Great Australian Bight, known as Tasman Leakage (Speich et al., 2002), propagates westward towards the Agulhas region through the southern Indian Ocean (Drijfhout, 2005; Speich et al., 2007). Our results show that thermohaline staircases occur over the entire southern Indian Ocean (Fig. 6.2, red histograms in Fig. 6.5a) and that the characteristics of the thermohaline staircases change from east to west. In the east, the thermohaline staircases found contain more steps (Fig. 6.5b). However, the part of the water column that is susceptible to strong salt-fingering ($71.6° <$Tu$< 90°$ or $R_\rho >2$, depths between thick white contour in Fig. 6.5a) (Ruddick, 1983) is relatively constant from east to west. This illustrates that strong salt fingering most likely occurs along this cross-section in the southern Indian Ocean.
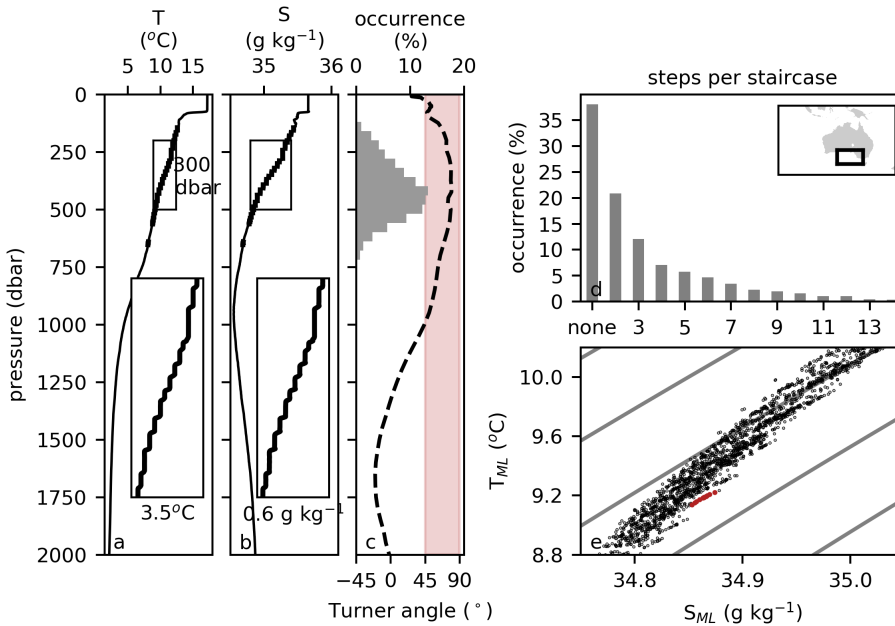
Figure 6.4: Properties of thermohaline staircases in the Great Australian Bight (32°S-42°S, 125°E-145°E). (a) Example temperature and (b) salinity profile with a thermohaline staircase obtained by an Argo float (float-id: 5905189) at 37.6°S, 135.1°E on 8 April 2019. The inlays show a zoom of the profiles between 200 and 500 dbar. (c) Distribution of mixed layers over depth (grey bars) and the average Turner angle (Ruddick, 1983) in the Great Australian Bight (dashed line). The red shading indicates Turner angles corresponding to the salt-finger regime (45° < Tu < 90°). (d) Distribution of number of steps per profile in percentage. (e) Scatter plot of the temperature and salinity of the mixed layers of the detected staircases, where red dots indicate mixed layers that are used to compute the lateral coherence. Data in panels (c), (d) and (e) is obtained between 23 April 2007 and 13 May 2020. Inlay in (d) shows the considered region.

6.3.2   Contribution to the ocean energy budget

To estimate the combined contribution of double-diffusive fluxes in thermohaline staircases to the global mechanical energy budget, we compute the average effective diffusivity of buoyancy in each detected interface based on the temperature and salinity steps between mixed layers (Radko, 2013; Nakano and Yoshida, 2019). A comparison between the characteristics of temperature and salinity steps found by the algorithm and those found in previous studies on thermohaline staircases indicated that the global dataset contains temperature and salinity steps of the correct magnitude in the salt-finger regime and provides an upper bound for steps in the double-diffusive regime (see Section 6.2). Because the density flux ratio is different in the two regimes ($\gamma^{DC} > 1$ and $\gamma^{SF} < 1$), the effective diffusivities and thus their contributions to the global mechanical energy
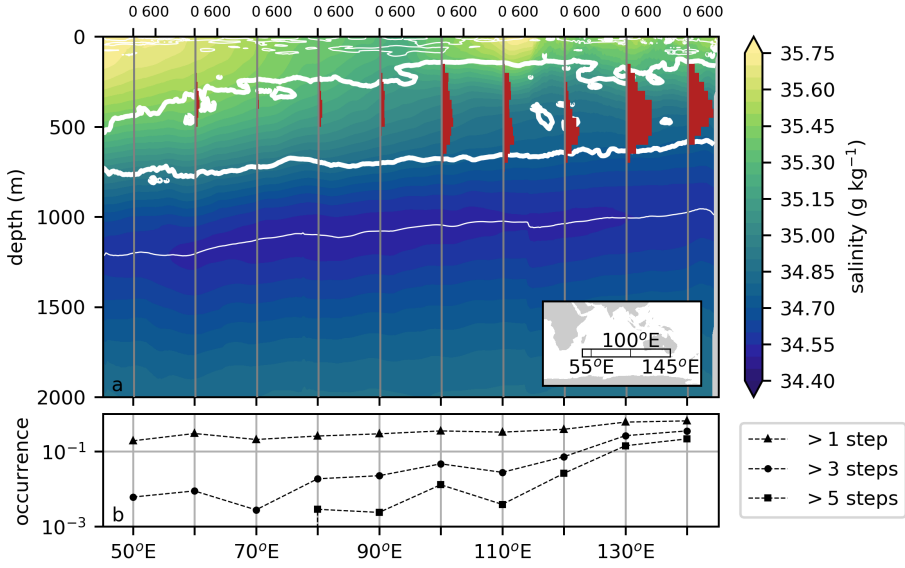
Figure 6.5: Thermohaline staircases in the southern Indian Ocean. (a) Red histograms show the vertical distribution of number of detected mixed layers in thermohaline staircases per 10 degrees longitude. The thick (thin) white contour corresponds to Turner angles (Ruddick, 1983) of Tu = 71.6° (Tu = 45°), indicating the susceptibility of the water column to double diffusion in the salt-finger regime (45° < Tu < 90°). Background shading indicates the mean vertical salinity profile obtained from the World Ocean Atlas 2018 (Zweng et al., 2019). The inlay shows the considered region: 45°E-145°E, 32°S-42°S. (b) Occurrence of number of steps per profile in per 10 degrees longitude (note the logarithmic vertical axis).

budget are computed separately.

To estimate the contribution of diffusive convection to the global mechanical energy budget, we compute the effective diffusivity of density with flux laws (Kelley, 1990) (see Section 6.2). This yields an upper bound for the average effective diffusivity of $K_\rho^{\mathrm{DC}} = -1.47 \times 10^{-5}$ m^2 s^{-1} [-7.5×10^{-5} m^2 s^{-1}; -1.6×10^{-7} m^2 s^{-1}] (Fig. 6.3c). Next, we use this effective diffusivity to compute the dissipation (D^{DC}) from Munk and Wunsch (1998), using their equation for the vertical fluxes through any depth level in the ocean:

$$D^{\mathrm{DC}} = \Gamma^{-1} K_\rho^{\mathrm{DC}} g A \Delta\rho, \qquad (6.7)$$

where Γ is the mixing efficiency. We use standard values for the gravitational acceleration (g = 9.8 m s^{-2}), area of the ocean ($A = 3.6 \times 10^{14}$ m^2) and verti-cal density difference ($\Delta\rho = 1$ kg m^{-3}) (Munk and Wunsch, 1998). The mixing efficiency of double-diffusive mixing approaches $\Gamma = -1$, because it is driven by the release of potential energy and the production term of the turbulent kinetic energy budget becomes negligible (Osborn, 1980; Radko, 2013). In equation

6.7, Munk and Wunsch (1998) assumes that the mixing in the ocean is evenly distributed. To account for the fact that thermohaline staircases do not occur everywhere (Fig. 6.2), we multiply equation 6.7 with the fraction of the staircase occurrence (n^{DC}). Moreover, because the depth of thermohaline staircases is variable (Chapter 5 of this thesis), equation 6.7 is considered as an upper bound. Using these numbers, we obtain a value of $D^{DC} = 3.3$ GW [0.0 GW; 16 GW] for dissipation by diffusive-convective thermohaline staircases.

We use a similar method to estimate the contribution of thermohaline staircases in the salt-finger regime to the dissipation (D^{SF}). However, because the flux laws based on laboratory experiments are known to overestimate salt-finger fluxes in the real ocean by an order of magnitude (Taylor and Veronis, 1996; Radko, 2005), we compute the effective diffusivity of buoyancy in the salt-finger regime based on an empirical estimate (Radko and Smith, 2012). Using this estimate (Radko and Smith, 2012), we obtain an effective diffusivity of $K_\rho^{SF} = -1.47 \times 10^{-5}$ m^2 s^{-1} [-6.2×10^{-7} m^2 s^{-1}; -5.6×10^{-5} m^2 s^{-1}], which yield a contribution of salt fingers to the global mixing energetics of $D^{SF} = 4.2$ GW [0.2 GW; 18 GW]. Similar to the dissipation obtained in the diffusive-convective regime, this should be considered as an upper bound, because the depth of the thermohaline staircases is variable.

Our estimate for the total contribution of double diffusion to the global mechanical energy budget by diffusive convection and salt fingers combined thus adds up to $D = 7.5$ GW [0.1 GW; 32.8 GW]. Due to the high mixing efficiency of double diffusion ($\Gamma = -1$) compared to turbulent mixing ($\Gamma^{turb} = 0.2$), double diffusion is able to mix five times more than down-gradient turbulence with the same amount of energy. Notably, the mixing by double diffusion restratifies the water column in contrast to the mixing by down-gradient turbulence. Consequently, double-diffusive mixing contributes to the mechanical energy necessary to maintain the stratification. Depending on its location, the double-diffusive mixing can thus either enhance the downwelling in regions with deep convection in the North Atlantic Ocean or it can prevent the upwelling at lower latitudes (Radko, 2013). This implies that a part of the double-diffusive mixing in downwelling regions is already contained in the estimates for the amount of abyssal mixing that were previously computed (Munk and Wunsch, 1998). Therefore, we conclude that the contribution of double-diffusive mixing to the global mechanical energy budget is limited.

6.4   Summary and global implications

In this study we presented a global analysis of thermohaline staircases identified in profiles of Argo floats and Ice-Tethered Profilers. The global distribution of thermohaline staircases shows that thermohaline staircases are confined to specific regions determined by the local water-mass characteristics: thermohaline staircases in the diffusive-convective regime are predominantly found at high lat-

itudes, while staircases in the salt-finger regime dominate at low latitudes. Our analysis revealed a new staircase region in the Great Australian Bight and southern Indian Ocean. Because the waters in the southern Indian Ocean are likely to become more susceptible to double-diffusive mixing (Johnson and Kearney, 2009) and previous studies showed that double-diffusive fluxes in thermohaline staircases can modify water-mass characteristics (Zodiatis and Gasparini, 1996; Schroeder et al., 2016), we speculate on the potential implications of this new staircase region.

The thermohaline staircases in the southern Indian Ocean overlie the waters of the Tasman Leakage. Because the salt content of the Tasman Leakage waters is considered to affect the stability of the Atlantic Meridional Overturning Circulation (AMOC) (Gordon, 2003; Speich et al., 2007), the double-diffusive salt fluxes in this region might impact AMOC stability. This impact can be determined qualitatively by using an indicator of AMOC stability, usually referred to M_{ov}, measuring the freshwater transport of the AMOC at 35°S in the Atlantic (Rahmstorf, 1996; de Vries and Weber, 2005; Dijkstra, 2007; Castellana et al., 2019). When $M_{ov} > 0$, the AMOC transports salt out of the Atlantic and it is less sensitive to North Atlantic surface freshwater anomalies (Rahmstorf, 1996; de Vries and Weber, 2005; Dijkstra, 2007; Castellana et al., 2019). For $M_{ov} < 0$, the AMOC imports salt and can undergo transitions to a weak AMOC state due to the positive salt advection feedback. Further research is necessary to quantify whether stronger double-diffusive salt fluxes in a future climate (Johnson and Kearney, 2009) can increase the salt content of the Tasman Leakage waters and, consequently, have a destabilizing effect on the AMOC by changing the M_{ov}.

By analyzing the occurrence and properties of the thermohaline staircases, we also estimated the impact of double-diffusive mixing in this study. Of each thermohaline staircase, we estimated the effective diffusivity of buoyancy based on both flux laws (diffusive convection, Kelley, 1990) and empirical estimates (salt fingers, Radko and Smith, 2012). Although there are some uncertainties regarding the diffusivities obtained from these computations that most likely result in an overestimation of the magnitude of these diffusivities (see Section 6.2, Flanagan et al., 2013; Bebieva and Timmermans, 2017), these computations are necessary to obtain an observationally-based estimate of the contribution of double-diffusive mixing to the global mechanical energy budget. Using these values, we estimated an upper bound of the contribution of double-diffusive mixing to the global mechanical energy budget (7.5 GW [0.1 GW; 32.8 GW]), which is relatively small (< 1 %). The robustness of these results to different input variables of the detection algorithm that was used to obtain the global dataset is confirmed by a sensitivity analysis (Table 6.1). Hence we conclude that the direct effect of double-diffusive mixing to the maintenance of the abyssal stratification is negligible.

However, the global distribution of thermohaline staircases indicated that double-diffusive mixing is widespread. This implies that in a large part of the ocean the magnitudes of the effective diffusivity of heat and salt differ from each
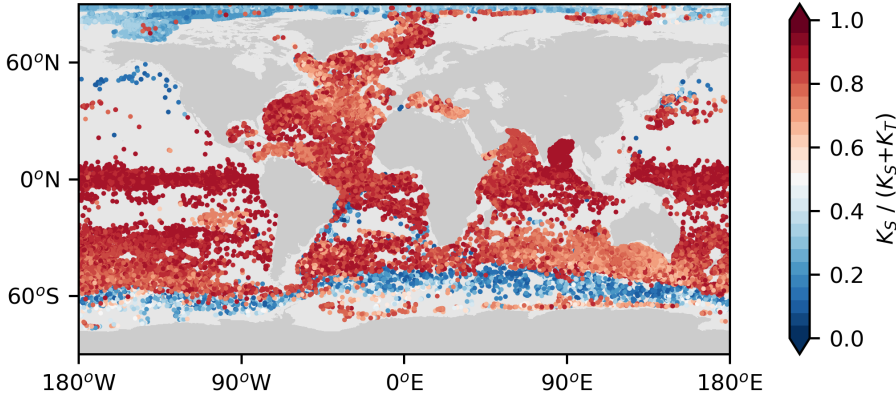
Figure 6.6: Relative magnitude of the effective diffusivity of salt compared to the combined effective diffusivities of heat and salt ($K_S/(K_S + K_T)$). Thermohaline staircases in the salt-finger regime ($K_S > K_T$) are denoted by red dots and thermohaline staircases in the diffusive convection regime ($K_T > K_S$) are denoted by blue dots

Table 6.1: Percentage of profiles with thermohaline staircases in the global dataset and dissipation computed for different input parameters of the detection algorithm (Chapter 5 of this thesis). One input variable is varied per computation compared to the standard setting (MA: moving average window; $\partial\sigma_1/\partial p_{max}$: threshold for mixed layer density gradient; $\Delta\sigma_{1,max}$: maximum density difference over the extent of of the mixed layer; $h_{max,IF}$: maximum interface height). The 2.5 and 97.5-percentile values are given between brackets.

input	occurrence (%)	D (GW)
MA: 50 dbar	14.3	8.2 [0.1; 34.4]
MA: 100 dbar	14.5	8.5 [0.1; 34.5]
MA: 300 dbar	13.9	6.4 [0.1; 28.1]
MA: 350 dbar	13.4	5.8 [0.1; 24.8]
$\partial\sigma_1/\partial p_{max} = 0.5\text{x}10^{-4}$ kg m^{-3} dbar^{-1}	1.2	6.3 [0.0; 20.7]
$\partial\sigma_1/\partial p_{max} = 2.5\text{x}10^{-4}$ kg m^{-3} dbar^{-1}	6.6	4.0 [0.0; 15.8]
$\partial\sigma_1/\partial p_{max} = 7.5\text{x}10^{-4}$ kg m^{-3} dbar^{-1}	21.2	9.8 [0.2; 42.7]
$\partial\sigma_1/\partial p_{max} = 10\text{x}10^{-4}$ kg m^{-3} dbar^{-1}	27.5	18.1 [0.3; 48.8]
$\Delta\sigma_{1,max} = 0.5\text{x}10^{-3}$ kg m^{-3}	18.5	12.3 [0.2; 41.8]
$\Delta\sigma_{1,max} = 2.5\text{x}10^{-3}$ kg m^{-3}	17.4	8.9 [0.2; 39.2]
$\Delta\sigma_{1,max} = 7.5\text{x}10^{-3}$ kg m^{-3}	11.8	8.4 [0.1; 28.4]
$\Delta\sigma_{1,max} = 10\text{x}10^{-3}$ kg m^{-3}	9.8	7.9 [0.1; 24.9]
$h_{max,IF} = 10$ dbar	14.1	7.2 [0.1; 31.6]
$h_{max,IF} = 20$ dbar	14.3	7.5 [0.1; 33.3]
$h_{max,IF} = 40$ dbar	11.4	5.2 [0.1; 23.4]
$h_{max,IF} = $ infinity	14.5	7.6 [0.1; 33.5]

other. By including an inequality of these effective diffusivities in global ocean models based on the characteristics of thermohaline staircases, double-diffusive mixing can in principle be parameterized in ocean models (Fig. 6.6). Especially in regions with high staircase occurrence, this is expected to yield more realistic model results on both regional and global scales.

Chapter 7

Double-diffusive fluxes densify Antarctic Intermediate Water in the Caribbean Sea

Abstract

The stability of the Atlantic Meridional Overturning Circulation is partly regulated by the freshwater content of Antarctic Intermediate Water (AAIW). However, the impact of double-diffusive salt fluxes induced by thermohaline staircases on this freshwater content remains unknown. Here, we show that double-diffusive fluxes can explain the observed time-averaged spatial variation of the temperature and salinity of AAIW and hence the freshwater content of this water mass in the Caribbean Sea. To do so, we define advection-diffusion equations for temperature and salinity and implement the flux ratio ($\gamma = \frac{\alpha F_T}{\beta F_S} = 0.8$) and the occurrence rate of thermohaline staircases (7 % in the Caribbean Sea). Overall these results show how double-diffusive processes modify water mass properties in the Caribbean Sea.

7.1   Introduction

Antarctic Intermediate Water (AAIW) is one of the major water masses in the Atlantic Ocean. This water mass, characterized by a pronounced salinity minimum, propagates northward through the Atlantic Ocean, where it contributes to the northward flowing branch of the Atlantic Meridional Overturning Circulation (Tsuchiya, 1989; Talley et al., 2011). Along its path, the salinity minimum of AAIW gets eroded through mixing in lateral and vertical directions (Tsuchiya, 1989). As a result, the characteristic salinity minimum can only be traced as far north as 20°N (Tsuchiya, 1989).

In the North Atlantic, AAIW mixes laterally with Mediterranean Under Water (Tsuchiya, 1989; Machín and Pelegrí, 2009; Talley et al., 2011). Simultaneously, vertical mixing induced by double-diffusive mixing in the salt-finger regime in the layer above could also affect the properties of AAIW (You, 1999; St. Laurent and Schmitt, 1999; Schmitt, 2005). Double-diffusive mixing occurs because the molecular diffusivity of heat is two orders of magnitude larger than that of salt (e.g., Radko, 2013). In the North Atlantic and Caribbean Sea, this mixing arises between the cold and fresh AAIW and the overlying warm and saline Subtropical Underwater (STUW). In this case, a disturbed water parcel from, for example, STUW will cool relatively fast, while its salt content remains the same. This results in an increase of the water parcels' density and the formation of double-diffusive salt fingers (Stern, 1960). When this double-diffusive mixing takes place, thermohaline staircases can be formed: sequences of subsurface mixed layers separated by thin interfaces (e.g., Stern, 1960; Radko, 2013). At these interfaces, the downward salt flux typically exceeds the downward heat flux (Lambert and Sturges, 1977; Schmitt, 2005), resulting in a flux ratio ($\gamma = \frac{\alpha F_T}{\beta F_S}$, where αF_T and βF_S are the density components of the heat and salt fluxes, respectively) below unity (e.g., Radko, 2013). This implies that double-diffusive mixing is, in contrast to regular turbulent mixing, characterized by a negative effective diffusivity of buoyancy.

The strength of the mixing processes in both lateral and vertical directions is affected by variations in the properties of water masses and in their spreading on inter-annual and decadal time scales. Remarkably, in the North Atlantic Ocean, AAIW became warmer and more saline in the last decades, while it became warmer and lighter in the South Atlantic Ocean (Arbic and Brechner Owens, 2001; Sarafanov et al., 2007; McCarthy et al., 2011; Schmidtko and Johnson, 2012; Fu et al., 2018). The South Atlantic trend has been attributed to warming trends near the AAIW formation region and to the decadal variability of the Agulhas Leakage (Schmidtko and Johnson, 2012; Lübbecke et al., 2015; Hummels et al., 2015). In contrast, the trend in the North Atlantic appeared to coincide with a slower northward and westward spreading of AAIW in this region (Fu et al., 2018, 2019). Another difference between the trends in the two hemispheres is that the salinity trends of AAIW are not uniformly positive in the South Atlantic, while this is the case in the North Atlantic (Curry et al., 2003; Durack

and Wijffels, 2010; McCarthy et al., 2011; Schmidtko and Johnson, 2012; Fu et al., 2018).

These different trends might, in part, be attributed to double-diffusive mixing, as (i) thermohaline staircases are more pronounced in the North Atlantic than in the South Atlantic Ocean (Chapter 6 of this thesis), and (ii) the slower northward spreading of AAIW in the North Atlantic Ocean (Fu et al., 2018, 2019) results in a longer exposure of the AAIW core to the double-diffusive salt fluxes. As a consequence, the salinity of AAIW would increase more in the North Atlantic than that of its counterpart in the South Atlantic Ocean. However, it remains unclear to what extent the double-diffusive salt fluxes are able to modify the properties of AAIW. Therefore, we assess here, for the first time, whether the observed spatial variations of AAIW in the Caribbean Sea can be explained by double-diffusive mixing induced by thermohaline staircases in the layer above. To that end, we use advection-diffusion equations for temperature and salinity, which are discussed in detail in Section 7.5.

7.2   Approach

The characteristics of AAIW are studied by computing its time-averaged spatial variations in the western tropical North-Atlantic Ocean and in the Caribbean Sea (40°W-100°W and 0°N-33°N). We use a monthly-averaged isopycnal climatology (MIMOC) provided by Schmidtko et al. (2013). The temperature and salinity fields are averaged in time to obtain a year-averaged isopycnal climatology. Similar to Fu et al. (2019) and Schmidtko and Johnson (2012), we define AAIW as the salinity minimum between the neutral density ranges of 27.38 kg m^{-3} to 27.82 kg m^{-3}. We convert these neutral density ranges to potential density anomalies (27.2 kg m^{-3} < σ_0 < 27.6 kg m^{-3}) using Fig. S15 of Abernathey et al. (2016). To obtain the salinity minimum of AAIW, we first interpolate the temperature and salinity between the σ_0-layers of the climatology with a cubic spline interpolator and then extract the salinity minimum from the interpolated curve.

In the remainder of this study, we interpret the spatial variations of temperature and salinity in the core of AAIW as the average trends of AAIW along its propagation path. That is, we assume that the time-averaged spatial variations of this subsurface water mass are solely induced by lateral and vertical mixing. This assumption is valid when the advective time scale of the AAIW propagation is much larger than the adjustment time scale of the AAIW salt distribution to the double-diffusive salt flux ($L/U \gg S_0/Q$). In this case, we can use a spatial scale of $L > \mathcal{O}\left(10^6 \text{ m}\right)$, a velocity of AAIW of $U = \mathcal{O}\left(5 \times 10^{-2} \text{ m s}^{-1}\right)$ following Fu et al. (2019), a reference salinity of $S_0 \approx 35 \text{ g kg}^{-1}$ and a salt flux of $Q_{\max} = \mathcal{O}\left(10^{-7}\text{g kg}^{-1} \text{ s}^{-1}\right)$ as estimated by Lambert and Sturges (1977). Because multiple studies (Taylor and Veronis, 1996; Radko, 2005) showed that this estimate of Lambert and Sturges (1977) is at least order of magnitude too large, this implies that indeed $L/U \gg S_0/Q$. Hence the assumption that the time-averaged

spatial variations of this subsurface water mass are solely induced by lateral and vertical mixing is considered valid.

To analyze whether the along-path property variations of AAIW can be explained by double-diffusive fluxes, we use a global dataset of thermohaline staircases obtained from Argo float profiles (Chapter 5 of this thesis). The thermohaline staircases in this dataset are detected with an algorithm that exploits the vertical structure of staircase profiles. This algorithm first detects subsurface mixed layers, and then analyzes the properties and height of the interfaces in between. Next, sequences of mixed layers are identified as thermohaline staircases. Further details on the algorithm can be found in Chapter 5 of this thesis. We extracted all 21,916 Argo float profiles that were located in the Caribbean Sea and western tropical North Atlantic from this global dataset to obtain the information necessary for this study.

We study 1,565 Argo float profiles that are located in the Caribbean Sea (62°W-82°W and 10°N-18°N) in more detail. In particular, we analyse the temperature and salinity of the mixed layers in the thermohaline staircases. We find that, similar to other staircase regions (Schmitt et al., 1987; Timmermans et al., 2008), the mixed-layer properties of different profiles are aligned (see Section 7.4). The relation between the aligned temperature and salinity are referred to as the lateral density gradients. These lateral density gradients can be used as a measure for the flux ratio inside the staircase layer (Schmitt et al., 1987; Timmermans et al., 2008). McDougall (1991) validated this relation for a staircase region in the tropical North Atlantic Ocean. He found that there, the lateral density gradients of the mixed layers result from a combination of the salt-finger fluxes and the vertical motion of the layer. The latter can be interpreted as a vertical flux divergence, which appears to be an effective mechanism to convert the properties of water masses (McDougall, 1991). Following previous examples of Schmitt et al. (1987) and McDougall (1991) near the Caribbean Sea, we assume that the lateral density ratio ($R_{x,\rho} = \alpha T_x/(\beta S_x)$) of the mixed layers is equal to the flux ratio (γ). In this expression, α and β are the thermal expansion and haline contraction coefficients, respectively, and the subscript x indicates the spatial derivative.

7.3   Spatial variations of AAIW

The time-averaged properties of AAIW are used to analyze the spatial variations of this water mass in the North Atlantic Ocean and Caribbean Sea (Fig. 7.1). Recall that we assumed that these spatial gradients represent the average temporal variation of AAIW along its propagation path. We therefore assess the properties AAIW along the main branch, following Tsuchiya (1989) who identified this branch by analysing the silica concentrations in the Atlantic Ocean.

The main branch of AAIW crosses the equator along the western boundary of the Atlantic Ocean (A in Fig. 7.1a). From there, the branch continues north-
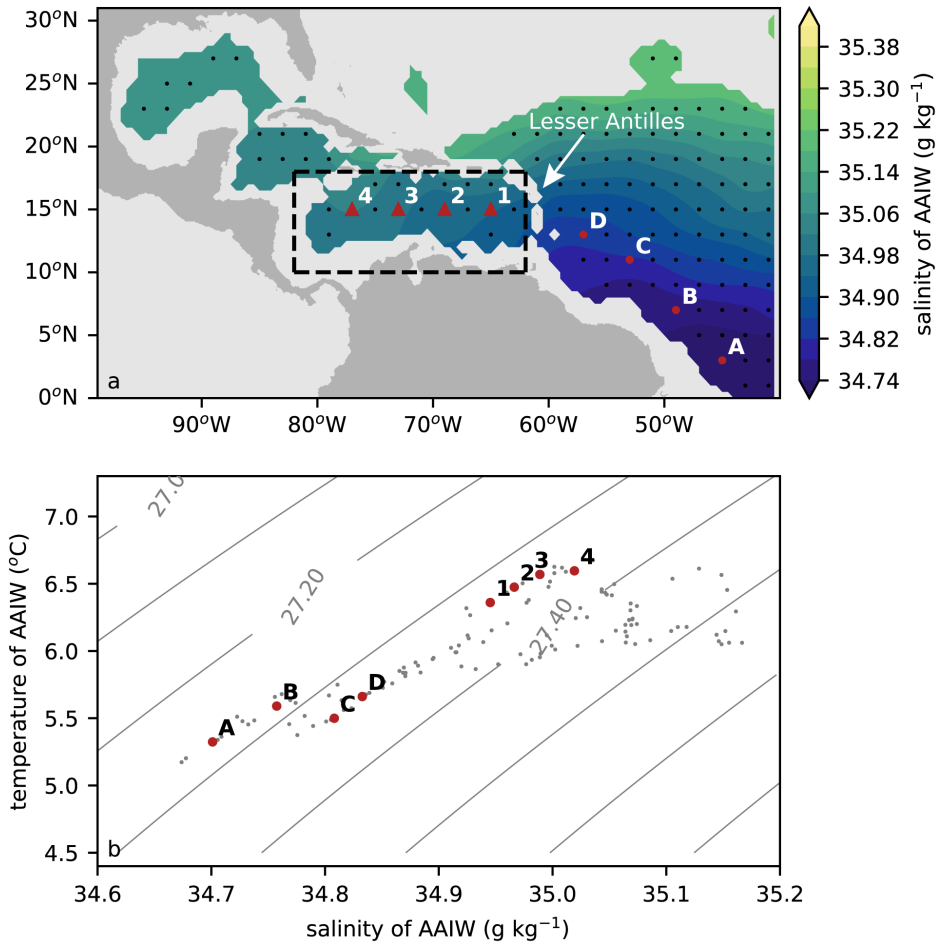
Figure 7.1: (a) Salinity of the AAIW core obtained from MIMOC (Schmidtko et al., 2013). The dashed box (62°W-82°W and 10°N-18°N) is used to compute properties of AAIW in the Caribbean Sea. (b) Conservative temperature and absolute salinity of AAIW core averaged per 2°x2°. Location of the data points are indicated with black dots in panel (a). Grey contours highlight the isopycnals (σ_0). Letters A-D correspond to the path of AAIW in the Atlantic Ocean; Numbers 1-4 correspond to the path of AAIW in the Caribbean Sea.

ward along the continental slope. Along this path (A-D in Fig. 7.1a), both the temperature and salinity of AAIW increase. At first, these variations follow approximately the $\sigma_0 = 27.3$ kg m^{-3}-isopycnal (A-B in Fig. 7.1b), but the density of AAIW increases as it approaches the Caribbean Sea (B-D in Fig. 7.1b). This density increase results from a relatively strong salinity increase accompanied by weaker warming, implying that the flux ratio into AAIW along this path is below unity.

Next, AAIW deflects towards the west and passes the Lesser Antilles (Tsuchiya, 1989). During this passage, enhanced turbulent mixing changes the properties of AAIW (Garrett, 2003; Kunze and Llewellyn Smith, 2004; Whalen et al., 2012). The effects of turbulent mixing at the Lesser Antilles are visible as a warmer and more saline AAIW in the Caribbean Sea compared to the North Atlantic Ocean. In contrast to double-diffusive mixing, this turbulent mixing predominantly induces changes along the isopycnal, as the density of AAIW in the Atlantic Ocean (D in Fig. 7.1b) is similar to the density of AAIW in the Caribbean (1 in Fig. 7.1b).

The density of AAIW increases again in the direction of the mean flow in the Caribbean Sea (1-4 in Fig. 7.1b). Similar to the density increase in the Atlantic Ocean, the density increase in the Caribbean Sea is dominated by an increase in salinity. Moreover, the temperature also increases along this path, which results in a flux ratio is below unity. We quantify these temperature and salinity variations by correlating the temperature with the salinity in the Caribbean Sea (62°W-82°W, 10°N-18°N, dashed box in Fig. 7.1a), and obtain a correlation with a slope of $T_x S_x^{-1} = 3.4$ °C kg g^{-1}, where T_x and S_x are the horizontal gradients in temperature and salinity, respectively. This correlation is significant on a confidence interval of 90 %. The properties were averaged per $2° \times 2°$ (black dots in Fig. 7.1a). This tendency to warmer and more saline properties of AAIW are in line with expectations that the properties of this water mass could be modulated by double-diffusive mixing.

7.4   Double-diffusive fluxes in the staircase layer

Next, we assess whether these spatial variations of AAIW could be related to double-diffusive mixing in thermohaline staircases. To analyze this, we extract their distribution, occurrence rate, and properties of the mixed layers of the Caribbean staircases from the global dataset of thermohaline staircases (Section 7.2).

An example of a thermohaline staircase in the Caribbean Sea is shown in Figure 7.2a. This staircase is located on the main thermocline and halocline between STUW and AAIW (Fig. 7.2b). This depth is typical for all thermohaline staircases in the Caribbean Sea, as all mixed layers are located at similar depth ranges (Fig. 7.2c). To confirm that these mixed layers are indeed double-diffusive thermohaline staircases, we compute the Turner angle (Tu), which is an indicator for whether the water column is susceptible to double-diffusive mixing (Ruddick,
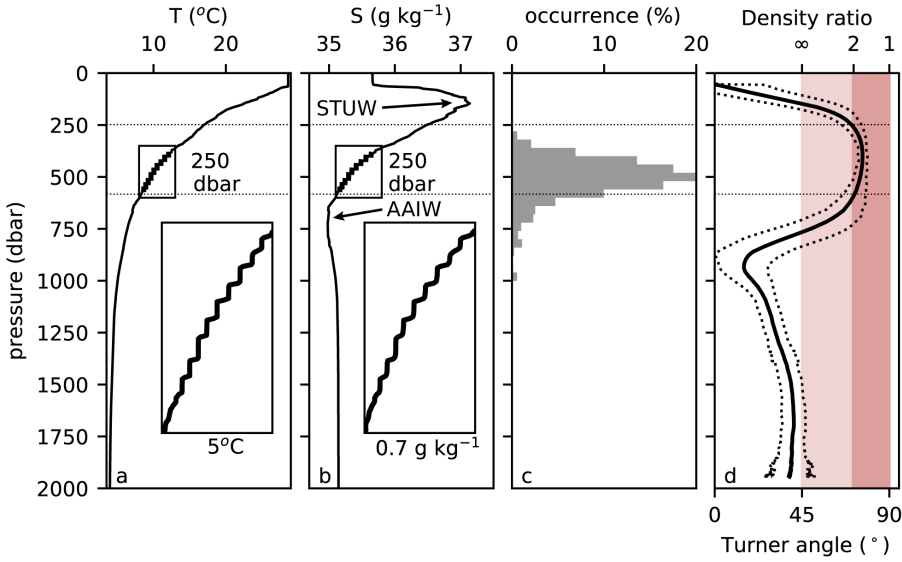
Figure 7.2: (a) Temperature and (b) salinity profile of Caribbean staircase obtained with Argo float 4901720 at 75.5°W and 13.9°N on 9 November 2018. (c) Depth of detected mixed layers of all thermohaline staircases in the Caribbean Sea (62°W-82°W and 10°N-18°N, dashed box in Fig. 7.1) obtained from the global dataset of thermohaline staircases (Chapter 5 of this thesis). (d) Average Turner angle (Ruddick, 1983) computed from 1565 Argo float profiles in the Caribbean Sea. The dashed lines correspond to one standard deviation from the mean Turner angle. The (dark) red shading corresponds to Turner angles that are susceptible to (strong) salt fingering. The upper and lower bound of the Turner angles with strong salt-fingering are indicated by the horizontal lines in all panels. The density ratios that correspond to these Turner angles are indicated on the upper axis. The inlays show a zoom over 250 dbar and 5°C and 0.7 g kg^{-1} of the thermohaline staircase. The approximate locations of Antarctic Intermediate Water (AAIW) and Subtropical Underwater (STUW) are indicated in panel (b).

1983), for all profiles in the Caribbean Sea, with:

$$\text{Tu} = \tan^{-1}\left(\alpha \frac{\partial T}{\partial p} - \beta \frac{\partial S}{\partial p}, \alpha \frac{\partial T}{\partial p} + \beta \frac{\partial S}{\partial p} \right). \tag{7.1}$$

Here the vertical gradients of the background temperature and salinity profiles are approximated with a central differences scheme after these were smoothed with a Hanning window of 100 dbar. We find that indeed most mixed layers are located at depth ranges with strong salt fingering (71.3° < Tu < 90°, Fig. 7.2d, Ruddick, 1983). This confirms that the thermohaline staircases in the Caribbean Sea are adequately captured in the global dataset. We refer to Chapter 5 of this thesis for a more detailed validation of this dataset.

The spatial distribution of thermohaline staircases in the Caribbean Sea (Fig. 7.3a) is in line with expectations based on previous observations (Chapter 2 of

this thesis, Lambert and Sturges, 1977; Morell et al., 2006). In total, 7 % of the profiles in the Caribbean Sea contain staircases. The staircases appear to be clustered in two regions: one around 70°W and one in the Panama Colombia Gyre (PCG) in the southwest of the basin. Another staircase region is present in the adjacent part of the North Atlantic Ocean. The latter is known as the C-SALT region, and, notably, coincides with a region where the average density of AAIW also increases along its path (point B-D in Fig. 7.1a).

When staircases are persistent in time and space, the temperature and salinity in each mixed layer increase due to the vertical heat and salt flux through the interface above (Schmitt et al., 1987; McDougall, 1991). This gradual increase of the temperature and salinity, visible by the alignment of the properties of each subsequent mixed layer, is the lateral density ratio (see Section 7.2). Based on the findings of McDougall (1991), we assume that this lateral density ratio equals the flux ratio. Because the Caribbean staircases show such alignment (Fig. 7.3b), we can compute the flux ratio inside this layer. We find that the flux ratio decreases with depth from $\gamma = 0.83$ in the warmest layer towards $\gamma = 0.79$ in the coldest layer.

7.5   The effective diffusivity of salt in AAIW

In this section, we combine the results obtained in the previous sections in steady-state advection-diffusion equations for temperature and salinity to assess whether double-diffusive fluxes induced by thermohaline staircases can quantitatively explain the time-averaged spatial variations of AAIW. To obtain these equations, we define the relation between the effective diffusivity of heat (K_T) and the effective diffusivity of salt (K_S) following Kelley (1990):

$$K_T = \gamma R_\rho^{-1} K_S, \tag{7.2}$$

where R_ρ is the density ratio, defined as $R_\rho = \alpha T_z/(\beta S_z)$. In this expression, the subscript z indicates the vertical derivative. Moreover, following Toole et al. (1994), we assume that turbulent mixing in the ocean interior, represented by an effective diffusivity for heat and salt ($K^{\text{turb}} = 10^{-5}$ m^2 s^{-1}), is limited. For simplicity, we assume that double-diffusive mixing does not occur simultaneously with turbulent mixing. To distinguish between double-diffusive and turbulent mixing, we use the occurrence of thermohaline staircases (a = 0.07) as a measure for the occurrence of double diffusion. This results in the following steady-state advection-diffusion equation for salt:

$$US_x = aK_S S_{zz} + (1-a)K^{\text{turb}} S_{zz}, \tag{7.3}$$

and for heat:

$$UT_x = a\gamma R_\rho^{-1} K_S T_{zz} + (1-a)K^{\text{turb}} T_{zz}, \tag{7.4}$$
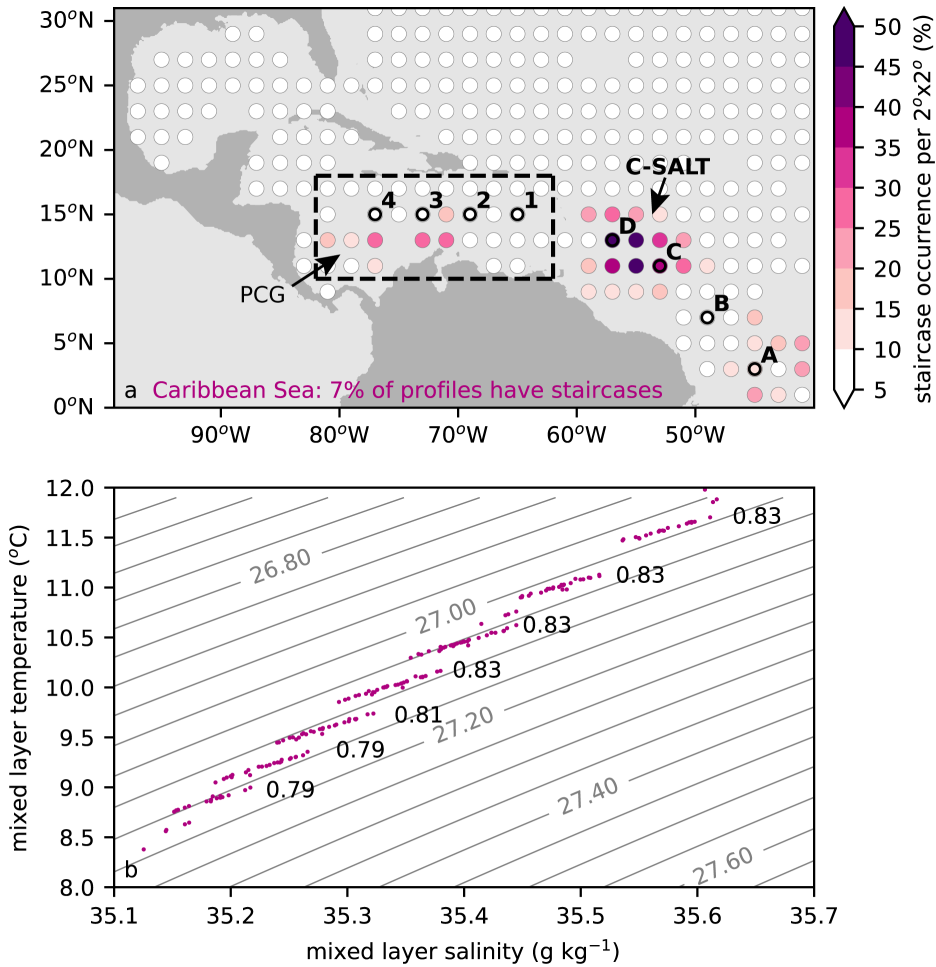
Figure 7.3: (a) Occurrence of thermohaline staircases in the Caribbean Sea and North Atlantic Ocean averaged per $2° \times 2°$ and obtained from a global dataset of thermohaline staircases (Chapter 5 of this thesis). Only data points containing more than 10 observations are shown. Dashed box (62°W-82°W and 10°N-18°N) is used to compute the occurrence of staircases in the Caribbean Sea. Numbers 1-4 and Letters A-D indicate the same locations as in Fig. 7.1. (b) Temperature and salinity in the thermohaline staircases with more than 4 steps in the Caribbean Sea (dashed box in panel a); grey contour lines highlight the isopycnals (σ_0). Numbers indicate the slope the aligned points, corresponding to the lateral density ratio ($R_{x,\rho}$) and are approximately equal to flux ratio (γ). The locations of the Panama Colombia Gyre (PCG) and C-SALT and indicated in panel (a).

where U is the advective velocity of AAIW and T_x and S_x correspond the time-averaged spatial derivatives of AAIW temperature and salinity that were obtained in Section 7.3 ($T_x S_x^{-1} = 3.4$ ^{o}C kg g^{-1}). The second order vertical derivatives of temperature and salinity are indicated with T_{zz} and S_{zz}, respectively.

Using these two equations, we can estimate the magnitude of K_S (see Section 7.A). To study how the vertical variations of temperature and salinity affect the effective diffusivity, we computed the dependence of K_S on these parameters: the flux ratio and the ratio between the second derivatives of salinity and temperature $b = S_{zz} T_{zz}^{-1}$ (Fig. 7.4). The observed values of b and R_ρ yield effective diffusivities of salt of 3.7×10^{-8} m^2 s^{-1} $< K_S < 1.3 \times 10^{-3}$ m^2 s^{-1} (Fig. 7.4b). The most frequently obtained values (orange shading in Fig. 7.4b) are very similar to effective diffusivities of salt that were directly observed within the staircase layer (Schmitt, 2005, green line in Fig. 7.4). This implies that our computed effective diffusivities of salt are in the right order of magnitude. Moreover, these results suggest that we can explain the time-averaged property changes of AAIW by considering vertical fluxes only.

7.6   Discussion

In this study, we explored whether double-diffusive fluxes from thermohaline staircases in the Caribbean Sea can explain the time-averaged spatial variability of AAIW along its pathway from the North Atlantic through the Caribbean Sea. We found that the temperature, salinity and density of AAIW increase along its path of propagation and that these increases are consistent with changes induced by double-diffusive processes. We provide the first observationally-based evidence that the vertical fluxes from turbulence and double-diffusive mixing can fully explain the observed variations in AAIW properties in the Caribbean Sea. We do this by estimating the magnitude of all the terms in steady-state advection diffusion equations. This estimate indicates that double-diffusive fluxes from thermohaline staircases, in combination with background turbulence, can induce water-mass transformation of AAIW in the Caribbean Sea of the observed magnitude.

In the last decades, AAIW became warmer and more saline in the North Atlantic (Curry et al., 2003; Durack and Wijffels, 2010; McCarthy et al., 2011). Because this trend was analyzed east of the Caribbean Sea, we project our results to the C-SALT staircase region to speculate on the potential impact of double diffusion on AAIW properties in this region (C-D in Fig. 7.3a). There, the location of the density increase of the main branch of AAIW also coincides with the staircase region, which suggests that double-diffusive mixing affects AAIW properties there, as was also suggested by Schmitt et al. (1987). The weak northward transport of AAIW at this location during the last decades (Fu et al., 2019) implies a longer exposure to double-diffusive fluxes from the staircase above. Consequently, this would yield a salinity and temperature increase in AAIW that is in
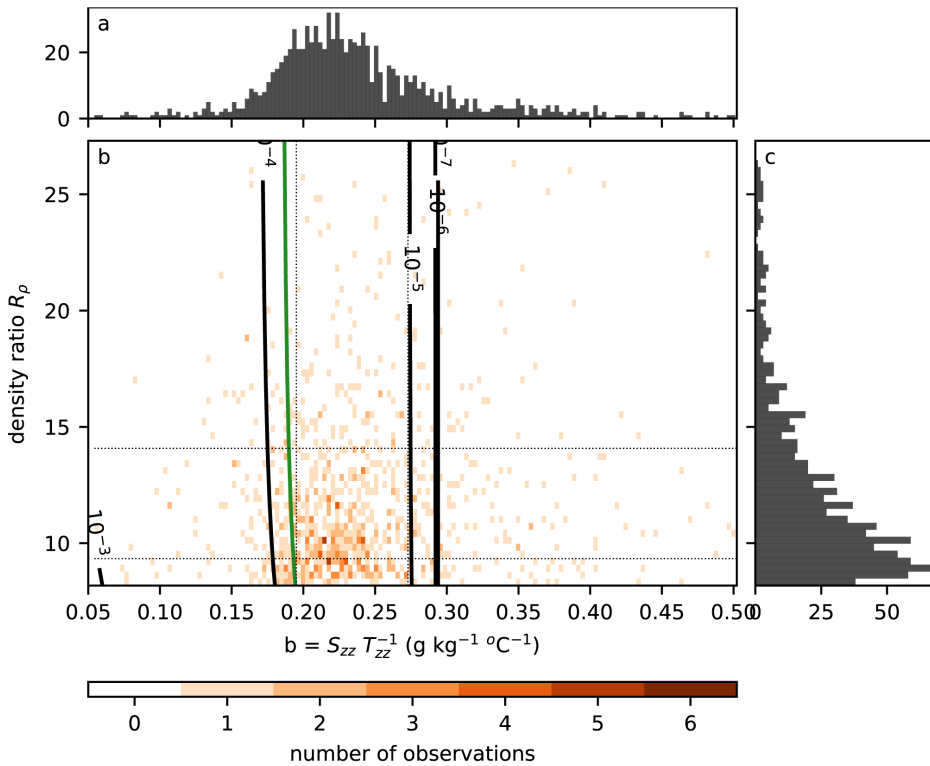
Figure 7.4: (a) Histogram of values of b obtained from observations from Argo floats profiles between 600 and 750 dbar. (b) Effective diffusivity of salt (K_S) as a function of b and R_ρ. The green line corresponds to observations of (Schmitt, 2005). The orange shading shows the number of observations with values of b and R_ρ. (c) Histogram of values of the density ratio, R_ρ, obtained from Argo floats profiles between 600 and 750 dbar. Dashed lines in panel (b) indicated the 25th and 75th percentile of the values in panels (a) and (c). The ranges of the axes in panels (a) and (c) correspond to the 5th and 95th percentile of the observed values of b and R_ρ. Details on the computations of R_ρ, K_S, and b can be found in the Section 7.A

line the long-term changes seen in observations (Curry et al., 2003; Durack and Wijffels, 2010; McCarthy et al., 2011).

Besides the longer exposure of AAIW to the double-diffusive fluxes, their strength may also have changed in the past years due to changes in the salinity stratification (e.g., Johnson and Kearney, 2009). More specifically, the waters overlying AAIW became fresher, while the waters below AAIW became more saline (Durack and Wijffels, 2010). This trend towards more saline waters of STUW will decrease the density ratio (R_ρ). In turn, this will increase the diffusivity of salt (Fig. 7.4). These changes are worth investigating in future research. For example, the decadal variability of K_S can be assessed using the advection-diffusion equations with estimates of the decadal variability of each term in the equations.

Overall, the results of this study provide a plausible explanation for the observed long-term trends of AAIW. Moreover, these results are in line with previous findings in other regions that double-diffusive fluxes in thermohaline staircases may adjust the properties of water masses (Johnson and Kearney, 2009; Schroeder et al., 2016). This implies that they double diffusion might affect the density of water masses (such as AAIW) in and downstream of regions with thermohaline staircases. Therefore, we speculate that double-diffusive mixing may adjust the strength and direction of the geostrophic flow in the ocean. To study these impacts with ocean models, adequate parameterizations of double-diffusive mixing are necessary. We argue that the approach and results of this study provide a starting point for these parameterizations. For example, the quantities that depend on the vertical variation of temperature and salinity (b and R_ρ) can be obtained directly from the ocean model. In combination with the occurrence of thermohaline staircases obtained from the global dataset of thermohaline staircases, the effective diffusivity of salt can be computed using the large-scale vertical temperature and salinity gradients. As a result, the effects of double-diffusive mixing are captured in an ocean model, and the large-scale impact of double-diffusive mixing can be studied.

7.A   Computation of the effective diffusivity of salt

To compute the effective diffusivity of salt, we rewrite equation 7.3 as a relation for advective velocity:

$$U = T_x^{-1}\left(a\gamma R_\rho^{-1}K_S T_{zz} + (1-a)K^{\text{turb}}T_{zz}\right) \qquad (7.5)$$

and substitute that into equation 7.4 to obtain an expression for the effective diffusivity of salt:

$$K_S = \frac{(1-a)K^{\text{turb}}}{a}\frac{1-S_x^{-1}T_x S_{zz}T_{zz}^{-1}}{S_x^{-1}T_x S_{zz}T_{zz}^{-1}-\gamma R_\rho^{-1}} = \frac{(1-a)K^{\text{turb}}}{a}\frac{1-bS_x^{-1}T_x}{bS_x^{-1}T_x-\gamma R_\rho^{-1}}. \qquad (7.6)$$

In equation 7.6, the remaining unknowns are: the density-flux ratio (γ), the density ratio (R_ρ) and the ratio between the second derivatives of salinity and temperature $b = S_{zz}T_{zz}^{-1}$. We use a value of $\gamma = 0.8$ for the density-flux ratio, as obtained in Section 7.4. To compute R_ρ and b, we analyze the properties in the layer between the core of AAIW and below the core of the staircase layer (600-750 dbar, see Fig. 7.2) as this is the depth range where the salt would be transported downward towards the AAIW core. To that end, we use the data from the Argo float profiles in the Caribbean Sea that were smoothed with a Hanning window of 100 dbar (dashed box in Fig. 7.1a, Fig. 7.4c). Because the second vertical derivatives of salinity and temperature are noisy, we use the mean value of T_{zz} and S_{zz} of each profile to compute b (Fig. 7.4a).

7.B   Horizontal mixing

In the computations in Section 7.5 and Section 7.A, we assumed that all mixing was caused by vertical mixing, and horizontal mixing was absent. To gain confidence that it are indeed vertical fluxes that modify the properties of AAIW, this assumption needs to be validated by an order of magnitude analysis. We estimate the magnitude of the horizontal salt fluxes with:

$$F_{\mathrm{H}} = K_{\mathrm{H}} S_{\mathrm{xx}}, \tag{7.7}$$

where K_{H} is the horizontal effective diffusivity and S_{xx} is the second horizontal derivative of the salinity. The effective diffusivity has a typical value in the order of $K_{\mathrm{H}} = \mathcal{O}(10^2 \ \mathrm{m}^2 \ \mathrm{s}^{-1})$ (Groeskamp et al., 2020). We estimated the average S_{xx} from the WOA2018 in within AAIW core at $S_{\mathrm{xx}} = \mathcal{O}(10^{-13} \ \mathrm{g} \ \mathrm{kg}^{-1} \ \mathrm{m}^{-2})$. This results in $F_{\mathrm{H}} \approx \mathcal{O}\left(10^{-11} \mathrm{g} \ \mathrm{kg}^{-1} \ \mathrm{s}^{-1}\right)$

Next, we use a similar approach to estimate the vertical mixing:

$$F_{\mathrm{V}} = K_S S_{\mathrm{zz}}. \tag{7.8}$$

For K_S we use $K_S = \mathcal{O}(5 \times 10^{-5} \ \mathrm{m}^2 \ \mathrm{s}^{-1})$, as found in Figure 7.4. Using a similar approach as in Section 7.A, we obtain an average value of S_{zz} of the order of $\mathcal{O}(10^{-5} \ \mathrm{g} \ \mathrm{kg}^{-1} \ \mathrm{m}^{-2})$ with a 5 and 95 percentile of 6.3×10^{-7} g kg^{-1} m^{-2} and 2.0×10^{-5} g kg^{-1} m^{-2}, respectively. This results in $F_{\mathrm{V}} \approx \mathcal{O}\left(5 \times 10^{-10} \mathrm{g} \ \mathrm{kg}^{-1} \ \mathrm{s}^{-1}\right)$. A comparison between these estimated magnitudes of the horizontal and vertical mixing indicates that the vertical fluxes into AAIW are roughly up to one order of magnitude larger than the horizontal mixing. Note that, due to the wide range of values of S_{zz}, the vertical mixing could in principle be smaller than horizontal mixing. However, these computations indicate that, on average, this is not the case.

Chapter 8

Conclusions and recommendations

The aim of this thesis is to gain insight in the dynamics and mixing in the Caribbean Sea with the focus on mesoscale anticyclonic eddies and double-diffusive mixing. In total, six research questions have been formulated in the Introduction (Chapter 1 of this thesis) and answered in the previous chapters. In this chapter, the answers to each research question are summarized first. Next, the results are combined and discussed. The chapter concludes with a few recommendations for further research.

8.1 Answers to the research questions

What is the vertical structure of Caribbean anticyclones and where do they originate?

To gain insight in the vertical structure of a Caribbean anticyclone, we performed a hydrographic survey. This hydrographic survey resulted in the first observations of the full depth of an anticyclonic eddy in the Caribbean Sea. The results were presented in Chapter 2 of this thesis. We found that this anticyclone was strongly intensified at the surface and that the highest velocities were located in the upper 150 m and along the southern perimeter of the anticyclone. The anticyclone originated near Grenada Passage. The low salinity and elevated silicate concentrations in the surface waters of the anticyclone, suggested that the anticyclone entrained surface waters originating from the Orinoco River. Below the surface, the anticyclone contained a strong and thick barrier layer with a temperature inversion. While the results of this survey contain only one example of an anticyclonic eddy in the Caribbean Sea, we showed that some Caribbean anticyclones have strong surface-intensified velocity structure.

Are Caribbean anticyclones remnants of NBC rings?

Because it was unclear whether Caribbean anticyclones should be considered as remnants of NBC rings, we studied this in more detail using a realistic setup of

the eastern Caribbean Sea in Chapter 3 of this thesis. The high resolution of this model allowed for an accurate representation of the complex island bathymetry of the Lesser Antilles. We showed that during a collision of an NBC ring with the Lesser Antilles the bulk of the vorticity influx into the Caribbean Sea that allows for the formation of Caribbean anticyclones is generated locally at the islands. Consequently, a smaller part is governed by the advection of anticyclonic vorticity from the NBC rings themselves. A further analysis of two years of model data indicated that most vorticity in the Caribbean Sea is generated locally at St. Lucia and Grenada. Therefore, we concluded that Caribbean anticyclones are not remnants of NBC rings.

Is the westward intensification of Caribbean anticyclones governed by upwelling?

It was hypothesized in the Introduction (Chapter 1 of this thesis) that the advection of cold upwelling filaments strengthens the horizontal density gradients of the anticyclones. This strengthening is necessary for their observed westward intensification. Using an idealized model, This hypothesis was confirmed in Chapter 4 of this thesis. We showed that the anticyclones that advect upwelling filaments dominated the eddy kinetic energy in the Caribbean Sea. The westward intensification of these anticyclones was steered by an increase of the horizontal density gradients between the core and the background. These increased density gradients resulted from the advection of the cold upwelling filaments and that this, in turn, increased the vertical shear in the anticyclones.

Which characteristics and properties of thermohaline staircases can be used to detect them?

The Caribbean Sea is a well-known formation site of thermohaline staircases. This was, for example, seen during the survey described in Chapter 2 of this thesis, where 12 out of 15 observations contained staircases. To study the staircases in more detail, we developed an algorithm in Chapter 5 of this thesis to automatically detect thermohaline staircases in vertical temperature and salinity profiles. In this algorithm, we use typical characteristics of the stepped structure of the staircases to distinguish them from other vertical variations. More specifically, the combination of the weak gradients in the mixed layers and the nearby large gradients are unique for thermohaline staircases. A validation using the Turner angle indicated that the detection algorithm can indeed successfully detect staircases are within double-diffusive regimes. We applied the detection algorithm to 487,493 temperature and salinity profiles to obtain a global dataset with the distribution and properties of thermohaline staircases.

What is the contribution of double diffusion to the global mechanical energy budget?

We used the global dataset of thermohaline staircases to estimate the contribution of double-diffusive mixing to the global mechanical energy budget in Chapter 6 of this thesis. We concluded that double-diffusive mixing does not contribute significantly to this global mechanical energy budget. Our estimated contribution of 7.5 GW is much smaller than the 2 TW of turbulent mixing necessary to compensate for the sinking branch of the Atlantic Meridional Overturning Circulation (Munk, 1966). However, this does not imply that the impact of double-diffusive mixing can be neglected. In particular, our analysis revealed multiple hot-spot regions where double-diffusive mixing is persistent, including in a so-far unknown staircase region overlying the Tasman Leakage Waters.

Can double-diffusive fluxes explain the observed variations of the properties of AAIW in the Caribbean Sea?

Double-diffusive mixing has a counter-gradient buoyancy flux that restratifies the water column. Previous studies hypothesized that in theory this buoyancy-flux could affect the properties of the layers above and below (Schmitt, 2005; Radko, 2013). However, this buoyancy flux had not yet been quantified. In Chapter 7 of this thesis, we assessed whether thermohaline staircases in the Caribbean Sea affect the properties of the underlying Antarctic Intermediate Water based on observations. We computed the staircase occurrence and the flux ratio in these layers. Using steady-state advection-diffusion equations of the temperature and salinity, we showed that double-diffusive fluxes from thermohaline staircases can explain the spatial variability of Antarctic Intermediate Water in the Caribbean Sea.

8.2   Summary and discussion

In the previous section, short answers to the six research questions that were formulated in the Introduction (Chapter 1 of this thesis) were presented. The first three research questions concern the life cycle of Caribbean anticyclones, while the other research questions concern the impact double-diffusive mixing on regional and global ocean circulation. In this section, we discuss the insights that we obtained from the both sets of research questions. A summarizing schematic of the new insights regarding the anticyclones is depicted in Figure 8.1. Using observations and numerical models, we showed that these Caribbean anticyclones originate at the Lesser Antilles. There, the anticyclonic vorticity, which is necessary for the formation of such anticyclones, is generated locally at the islands. This generation is regulated by the magnitude of the transport through the passages between the islands, which is, in turn, regulated by the collision of NBC rings with the Lesser Antilles.
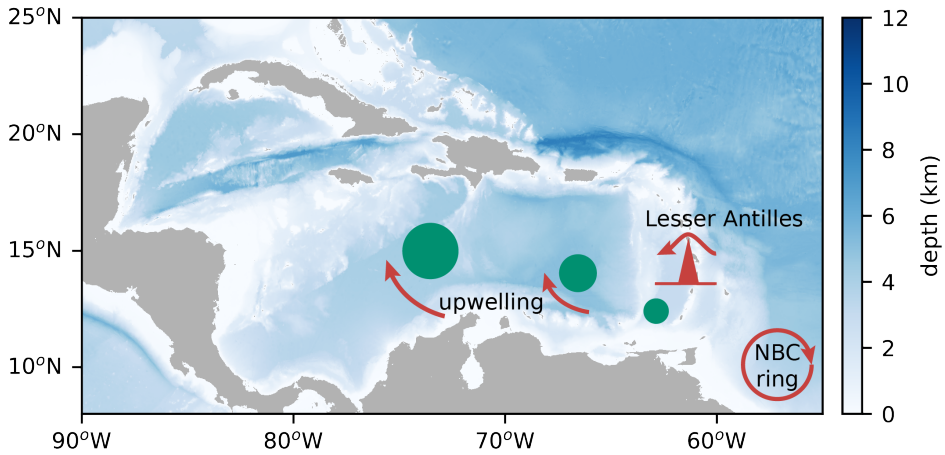
Figure 8.1: Schematic illustrating the main conclusions of the first part of this thesis containing the life cycle of Caribbean anticyclones.

During their formation, Caribbean anticyclones can entrain water from the Amazon and Orinoco River plumes. This results in a negative surface salinity anomaly inside the core of the anticyclones. The combination of these salinity anomalies with the slighter weaker temperature anomalies in the anticyclone compared to its surroundings determines their horizontal density gradients of the anticyclones in the eastern part of the basin. These horizontal density gradients appear to strengthen during the westward propagation of the anticyclones. This strengthening is the result of the advection of cold and saline upwelling filaments by the anticyclones themselves and could explain why the anticyclones intensify.

We also showed that not all anticyclones intensify on their path westward: Most energetic anticyclones advect upwelling filaments, while less energetic anticyclones do not. The anticyclone observed during the hydrographic survey belonged to the latter category, judging on a visual inspection of the sea-surface temperatures in the Caribbean Sea. In contrast to previous surveys (Silander, 2005; Rudzin et al., 2017), this anticyclone was shallow. These contrasting observations of the vertical extent of Caribbean anticyclones were captured by the realistic model in Chapter 3 of this thesis, which showed contained both shallow and deep anticyclones. This suggests that it is likely that the Caribbean anticyclones can have different vertical structures. We hypothesize that this might be related to the advection of upwelling filaments by the anticyclones, as, it is expected that this advection will adjust the vertical shear of the anticyclones.

The last three research questions concerned the global and regional impact of double-diffusive mixing. We developed an algorithm to automatically detect thermohaline staircases in vertical temperature and salinity profiles, and applied this algorithm on more than 480,000 observations to obtain a global dataset (Fig. 8.2). Using this global dataset, it was shown that the contribution of double-diffusive mixing to the global mechanical energy budget is very limited.
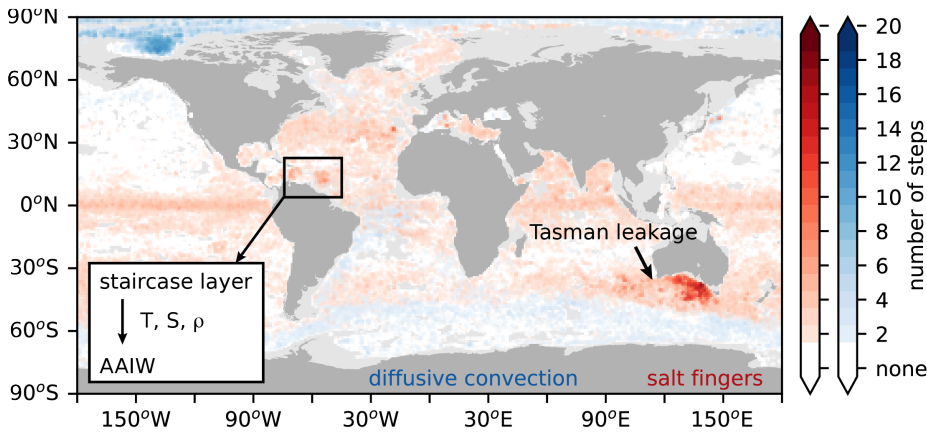
Figure 8.2: Figure summarizing the major conclusions of the second part of this thesis. The inlay schematizes the vertical transport in heat (T), salt (S) and density (ρ) between the staircase layer and Antarctic Intermediate Water (AAIW).

Moreover, the global dataset of thermohaline staircases also resulted in the discovery of a so-far unknown staircase region in the Great Australian Bight and Tasman Leakage (Fig. 8.2). In this region, the staircases overlie Antarctic Intermediate Water that is transported westwards towards the Atlantic Ocean. Although it remains unclear whether the double-diffusive fluxes can adjust the properties of AAIW in this region, we showed that double-diffusive mixing could have this capability in the Caribbean Sea. There, the vertical fluxes due to double-diffusive mixing are estimated to be larger than fluxes due to the horizontal mixing. These vertical double-diffusive fluxes can explain the observed spatial variation of the properties of Antarctic Intermediate Water.

Interaction between thermohaline staircases and Caribbean anti-cyclones

A combination of the results of the first three research questions with the results of the last three research questions reveals some aspects of the potential inter-actions between anticyclones and thermohaline staircases in the Caribbean Sea. The interaction between eddies and staircases could occur through a depression of the isopycnals or through enhanced shear (Morell et al., 2006; Radko, 2013): The depression of the isopycnals can facilitate the formation of thermohaline staircases below (Morell et al., 2006), and the enhanced shear of an eddy may increase the turbulence at depth which can break up the staircase (e.g., Radko, 2013).

During the survey presented in Chapter 2 of this thesis, thermohaline stair-cases were present below both the core and flanks of the anticyclone (Fig. 2.7). Remarkably, other eddy surveys in the Caribbean Sea showed different results

(Silander, 2005; Morell et al., 2006) as these studies indicated that the thermohaline staircases were better developed at the flanks of the eddy. Because the vertical shear and the isopycnal displacements in the staircase layer induced by the anticyclone could affect the development of the thermohaline staircases, one possible explanation for these different observations might be that Caribbean anticyclones have different vertical structures. In particular, the anticyclone surveyed by Silander (2005) had a deep structure and better defined staircases at the flanks, while the anticyclone surveyed in this thesis was shallow and contained staircases below both core and flanks of the anticyclone.

In a more detailed analysis of the thermohaline staircases in the Caribbean Sea, Koetsier (2019) showed that the passage of Caribbean anticyclones coincided with the destruction of thermohaline staircases. This might also explain why only 7 % of the profiles in the Caribbean Sea contain staircases as was found in Chapter 7 of this thesis. Although we cannot draw firm conclusions on this topic based on the results in this thesis, these findings highlight how the thermohaline staircases and Caribbean anticyclones might interact.

The Caribbean Sea in a changing climate

A motivation to study the dynamics of the Caribbean Sea is to be able to predict how the dynamics in the Caribbean Sea might be affected by climate change. Although it is impossible to precisely determine how climate change will affect the basin, it is possible to discuss the observed trends in light of the findings in this thesis and to qualitatively consider the potential future of the Caribbean Sea.

The most remarkable recent change in the Caribbean Sea is of ecological nature: the inundation of massive amounts of Sargassum algae (Gower et al., 2013; Wang and Hu, 2017; Putman et al., 2018; Johns et al., 2020). These algae have been appearing since 2011, and have negatively impacted the local fisheries and tourism (Gower et al., 2013; Wang and Hu, 2017; Resiere et al., 2018). A part of the Sargassum algae is transported towards the Caribbean by NBC rings (Putman et al., 2018). Based on the results in this thesis, it seems that the NBC rings are destroyed at the Lesser Antilles. During this interaction, the Sargassum algae contained in these rings could be entrained in the Caribbean anticyclones that are formed on the Caribbean side of the islands. Moreover, because both Caribbean cyclones and anticyclones entrain river water from the Orinoco River (Chapter 2 of this thesis, Corredor et al., 2004; Chérubin and Richardson, 2007), this river water could provide an additional source of nutrients to the Sargassum algae captures in these eddies. Not only could lead to the additional growth of the Sargassum in the Caribbean Sea (Johns et al., 2020), the pathways of the Caribbean eddies might also determine to a certain extent the pathways of the Sargassum algae.

Furthermore, the results in this thesis also highlight which climatic changes might impact the dynamics of the Caribbean Sea more than others. We found, for example, that stronger upwelling winds directly resulted in more variability in the

western part of the basin through the strengthening of the anticyclones (Chapter 4 of this thesis). While this strengthens the temperature gradients along the path of the anticyclones, the initial density difference between the anticyclone and its surrounding appeared to be dominated by salinity differences. This initial density difference highlights the importance of the river plumes of the Amazon and Orinoco Rivers in the Caribbean Sea, as was also mentioned by, for example, Hellweger and Gordon (2002) and Chérubin and Richardson (2007). These river plumes decrease the salinity of the surface layer, which benefits the formation of barrier layers that arise in regions with strong vertical salinity gradients (Pailler et al., 1999; Foltz and McPhaden, 2009).

In this thesis, it is shown that the observed anticyclone entrained river water and that it contained a relatively thick barrier layer compared to its surroundings, which is similar to observations of Rudzin et al. (2017). Because we found in Chapter 4 of this thesis that the horizontal salinity gradients in the anticyclones are determined at the Lesser Antilles, where the anticyclones entrain river water during their formation, changes in the availability of fresh river water at the Lesser Antilles might affect the strength of the Caribbean anticyclones. Although it is unclear whether the salinity of the river plume at the Lesser Antilles will decrease in a future climate due to a weakening of the wind forcing (Campbell et al., 2011; Lima and Wethey, 2012; Torres and Tsimplis, 2013) or change due to a stronger seasonal cycle of the precipitation over South America (Aguilar et al., 2005; Liang et al., 2020), we hypothesize that changes in the salinity of the river plume could affect the surface dynamics in the Caribbean Sea.

Climate change might also impact the subsurface waters in the Caribbean Sea, as the properties of the subsurface water masses depend on atmospheric variations in their formation regions (e.g., Speer and Tziperman, 1992; Ganachaud, 2003). An example of how minor changes in the properties of the subsurface water masses affects the abyssal mixing is given in Chapter 7 of this thesis. In that case, the diapycnal mixing depends on the ratio of the second derivatives of temperature and salinity, which is very sensitive to the properties of the water masses. Recent studies have shown that the properties of both STUW and AAIW are variable on decadal time scales (Arbic and Brechner Owens, 2001; Yu et al., 2018; Fu et al., 2018; Liu et al., 2019). For example, a salinity increase of Subtropical Underwater affects the stratification. This could result in an increase of the Turner angle, which would in turn make the water column more favorable for the formation of thermohaline staircases. Because these thermohaline staircases affect the vertical fluxes of heat and salt, changes in the salinity of Subtropical Underwater could affect the magnitude of the vertical mixing as well.

Moreover, multiple studies suggested that the strength of the volume transport of the AMOC could decrease in the future (e.g., Robson et al., 2014; McCarthy et al., 2015). This weaker transport of the AMOC is associated with a weaker inflow into the Caribbean Sea. This could not only affect the interaction of the ocean currents with the Lesser Antilles, but also the advection of upwelling waters by the anticyclones. Furthermore, it might weaken the inflow of deeper

water masses as well. For example, a decrease of the flow is expected to result in less mixing at the Lesser Antilles, where we found distinctive changes in the properties of Antarctic Intermediate Water (Chapter 7 of this thesis). Overall, this broad range of possible consequences of climate change indicate that the Caribbean Sea is a highly dynamical basin, where the dynamics of the flow are set by both upstream variability as well as the forcing within the basin.

8.3   Recommendations

In this thesis, the dynamics of mesoscale anticyclones and double diffusion have been assessed. In this section, we provide some recommendations for future research. The first suggestions contain recommendations for studies in other regions based on the findings presented in this thesis. These recommendations are based on the assumption that other ocean basins should contain similar dynamics as found in the Caribbean Sea. For example, approximately 40 % of the ocean is susceptible to double-diffusive mixing (You, 2002) and that nearly one-third of the ocean surface is covered by mesoscale eddies at any given time (Gaube et al., 2019). Therefore, the analyses and results in this thesis can be useful to clarify some aspects of the flow in other basins. The last two recommendations describe possible directions for further research in the Caribbean Sea.

Eddy-island interaction

First of all, the interaction of eddies with islands is not unique and there are numerous regions that show this type of interaction (e.g., Schouten et al., 2000; Wang and Dewar, 2003; Johnson and McDonald, 2005; Rennie et al., 2007). In the case of the Caribbean Sea, it turned out that the anticyclonic vorticity of Caribbean anticyclones originates from the interaction of the flow with the Lesser Antilles. The anticyclonic vorticity in remnants of NBC rings that is advected into the basin seems of lesser importance. Because these findings highlight the importance of vorticity generation near topography, we suggest to revisit the eddy-island interaction in other ocean basins and apply a similar approach to quantify the vorticity generation in those regions.

Barrier layers

Also the formation of barrier layers is not a unique feature of the Caribbean Sea (Sprintall and Tomczak, 1992; de Boyer Montégut et al., 2004). In this thesis, the hydrographic survey revealed that the barrier layer in the anticyclone was thicker and contained a stronger temperature inversion than the waters surrounding the anticyclone. This is in line with previous observations (Rudzin et al., 2017) and suggests that anticyclones can potentially store extra heat below the surface. Because thick barrier layers, and especially those with strong temperature inversions, are associated with rapid intensification of tropical cyclones (Foltz and

McPhaden, 2009; Wang et al., 2011; Balaguru et al., 2012), the relationship between anticyclones and barrier layers deserves more attention. This will increase the understanding of the variation and impact of barrier layers, not only in the Caribbean, but also in all other regions, in for example the Indian Ocean and Pacific Ocean (de Boyer Montégut et al., 2004), that contain barrier layers.

Intensification of anticyclones

The analysis of the westward intensification of the Caribbean anticyclones revealed that part of the intensification could be explained by a variation of the background properties. In particular, the anticyclones are formed in the eastern part of the basin, where the waters are relatively light. They travel towards the west, where the surface waters are denser due to the wind-driven upwelling in the southern part of the basin. This intensification is not unique for the Caribbean Sea, and anticyclones in other ocean basins also have the tendency to grow over time (Dewar and Killworth, 1995; Yavneh et al., 1997; Koszalka et al., 2009; Chen and Han, 2019). Similar to the Caribbean Sea, the anticyclones at other locations have, on average, longer tracks than cyclones (Chelton et al., 2011b). The results of this thesis highlight the importance to study also the surroundings of ocean eddies to explain their behavior.

Water-mass changes induced by double-diffusive mixing

The analysis of the double-diffusive mixing in the Caribbean Sea indicates a mechanism through which thermohaline staircases could affect the water masses below the staircase layer. Studies of the Mediterranean (Bryden et al., 2014; Schroeder et al., 2016) indicate that the Caribbean Sea is not the only basin where this mechanism takes place, and it is plausible that also water masses in other regions with a frequent staircase occurrence are modulated by double-diffusive mixing. As argued in Chapter 6 of this thesis, it is important to quantify these vertical fluxes in, for example, the Tasman Leakage, because these waters are known to affect the stability of the Atlantic Meridional Overturning Circulation (Gordon, 2003; Speich et al., 2007).

Implementation of the effects of double-diffusive mixing in ocean models

In most ocean models, the role of double-diffusive mixing is neglected. Although our results suggest that this is valid regarding the global mechanical energy budget, it most likely not valid regarding local water mass transformation by double-diffusive fluxes. Using the global analysis of the staircase occurrence, regions where the mixing is dominated by double diffusion are identified. In these regions, the heat and salt flux do not have the same magnitude, and double-diffusive fluxes can modulate the regional climate as illustrated by changes in

AAIW (Chapter 7 of this thesis). This, consequently, is expected to impact the ocean circulation. The most simple way to account for double-diffusion in global ocean models, is to modify the ratio of the effective diffusivities in these specific regions, which is expected to result in a more accurate representation of the ocean circulation.

Double diffusion and Atlantic Meridional Overturning Circulation

The discovery of the thermohaline staircases in the Tasman Leakage region and the fact that double-diffusive fluxes in thermohaline staircases can modify Antarctic Intermediate Water raises the question whether double diffusion impacts the stability of the Atlantic Meridional Overturning Circulation (AMOC). To resolve this question, inverse models can be used to extract average effective diffusivities of heat and salt in regions with high staircase occurrence. The ratio between the effective diffusivity of heat and salt will give insight into whether double-diffusion affects the salt content of the Tasman Leakage Waters, which in turn are associated with the stability of the AMOC.

River outflow of the Amazon and Orinoco Rivers

The river plumes of the Amazon and Orinoco Rivers are advected into the Caribbean Sea. The arrival of the combined Amazon-Orinoco river plume coincides with an increase of the eddy kinetic energy (Chérubin and Richardson, 2007). Because the two river plumes arrive simultaneously at the Lesser Antilles, it remains unknown how each river plume affects the surface flow in the Caribbean. The discharge of the Amazon River exceeds the discharge of the Orinoco River, but the mouth of the Orinoco River is located at the Lesser Antilles. This implies that the Orinoco River plume is most likely fresher than the Amazon River plume, but has a much smaller area. To understand the interaction between these two river plumes better, it would be interesting to identify how each river plume affects the surface dynamics in the Caribbean Sea.

Eddies and staircases

In his master thesis, Koetsier (2019) analyzed four Argo floats deployed during the hydrographic survey presented in Chapter 2 of this thesis. He suggested that Caribbean anticyclones might have the capability to destroy thermohaline staircases. In particular, he found that the passage of a strong anticyclonic eddy coincided with the destruction of a staircase structure. It would be interesting to explore this connection in more detail and extend the analysis towards the staircase region in the western tropical Atlantic Ocean, where the surface flow is dominated by the passage of large North Brazil Current rings.

Bibliography

Abernathey, R. P., Cerovecki, I., Holland, P. R., Newsom, E., Mazloff, M., and Talley, L. D.: Water-Mass Transformation by Sea Ice in the Upper Branch of the Southern Ocean Overturning, Nature Geoscience, 9, 596–601, doi:10.1038/ngeo2749, 2016.

Aguilar, E., Peterson, T. C., Obando, P. R., Frutos, R., Retana, J. A., Solera, M., Soley, J., García, I. G., Araujo, R. M., Santos, A. R., Valle, V. E., Brunet, M., Aguilar, L., Álvarez, L., Bautista, M., Castañón, C., Herrera, L., Ruano, E., Sinay, J. J., Sánchez, E., Oviedo, G. I. H., Obed, F., Salgado, J. E., Vázquez, J. L., Baca, M., Gutiérrez, M., Centella, C., Espinosa, J., Martínez, D., Olmedo, B., Espinoza, C. E. O., Núñez, R., Haylock, M., Benavides, H., and Mayorga, R.: Changes in Precipitation and Temperature Extremes in Central America and Northern South America, 1961–2003, Journal of Geophysical Research, 110, D23 107, doi:10.1029/2005JD006119, 2005.

Alvera-Azcárate, A., Barth, A., and Weisberg, R. H.: The Surface Circulation of the Caribbean Sea and the Gulf of Mexico as Inferred from Satellite Altimetry, Journal of Physical Oceanography, 39, 640–657, doi:10.1175/2008JPO3765.1, 2009.

Andersson, A., Fennig, K., Klepp, C., Bakan, S., Graßl, H., and Schulz, J.: The Hamburg Ocean Atmosphere Parameters and Fluxes from Satellite Data – HOAPS-3, Earth System Science Data, 2, 215–234, doi:10.5194/essd-2-215-2010, 2010.

Andrade, C. A.: Evidence for an Eastward Flow along the Central and South American Caribbean Coast, Journal of Geophysical Research, 108, 3185, doi:10.1029/2002JC001549, 2003.

Andrade, C. A. and Barton, E. D.: Eddy Development and Motion in the Caribbean Sea, Journal of Geophysical Research: Oceans, 105, 26 191–26 201, doi:10.1029/2000JC000300, 2000.

Andrade, C. A. and Barton, E. D.: The Guajira Upwelling System, Continental Shelf Research, 25, 1003–1022, doi:10.1016/j.csr.2004.12.012, 2005.

Arbic, B. K. and Brechner Owens, W.: Climatic Warming of Atlantic Intermediate Waters*, Journal of Climate, 14, 4091–4108, doi:10.1175/1520-0442(2001)014<4091:CWOAIW>2.0.CO;2, 2001.

Argo: Argo User's Manual V3.3, Ifremer, doi:10.13155/29825, 2019.

Argo: Argo Float Data and Metadata from Global Data Assembly Centre (Argo GDAC), doi:10.17882/42182, 2020.

Ashmole, N. P.: The Regulation of Numbers of Tropical Oceanic Birds, Ibis, 103, 458–473, 1963.

Astor, Y., Müller-Karger, F., and Scranton, M. I.: Seasonal and Interannual Variation in the Hydrography of the Cariaco Basin: Implications for Basin Ventilation, Continental Shelf Research, 23, 125–144, 2003.

Bakun, A.: Fronts and Eddies as Key Structures in the Habitat of Marine Fish Larvae: Opportunity, Adaptive Response and Competitive Advantage, Scientia Marina, 70, 105–122, doi:10.3989/scimar.2006.70s2105, 2006.

Balaguru, K., Chang, P., Saravanan, R., and Jang, C. J.: The Barrier Layer of the Atlantic Warmpool: Formation Mechanism and Influence on the Mean Climate, Tellus A: Dynamic Meteorology and Oceanography, 64, 18 162, doi:10.3402/tellusa.v64i0.18162, 2012.

Baums, I. B., Miller, M. W., and Hellberg, M. E.: Geographic Variation in Clonal Structure in a Reef–Building Caribbean Coral, Acropora Palmata, Ecological monographs, 76, 503–519, 2006.

Bebieva, Y. and Speer, K.: The Regulation of Sea Ice Thickness by Double-Diffusive Processes in the Ross Gyre, Journal of Geophysical Research: Oceans, 124, 7068–7081, doi:10.1029/2019JC015247, 2019.

Bebieva, Y. and Timmermans, M.-L.: An Examination of Double–Diffusive Processes in a

Mesoscale Eddy in the Arctic Ocean, Journal of Geophysical Research: Oceans, 121, 457–475, doi:10.1002/2015JC011105, 2016.

Bebieva, Y. and Timmermans, M.-L.: The Relationship between Double-Diffusive Intrusions and Staircases in the Arctic Ocean, Journal of Physical Oceanography, 47, 867–878, doi:10.1175/JPO-D-16-0265.1, 2017.

Bebieva, Y. and Timmermans, M.-L.: Double-diffusive Layering in the Canada Basin: An Explanation of Along-layer Temperature and Salinity Gradients, Journal of Geophysical Research: Oceans, 124, 723–735, doi:10.1029/2018JC014368, 2019.

Beier, E., Bernal, G., Ruiz-Ochoa, M., and Barton, E. D.: Freshwater Exchanges and Surface Salinity in the Colombian Basin, Caribbean Sea, PLoS ONE, 12, doi:10.1371/journal.pone.0182116, 2017.

Bertrand, S., Gohin, F., and Garello, R.: Regional Objective Analysis for Merging MERIS, MODIS/Aqua and SeaWiFS Chlorophyll–a Data from 1998 to 2008 on the European Atlantic Shelf at a Resolution of 1.1 Km, in: Oceans 2009–Europe, pp. 1–10, IEEE, 2009.

Bidigare, R. R., Ondrusek, M. E., and Brooks, J. M.: Influence of the Orinoco River Outflow on Distributions of Algal Pigments in the Caribbean Sea, Journal of Geophysical Research: Oceans, 98, 2259–2269, doi:10.1029/92JC02762, 1993.

Bosch, W., Acuña, G., and Kaniuth, R.: Caribbean Sea Level Variability from TOPEX/Poseidon Altimetry, in: Vertical Reference Systems, edited by Sansò, F., Drewes, H., Dodson, A. H., Fortes, L. P. S., Sánchez, L., and Sandoval, P., vol. 124, pp. 249–254, Springer Berlin Heidelberg, Berlin, Heidelberg, doi:10.1007/978-3-662-04683-8_47, 2002.

Bower, A., Lozier, S., Biastoch, A., Drouin, K., Foukal, N., Furey, H., Lankhorst, M., Rühs, S., and Zou, S.: Lagrangian Views of the Pathways of the Atlantic Meridional Overturning Circulation, Journal of Geophysical Research: Oceans, 124, 5313–5335, doi:10.1029/2019JC015014, 2019.

Brooks, M. T., Coles, V. J., and Coles, W. C.: Inertia Influences Pelagic Sargassum Advection and Distribution, Geophysical Research Letters, 46, 2610–2618, doi:10.1029/2018GL081489, 2019.

Bryden, H. L., Schroeder, K., Sparnocchia, S., Borghini, M., and Vetrano, A.: Thermohaline Staircases in the Western Mediterranean Sea, Journal of Marine Research, 72, 1–18, doi:10.1357/002224014812655198, 2014.

Buffett, G. G., Krahmann, G., Klaeschen, D., Schroeder, K., Sallarès, V., Papenberg, C., Ranero, C. R., and Zitellini, N.: Seismic Oceanography in the Tyrrhenian Sea: Thermohaline Staircases, Eddies, and Internal Waves, Journal of Geophysical Research: Oceans, 122, 8503–8523, doi:10.1002/2017JC012726, 2017.

Campbell, J. D., Taylor, M. A., Stephenson, T. S., Watson, R. A., and Whyte, F. S.: Future Climate of the Caribbean from a Regional Climate Model, International Journal of Climatology, 31, 1866–1878, doi:10.1002/joc.2200, 2011.

Camphuysen, C. J. and Garthe, S.: Recording Foraging Seabirds at Sea: Standardised Recording and Coding of Foraging Behaviour and Multi–Species Foraging Associations, Atlantic Seabirds, 5, 1–23, 2004.

Candela, J.: Yucatan Channel Flow: Observations versus CLIPPER ATL6 and MERCATOR PAM Models, Journal of Geophysical Research, 108, 3385, doi:10.1029/2003JC001961, 2003.

Cardoso, C., Caldeira, R. M., Relvas, P., and Stegner, A.: Islands as Eddy Transformation and Generation Hotspots: Cabo Verde Case Study, Progress in Oceanography, 184, 102 271, doi:10.1016/j.pocean.2020.102271, 2020.

CARIACO–project: Variation in the Salinity at the CARIACO Time–Series Station, 2018.

Carrillo, L., Johns, E., Smith, R., Lamkin, J., and Largier, J.: Pathways and Hydrography in the Mesoamerican Barrier Reef System Part 2: Water Masses and Thermohaline Structure, Continental Shelf Research, 120, 41–58, doi:10.1016/j.csr.2016.03.014, 2016.

Carton, J. A. and Chao, Y.: Caribbean Sea Eddies Inferred from TOPEX/Poseidon Altimetry and a 1/6 Atlantic Ocean Model Simulation, Journal of Geophysical Research: Oceans, 104, 7743–7752, doi:10.1029/1998JC900081, 1999.

Casanova-Masjoan, M., Joyce, T., Pérez-Hernández, M., Vélez-Belchí, P., and Hernández-Guerra, A.: Changes across 66W, the Caribbean Sea and the Western Boundaries of the North Atlantic Subtropical Gyre, Progress in Oceanography, 168, 296–309, doi:10.1016/j.pocean.2018.09.013,

2018.

Castellana, D., Baars, S., Wubs, F. W., and Dijkstra, H. A.: Transition Probabilities of Noise-Induced Transitions of the Atlantic Ocean Circulation, Scientific Reports, 9, 20 284, doi:10.1038/s41598-019-56435-6, 2019.

Cenedese, C., Adduce, C., and Fratantoni, D. M.: Laboratory Experiments on Mesoscale Vortices Interacting with Two Islands, Journal of Geophysical Research, 110, C09 023, doi:10.1029/2004JC002734, 2005.

Centurioni, L. R. and Niiler, P. P.: On the Surface Currents of the Caribbean Sea, Geophysical Research Letters, 30, doi:10.1029/2002GL016231, 2003.

Chang, Y. and Oey, L.: Coupled Response of the Trade Wind, SST Gradient, and SST in the Caribbean Sea, and the Potential Impact on Loop Current's Interannual Variability*, Journal of Physical Oceanography, 43, 1325–1344, doi:10.1175/JPO-D-12-0183.1, 2013.

Chassignet, E. P. and Verron, J., eds.: Ocean Modeling and Parameterization, Springer Netherlands, Dordrecht, doi:10.1007/978-94-011-5096-5, 1998.

Chelton, D. B., DeSzoeke, R. A., Schlax, M. G., El Naggar, K., and Siwertz, N.: Geographical Variability of the First Baroclinic Rossby Radius of Deformation, Journal of Physical Oceanography, 28, 433–460, doi:10.1175/1520-0485(1998)028<0433:GVOTFB>2.0.CO;2, 1998.

Chelton, D. B., Schlax, M. G., Samelson, R. M., and de Szoeke, R. A.: Global Observations of Large Oceanic Eddies, Geophysical Research Letters, 34, doi:10.1029/2007GL030812, 2007.

Chelton, D. B., Gaube, P., Schlax, M. G., Early, J. J., and Samelson, R. M.: The Influence of Nonlinear Mesoscale Eddies on near–Surface Oceanic Chlorophyll, Science, 334, 328–332, doi:10.1126/science.1208897, 2011a.

Chelton, D. B., Schlax, M. G., and Samelson, R. M.: Global Observations of Nonlinear Mesoscale Eddies, Progress in Oceanography, 91, 167–216, doi:10.1016/j.pocean.2011.01.002, 2011b.

Chen, G. and Han, G.: Contrasting Short-lived with Long-lived Mesoscale Eddies in the Global Ocean, Journal of Geophysical Research: Oceans, 124, 3149–3167, doi:10.1029/2019JC014983, 2019.

Chérubin, L. and Richardson, P.: Caribbean Current Variability and the Influence of the Amazon and Orinoco Freshwater Plumes, Deep Sea Research Part I: Oceanographic Research Papers, 54, 1451–1473, doi:10.1016/j.dsr.2007.04.021, 2007.

Coles, V. J., Brooks, M. T., Hopkins, J., Stukel, M. R., Yager, P. L., and Hood, R. R.: The Pathways and Properties of the Amazon River Plume in the Tropical North Atlantic Ocean, Journal of Geophysical Research: Oceans, 118, 6894–6913, doi:10.1002/2013JC008981, 2013.

Corredor, J., Morell, J., López, J., Armstrong, R., Dieppa, A., Cabanillas, C., Cabrera, A., and Hensley, V.: Remote Continental Forcing of Phytoplankton Biogeochemistry: Observations across the "Caribbean-Atlantic Front", Geophysical Research Letters, 30, 2003GL018 193, doi:10.1029/2003GL018193, 2003.

Corredor, J. E. and Morell, J. M.: Seasonal Variation of Physical and Biogeochemical Features in Eastern Caribbean Surface Water, Journal of Geophysical Research: Oceans, 106, 4517–4525, doi:10.1029/2000JC000291, 2001.

Corredor, J. E., Morell, J. M., Lopez, J. M., Capella, J. E., and Armstrong, R. A.: Cyclonic Eddy Entrains Orinoco River Plume in Eastern Caribbean, Eos, Transactions American Geophysical Union, 85, 197–202, doi:10.1029/2004EO200001, 2004.

Cruz-Gómez, R. C. and Vazquez, H. J.: Interaction of North Brazil Current Rings with the Lesser Antilles Arc and Barbados Island: Laboratory Experiments and Observations, Environmental Fluid Mechanics, 18, 1203–1226, doi:10.1007/s10652-018-9592-x, 2018.

Curry, R., Dickson, B., and Yashayaev, I.: A Change in the Freshwater Balance of the Atlantic Ocean over the Past Four Decades, Nature, 426, 826–829, doi:10.1038/nature02206, 2003.

Dai, A. and Trenberth, K. E.: Estimates of Freshwater Discharge from Continents: Latitudinal and Seasonal Variations, Journal of Hydrometeorology, 3, 660–687, doi:10.1175/1525-7541(2002)003<0660:EOFDFC>2.0.CO;2, 2002.

Danabasoglu, G., McWilliams, J. C., and Gent, P. R.: The Role of Mesoscale Tracer Transports in the Global Ocean Circulation, Science, 264, 1123–1126, doi:10.1126/science.264.5162.1123, 1994.

de Boyer Montégut, C., Madec, G., Fischer, A. S., Lazar, A., and Iudicone, D.: Mixed Layer Depth

over the Global Ocean: An Examination of Profile Data and a Profile–Based Climatology, Journal of Geophysical Research C: Oceans, 109, 1–20, doi:10.1029/2004JC002378, 2004.

de Boyer Montégut, C., Mignot, J., Lazar, A., and Cravatte, S.: Control of Salinity on the Mixed Layer Depth in the World Ocean: 1. General Description, Journal of Geophysical Research: Oceans, 112, doi:10.1029/2006JC003953, 2007.

de Jong, M. F.: Cruise Report 64PE431, Tech. rep., Royal Netherlands Institute for Sea Research, 2018.

de Jong, Maria: Ocean Current Patterns and Variability around Curaçao for Ocean Thermal Energy Conversion, Master thesis, Delft University of Technology, Delft, 2017.

de Vries, P. and Weber, S. L.: The Atlantic Freshwater Budget as a Diagnostic for the Existence of a Stable Shut down of the Meridional Overturning Circulation, Geophysical Research Letters, 32, doi:10.1029/2004GL021450, 2005.

Dee, D. P., Uppala, S. M., Simmons, A., Berrisford, P., Poli, P., Kobayashi, S., Andrae, U., Balmaseda, M., Balsamo, G., Bauer, d. P., et al.: The ERA-Interim Reanalysis: Configuration and Performance of the Data Assimilation System, Quarterly Journal of the royal meteorological society, 137, 553–597, 2011.

Deremble, B., Dewar, W. K., and Chassignet, E. P.: Vorticity Dynamics near Sharp Topographic Features, Journal of Marine Research, 74, 249–276, doi:10.1357/002224016821744142, 2016.

Dewar, W. K. and Killworth, P. D.: On the Stability of Oceanic Rings, Journal of Physical Oceanography, 25, 1467–1487, doi:10.1175/1520-0485(1995)025<1467:OTSOOR>2.0.CO;2, 1995.

Didden, N. and Schott, F.: Eddies in the North Brazil Current Retroflection Region Observed by Geosat Altimetry, Journal of Geophysical Research, 98, 20 121, doi:10.1029/93JC01184, 1993.

Dijkstra, H. A.: Characterization of the Multiple Equilibria Regime in a Global Ocean Model, Tellus A: Dynamic Meteorology and Oceanography, 59, 695–705, doi:10.1111/j.1600-0870.2007.00267.x, 2007.

Dong, C. and McWilliams, J. C.: A Numerical Study of Island Wakes in the Southern California Bight, Continental Shelf Research, 27, 1233–1248, doi:10.1016/j.csr.2007.01.016, 2007.

Dong, S., Sprintall, J., Gille, S. T., and Talley, L.: Southern Ocean Mixed-Layer Depth from Argo Float Profiles, Journal of Geophysical Research, 113, C06 013, doi:10.1029/2006JC004051, 2008.

Drijfhout, S. S.: The Origin of Intermediate and Subpolar Mode Waters Crossing the Atlantic Equator in OCCAM, Geophysical Research Letters, 32, L06 602, doi:10.1029/2004GL021851, 2005.

Ducet, N., Le Traon, P.-Y., and Reverdin, G.: Global High-Resolution Mapping of Ocean Circulation from TOPEX/Poseidon and ERS-1 and-2, Journal of Geophysical Research: Oceans, 105, 19 477–19 498, 2000.

Dufois, F., Hardman–Mountford, N. J., Greenwood, J., Richardson, A. J., Feng, M., and Matear, R. J.: Anticyclonic Eddies Are More Productive than Cyclonic Eddies in Subtropical Gyres Because of Winter Mixing, Science Advances, 2, e1600 282, doi:10.1126/sciadv.1600282, 2016.

Durack, P. J. and Wijffels, S. E.: Fifty-Year Trends in Global Ocean Salinities and Their Relationship to Broad-Scale Warming, Journal of Climate, 23, 4342–4362, doi:10.1175/2010JCLI3377.1, 2010.

Duran-Matute, M. and Fuentes, O. U. V.: Passage of a Barotropic Vortex through a Gap, Journal of Physical Oceanography, 38, 2817–2831, doi:10.1175/2008JPO3887.1, 2008.

Durante, S., Schroeder, K., Mazzei, L., Pierini, S., Borghini, M., and Sparnocchia, S.: Permanent Thermohaline Staircases in the Tyrrhenian Sea, Geophysical Research Letters, 46, 1562–1570, doi:10.1029/2018GL081747, 2019.

Early, J. J., Samelson, R. M., and Chelton, D. B.: The Evolution and Propagation of Quasigeostrophic Ocean Eddies, Journal of Physical Oceanography, 41, 1535–1555, doi:10.1175/2011JPO4601.1, 2011.

Egbert, G. D. and Erofeeva, S. Y.: Efficient Inverse Modeling of Barotropic Ocean Tides, Journal of Atmospheric and Oceanic Technology, 19, 183–204, 2002.

Ezer, T., Thattai, D. V., Kjerfve, B., and Heyman, W. D.: On the Variability of the Flow along the Meso–American Barrier Reef System: A Numerical Model Study of the Influence of the Caribbean Current and Eddies, Ocean Dynamics, 55, 458–475, doi:10.1007/s10236-005-0033-2, 2005.

Falkowski, P. G., Ziemann, D., Kolber, Z., and Bienfang, P. K.: Role of Eddy Pumping in Enhancing Primary Production in the Ocean, Nature, 352, 55, doi:10.1038/352055a0, 1991.

Fekete, B., Vorosmarty, C., and Grabs, W.: Global Composite Runoff Fields Based on Observed Discharge and Simulated Water Balance, Rep. 22, Tech. rep., Global Runoff Data Cent., Koblenz, Germany, doi:10.1029/1999GB001254, 2000.

Fer, I., Nandi, P., Holbrook, W. S., Schmitt, R. W., and Páramo, P.: Seismic Imaging of a Thermohaline Staircase in the Western Tropical North Atlantic, Ocean Science, 6, 621–631, doi:10.5194/os-6-621-2010, 2010.

Ferrari, R. and Wunsch, C.: Ocean Circulation Kinetic Energy: Reservoirs, Sources, and Sinks, Annual Review of Fluid Mechanics, 41, 253–282, doi:10.1146/annurev.fluid.40.111406.102139, 2009.

Ffield, A.: North Brazil Current Rings Viewed by TRMM Microwave Imager SST and the Influence of the Amazon Plume, Deep Sea Research Part I: Oceanographic Research Papers, 52, 137–160, doi:10.1016/j.dsr.2004.05.013, 2005.

Fine, R. A.: Circulation of Antarctic Intermediate Water in the South Indian Ocean, Deep Sea Research Part I: Oceanographic Research Papers, 40, 2021–2042, doi:10.1016/0967-0637(93)90043-3, 1993.

Flanagan, J. D., Lefler, A. S., and Radko, T.: Heat Transport through Diffusive Interfaces, Geophysical Research Letters, 40, 2466–2470, doi:10.1002/grl.50440, 2013.

Foltz, G. R. and McPhaden, M. J.: Impact of Barrier Layer Thickness on SST in the Central Tropical North Atlantic*, Journal of Climate, 22, 285–299, doi:10.1175/2008JCLI2308.1, 2009.

Fournier, S., Vandemark, D., Gaultier, L., Lee, T., Jonsson, B., and Gierach, M. M.: Interannual Variation in Offshore Advection of Amazon-Orinoco Plume Waters: Observations, Forcing Mechanisms, and Impacts, Journal of Geophysical Research: Oceans, 122, 8966–8982, doi:10.1002/2017JC013103, 2017.

Fratantoni, D. M. and Glickson, D. A.: North Brazil Current Ring Generation and Evolution Observed with SeaWiFS, Journal of Physical Oceanography, 32, 1058–1074, 2002.

Fratantoni, D. M. and Richardson, P. L.: The Evolution and Demise of North Brazil Current Rings*, Journal of Physical Oceanography, 36, 1241–1264, doi:10.1175/JPO2907.1, 2006.

Froelich Jr., P. N., Atwood, D. K., and Giese, G. S.: Influence of Amazon River Discharge on Surface Salinity and Dissolved Silicate Concentration in the Caribbean Sea, Deep Sea Research, 25, 735–744, doi:10.1016/0146-6291(78)90627-6, 1978.

Fu, L.-L., Chelton, D. B., Le Traon, P.-Y., and Morrow, R.: Eddy Dynamics from Satellite Altimetry, Oceanography, 23, 14–25, 2010.

Fu, Y., Karstensen, J., and Brandt, P.: Atlantic Meridional Overturning Circulation at 14.5N in 1989 and 2013 and 24.5N in 1992 and 2015: Volume, Heat, and Freshwater Transports, Ocean Science, 14, 589–616, doi:10.5194/os-14-589-2018, 2018.

Fu, Y., Wang, C., Brandt, P., and Greatbatch, R. J.: Interannual Variability of Antarctic Intermediate Water in the Tropical North Atlantic, Journal of Geophysical Research: Oceans, 124, 4044–4057, doi:10.1029/2018JC014878, 2019.

Ganachaud, A.: Large-Scale Mass Transports, Water Mass Formation, and Diffusivities Estimated from World Ocean Circulation Experiment (WOCE) Hydrographic Data, Journal of Geophysical Research, 108, 3213, doi:10.1029/2002JC001565, 2003.

Garaud, P.: Double-Diffusive Convection at Low Prandtl Number, Annual Review of Fluid Mechanics, 50, 275–298, doi:10.1146/annurev-fluid-122316-045234, 2018.

Gargett, A. E. and Holloway, G.: Sensitivity of the GFDL Ocean Model to Different Diffusivities for Heat and Salt, Journal of Physical Oceanography, 22, 1158–1177, doi:10.1175/1520-0485(1992)022<1158:SOTGOM>2.0.CO;2, 1992.

Garrett, C.: Internal Tides and Ocean Mixing, Science, 301, 1858, doi:10.1126/science.1090002, 2003.

Gaspar, P., Goris, Y. G. R. I., and Lefevre, J.: A Simple Eddy Kinetic Energy Model for Simulations of the Oceanic Vertical Mixing: Tests at Station Papa and Long–Term Upper Ocean Study Site, Journal of Geophysical Research: Oceans, 95, 179–193, 1990.

Gaube, P.: Satellite Observations of Mesoscale Eddy–Induced Ekman Pumping, Journal of Physical

Oceanography, 45, 104–132, doi:10.1175/JPO-D-14-0032.1, 2015.

Gaube, P., Chelton, D. B., Strutton, P. G., and Behrenfeld, M. J.: Satellite Observations of Chlorophyll, Phytoplankton Biomass, and Ekman Pumping in Nonlinear Mesoscale Eddies, Journal of Geophysical Research: Oceans, 118, 6349–6370, doi:10.1002/2013JC009027, 2013.

Gaube, P., McGillicuddy, D. J., Chelton, D. B., Behrenfeld, M. J., and Strutton, P. G.: Regional Variations in the Influence of Mesoscale Eddies on near–Surface Chlorophyll, Journal of Geophysical Research: Oceans, 119, 8195–8220, doi:10.1002/2014JC010111, 2014.

Gaube, P., J. McGillicuddy, D., and Moulin, A. J.: Mesoscale Eddies Modulate Mixed Layer Depth Globally, Geophysical Research Letters, 46, 1505–1512, doi:10.1029/2018GL080006, 2019.

Georgiou, S., Ypma, S. L., Brüggemann, N., Sayol, J.-M., Pietrzak, J. D., and Katsman, C. A.: Pathways of the Water Masses Exiting the Labrador Sea: The Importance of Boundary–Interior Exchanges, Ocean Modelling, 150, 101 623, doi:10.1016/j.ocemod.2020.101623, 2020.

Gilbes, F. and Armstrong, R. A.: Phytoplankton Dynamics in the Eastern Caribbean Sea as Detected with Space Remote Sensing, International Journal of Remote Sensing, 25, 1449–1453, doi:10.1080/01431160310001592427, 2004.

Gill, A., Green, J., and Simmons, A.: Energy Partition in the Large-Scale Ocean Circulation and the Production of Mid-Ocean Eddies, Deep Sea Research and Oceanographic Abstracts, 21, 499–528, doi:10.1016/0011-7471(74)90010-2, 1974.

Girishkumar, M. S., Ravichandran, M., and McPhaden, M. J.: Temperature Inversions and Their Influence on the Mixed Layer Heat Budget during the Winters of 2006–2007 and 2007–2008 in the Bay of Bengal, Journal of Geophysical Research: Oceans, 118, 2426–2437, doi:10.1002/jgrc.20192, 2013.

Goni, G. J. and Johns, W. E.: A Census of North Brazil Current Rings Observed from TOPEX/POSEIDON Altimetry: 1992-1998, Geophysical Research Letters, 28, 1–4, doi:10.1029/2000GL011717, 2001.

Goni, G. J. and Johns, W. E.: Synoptic Study of Warm Rings in the North Brazil Current Retroflection Region Using Satellite Altimetry, Elsevier Oceanography Series, 68, 335–356, doi:10.1016/S0422-9894(03)80153-8, 2003.

Gordon, A. L.: Circulation of the Caribbean Sea, Journal of Geophysical Research, 72, 6207, doi:10.1029/JZ072i024p06207, 1967.

Gordon, A. L.: The Brawniest Retroflection, Nature, 421, 904–905, doi:10.1038/421904a, 2003.

Gower, J., Young, E., and King, S.: Satellite Images Suggest a New Sargassum Source Region in 2011, Remote Sensing Letters, 4, 764–773, doi:10.1080/2150704X.2013.796433, 2013.

Graham, F. S. and McDougall, T. J.: Quantifying the Nonconservative Production of Conservative Temperature, Potential Temperature, and Entropy, Journal of Physical Oceanography, 43, 838–862, doi:10.1175/JPO-D-11-0188.1, 2013.

Groeskamp, S., LaCasce, J. H., McDougall, T. J., and Rogé, M.: Full-Depth Global Estimates of Ocean Mesoscale Eddy Mixing From Observations and Theory, Geophysical Research Letters, 47, doi:10.1029/2020GL089425, 2020.

Gula, J., Molemaker, M. J., and McWilliams, J. C.: Topographic Vorticity Generation, Submesoscale Instability and Vortex Street Formation in the Gulf Stream, Geophysical Research Letters, 42, 4054–4062, doi:10.1002/2015GL063731, 2015.

Guthrie, J. D., Fer, I., and Morison, J. H.: Thermohaline Staircases in the Amundsen Basin: Possible Disruption by Shear and Mixing, Journal of Geophysical Research: Oceans, 122, 7767–7782, doi:10.1002/2017JC012993, 2017.

Hansell, D. A. and Follows, M. J.: Nitrogen in the Atlantic Ocean, in: Nitrogen in the Marine Environment, chap. Nitrogen i, pp. 597–630, Elsevier, doi:10.1016/B978-0-12-372522-6.00013-X, 2008.

Hellweger, F. L. and Gordon, A. L.: Tracing Amazon River Water into the Caribbean Sea, Journal of Marine Research, 60, 537–549, 2002.

Hernández–Guerra, A. and Joyce, T. M.: Water Masses and Circulation in the Surface Layers of the Caribbean at 66W, Geophysical Research Letters, 27, 3497–3500, doi:10.1029/1999GL011230, 2000.

Holte, J., Talley, L. D., Gilson, J., and Roemmich, D.: An Argo Mixed Layer Climatology and Database, Geophysical Research Letters, 44, 5618–5626, doi:10.1002/2017GL073426, 2017.

Hu, C., Montgomery, E. T., Schmitt, R. W., and Muller–Karger, F. E.: The Dispersal of the Amazon and Orinoco River Water in the Tropical Atlantic and Caribbean Sea: Observation from Space and S–PALACE Floats, Deep Sea Research Part II: Topical Studies in Oceanography, 51, 1151–1171, doi:10.1016/j.dsr2.2004.04.001, 2004.

Hughes, C. W., Williams, J., Hibbert, A., Boening, C., and Oram, J.: A Rossby Whistle: A Resonant Basin Mode Observed in the Caribbean Sea, Geophysical Research Letters, 43, 7036–7043, doi:10.1002/2016GL069573, 2016.

Hummels, R., Brandt, P., Dengler, M., Fischer, J., Araujo, M., Veleda, D., and Durgadoo, J. V.: Interannual to Decadal Changes in the Western Boundary Circulation in the Atlantic at 11S, Geophysical Research Letters, 42, 7615–7622, doi:10.1002/2015GL065254, 2015.

Itoh, S. and Yasuda, I.: Characteristics of Mesoscale Eddies in the Kuroshio–Oyashio Extension Region Detected from the Distribution of the Sea Surface Height Anomaly, Journal of Physical Oceanography, 40, 1018–1034, doi:10.1175/2009JPO4265.1, 2010.

Jagannathan, A., Srinivasan, K., McWilliams, J. C., Molemaker, M. J., and Stewart, A. L.: Boundary Layer-Mediated Vorticity Generation in Currents over Sloping Bathymetry, under review for publication in Journal of Physiscal Oceanography, 2021.

Jayne, S. R. and Marotzke, J.: The Oceanic Eddy Heat Transport*, Journal of Physical Oceanography, 32, 3328–3345, doi:10.1175/1520-0485(2002)032<3328:TOEHT>2.0.CO;2, 2002.

Jiménez, B., Sangrà, P., and Mason, E.: A Numerical Study of the Relative Importance of Wind and Topographic Forcing on Oceanic Eddy Shedding by Tall, Deep Water Islands, Ocean Modelling, 22, 146–157, doi:10.1016/j.ocemod.2008.02.004, 2008.

Jochumsen, K., Rhein, M., Hüttl–Kabus, S., and Böning, C. W.: On the Propagation and Decay of North Brazil Current Rings, Journal of Geophysical Research: Oceans, 115, 1–19, doi:10.1029/2009JC006042, 2010.

Johns, E. M., Lumpkin, R., Putman, N. F., Smith, R. H., Muller-Karger, F. E., T. Rueda-Roa, D., Hu, C., Wang, M., Brooks, M. T., Gramer, L. J., and Werner, F. E.: The Establishment of a Pelagic Sargassum Population in the Tropical Atlantic: Biological Consequences of a Basin-Scale Long Distance Dispersal Event, Progress in Oceanography, 182, 102 269, doi:10.1016/j.pocean.2020.102269, 2020.

Johns, W. E., Townsend, T. L., Fratantoni, D. M., and Wilson, W. D.: On the Atlantic Inflow to the Caribbean Sea, Deep–Sea Research Part I: Oceanographic Research Papers, 49, 211–243, doi:10.1016/S0967-0637(01)00041-3, 2002.

Johnson, E. R. and McDonald, N. R.: Vortices near Barriers with Multiple Gaps, Journal of Fluid Mechanics, 531, 335–358, doi:10.1017/S0022112005003976, 2005.

Johnson, G. C. and Kearney, K. A.: Ocean Climate Change Fingerprints Attenuated by Salt Fingering?, Geophysical Research Letters, 36, doi:10.1029/2009GL040697, 2009.

Johnston, T. S., Schönau, M. C., Paluszkiewicz, T., MacKinnon, J. A., Arbic, B. K., Colin, P. L., Alford, M. H., Andres, M., Centurioni, L., Graber, H. C., Helfrich, K. R., Hormann, V., Lermusiaux, P. F., Musgrave, R. C., Powell, B. S., Qiu, B., Rudnick, D. L., Simmons, H. L., St. Laurent, L., Terrill, E. J., Trossman, D. S., Voet, G., Wijesekera, H. W., and Zeiden, K. L.: Flow Encountering Steep Topography (FLEAT), Oceanography, 32, 10–21, doi:10.2307/26845634, 2019.

Jouanno, J. and Sheinbaum, J.: Heat Balance and Eddies in the Caribbean Upwelling System, Journal of Physical Oceanography, 43, 1004–1014, doi:10.1175/JPO-D-12-0140.1, 2013.

Jouanno, J., Sheinbaum, J., Barnier, B., Molines, J., Debreu, L., and Lemarié, F.: The Mesoscale Variability in the Caribbean Sea. Part I: Simulations and Characteristics with an Embedded Model, Ocean Modelling, 23, 82–101, doi:10.1016/j.ocemod.2008.04.002, 2008.

Jouanno, J., Sheinbaum, J., Barnier, B., and Molines, J.: The Mesoscale Variability in the Caribbean Sea. Part II: Energy Sources, Ocean Modelling, 26, 226–239, doi:10.1016/j.ocemod.2008.10.006, 2009.

Jouanno, J., Sheinbaum, J., Barnier, B., Marc Molines, J., and Candela, J.: Seasonal and Interannual Modulation of the Eddy Kinetic Energy in the Caribbean Sea., Journal of Physical Oceanography, 42, 2015–2055, doi:10.1175/JPO-D-12-048.1, 2012.

Joyce, T. M., Pickart, R. S., and Millard, R. C.: Long–Term Hydrographic Changes at 52 and 66W in the North Atlantic Subtropical Gyre and Caribbean, Deep Sea Research Part II: Topical Studies in Oceanography, 46, 245–278, doi:10.1016/S0967-0645(98)00102-7, 1999.

Joyce, T. M., Hernandez-Guerra, A., and Smethie, W. M.: Zonal Circulation in the NW Atlantic and Caribbean from a Meridional World Ocean Circulation Experiment Hydrographic Section at 66W, Journal of Geophysical Research: Oceans, 106, 22 095–22 113, doi:10.1029/2000JC000268, 2001.

Kelley, D., Fernando, H., Gargett, A., Tanny, J., and Özsoy, E.: The Diffusive Regime of Double-Diffusive Convection, Double-Diffusion in Oceanography, 56, 461–481, doi:10.1016/S0079-6611(03)00026-0, 2003.

Kelley, D. E.: Fluxes through Diffusive Staircases: A New Formulation, Journal of Geophysical Research, 95, doi:10.1029/JC095iC03p03365, 1990.

Kermabon, C., Lherminier, P., Le Bot, P., and Gaillard, F.: CASCADE V7.2: Logiciel de Validation et de Visualisation Des Mesures ADCP de Coque, Tech. rep., Ifremer, 2018.

Kinard, W. F., Atwood, D. K., and Giese, G. S.: Dissolved Oxygen as Evidence for 18C Sargasso Sea Water in the Eastern Caribbean Sea, Deep Sea Research and Oceanographic Abstracts, 21, 79–82, doi:10.1016/0011-7471(74)90021-7, 1974.

Kirchner, K., Rhein, M., Mertens, C., Böning, C. W., and Hüttl, S.: Observed and Modeled Meridional Overturning Circulation Related Flow into the Caribbean, Journal of Geophysical Research, 113, C03 028, doi:10.1029/2007JC004320, 2008.

Klapp, J., ed.: Fluid Dynamics in Physics, Engineering and Environmental Applications, Environmental Science and Engineering. Environmental Engineering, Springer, Heidelberg ; New York, 2013.

Klein, P., Treguier, A.-M., and Hua, B. L.: Three-Dimensional Stirring of Thermohaline Fronts, Journal of Marine Research, 56, 589–612, doi:10.1357/002224098765213595, 1998.

Koetsier, J. O.: Thermohaline Staircases in the Caribbean Sea, Master thesis, Delft University of Technology, Delft, 2019.

Koszalka, I., Bracco, A., McWilliams, J. C., and Provenzale, A.: Dynamics of Wind-Forced Coherent Anticyclones in the Open Ocean, Journal of Geophysical Research, 114, C08 011, doi:10.1029/2009JC005388, 2009.

Krishfield, R., Toole, J., Proshutinsky, A., and Timmermans, M.-L.: Automated Ice-Tethered Profilers for Seawater Observations under Pack Ice in All Seasons, Journal of Atmospheric and Oceanic Technology, 25, 2091–2105, doi:10.1175/2008JTECHO587.1, 2008.

Kunze, E. and Llewellyn Smith, S.: The Role of Small-Scale Topography in Turbulent Mixing of the Global Ocean, Oceanography, 17, 55–64, doi:10.5670/oceanog.2004.67, 2004.

Lambert, R. B. and Sturges, W.: A Thermohaline Staircase and Vertical Mixing in the Thermocline, Deep Sea Research, 24, 211–222, doi:10.1016/S0146-6291(77)80001-5, 1977.

Large, W. G. and Yeager, S. G.: The Global Climatology of an Interannually Varying Air–Sea Flux Data Set, Climate Dynamics, 33, 341–364, doi:10.1007/s00382-008-0441-3, 2009.

Large, W. G., McWilliams, J. C., and Doney, S. C.: Oceanic Vertical Mixing: A Review and a Model with a Nonlocal Boundary Layer Parameterization, Reviews of Geophysics, 32, 363, doi:10.1029/94RG01872, 1994.

Le Bars, D., Viebahn, J. P., and Dijkstra, H. A.: A Southern Ocean Mode of Multidecadal Variability, Geophysical Research Letters, 43, 2102–2110, doi:10.1002/2016GL068177, 2016.

Lee, C., Chang, K.-I., Lee, J. H., and Richards, K. J.: Vertical Mixing Due to Double Diffusion in the Tropical Western Pacific, Geophysical Research Letters, 41, 7964–7970, doi:10.1002/2014GL061698, 2014.

Lemarié, F., Kurian, J., Shchepetkin, A. F., Jeroen Molemaker, M., Colas, F., and McWilliams, J. C.: Are There Inescapable Issues Prohibiting the Use of Terrain-Following Coordinates in Climate Models?, Ocean Modelling, 42, 57–79, doi:10.1016/j.ocemod.2011.11.007, 2012.

Leopold, M. F., Geelhoed, S. C. V., Scheidat, M., Cremer, J., Debrot, A. O., Buiter, R., and Halewijn, R.: The Distribution of the Black–Capped Petrel Pterodroma Hasitata in the Caribbean Sea, Marine Ornithology, 47, 235–241, 2019.

Liang, Y.-C., Lo, M.-H., Lan, C.-W., Seo, H., Ummenhofer, C. C., Yeager, S., Wu, R.-J., and Steffen,

J. D.: Amplified Seasonal Cycle in Hydroclimate over the Amazon River Basin and Its Plume Region, Nature Communications, 11, 4390, doi:10.1038/s41467-020-18187-0, 2020.

Lima, F. P. and Wethey, D. S.: Three Decades of High–Resolution Coastal Sea Surface Temperatures Reveal More than Warming, Nature Communications, 3, 1–13, doi:10.1038/ncomms1713, 2012.

Lin, Y., Sheng, J., and Greatbatch, R. J.: A Numerical Study of the Circulation and Monthly-to-Seasonal Variability in the Caribbean Sea: The Role of Caribbean Eddies, Ocean Dynamics, 62, 193–211, 2012.

Liu, H., Yu, L., and Lin, X.: Recent Decadal Change in the North Atlantic Subtropical Underwater Associated with the Poleward Expansion of the Surface Salinity Maximum, Journal of Geophysical Research: Oceans, 124, 4433–4448, doi:10.1029/2018JC014508, 2019.

Locarnini, R. A., Mishonov, A. V., Baranova, O. K., Boyer, T. P., Zweng, M. M., Garcia, H. E., Reagan, J. R., Seidov, D., Weathers, K., Paver, C. R., and Smolyar, I.: World Ocean Atlas 2018, Volume 1: Temperature, Tech. rep., Mishonov Technical Ed.; NOAA Atlas NESDIS 81, 2019.

Lowrie, K., Lowrie, D., and Collier, N.: Seabird Breeding Atlas of the Lesser Antilles, Environmental Protection in the Caribbean (EPIC), 2012.

Lübbecke, J. F., Durgadoo, J. V., and Biastoch, A.: Contribution of Increased Agulhas Leakage to Tropical Atlantic Warming, Journal of Climate, 28, 9697–9706, doi:10.1175/JCLI-D-15-0258.1, 2015.

Machín, F. and Pelegrí, J. L.: Northward Penetration of Antarctic Intermediate Water off Northwest Africa, Journal of Physical Oceanography, 39, 512–535, doi:10.1175/2008JPO3825.1, 2009.

Madec, G. et al.: NEMO Ocean Engine, Tech. rep., Institut Pierre–Simon Laplace, 2015.

Marshall, J. and Schott, F.: Open-Ocean Convection: Observations, Theory, and Models, Reviews of Geophysics, 37, 1–64, doi:10.1029/98RG02739, 1999.

Marshall, J., Adcroft, A., Hill, C., Perelman, L., and Heisey, C.: A Finite–Volume, Incompressible Navier Stokes Model for Studies of the Ocean on Parallel Computers, Journal of Geophysical Research: Oceans, 102, 5753–5766, doi:10.1029/96JC02775, 1997.

Mason, E., Molemaker, J., Shchepetkin, A. F., Colas, F., McWilliams, J. C., and Sangrà, P.: Procedures for Offline Grid Nesting in Regional Ocean Models, Ocean Modelling, 35, 1–15, doi:10.1016/j.ocemod.2010.05.007, 2010.

Mason, E., Colas, F., Molemaker, J., Shchepetkin, A. F., Troupin, C., McWilliams, J. C., and Sangrà, P.: Seasonal Variability of the Canary Current: A Numerical Study, Journal of Geophysical Research, 116, C06 001, doi:10.1029/2010JC006665, 2011.

Mason, E., Pascual, A., and McWilliams, J. C.: A New Sea Surface Height–Based Code for Oceanic Mesoscale Eddy Tracking, Journal of Atmospheric and Oceanic Technology, 31, 1181–1188, doi:10.1175/JTECH-D-14-00019.1, 2014.

Masson, S. and Delecluse, P.: Influence of the Amazon River Runoff on the Tropical Atlantic, Physics and Chemistry of the Earth, Part B: Hydrology, Oceans and Atmosphere, 26, 137–142, doi:10.1016/S1464-1909(00)00230-6, 2001.

McCarthy, G., McDonagh, E., and King, B.: Decadal Variability of Thermocline and Intermediate Waters at 24S in the South Atlantic, Journal of Physical Oceanography, 41, 157–165, doi:10.1175/2010JPO4467.1, 2011.

McCarthy, G., Smeed, D., Johns, W., Frajka-Williams, E., Moat, B., Rayner, D., Baringer, M., Meinen, C., Collins, J., and Bryden, H.: Measuring the Atlantic Meridional Overturning Circulation at 26N, Progress in Oceanography, 130, 91–111, doi:10.1016/j.pocean.2014.10.006, 2015.

McDougall, T. J.: Interfacial Advection in the Thermohaline Staircase East of Barbados, Deep Sea Research Part A. Oceanographic Research Papers, 38, 357–370, doi:10.1016/0198-0149(91)90073-O, 1991.

McDougall, T. J. and Barker, P. M.: Getting Started with TEOS-10 and the Gibbs Seawater (GSW) Oceanographic Toolbox, SCOR/IAPSO WG, 127, 1–28, 2011.

McPhaden, M. J. and Foltz, G. R.: Intraseasonal Variations in the Surface Layer Heat Balance of the Central Equatorial Indian Ocean: The Importance of Zonal Advection and Vertical Mixing, Geophysical Research Letters, 40, 2737–2741, doi:10.1002/grl.50536, 2013.

Mélice, J.-L. and Arnault, S.: Investigation of the Intra-Annual Variability of the North Equatorial

Countercurrent/North Brazil Current Eddies and of the Instability Waves of the North Tropical Atlantic Ocean Using Satellite Altimetry and Empirical Mode Decomposition, Journal of Atmospheric and Oceanic Technology, 34, 2295–2310, doi:10.1175/JTECH-D-17-0032.1, 2017.

Merryfield, W. J.: Origin of Thermohaline Staircases, Journal of Physical Oceanography, 30, 1046–1068, doi:10.1175/1520-0485(2000)030<1046:OOTS>2.0.CO;2, 2000.

Merryfield, W. J., Holloway, G., and Gargett, A. E.: A Global Ocean Model with Double-Diffusive Mixing, Journal of Physical Oceanography, 29, 1124–1142, doi:10.1175/1520-0485(1999)029<1124:AGOMWD>2.0.CO;2, 1999.

Mertens, C., Rhein, M., Walter, M., and Kirchner, K.: Modulation of the Inflow into the Caribbean Sea by North Brazil Current Rings, Deep Sea Research Part I: Oceanographic Research Papers, 56, 1057–1076, doi:10.1016/j.dsr.2009.03.002, 2009.

Mignot, J., de Boyer Montégut, C., Lazar, A., and Cravatte, S.: Control of Salinity on the Mixed Layer Depth in the World Ocean: 2. Tropical Areas, Journal of Geophysical Research, 112, doi:10.1029/2006JC003954, 2007.

Mignot, J., Lazar, A., and Lacarra, M.: On the Formation of Barrier Layers and Associated Vertical Temperature Inversions: A Focus on the Northwestern Tropical Atlantic, Journal of Geophysical Research: Oceans, 117, doi:10.1029/2011JC007435, 2012.

Miloslavich, P., Díaz, J. M., Klein, E., Alvarado, J. J., Díaz, C., Gobin, J., Escobar–Briones, E., Cruz–Motta, J. J., Weil, E., Cortés, J., Bastidas, A. C., Robertson, R., Zapata, F., Martín, A., Castillo, J., Kazandjian, A., and Ortiz, M.: Marine Biodiversity in the Caribbean: Regional Estimates and Distribution Patterns, PLoS ONE, 5, e11 916, doi:10.1371/journal.pone.0011916, 2010.

Mo, K. C., Chelliah, M., Carrera, M. L., Higgins, R. W., and Ebisuzaki, W.: Atmospheric Moisture Transport over the United States and Mexico as Evaluated in the NCEP Regional Reanalysis, Journal of Hydrometeorology, 6, 710–728, doi:10.1175/JHM452.1, 2005.

Molemaker, M. J., McWilliams, J. C., and Dewar, W. K.: Submesoscale Instability and Generation of Mesoscale Anticyclones near a Separation of the California Undercurrent, Journal of Physical Oceanography, 45, 613–629, doi:10.1175/JPO-D-13-0225.1, 2015.

Molinari, R. L., Spillane, M., Brooks, I., Atwood, D., and Duckett, C.: Surface Currents in the Caribbean Sea as Deduced from Lagrangian Observations, Journal of Geophysical Research: Oceans, 86, 6537, doi:10.1029/JC086iC07p06537, 1981.

Molleri, G. S., Novo, E. M. M., and Kampel, M.: Space–Time Variability of the Amazon River Plume Based on Satellite Ocean Color, Continental Shelf Research, 30, 342–352, doi:10.1016/j.csr.2009.11.015, 2010.

Montes, E., Muller–Karger, F. E., Cianca, A., Lomas, M. W., Lorenzoni, L., and Habtes, S.: Decadal Variability in the Oxygen Inventory of North Atlantic Subtropical Underwater Captured by Sustained, Long–Term Oceanographic Time Series Observations, Global Biogeochemical Cycles, 30, 460–478, doi:10.1002/2015GB005183, 2016.

Montoya–Sánchez, R., Devis–Morales, A., Bernal, G., and Poveda, G.: Seasonal and Interannual Variability of the Mixed Layer Heat Budget in the Caribbean Sea, Journal of Marine Systems, 187, 111–127, doi:10.1016/j.jmarsys.2018.07.003, 2018.

Morell, J. M. and Corredor, J. E.: Photomineralization of Fluorescent Dissolved Organic Matter in the Orinoco River Plume: Estimation of Ammonium Release, Journal of Geophysical Research: Oceans, 106, 16 807–16 813, doi:10.1029/1999JC000268, 2001.

Morell, J. M., Corredor, J. E., and Merryfield, W. J.: Thermohaline Staircases in a Caribbean Eddy and Mechanisms for Staircase Formation, Deep Sea Research Part II: Topical Studies in Oceanography, 53, 128–139, doi:10.1016/j.dsr2.2005.09.013, 2006.

Morrison, J. M. and Nowlin, W. D.: General Distribution of Water Masses within the Eastern Caribbean Sea during the Winter of 1972 and Fall of 1973, Journal of Geophysical Research: Oceans, 87, 4207, doi:10.1029/JC087iC06p04207, 1982.

Muench, R. D., Fernando, H. J. S., and Stegen, G. R.: Temperature and Salinity Staircases in the Northwestern Weddell Sea, Journal of Physical Oceanography, 20, 295–306, doi:10.1175/1520-0485(1990)020<0295:TASSIT>2.0.CO;2, 1990.

Muller–Karger, F., McClain, C., Fisher, T., Esaias, W., and Varela, R.: Pigment Distribution

in the Caribbean Sea: Observations from Space, Progress in Oceanography, 23, 23–64, doi:10.1016/0079-6611(89)90024-4, 1989.

Muller–Karger, F. E. and Castro, R. A.: Mesoscale Processes Affecting Phytoplankton Abundance in the Southern Caribbean Sea, Continental Shelf Research, 14, 199–221, doi:10.1016/0278-4343(94)90013-2, 1994.

Munk, W. and Wunsch, C.: Abyssal Recipes II: Energetics of Tidal and Wind Mixing, Deep Sea Research Part I: Oceanographic Research Papers, 45, 1977–2010, doi:10.1016/S0967-0637(98)00070-3, 1998.

Munk, W. H.: Abyssal Recipes, Deep Sea Research and Oceanographic Abstracts, 13, 707–730, doi:10.1016/0011-7471(66)90602-4, 1966.

Muñoz, E., Busalacchi, A. J., Nigam, S., and Ruiz-Barradas, A.: Winter and Summer Structure of the Caribbean Low-Level Jet, Journal of Climate, 21, 1260–1276, doi:10.1175/2007JCLI1855.1, 2008.

Murphy, S. J., Hurlburt, H. E., and O'Brien, J. J.: The Connectivity of Eddy Variability in the Caribbean Sea, the Gulf of Mexico, and the Atlantic Ocean, Journal of Geophysical Research, 104, 1431, doi:10.1029/1998JC900010, 1999.

Nakano, H. and Yoshida, J.: A Note on Estimating Eddy Diffusivity for Oceanic Double-Diffusive Convection, Journal of Oceanography, 75, 375–393, doi:10.1007/s10872-019-00514-9, 2019.

Ni, Q., Zhai, X., Wang, G., and Marshall, D. P.: Random Movement of Mesoscale Eddies in the Global Ocean, Journal of Physical Oceanography, pp. 1–39, doi:10.1175/JPO-D-19-0192.1, 2020.

Nieuwstadt, F. T. M.: Turbulentie: Theorie En Toepassingen van Turbulente Stromingen, Epsilon Uitgaven, Utrecht, 1998.

Nystuen, J. A. and Andrade, C. A.: Tracking Mesoscale Ocean Features in the Caribbean Sea Using Geosat Altimetry, Journal of Geophysical Research: Oceans, 98, 8389–8394, doi:10.1029/93JC00125, 1993.

O'Connor, B. M., Fine, R. A., and Olson, D. B.: A Global Comparison of Subtropical Underwater Formation Rates, Deep Sea Research Part I: Oceanographic Research Papers, 52, 1569–1590, doi:10.1016/j.dsr.2005.01.011, 2005.

Oey, L., Lee, H., and Schmitz Jr., W.: Effects of Winds and Caribbean Eddies on the Frequency of Loop Current Eddy Shedding: A Numerical Model Study, Journal of Geophysical Research: Oceans, 108, 3324, doi:10.1029/2002JC001698, 2003.

Oey, L., Ezer, T., and Lee, H.: Loop Current, Rings and Related Circulation in the Gulf of Mexico: A Review of Numerical Models and Future Challenges, in: Circulation in the Gulf of Mexico: Observations and Models, edited by Sturges, W. and Lugo–Fernandez, A., pp. 31–56, American Geophysical Union, doi:10.1029/161GM04, 2005.

Osborn, T. R.: Estimates of the Local Rate of Vertical Diffusion from Dissipation Measurements, Journal of Physical Oceanography, 10, 83–89, doi:10.1175/1520-0485(1980)010<0083:EOTLRO>2.0.CO;2, 1980.

Oschlies, A.: Can Eddies Make Ocean Deserts Bloom?, Global Biogeochemical Cycles, 16, 53–1–53–11, doi:10.1029/2001GB001830, 2002.

Oschlies, A., Dietze, H., and Kähler, P.: Salt-Finger Driven Enhancement of Upper Ocean Nutrient Supply, Geophysical Research Letters, 30, doi:10.1029/2003GL018552, 2003.

Padman, L. and Dillon, T. M.: Vertical Heat Fluxes through the Beaufort Sea Thermohaline Staircase, Journal of Geophysical Research, 92, doi:10.1029/JC092iC10p10799, 1987.

Padman, L. and Dillon, T. M.: Thermal Microstructure and Internal Waves in the Canada Basin Diffusive Staircase, Deep Sea Research Part A. Oceanographic Research Papers, 36, 531–542, doi:10.1016/0198-0149(89)90004-6, 1989.

Pailler, K., Bourlès, B., and Gouriou, Y.: The Barrier Layer in the Western Tropical Atlantic Ocean, Geophysical Research Letters, 26, 2069–2072, doi:10.1029/1999GL900492, 1999.

Paramo, J., Quiñones, R. A., Ramirez, A., and Wiff, R.: Relationship between Abundance of Small Pelagic Fishes and Environmental Factors in the Colombian Caribbean Sea: An Analysis Based on Hydroacoustic Information, Aquatic Living Resources, 16, 239–245, doi:10.1016/S0990-7440(03)00043-3, 2003.

Pauluhn, A. and Chao, Y.: Tracking Eddies in the Subtropical North–Western Atlantic Ocean, Physics and Chemistry of the Earth, Part A: Solid Earth and Geodesy, 24, 415–421, doi:10.1016/S1464-1895(99)00052-6, 1999.

Polyakov, I. V., Pnyushkov, A. V., Rember, R., Ivanov, V. V., Lenn, Y.-D., Padman, L., and Carmack, E. C.: Mooring-Based Observations of Double-Diffusive Staircases over the Laptev Sea Slope*, Journal of Physical Oceanography, 42, 95–109, doi:10.1175/2011JPO4606.1, 2012.

Portela, E., Tenreiro, M., Pallàs–Sanz, E., Meunier, T., Ruiz–Angulo, A., Sosa–Gutiérrez, R., and Cusí, S.: Hydrography of the Central and Western Gulf of Mexico, Journal of Geophysical Research: Oceans, 123, 5134–5149, doi:10.1029/2018JC013813, 2018.

Prants, S., Lobanov, V., Budyansky, M., and Uleysky, M.: Lagrangian Analysis of Formation, Structure, Evolution and Splitting of Anticyclonic Kuril Eddies, Deep Sea Research Part I: Oceanographic Research Papers, 109, 61–75, doi:10.1016/j.dsr.2016.01.003, 2016.

Putman, N. F., Goni, G. J., Gramer, L. J., Hu, C., Johns, E. M., Trinanes, J., and Wang, M.: Simulating Transport Pathways of Pelagic Sargassum from the Equatorial Atlantic into the Caribbean Sea, Progress in Oceanography, 165, 205–214, doi:10.1016/j.pocean.2018.06.009, 2018.

Qu, T., Gao, S., and Fukumori, I.: Formation of Salinity Maximum Water and Its Contribution to the Overturning Circulation in the North Atlantic as Revealed by a Global General Circulation Model, Journal of Geophysical Research: Oceans, 118, 1982–1994, doi:10.1002/jgrc.20152, 2013.

Rabinovich, A. B., Thomson, R. E., and Bograd, S. J.: Drifter Observations of Anticyclonic Eddies near Bussol' Strait, the Kuril Islands, Journal of Oceanography, 58, 661–671, doi:10.1023/A:1022890222516, 2002.

Radko, T.: A Mechanism for Layer Formation in a Double-Diffusive Fluid, Journal of Fluid Mechanics, 497, 365–380, doi:10.1017/S0022112003006785, 2003.

Radko, T.: What Determines the Thickness of Layers in a Thermohaline Staircase?, Journal of Fluid Mechanics, 523, 79–98, doi:10.1017/S0022112004002290, 2005.

Radko, T.: Double-Diffusive Convection, Cambridge University Press, Cambridge, doi:10.1017/CBO9781139034173, 2013.

Radko, T. and Smith, D. P.: Equilibrium Transport in Double-Diffusive Convection, Journal of Fluid Mechanics, 692, 5–27, doi:10.1017/jfm.2011.343, 2012.

Rahmstorf, S.: On the Freshwater Forcing and Transport of the Atlantic Thermohaline Circulation, Climate Dynamics, 12, 799–811, doi:10.1007/s003820050144, 1996.

Redi, M.: Oceanic Isopycnal Mixing by Coordinate Rotation, Journal of Physical Oceanography, 12, 1154–1158, 1982.

Rennie, S. J., Pattiaratchi, C. P., and McCauley, R. D.: Eddy Formation through the Interaction between the Leeuwin Current, Leeuwin Undercurrent and Topography, Deep Sea Research Part II: Topical Studies in Oceanography, 54, 818–836, doi:10.1016/j.dsr2.2007.02.005, 2007.

Resiere, D., Valentino, R., Nevière, R., Banydeen, R., Gueye, P., Florentin, J., Cabié, A., Lebrun, T., Mégarbane, B., Guerrier, G., and Mehdaoui, H.: Sargassum Seaweed on Caribbean Islands: An International Public Health Concern, The Lancet, 392, 2691, doi:10.1016/S0140-6736(18)32777-6, 2018.

Rhein, M., Kirchner, K., Mertens, C., Steinfeldt, R., Walter, M., and Fleischmann-Wischnath, U.: Transport of South Atlantic Water through the Passages South of Guadeloupe and across 16N, 2000–2004, Deep Sea Research Part I: Oceanographic Research Papers, 52, 2234–2249, doi:10.1016/j.dsr.2005.08.003, 2005.

Richardson, P. L.: Eddy Kinetic Energy in the North Atlantic from Surface Drifters, Journal of Geophysical Research, 88, 4355, doi:10.1029/JC088iC07p04355, 1983.

Richardson, P. L.: Caribbean Current and Eddies as Observed by Surface Drifters, Deep Sea Research Part II: Topical Studies in Oceanography, 52, 429–463, doi:10.1016/j.dsr2.2004.11.001, 2005.

Richardson, P. L. and Tychensky, A.: Meddy Trajectories in the Canary Basin Measured during the SEMAPHORE Experiment, 1993-1995, Journal of Geophysical Research: Oceans, 103, 25 029–25 045, doi:10.1029/97JC02579, 1998.

Risien, C. M. and Chelton, D. B.: A Global Climatology of Surface Wind and Wind Stress Fields from Eight Years of QuikSCAT Scatterometer Data, Journal of Physical Oceanography, 38, 2379–2413,

doi:10.1175/2008JPO3881.1, 2008.

Roberts, C. M., McClean, C. J., Veron, J. E. N., Hawkins, J. P., Allen, G. R., McAllister, D. E., Mittermeier, C. G., Schueler, F. W., Spalding, M., Wells, F., Vynne, C., and Werner, T. B.: Marine Biodiversity Hotspots and Conservation Priorities for Tropical Reefs, Science, 295, 1280–1284, doi:10.1126/science.1067728, 2002.

Robertson, R., Padman, L., and Levine, M. D.: Fine Structure, Microstructure, and Vertical Mixing Processes in the Upper Ocean in the Western Weddell Sea, Journal of Geophysical Research, 100, doi:10.1029/95JC01742, 1995.

Robson, J., Hodson, D., Hawkins, E., and Sutton, R.: Atlantic Overturning in Decline?, Nature Geoscience, 7, 2–3, doi:10.1038/ngeo2050, 2014.

Roemmich, Dean, D., Johnson, G. C., Riser, S., Davis, R., Gilson, J., Owens, W. B., Garzoli, S. R., Schmid, C., and Ignaszewski, M.: The Argo Program, Oceanography, 22, 34–43, 2009.

Ruddick, B.: A Practical Indicator of the Stability of the Water Column to Double-Diffusive Activity, Deep Sea Research Part A. Oceanographic Research Papers, 30, 1105–1107, doi:10.1016/0198-0149(83)90063-8, 1983.

Ruddick, B. and Kerr, O.: Oceanic Thermohaline Intrusions: Theory, Double-Diffusion in Oceanography, 56, 483–497, doi:10.1016/S0079-6611(03)00029-6, 2003.

Rudels, B.: Arctic Ocean Circulation, Processes and Water Masses: A Description of Observations and Ideas with Focus on the Period Prior to the International Polar Year 2007–2009, Progress in Oceanography, 132, 22–67, doi:10.1016/j.pocean.2013.11.006, 2015.

Rudzin, J. E., Shay, L. K., Jaimes, B., and Brewster, J. K.: Upper Ocean Observations in Eastern Caribbean Sea Reveal Barrier Layer within a Warm Core Eddy, Journal of Geophysical Research: Oceans, 122, 1057–1071, doi:10.1002/2016JC012339, 2017.

Rueda-Roa, D., Ezer, T., and Muller-Karger, F.: Description and Mechanisms of the Mid-Year Upwelling in the Southern Caribbean Sea from Remote Sensing and Local Data, Journal of Marine Science and Engineering, 6, 36, doi:10.3390/jmse6020036, 2018.

Rueda–Roa, D. T. and Muller–Karger, F. E.: The Southern Caribbean Upwelling System: Sea Surface Temperature, Wind Forcing and Chlorophyll Concentration Patterns, Deep Sea Research Part I: Oceanographic Research Papers, 78, 102–114, doi:10.1016/j.dsr.2013.04.008, 2013.

Sarafanov, A., Sokov, A., and Demidov, A.: Water Mass Characteristics in the Equatorial North Atlantic: A Section Nominally along 6.5N, July 2000, Journal of Geophysical Research, 112, C12 023, doi:10.1029/2007JC004222, 2007.

Sayol, J.-M., Dijkstra, H., and Katsman, C.: Seasonal and Regional Variations of Sinking in the Subpolar North Atlantic from a High-Resolution Ocean Model, Ocean Science, 15, 1033–1053, doi:10.5194/os-15-1033-2019, 2019.

Schmidtko, S. and Johnson, G. C.: Multidecadal Warming and Shoaling of Antarctic Intermediate Water*, Journal of Climate, 25, 207–221, doi:10.1175/JCLI-D-11-00021.1, 2012.

Schmidtko, S., Johnson, G. C., and Lyman, J. M.: MIMOC: A Global Monthly Isopycnal Upper-Ocean Climatology with Mixed Layers: MIMOC, Journal of Geophysical Research: Oceans, 118, 1658–1672, doi:10.1002/jgrc.20122, 2013.

Schmitt, R. W.: Flux Measurements on Salt Fingers at an Interface, Journal of Marine Research, 37, 419–436, 1979.

Schmitt, R. W.: Form of the Temperature-Salinity Relationship in the Central Water: Evidence for Double-Diffusive Mixing, Journal of Physical Oceanography, 11, 1015–1026, doi:10.1175/1520-0485(1981)011<1015:FOTTSR>2.0.CO;2, 1981.

Schmitt, R. W.: Double Diffusion in Oceanography, Annual Review of Fluid Mechanics, 26, 255–285, doi:10.1146/annurev.fl.26.010194.001351, 1994.

Schmitt, R. W.: Spice and the Demon, Science, 283, 498–499, doi:10.1126/science.283.5401.498, 1999.

Schmitt, R. W.: Enhanced Diapycnal Mixing by Salt Fingers in the Thermocline of the Tropical Atlantic, Science, 308, 685–688, doi:10.1126/science.1108678, 2005.

Schmitt, R. W., Perkins, H., Boyd, J., and Stalcup, M.: C-SALT: An Investigation of the Thermohaline Staircase in the Western Tropical North Atlantic, Deep Sea Research Part A. Oceanographic

Research Papers, 34, 1655–1665, doi:10.1016/0198-0149(87)90014-8, 1987.

Schouten, M. W., de Ruijter, W. P. M., van Leeuwen, P. J., and Lutjeharms, J. R. E.: Translation, Decay and Splitting of Agulhas Rings in the Southeastern Atlantic Ocean, Journal of Geophysical Research: Oceans, 105, 21 913–21 925, doi:10.1029/1999JC000046, 2000.

Schroeder, K., Chiggiato, J., Bryden, H. L., Borghini, M., and Ben Ismail, S.: Abrupt Climate Shift in the Western Mediterranean Sea, Scientific Reports, 6, 23 009, doi:10.1038/srep23009, 2016.

Seki, M. P., Polovina, J. J., Brainard, R. E., Bidigare, R. R., Leonard, C. L., and Foley, D. G.: Biological Enhancement at Cyclonic Eddies Tracked with GOES Thermal Imagery in Hawaiian Waters, Geophysical Research Letters, 28, 1583–1586, doi:10.1029/2000GL012439, 2001.

Shchepetkin, A. F.: An Adaptive, Courant-Number-Dependent Implicit Scheme for Vertical Advection in Oceanic Modeling, Ocean Modelling, 91, 38–69, doi:10.1016/j.ocemod.2015.03.006, 2015.

Shchepetkin, A. F. and McWilliams, J. C.: A Method for Computing Horizontal Pressure-Gradient Force in an Oceanic Model with a Nonaligned Vertical Coordinate, Journal of Geophysical Research: Oceans, 108, doi:10.1029/2001JC001047, 2003.

Shchepetkin, A. F. and McWilliams, J. C.: The Regional Oceanic Modeling System (ROMS): A Split-Explicit, Free-Surface, Topography-Following-Coordinate Oceanic Model, Ocean Modelling, 9, 347–404, doi:10.1016/j.ocemod.2004.08.002, 2005.

Shchepetkin, A. F. and McWilliams, J. C.: Accurate Boussinesq Oceanic Modeling with a Practical, "Stiffened" Equation of State, Ocean Modelling, 38, 41–70, doi:10.1016/j.ocemod.2011.01.010, 2011.

Shi, C. and Nof, D.: The Destruction of Lenses and Generation of Wodons, Journal of Physical Oceanography, 24, 1120–1136, doi:10.1175/1520-0485(1994)024<1120:TDOLAG>2.0.CO;2, 1994.

Shibley, N. C., Timmermans, M.-L., Carpenter, J. R., and Toole, J. M.: Spatial Variability of the Arctic Ocean's Double-Diffusive Staircase, Journal of Geophysical Research: Oceans, 122, 980–994, doi:10.1002/2016JC012419, 2017.

Silander, M. F.: On the Three–Dimensional Structure of Caribbean Mesoscale Eddies, University of Puerto Rico, pp. 1–91, 2005.

Simmons, H. L. and Nof, D.: The Squeezing of Eddies through Gaps, Journal of Physical Oceanography, 32, 314–335, doi:10.1175/1520-0485(2002)032<0314:TSOETG>2.0.CO;2, 2002.

Smagorinsky, J., Galperin, B., and Orszag, S.: Large Eddy Simulation of Complex Engineering and Geophysical Flows, Evolution of physical oceanography, pp. 3–36, 1993.

Spall, M. A. and Pickart, R. S.: Where Does Dense Water Sink? A Subpolar Gyre Example*, Journal of Physical Oceanography, 31, 810–826, doi:10.1175/1520-0485(2001)031<0810:WDDWSA>2.0.CO;2, 2001.

Speer, K. and Tziperman, E.: Rates of Water Mass Formation in the North Atlantic Ocean, Journal of Physical Oceanography, 22, 93–104, doi:10.1175/1520-0485(1992)022<0093:ROWMFI>2.0.CO;2, 1992.

Speich, S., Blanke, B., de Vries, P., Drijfhout, S., Döös, K., Ganachaud, A., and Marsh, R.: Tasman Leakage: A New Route in the Global Ocean Conveyor Belt, Geophysical Research Letters, 29, doi:10.1029/2001GL014586, 2002.

Speich, S., Blanke, B., and Cai, W.: Atlantic Meridional Overturning Circulation and the Southern Hemisphere Supergyre, Geophysical Research Letters, 34, doi:10.1029/2007GL031583, 2007.

Sprintall, J. and Tomczak, M.: Evidence of the Barrier Layer in the Surface Layer of the Tropics, Journal of Geophysical Research, 97, 7305, doi:10.1029/92JC00407, 1992.

Srinivasan, K., McWilliams, J. C., Renault, L., Hristova, H. G., Molemaker, J., and Kessler, W. S.: Topographic and Mixed Layer Submesoscale Currents in the Near-Surface Southwestern Tropical Pacific, Journal of Physical Oceanography, 47, 1221–1242, doi:10.1175/JPO-D-16-0216.1, 2017.

Srinivasan, K., McWilliams, J. C., Molemaker, M. J., and Barkan, R.: Submesoscale Vortical Wakes in the Lee of Topography, Journal of Physical Oceanography, 49, 1949–1971, doi:10.1175/JPO-D-18-0042.1, 2019.

St. Laurent, L. and Schmitt, R. W.: The Contribution of Salt Fingers to Vertical Mixing in the North Atlantic Tracer Release Experiment*, Journal of Physical Oceanography, 29, 1404–1424,

doi:10.1175/1520-0485(1999)029<1404:TCOSFT>2.0.CO;2, 1999.

Stammer, D. and Wunsch, C.: Temporal Changes in Eddy Energy of the Oceans, Deep Sea Research Part II: Topical Studies in Oceanography, 46, 77–108, doi:10.1016/S0967-0645(98)00106-4, 1999.

Stern, M. E.: The "Salt-Fountain" and Thermohaline Convection, Tellus, 12, 172–175, doi:10.3402/tellusa.v12i2.9378, 1960.

Stern, M. E.: Collective Instability of Salt Fingers, Journal of Fluid Mechanics, 35, 209–218, doi:10.1017/S0022112069001066, 1969.

Stramma, L., Bange, H. W., Czeschel, R., Lorenzo, A., and Frank, M.: On the Role of Mesoscale Eddies for the Biological Productivity and Biogeochemistry in the Eastern Tropical Pacific Ocean off Peru, Biogeosciences, 10, 7293–7306, doi:10.5194/bg-10-7293-2013, 2013.

Tait, R. I. and Howe, M. R.: Thermohaline Staircase, Nature, 231, 178–179, doi:10.1038/231178a0, 1971.

Talley, L. D.: Antarctic Intermediate Water in the South Atlantic, pp. 219–238, Springer Berlin Heidelberg, Berlin, Heidelberg, doi:10.1007/978-3-642-80353-6_11, 1996.

Talley, L. D., Pickard, G. L., and Emery, W. J., eds.: Descriptive Physical Oceanography: An Introduction, Academic Press, Amsterdam ; Boston, sixth edn., 2011.

Tanabe, A. and Cenedese, C.: Laboratory Experiments on Mesoscale Vortices Colliding with an Island Chain, Journal of Geophysical Research, 113, C04 022, doi:10.1029/2007JC004322, 2008.

Tasker, M. L., Jones, P. H., Dixon, T., and Blake, B. F.: Counting Seabirds at Sea from Ships: A Review of Methods Employed and a Suggestion for a Standardized Approach, The Auk, 101, 567–577, 1984.

Taylor, J. R. and Veronis, G.: Experiments on Double-Diffusive Sugar–Salt Fingers at High Stability Ratio, Journal of Fluid Mechanics, 321, 315–333, doi:10.1017/S0022112096007744, 1996.

Taylor, M. A. and Alfaro, E. J.: Climate of Central America and the Caribbean, in: Encyclopedia of World Climatology, edited by Oliver, J. E., pp. 183–189, Springer Netherlands, Dordrecht, doi:10.1007/1-4020-3266-8_37, 2005.

Thorpe, S. A.: The Turbulent Ocean, Cambridge University Press, first edn., doi:10.1017/CBO9780511819933, 2005.

Thyng, K., Greene, C., Hetland, R., Zimmerle, H., and DiMarco, S.: True Colors of Oceanography: Guidelines for Effective and Accurate Colormap Selection, Oceanography, 29, 9–13, doi:10.5670/oceanog.2016.66, 2016.

Timmermans, M.-L., Garrett, C., and Carmack, E.: The Thermohaline Structure and Evolution of the Deep Waters in the Canada Basin, Arctic Ocean, Deep Sea Research Part I: Oceanographic Research Papers, 50, 1305–1321, doi:10.1016/S0967-0637(03)00125-0, 2003.

Timmermans, M.-L., Toole, J., Krishfield, R., and Winsor, P.: Ice-Tethered Profiler Observations of the Double-Diffusive Staircase in the Canada Basin Thermocline, Journal of Geophysical Research, 113, doi:10.1029/2008JC004829, 2008.

Toole, J. M., Schmitt, R. W., and Polzin, K. L.: Estimates of Diapycnal Mixing in the Abyssal Ocean, Science, 264, 1120, doi:10.1126/science.264.5162.1120, 1994.

Toole, J. M., Krishfield, R., Timmermans, M.-L., and Proshutinsky, A.: The Ice-Tethered Profiler: Argo of the Arctic, Oceanography, 24, 126–135, 2011.

Torres, R. R. and Tsimplis, M. N.: Sea–Level Trends and Interannual Variability in the Caribbean Sea, Journal of Geophysical Research: Oceans, 118, 2934–2947, doi:10.1002/jgrc.20229, 2013.

Tsuchiya, M.: Circulation of the Antarctic Intermediate Water in the North Atlantic Ocean, Journal of Marine Research, 47, 747–755, doi:10.1357/002224089785076136, 1989.

Turner, J.: The Coupled Turbulent Transports of Salt and and Heat across a Sharp Density Interface, International Journal of Heat and Mass Transfer, 8, 759–767, doi:10.1016/0017-9310(65)90022-0, 1965.

van der Boog, C. G., de Jong, M. F., Scheidat, M., Leopold, M. F., Geelhoed, S. C. V., Schulz, K., Dijkstra, H. A., Pietrzak, J. D., and Katsman, C. A.: Hydrographic and Biological Survey of a Surface-Intensified Anticyclonic Eddy in the Caribbean Sea, Journal of Geophysical Research: Oceans, 124,

6235–6251, doi:10.1029/2018JC014877, 2019.

Van Halewijn, R. and Norton, R. L.: Status and Conservation of Seabirds of the Caribbean, in: Status and Conservation of the World's Seabirds., edited by Croxall, J., Evans, P., and Schreiber, R., pp. 169–222, International council on bird preservation technical publication 2, 1984.

van Westen, R. M., Dijkstra, H. A., Klees, R., Riva, R. E. M., Slobbe, D. C., van der Boog, C. G., Katsman, C. A., Candy, A. S., Pietrzak, J. D., Zijlema, M., James, R. K., and Bouma, T. J.: Mechanisms of the 40-70 Day Variability in the Yucatan Channel Volume Transport, Journal of Geophysical Research: Oceans, 123, 1286–1300, doi:10.1002/2017JC013580, 2018.

Vic, C., Roullet, G., Capet, X., Carton, X., Molemaker, M. J., and Gula, J.: Eddy-topography Interactions and the Fate of the Persian Gulf Outflow, Journal of Geophysical Research: Oceans, 120, 6700–6717, doi:10.1002/2015JC011033, 2015.

Villamizar G., E. Y. and Cervigón, F.: Variability and Sustainability of the Southern Sub-area of the Caribbean Sea Large Marine Ecosystem, Environmental Development, 22, 30–41, doi:10.1016/j.envdev.2017.02.005, 2017.

Vizy, E. K. and Cook, K. H.: Influence of the Amazon/Orinoco Plume on the Summertime Atlantic Climate, Journal of Geophysical Research, 115, D21 112, doi:10.1029/2010JD014049, 2010.

Wang, G. and Dewar, W. K.: Meddy–Seamount Interactions: Implications for the Mediterranean Salt Tongue, Journal of Physical Oceanography, 33, 2446–2461, doi:10.1175/1520-0485(2003)033<2446:MIIFTM>2.0.CO;2, 2003.

Wang, M. and Hu, C.: Predicting Sargassum Blooms in the Caribbean Sea from MODIS Observations: Sargassum Bloom Prediction, Geophysical Research Letters, 44, 3265–3273, doi:10.1002/2017GL072932, 2017.

Wang, X., Han, G., Qi, Y., and Li, W.: Impact of Barrier Layer on Typhoon-Induced Sea Surface Cooling, Dynamics of Atmospheres and Oceans, 52, 367–385, doi:10.1016/j.dynatmoce.2011.05.002, 2011.

Wells, R. J. D., Rooker, J. R., Quigg, A., and Wissel, B.: Influence of Mesoscale Oceanographic Features on Pelagic Food Webs in the Gulf of Mexico, Marine Biology, 164, 92, doi:10.1007/s00227-017-3122-0, 2017.

Whalen, C. B., Talley, L. D., and MacKinnon, J. A.: Spatial and Temporal Variability of Global Ocean Mixing Inferred from Argo Profiles, Geophysical Research Letters, 39, doi:10.1029/2012GL053196, 2012.

Whyte, F. S., Taylor, M. A., Stephenson, T. S., and Campbell, J. D.: Features of the Caribbean Low Level Jet, International Journal of Climatology, 28, 119–128, 2008.

Wong, A. P. S., Wijffels, S. E., Riser, S. C., Pouliquen, S., Hosoda, S., Roemmich, D., Gilson, J., Johnson, G. C., Martini, K., Murphy, D. J., Scanderbeg, M., Bhaskar, T. V. S. U., Buck, J. J. H., Merceur, F., Carval, T., Maze, G., Cabanes, C., André, X., Poffa, N., Yashayaev, I., Barker, P. M., Guinehut, S., Belbéoch, M., Ignaszewski, M., Baringer, M. O., Schmid, C., Lyman, J. M., McTaggart, K. E., Purkey, S. G., Zilberman, N., Alkire, M. B., Swift, D., Owens, W. B., Jayne, S. R., Hersh, C., Robbins, P., West-Mack, D., Bahr, F., Yoshida, S., Sutton, P. J. H., Cancouët, R., Coatanoan, C., Dobbler, D., Juan, A. G., Gourrion, J., Kolodziejczyk, N., Bernard, V., Bourlès, B., Claustre, H., D'Ortenzio, F., Le Reste, S., Le Traon, P.-Y., Rannou, J.-P., Saout-Grit, C., Speich, S., Thierry, V., Verbrugge, N., Angel-Benavides, I. M., Klein, B., Notarstefano, G., Poulain, P.-M., Vélez-Belchí, P., Suga, T., Ando, K., Iwasaska, N., Kobayashi, T., Masuda, S., Oka, E., Sato, K., Nakamura, T., Sato, K., Takatsuki, Y., Yoshida, T., Cowley, R., Lovell, J. L., Oke, P. R., van Wijk, E. M., Carse, F., Donnelly, M., Gould, W. J., Gowers, K., King, B. A., Loch, S. G., Mowat, M., Turton, J., Rama Rao, E. P., Ravichandran, M., Freeland, H. J., Gaboury, I., Gilbert, D., Greenan, B. J. W., Ouellet, M., Ross, T., Tran, A., Dong, M., Liu, Z., Xu, J., Kang, K., Jo, H., Kim, S.-D., and Park, H.-M.: Argo Data 1999–2019: Two Million Temperature-Salinity Profiles and Subsurface Velocity Observations From a Global Array of Profiling Floats, Frontiers in Marine Science, 7, 700, doi:10.3389/fmars.2020.00700, 2020.

Wunsch, C.: Where Do Ocean Eddy Heat Fluxes Matter?, Journal of Geophysical Research: Oceans, 104, 13 235–13 249, doi:10.1029/1999JC900062, 1999.

Wunsch, C.: Ocean Mixing, pp. 1–30, Oxford University Press, doi:10.1093/acrefore/9780190228620.013.90, 2017.

Wüst, G.: Stratification and Circulation in the Antillean–Caribbean Basins, Columbia University Press, 1, 1964.

Wyrtki, K., Magaard, L., and Hager, J.: Eddy Energy in the Oceans, Journal of Geophysical Research, 81, 2641–2646, doi:10.1029/JC081i015p02641, 1976.

Yavneh, I., Shchepetkin, A. F., McWilliams, J. C., and Graves, L. P.: Multigrid Solution of Rotating, Stably Stratified Flows:, Journal of Computational Physics, 136, 245–262, doi:10.1006/jcph.1997.5775, 1997.

You, Y.: Dianeutral Mixing, Transformation and Transport of Antarctic Intermediate Water in the South Atlantic Ocean, Deep Sea Research Part II: Topical Studies in Oceanography, 46, 393–435, doi:10.1016/S0967-0645(98)00111-8, 1999.

You, Y.: A Global Ocean Climatological Atlas of the Turner Angle: Implications for Double-Diffusion and Water-Mass Structure, Deep Sea Research Part I: Oceanographic Research Papers, 49, 2075–2093, doi:10.1016/S0967-0637(02)00099-7, 2002.

Yu, L., Jin, X., and Liu, H.: Poleward Shift in Ventilation of the North Atlantic Subtropical Underwater, Geophysical Research Letters, 45, 258–266, doi:10.1002/2017GL075772, 2018.

Zhang, R., Sutton, R., Danabasoglu, G., Kwon, Y.-O., Marsh, R., Yeager, S. G., Amrhein, D. E., and Little, C. M.: A Review of the Role of the Atlantic Meridional Overturning Circulation in Atlantic Multidecadal Variability and Associated Climate Impacts, Reviews of Geophysics, 57, 316–375, doi:10.1029/2019RG000644, 2019.

Zhang, Z. and Qiu, B.: Evolution of Submesoscale Ageostrophic Motions through the Life Cycle of Oceanic Mesoscale Eddies, Geophysical Research Letters, 45, 11,847–11,855, doi:10.1029/2018GL080399, 2018.

Zhang, Z., Wang, W., and Qiu, B.: Oceanic Mass Transport by Mesoscale Eddies, Science, 345, 322–324, doi:10.1126/science.1252418, 2014.

Zodiatis, G. and Gasparini, G. P.: Thermohaline Staircase Formations in the Tyrrhenian Sea, Deep Sea Research Part I: Oceanographic Research Papers, 43, 655–678, doi:10.1016/0967-0637(96)00032-5, 1996.

Zweng, M. M., Reagan, J. R., Seidov, D., Boyer, T. P., Locarnini, R. A., Garcia, H. E., Mishonov, A. V., Baranova, O. K., Weathers, K., Paver, C. R., and Smolyar, I.: World Ocean Atlas 2018, Volume 2: Salinity, Tech. rep., Mishonov Technical Ed.; NOAA Atlas NESDIS 82, 2019.

Acknowledgements

This chapter contains additional sources of the data that have been used in this thesis, but are not referred to in the main body or supporting information.

Argo data

The Argo data were collected and made freely available by the International Argo Program and the national programs that contribute to it (http://www.argo.ucsd.edu, http://argo.jcommops.org). The Argo Program is part of the Global Ocean Observing System (Argo, 2020).

cmocean

The figures in this thesis have been made using the cmocean package. More details on this package with efficient and accurate colormaps for oceanography can be found in Thyng et al. (2016).

E.U. Copernicus Marine Service Information

This thesis contains data obtained from E.U. Copernicus Marine Service Information (http://marine.copernicus.eu). This data comprises gridded altimeter products and ocean reanalysis.

Ice-Tethered Profilers

The Ice-Tethered Profiler data were collected and made available by the Ice-Tethered Profiler Program (Krishfield et al., 2008; Toole et al., 2011) based at Woods Hole Oceanogaphic Institution (http://www.whoi.edu/itp).

List of Publications

van der Boog, C. G., Molemaker, M. J., Dijkstra, H. A., Pietrzak, J. D., Katsman, C. A.: Generation of Vorticity by Flow-Topography Interaction: Anticyclones in the Caribbean Sea. Submitted to Journal of Advances in Modeling Earth Systems.

   Parts of this manuscript are discussed in Chapter 3

van der Boog, C. G., Dijkstra, H. A., Pietrzak, J. D., Katsman, C. A.: Double-diffusive fluxes densify Antarctic Intermediate Water in the Caribbean Sea. Submitted to Geophysical Research Letters.

   Parts of this manuscript are discussed in Chapter 7

Kleptsova, O. S., Dijkstra, H. A., van Westen, R. M., **van der Boog, C. G.**, Katsman, C. A., James, R. K., Bouma, T. J., Klees, R., Riva, R. E. M., Slobbe, D. C., Zijlema, M. and Pietrzak, J. D.: Impacts of tropical cyclones on the Caribbean under future climate conditions. Under review for publication in Journal of Geophysical Research: Oceans.

van der Boog, C. G., Dijkstra, H. A., Pietrzak, J. D., Katsman, C. A.: Double-diffusive mixing makes a small contribution to the global ocean circulation. Communications Earth and Environment, 2021.

   Parts of this manuscript are discussed in Chapter 6

van der Boog, C. G., Koetsier, J. O., Dijkstra, H. A., Pietrzak, J. D., Katsman, C. A.: Global dataset of thermohaline staircases obtained from Argo floats and Ice Tethered Profilers. Earth System Science Data, 2021.

   van der Boog, C. G., Koetsier, J. O., Dijkstra, H. A., Pietrzak, J. D., Katsman, C. A.: Data supplement for 'Global dataset of thermohaline staircases obtained from Argo floats and Ice Tethered Profilers.' (Version 1, Data set). Zenodo, 2020.

   Parts of these publications are discussed in Chapter 5

Georgiou, S., Ypma, S. L., Brüggemann, N., Sayol, J. M., **van der Boog, C. G.**, Spence, P., Pietrzak, J. D. and Katsman, C. A.: Impact of direct and indirect pathways of water masses found in the Labrador Sea on its overturning dynamics. Journal of Geophysical Research: Oceans, 2021.

Keyzer, L. M., Herman, P. M. J., Smits, B. P., Pietrzak, J. D., James, R. K., Candy, A. S., Riva, R. E. M., Bouma, T. J., **van der Boog, C. G.**, Katsman, C. A., Slobbe,

D. C., Zijlema, M., van Westen, R. M., and Dijkstra, H. A.: The potential of coastal ecosystems to mitigate the impact of sea-level rise in shallow tropical bays. Estuarine, Coastal and Shelf Science, 2020.

Van Westen, R. M., Dijkstra, H. A., **van der Boog, C. G.**, Katsman, C. A., James, R. K., Bouma, T. J., Kleptsova, O. S., Klees, R., Riva, R. E. M., Slobbe, D. C., Zijlema, M. and Pietrzak, J. D.: Ocean model resolution dependence of Caribbean sea-level projections. Scientific Reports, 2020

James, R. K., Lynch, A., Herman, P. M. J., van Katwijk, M. M., van Tussenbroek, B. I., Dijkstra, H. A., van Westen, R. M., **van der Boog, C. G.**, Klees, R., Pietrzak, J. D., Slobbe, D. C., and Bouma, T. J.: Tropical biogeomorphic seagrass landscapes for coastal protection: persistence and wave attenuation under major storm events. Ecosystems, 2020.

Haakman, K., Sayol, J. M., **van der Boog, C. G.**, and Katsman, C. A.: Statistical characterization of the observed cold wake induced by North Atlantic hurricanes. Remote Sensing, 2019.

van der Boog, C. G., Pietrzak, J. D., Dijkstra, H. A., Brüggemann, N., Van Westen, R. M., James, R. K., Bouma, T. J., Riva, R. E. M., Slobbe, D. C., Klees, R., Zijlema, M. and Katsman, C. A.: The impact of upwelling on the intensification of anticyclonic ocean eddies in the Caribbean Sea. Ocean Science, 2019.

Parts of this publication are discussed in Chapter 4

van der Boog, C. G., de Jong, M. F., Scheidat, M., Leopold, M. F., Geelhoed, S. C. V., Schulz, K., Dijkstra, H. A., Pietrzak, J. D. and Katsman, C. A.: Hydrographic and biological survey of a surface-intensified anticyclonic eddy in the Caribbean Sea. Journal of Geophysical Research: Oceans, 2019.

Parts of this publication are discussed in Chapter 2

James, R. K., Silva, R., van Tussenbroek, B. I., Escudero-Castillo, M., Mariño-Tapia, I., Dijkstra, H. A., van Westen, R. M., Pietrzak, J. D., Candy, A. S., Katsman, C. A., **van der Boog, C. G.**, Riva, R. E. M., Slobbe, C., Klees, R., Stapel, J., van der Heide, T., van Katwijk, M. M., Herman, P. M. J. and Bouma, T. J.: Maintaining tropical beaches with seagrass and algae: A promising alternative to engineering solutions. BioScience, 2019.

Georgiou, S., **van der Boog, C. G.**, Brüggemann, N., Ypma, S. L., Pietrzak, J. D., and Katsman, C. A.: On the interplay between downwelling, deep convection and mesoscale eddies in the Labrador Sea. Ocean Modelling, 2019.

Van Westen, R. M., Dijkstra, H. A., Klees, R., Riva, R. E. M., Slobbe, D. C., **van der Boog, C. G.**, Katsman, C. A., Candy, A. S., Pietrzak, J. D., Zijlema, M., James, R. K. and Bouma, T. J.: Mechanisms of the 40-70 day variability in the Yucatan Channel volume transport. Journal of Geophysical Research: Oceans, 2018.

Curriculum Vitae

Je verwacht het nooit van
kinderen, maar sommigen van hen
worden zeer saaie volwassenen.

Nicolien Mizee

April 27, 1992	Born in Nieuwegein, the Netherlands
2004-2010	Adelbert College Wassenaar
2010-2013	Bachelor of Science in Architecture (cum laude) Delft University of Technology
2013-2014	Bridging program Architecture to Civil Engineering Delft University of Technology
2014-2016	Master of Science in Civil Engineering and Geosciences (cum laude), Delft University of Technology
2016-present	PhD candidate at Environmental Fluid Mechanics Delft University of Technology